An "InCLOSE" View of the Circumgalactic Medium of $z \sim 2$ Star-Forming Galaxies

Thesis by

Evan Haze Nunez-Cravin

In Partial Fulfillment of the Requirements for the
Degree of
Ph.D. in Astrophysics

Caltech

CALIFORNIA INSTITUTE OF TECHNOLOGY
Pasadena, California

2025
Defended May 23, 2025

Evan Haze Nunez-Cravin
ORCID: 0000-0001-5595-757X

ACKNOWLEDGEMENTS

First and foremost, I would not be writing this thesis if it were not for the life-long, consistent, unwavering support from my family. Specifically, Rosalind Cravin, my hard-working mother who single handedly raised me and continues to support me at every step of my life journey; Yvonne Cravin, my loving but no-bs grandmother who reminds me of the importance parts of life e.g., growing old is a privilege denied to many; Roland Haze Cravin, my kind and forward-thinking grandfather (the namesake of my middle name) whose last words to my little brother and I were to shoot for the stars then keep going; Bryan Lamar Souice, my little brother who continues to inspire me through his dedication and focus on nurturing relationships, bringing purpose to his work, and insistence on looking at the bright side; my aunties Renee Cravin, Yolanda Cravin, and Katrina Cravin who have always make it crystal clear how loved I am and if I ever need *anything* that they would move hell and high water to make it happen; my cousins Destinee and Jason Roberts, Victor Vallar and Shani Vallar, for keeping me sane, laughing, and grounded as we continue this journey called life.

Thank you to my three chosen brothers, Trevor (James) Williams, Jonathan Tecumseh Wright, and Trevor Lewis who have supported me since as early as middle school through hilarious conversations, late night talks, four years of football, family events, and life events including being groomsmen for my wedding.

Thank you to the friends that I have made along my academic journey who have always taken the time to spend time and stay close even though we have had years to grow apart, especially my groomsmen Justin Fuller, Dr. Alex Polanski, and Dr. Daniel Mukasa, but also Yra, Christina, Jose, Bianca, Jose, David, and DJ.

Thank you to my academic, professional, and research mentors that have always made me feel welcome in spaces that were not designed for people of my background; African-American and Mexican, single parent household, low-middle socioeconomic status, community college alumni, and public school education. Specifically, Matthew Werber, Shimonee Kadakia, Susan Stolovy, Perry Hacking, Leon Palmer, Matthew Povich, Breanna Binder, Robin Wilson, Alex Rudolph, and Carol Hood.

Thank you to my PhD advisors Evan Kirby and Chuck Steidel who always had faith in me, pushed me, and supported all of my academic endeavors that were both in and out of my dissertation, including my involvement with the Caltech Astro

Outreach Team and heavy involvement in the Black Scientists and Engineers of Caltech (BSEC). Thank you to my thesis committee Phil Hopkins, Mansi Kasliwal, Gregg Halinan, and Chris Martin for helping guide me through this thesis and offering the support to make it something to be proud of.

Huge thanks to my class: Dr. Samantha Wu (best roommate I have ever had!), Dr. Zhuyun Zhuang, Dr. Sarah Blunt, Dr. Max Goldberg, Dr. Viraj Karambelkar, Yashvi Sharma, Jean Badroos, and Jordan Benjamin. Thanks to the folks not in my class including Mia de Los Reyes, Ryan Rubenzahl, Sam Ponnada, Adolfo Carvalho, and Cam Jackson, who helped make this journey so much more enjoyable. Thank you to Gita Patel, Judy McClain, Mika Walton, and Nam Ung for quick reimbursements and running all of PMA. A huge thanks to BSEC (Black Scientists and Engineers of Caltech) and the Black @ Caltech organization, Tom Henning, Jasmine Emtage, and Sarah Weisflog, who have been putting in the work to keep the Conference for Emerging Black Academics in STEM (CEBAS; also thanks to the continued support from Tashiana Bryant-Myrick that made this a reality) going from its inception when we built it together in 2023.

A huge thanks to all of the students that I have gotten the honor and privilege to mentor through the WAVE Council (big thanks for Maria Manzanares), FSRI, SURF, and the FAST workshop (thanks to you Dr. Nicole Sanchez for creating the program); you all have brought so much meaning to work. Especially my first two research students Dilichi Nwankwo (Caltech '25) and America Luna (Caltech '25), and my most recent and longest supported research student Charis Hall (Caltech '27). I am thankful for the continued support from the Cal-Bridge program for support from community college all the way through PostDoc (and hopefully beyond)..

Last, but certainly not least, a sincere and special thank you to my soon to be wife, Rataẽja Antoinette Sholes-Cravin who has technically been supporting me since elementary school, but most recently has been a pillar of support since my second year in community college when a PhD felt so...distant, before I got sick both physically and mentally, before I lost myself and needed help to save myself, and th–apologies, I must end here otherwise I would not be able to stop so just...thank you.

In honor of José Flores-Velásquez and Dr. Leisa Townsley.

Collectively, these years have impacted my outlook on the most important consideration when conducting science-the deeply personal voyage of scientific inquiry

must always keep human well being as a compass.

ABSTRACT

This thesis focuses on using diffuse gas to investigate the galactic chemical evolution and circumgalactic medium of galaxies near the peak of cosmic star-formation rate density $z \sim 2$. There are many fundamental questions that remain unanswered about these processes due to the lack of large observational samples including what the typical yields of massive stars are, the interplay between diffuse circumgalactic and dense interstellar gas in terms of kinematic complexity, metal content, stellar mass, and star formation rate, and the evolution of circumgalactic gas over cosmic time. The common thread between each investigation is the use of QSO absorption line objects (QSO absorbers) to probe diffuse gas that otherwise would be unseen due to its diffusivity. The chemical evolution of galaxies requires accounting for all sources of nucleosynthesis. During the earliest stages of galactic chemical evolution, the metal yields from core-collapse supernovae (CCSNe) are very important but acquiring empirical constraints is difficult because they cannot be easily disentangled from objects that currently exist because they have been enriched by some fraction of CCSNe and late time nucleosynthetic processes e.g., Type Ia SN. To address this, I used the metal abundances of very-metal poor (VMP; $[\mathrm{Fe/H}] < -2$) Damped Lyman Alpha Absorbers (DLAs; QSO absorbers with high H I column density comparable to the interstellar medium, $\log{(N_{\rm HI}/\mathrm{cm}^{-2})} > 20.3$) to place empirical constraints on the yields of low-metallicity CCSNe. I found that this approach is comparable to, and sometimes superior to, using abundances from the atmospheres of metal poor stars because of the model-independent nature of measuring abundances from dense, cold gas provided by the DLA. It has been known in the literature that DLAs and other QSO absorbers have a variety of origins so I began an observational campaign to find galaxies associated with QSO absorbers that would allow detailed analysis of the circumgalactic medium (CGM) of $z \sim 2$ galaxies. This has historically been challenging at all z, but especially at $z \sim 2$ where, before this thesis, there were only nine galaxies with their inner CGM analyzed (within a projected distance of 100 kpc) *and* with characterized nebular emission and stellar population properties. To this end, I am leading a survey that builds on the Keck Baryonic Structure Survey (KBSS) that aims to find close-in galaxy-QSO pairs to directly connect the Inner CGM of QSO Line Of Sight Emitting (InCLOSE) galaxies with their ISM. KBSS-InCLOSE relies on new observations that I have conducted using the twin Keck telescopes on Mauna Kea in Hawaii. I use the new optical integral field unit (rest-

FUV at $z \sim 2.3$) called KCWI to discover new "InCLOSE" galaxies; obtain follow Keck/MOSFIRE near infrared (NIR) spectroscopy to confirm their redshifts and infer nebular properties including star-formation rate; use ground- and space-based optical and NIR images to infer stellar mass and age; and finally use high-resolution optical spectra of the KBSS QSOs to perform detailed analysis of CGM gas seen as absorption in the QSO spectra. The novelty of KBSS-InCLOSE goes beyond its large size (55 galaxies currently); the NIR spectra and images allow for the direct determination of galaxy properties, including stellar mass, which are rarely included in similar high-z surveys. The first results from KBSS-InCLOSE showcased the tools and techniques required to remove the bright QSOs from the datacubes, images, and spectra to reveal new faint, close-in galaxy-QSO pairs. Particular focus was payed on the processing of the IFU data because it serves as the main driving instrument for the survey since it provides both images and spectra of each galaxy in the field. By analyzing their CGM absorption, I showed that a $M = M_* = 10^{10}\ M_\odot\ z = 2.43$ galaxy exhibited strong, multiphase, kinematically complex, and gravitationally unbound metals in its CGM. This has been seen before in previous studies and may suggest that a consensus picture of the CGM of $z \sim 2.3$, M_* galaxies is emerging. In KBSS-InCLOSE II, I focused on the first low-mass galaxies examined in the sample. I showed that the galaxies were star-forming, at the same redshift, and had sizes and masses consistent with dwarf galaxies, and found preliminary insights into the low-mass CGM that would make it distinct from both the massive $z \sim 2$ CGM and low-mass local CGM suggesting that there may be strong evolution of the CGM across both stellar mass and redshift. In Chapter 5 I preview work that is yet to be completed, KBSS-InCLOSE III, where I examined the entire sample showing that the $z \sim 2$ CGM often shows strong of metal absorption, is likely clumpy, and multiphase, and that future IFU follow-up is necessary to find more galaxies, and NIR spectroscopic follow-up is necessary to secure redshifts to mitigate mismatches between galaxy's and absorbers.

Altogether, this thesis has laid fundamental groundwork towards expanding our understanding of the galaxy-scale baryon cycle of $z \sim 2$ star-forming galaxies by building the largest $z \sim 2$ close-in galaxy-QSO pair observational dataset thus far. It provides the data required to perform the most detailed examination of the connection between galaxies and their CGM during the peak epoch for galaxy formation.

PUBLISHED CONTENT AND CONTRIBUTIONS

Nuñez Evan H., Kirby Evan N., Steidel Charles C. Empirical Constraints on Core-collapse Supernova Yields Using Very Metal-poor Damped Lyα Absorbers // . III 2022. 927, 1. 64.

Nuñez Evan Haze, Steidel Charles C., Kirby Evan N., Rudie Gwen C., Prusinski Nikolaus Z., Chen Yuguang, Zhuang Zhuyun, Strom Allison L., Erb Dawn K., Pettini Max, Welsh Louise, Rupke David S. N., Cooke Ryan J. KBSS-InCLOSE. I. Design and First Results from the Inner Circumgalactic Medium of QSO Line-of-sight Emitting Galaxies at z ~ 2–3 // . XI 2024. 976, 1. 41.

TABLE OF CONTENTS

LIST OF ILLUSTRATIONS

LIST OF TABLES

NOMENCLATURE

Circumgalactic Medium (CGM). Diffuse, gravitationally bound gas that surrounds galaxies. Typically bound by the virial radius (R or the radial distance where the density is greater than 200 times the critical density of the universe (R_{200}).

Intergalactic Medium (IGM). Diffuse gas in between galaxies typically seen as foreground absorption of bright background objects..

Interstellar Medium (ISM). Gas and dust that are in between stars in a galaxy that can be seen in various phases across a wide range of temperatures ($T \sim 10 - 10^6$ K) and densities ($n = 0.1 - 100\ atoms\ cm^{-3}$)..

Quasi Stellar Object (QSO). Also known as a Quasar or Quasi stellar radio source. QSOs are galaxies with actively feeding supermassive black holes in their nuclei whose accretion disks completely outshine the entire galaxy. As a result, they look like point sources (i.e., stars) and require a spectrum to confirm their nature..

Chapter 1

DIFFUSE GAS AND THE CIRCUMGALACTIC MEDIUM IN THE CONTEXT OF GALAXY EVOLUTION

Studying how galaxies evolve over cosmic time is fundamental to understanding the Universe as we see it today. Decades of galaxy interstellar medium (ISM) investigations across all masses and epochs have shown that baryons must be flowing both in and out of the ISM. For example, the fact that galaxies are star-forming throughout cosmic time suggests that the ISM must be constantly refueled with gas, and the fact that the ISM does not contain all of the mass predicted by the halo-to-baryon fraction in ΛCDM suggests that there is "missing" gas in the halo. This implies there must be a galaxy-scale cycle where baryons flow through a massive reservoir of gas outside of the ISM: the circumgalactic medium (CGM. Indeed, the 2020 Decadal Survey of Astronomy and Astrophysics highlighted the CGM in the steps towards "Unveiling the Hidden Drivers of Galaxy Growth." Therefore, the CGM is pivotal in understanding the galaxy-scale baryon cycle, which itself is understanding galaxy evolution.

It has been shown that the majority of gas associated with a galaxy resides in the CGM (Tumlinson et al., 2017). This is even more important for galaxies at the cosmological peak of star formation ($z \sim 2$) because they ubiquitously show strong outflows that will enrich the CGM (and/or the intergalactic medium; IGM) with mass and metals. Short gas depletion timescales suggest there must be inflowing gas from the C/IGM that will fuel future star formation (McGaugh et al., 2010; Shapley, 2011; Steidel et al., 2010). This process by which baryons transition through different phases (Temperature T, density ρ) and mass reservoirs (ISM, CGM, IGM) during a galaxy's star formation history (SFH) is known as the galaxy scale baryon cycle. The CGM is a crucial interface whose physical properties must be observationally constrained to understand the galaxy scale baryon cycle, which drives the gas supply for star formation (Faucher-Giguère, Oh, 2023), metal budget (Anglés-Alcázar et al., 2017), and total baryonic mass (Werk et al., 2014).

Observing the CGM directly is difficult because its diffusivity reduces emission flux well below the typical flux of the ISM. This makes it difficult to detect unless the galaxy is nearby, and/or bright emission lines are targeted (e.g., Lyα). Instead, one must rely on bright background objects to see the diffuse halo gas in absorption, also known as Quasi Stellar Object (QSO) absorption line objects (see next section). Care must be taken when using QSO absorption line objects because they can have origins besides the CGM, such as the ISM of disk galaxies, IGM gas, and more (e.g., Wolfe et al., 1986).

1.1 A Brief History of QSO Absorption Line Objects

QSO absorption line systems (QSO absorbers hereafter) were discovered very soon after the discovery of QSOs by Maarteen Schmidt (Caltech Alumni) in 1963 (Schmidt, 1963). Schmidt used the Caltech owned and operated 200-inch Hale Telescope at Palomar Observatory to acquire and analyze the spectrum of a bright radio source known as 3C 273. The spectrum, taken with the prime-focus spectrograph, showed that it was a “Star-Like Object with Large Redshift.” 3C 273 was the highest redshift object discovered at the time at $z = 0.158$.

The nature of QSOs was shrouded in mystery for a while but we now know that they are galaxies with actively feeding supermassive black holes that are accreting gas very close to the stable limit before it blows itself apart known as the Eddington limit. This results in such bright emission from the accretion disk that it outshines the rest of the galaxy.

For this thesis, QSOs are essential because they are bright point sources that can be used to observe intervening gas absorption at high-redshifts. In general, QSO absorbers are most easily detected by absorption of Lyα blueward of the QSO emission peak because neutral Hydrogen (H I or H^0) is likely to be the most abundant ion in the absorber. Is also common to detect metal absorption lines at the same z as H I.

Absorbers can be characterized by their H I column density ($N_{\rm HI}$ [cm^{-2}]) and metal content. Table 1.1 lists the various types of QSO absorbers including Damped Lyman Alpha Absorbers (DLAs), sub-DLAs, Lyman Limit Systems (LLS), partial LLS, Super Lyman Alpha Forest Systems (SLYF), and Lyman Alpha Forest (LYF) objects. The last column shows their rough number density in the sky which is calculated by determining how many QSOs have aborbers of a given $\log N_{\rm HI}$ between $z \sim 2 - 6$ towards them. The DLA number density is from from the SDSS IV DR16 version of the Extended Baryon Oscillation Spectroscopic Survey (eBOSS) (Chabanier et al., 2022) which searched 263,201 spectra for high-$\log N_{\rm HI}$ absorbers. The sub-DLA (or SLLS) incidence rate was calculated from (O’Meara

Name	$\log{(N_{\rm HI}/cm^{-2})}$	Incidence[a]
Damped Lyman Alpha Absorbers (DLAs)	≥20.3	0.22
sub-DLA[b]	19-20.3	0.42
Lyman Limit System (LLS)[c]	17.2-19	$\sim 0.5^d$
Partial LLS (pLLS)	16.2-17.2	$\sim 0.7^d$
Super Lyman Alpha Forest (SLYF)	14.5-16.2	0.79
LYF[e,d]	<14.5	~ 1

Table 1.1: QSO absorber phenomenology.

a) Fraction of QSOs that have at least one absorber of a given $N_{\rm HI}$ towards it within $z_{\rm QSO} = 2 - 6$.

b) Also known as a Super Lyman Limit System (SLLS).

c) This $N_{\rm HI}$ results in optically thick gas at the Lyman Limit or 912 Å.

d) Interpolating between SLYF and sub-DLA due to lack of exact numbers.

e) Diffuse IGM densities.

et al., 2007). The column densities vary by 7 orders of magnitude: from those typical of the intergalactic medium (i.e., LYF or $\log N_{\rm HI} \leq 14.5$) to those typical of the dense ISM (i.e., DLA or $\log N_{\rm HI} \geq 20.3$). It is much more rare to find DLAs compared to lower $N_{\rm HI}$ absorbers.

The first systematic search for DLAs was carried out by Arthur Wolfe in 1986 at Lick Observatory with the goal of trying to study neutral gas in the ISM of high-z galaxies (Wolfe et al., 1986). During that time, it was generally thought that DLAs were the disks of galaxies; this was reasonable given that the H I column densities were comparable to the MW ISM $\log{(N_{\rm HI}/{\rm cm}^{-2})} \geq 20.3$ and some abundance ratios found in DLAs were reminiscent of the cold neutral ISM. We now know that DLAs can have many origins including dense CGM gas, the ISM of dwarf galaxies, stripped gas from mergers, and outflowing gas from stellar and/or black hole feedback. This leads to a rather intuitive physical picture of DLAs; they exist whenever there is a large concentration of H I and a bright background source to "illuminate" it.

DLAs have been used in the literature for studies ranging from stellar astrophysics (e.g., Nuñez et al., 2022; Pettini, 2011; Welsh et al., 2020), high-z ISM studies (e.g., Pettini et al., 1997), and precision cosmology (e.g., Cooke et al., 2016; O'Meara et al., 2001). DLAs are large reservoirs of H I, the precursor for the cold molecular phase of Hydrogen or H_2 that is required for star formation. Various studies have leveraged this fact to place constraints on the cosmic amount of star-forming gas as a function of redshift compared to cosmological predictions (e.g., Prochaska et al., 2005; Wolfe et al., 2003).

Due to their many uses, considerable effort has been put into finding more DLAs with various properties including H I column density, metallicity, and redshift. To date there are at least half a dozen surveys that have been conducted on 10-m class telescopes including the IUE Survey for DLAs (Lanzetta et al., 1995b), UCSD/Keck DLA survey (Prochaska et al., 2007b), KODIAQ survey (O'Meara et al., 2015), and the UVES Spectral Quasar Absorption Database (SQUAD) (Murphy et al., 2019).

DLAs are powerful for metal studies because their large H I column shields the gas from the extragalactic ultraviolet background , which significantly simplifies the determination of metallicity because partial ionization effects are minimal (Cooke et al., 2011b). As a result, DLAs have been used to estimate the cosmic abundance of metals over time, which can give strong constraints on the so called "cosmic baryon cycle" (Péroux, Howk, 2020) which describes the various phases (T, ρ) through which baryons transition during the Universes history.

Chapter 2 of this thesis demonstrates how metal abundances from metal-poor DLAs can be used to place empirical constraints on the metal yields of core-collapse supernovae. The main underlying assumption for this work is that regardless of the origin of the gas, it is early enough in the star formation history of the system that it has been primarily enriched by CCSNe and has minimal enrichment from delayed enriching events, such as AGB winds. The analysis showed that there were many abundance ratios that were better constrained with metal poor DLAs compared to metal-poor stars, which are more traditional sites for this type of research.

DLA self-shielding has another consequence: it allows for the survival of ions with low ionization potential that have different condensation temperatures. These ions (e.g., Fe II, Zn II) are useful for determining the amount of dust present in the absorber as long as the ions track each other nucleosynthetically and have very different condensation temperatures. Indeed, several authors have leveraged large, growing DLA surveys to place constraints on cosmic dust abundances as a function of redshift by using a combination of high-N_{HI} absorbers detected in the the MW, massive stars towards the LMC, and towards QSOs and gamma ray bursts (GRBs) (e.g., De Cia et al., 2016; Konstantopoulou et al., 2022; Ramburuth-Hurt et al., 2023).

Low-H I absorbers are typically highly ionized by the UVB, which becomes a significant source of uncertainty when trying to determine metal abundances and ratios due to their strong dependence on ionization parameter (e.g., Zahedy et al., 2021). Therefore, ionization modeling of low-H I absorbers is required to convert from observables (column density, Dopper width) to physical quantities (metallicity, H density). A more important uncertainty is associating metal absorption with individual H I components due to the large broadening of H I from its low mass, at $T \sim 2 \times 10^4$ K, $b_{\rm HI} \sim 18$ km s^{-1}. In this scenario, it is ideal to have ratios of ions of successive ionization (e.g., C II/C III, Si II/Si III, Al II/Al III) to directly measure the ionization parameter. Unfortunately, there is no guarantee that these ions will be detected in the halo so most studies rely on using average quantities instead of a component by component approach (e.g., Lehner et al., 2022).

The ground work for analyzing low-HI systems is laid out in this thesis but will be left to future work for more thorough modeling. Instead, I focus on the model-independent observables for both the high- and low-HI absorbers and analyze them under the assumption that they are associated with galaxies. As will be discussed in the next section, the connection between galaxies and QSO absorbers has been established since the very early days of QSO absorption line spectroscopy.

1.2 Our Evolving View of the Circumgalactic Medium

In 1956, Lyman Spitzer (Spitzer, 1956) hypothesized that the detection of neutral sodium (Na I) by Münch, Zirin (1961) suggested that there may be a (hot) medium of high pressure that kept the cold Na I clouds in pressure confinement. Spitzer suggested that this hot medium might be a "galactic corona", analogous to the solar corona, at least 8 kpc from the plane of the galaxy, temperature of $T \sim 10^6$ K, with a low e^- density of $n \sim 10^{-4}$ cm^{-3}. This hypothesis is remarkably accurate in the context of what we know today.

Indeed, the most direct evidence that gravitationally bound mass exists outside the disk of the MW is through the observations of high-velocity clouds (HVCs) at high galactic lattitudes. The first of such observations were conducted by Muller et al. (1963), who suggested that the HVCs are part of the galactic corona. HVCs are detected in the foreground spectra of massive stars and QSOs, including sightlines to the SMC and LMC. There is currently no consensus on the origin of HVCs except that they all contain H I and have radial velocities that deviate significantly from the galactic disk rotation velocity $\Delta V_{LSR} \gtrsim 90$ km s^{-1} (Wakker, van Woerden, 1997). HVCs may not have a single origin and instead may be explained by an ensemble of physical scenarios including the Magellenic Stream (the ram pressure stripped gas from the SMC) (Olano, 2004), extended features in an extended galactic arm (Wakker, van Woerden, 1997), infalling gas from the C/IGM (Blitz et al., 1999; Choi et al., 2024), and/or outflowing gas from recent stellar feedback (Fox et al., 2019). Regardless of the open questions surrounding HVCs and their origins, these studies established that there is indeed diffuse gas outside of the disk.

The CGM is now known to be very diffuse with typical densities between $n_{CGM} \sim 10^{-1} - 10^{-5}$ cm^{-3} (or 10^{15-19} cm^{-2}) which are several orders of magnitude more diffuse than the cold neutral and molecular ISM $n_{\rm ISM}$ $10^0 - 10^2$ cm^{-3} (or $\sim 10^{20-22}$ cm^{-2}) (Draine, 2011; Tumlinson et al., 2017). This diffusivity poses an observational challenge because the gas does not abundantly emit photons. Even using the world's largest telescopes, e.g., the twin Keck telescopes, requires more than 5 hours of exposure to get down to the sensitivity limits $SB \lesssim 10^{-21} - 10^{-19}$erg s^{-1} cm^{-2} arcsec^{-2} required to directly detect the CGM in non-resonant line emission. Though this is the ideal method to study the CGM, it is only practical for nearby galaxies (e.g., Cameron et al., 2021) or when searching for resonant line emission like Lyα (e.g., Chen et al., 2021).

Most studies of the CGM rely on using background sources to "illuminate" the diffuse gas. This background object could be the galaxy itself, a gamma ray burst/fast radio burst (GRB/FRB), or a star/QSO. Using the host galaxy to illuminate its own CGM is tantalizing because only a spectrum is required; the downside is that it is difficult, if not impossible, to determine whether the gas is circumagalactic or interstellar because the final spectrum is integrated along the line of sight between the observer and the emitting gas (i.e., there is no depth perception). Using foreground galaxy-background galaxy pairs, in which the background galaxy light is used to illuminate the foreground galaxy CGM, removes this ambiguity because it allows for the direct measurement of an impact parameter b or transverse distance from the foreground galaxy to the background galaxy ($D_{\rm Tran}$). This method has the benefit of allowing multiple sightlines through the same galaxy halo (assuming that the field is dense with background galaxies with spectroscopic coverage) with the main limit being the volume that the observations cover and the SNR of each galaxy observation.

Using transients (GRBs/FRBs) to probe CGM gas is a recent approach that offers albeit brief but otherwise unavailable sightlines through CGM gas that offer constraints on historically difficult quantities to infer including electron density; the downside is that their transient nature and heavy model dependence make them slightly unreliable, but it is likely that over the years they will become incredibly important and complimentary to current probes. Using a bright star/QSO offers almost all of the benefits of transients but with the ability to get much higher quality spectra (integrate longer). The main caveat with all of these methods is that they show only a single sightline through the halo, which may or may not be representative of the whole CGM. This implies that this method shines when there is a large statistical sample ($N \geq 50$) that can smooth over the stochasticty of the sightlines, which can be influenced by azimuthal angle from the galaxy's major axis, recent star formation, and inhomogeneities in the vicinity of the sightline.

QSO absorbers have been used to study the CGM of galaxies since the mid-80's (e.g., Bergeron, 1986) with continued effort through the 90's from Keck and *HST* (e.g., Lanzetta et al., 1995a). The surveys showed that the presence of a galaxy along the line of site is accompanied by enhanced H I and metal absorption and that the gas has distinct kinematic, density, and ionization structure from other absorbers (Chen et al., 1998).

Observational campaigns in the mid-90's further explored the connection between QSO absorbers and nearby galaxies. In particular, Steidel et al. (1995) searched for the host galaxies of strong Mg II and Fe II absorption complexes at $z \sim 2 - 3$. In an effort to more efficiently find candidate galaxies, they experimented with a technique that used the Lyman break of galaxies to find high-redshift candidates that could be followed up spectroscopically. This experiment effectively spawned the field of high-redshift galaxies. This method of targeting strong spectral features using multiple bands of photometry is now a main staple for searching for galaxies of all z (e.g., Finkelstein et al., 2022). Even with this incredibly efficient means of finding new galaxies, there was still a dearth of galaxies within small projected distances to background QSOs.

During the early 2000's, the Sloan Digital Sky Survey (SDSS) furthered and challenged our understanding of galaxy evolution using the large number of galaxy spectra it obtained (York et al., 2000). In particular, McGaugh et al. (2010) used a sample of $\sim 50,000$ SDSS galaxies across multiple decades of dark matter (DM) halo masses to show that when converting the DM to the theoretical prediction for baryonic mass ($\Omega_b/\Omega_m = 0.16$; Planck Collaboration et al., 2020), galaxies are missing more than $\sim 80\%$ of their predicted baryonic mass. Since the cosmological parameters are known to better than a percent there must be a significant amount of mass that is being missed due to the density and/or phase of the gas. Furthermore, Tremonti et al. (2004) used a sample 53,000 galaxies across a similarly wide mass range and constructed the largest (at that time) mass-metallicity relation to show conclusively that galaxies are missing a large fraction ($\sim 80\%$) of all of the metals that they ever produced. It is now accepted that this mass was lost via stellar feedback and/or SMBH feedback driven outflows, further adding evidence that there is a significant amount of mass that is both diffuse and in a different phases than the ISM. Along with this, the gas depletion timescales ($t_{dep} = M_{\rm HI+\mathit{H2}}/\mathrm{SFR}$) of local (e.g., Kennicutt et al., 1994) and high-z (e.g., Shapley, 2011) galaxies show that the ISM must have been constantly replenished with gas during its star formation history because depletion timescales are a fraction of the age of the galaxies (Peeples et al., 2014). The evidence up to this point suggests that accounting for the CGM is necessary for measuring a correct baryon mass, fully accounting for the metal budget, and for sustained star formation of a galaxy.

In the early 2010's, COS-HALOS set out to find nearby $z \sim 0.3$ MW-mass galaxy-QSO pairs to expand our understanding of the CGM and how it connects to and affects galaxy evolution. The team used the *HST*/COS spectrograph to acquire spectra of 39 QSOs within $R < 160$ kpc of 44 L_* star-forming and passive galaxies (Tumlinson et al., 2013). At the time this was the largest sample of $z \sim 0.3$ galaxy-QSO pairs within $b < 2R_{\rm vir}$ ever constructed. Some of the key results from the COS-HALOS survey were (1) the CGM is highly ionized by the UVB as seen in the volume density of H I, has a near unity covering fraction of cool ($T \sim 10^4$ K) photoionized H I gas (Werk et al., 2014), (2) there exists intermediate-high ionization gas out to multiple $R_{\rm vir}$ in star-forming galaxies but the halos of quiescent galaxies lacked such gas (Tumlinson et al., 2011), (3) the halos of dwarf galaxies lack low-ionization metal absorption (Bordoloi et al., 2014; Johnson et al., 2017), and (4) accounting for all phases of the CGM (cool, warm , hot) significantly reduces or eliminates the "missing baryons" and "missing metals" problems (Werk et al., 2013).

The recent DIISC Survey (Deciphering the Interplay between the Interstellar medium, Stars, and the Circumgalactic medium) is shedding light on the ISM-CGM transition, a region where one would expect strong imprints of stellar and/or SMBH feedback onto the CGM (Gim et al., 2021). The low-z survey ($z \leq 0.051$) is composed of 35 M_* galaxies with a QSO within $b \leq 200$ kpc or $b < 3.5R_{\rm HI}$ with unique, evenly sampled azimuthal angles and H I mass and disk measurements. The survey has shown that (1) strong correlations between CGM properties (e.g., $W_{\rm Ly\alpha}$) and impact parameter are revealed when normalized by $R_{\rm HI}$ as opposed to $b/R_{\rm vir}$, (2) the neutral gas in the CGM is closely connected to the gas disk as opposed to its stellar or DM content as inferred from a strong anti-corelation between $W_{\mathrm{Ly}\alpha}$ and b/R_{HI} (Borthakur et al., 2015, 2024), (3) the CGM has more kinematically complex metal absorption components with small b/R_{HI}, and (4) there is a rapid decline in metal covering fraction of low-ionization metal absorption (e.g., Si III, C II, Si II) with b_{HI} and absorption strength (as inferred through equivalent width) (Koplitz et al., 2025).

At low-z one can use the many all-sky surveys to find new close-in galaxies to background QSOs. One can leverage the crude spectra from the surveys as motivation to follow up the galaxies with higher-S/N data. But it is difficult to acquire QSO spectra with Lyα because it requires space-based coverage due to the atmospheric UV cutoff. At higher z, it becomes more challenging to find survey coverage with sufficient depth to find close-in galaxies but possible to observe Lyα absorption due to cosmological redshift. The recent commissioning of large-field of view (FOV) integral field unit (IFU) spectrographs on 10-m class telescopes has resulted in a significant increase in the the number of close-in galaxies within a few R_{vir} of background QSOs. IFUs are the most efficient means at finding these galaxies because each pixel (called a "spatial pixel" or spaxel) contains a spectrum of the source which allows for the determination of a redshift. The rest of the surveys discussed have leveraged IFUs on large telescopes to accelerate the discovery of galaxies surrounding QSOs.

The CUBS survey (Chen et al., 2020a) is focused on mapping the extended baryons of $z < 1$ galaxies, giving an in-depth view of the CGM approaching "cosmic noon." The galaxies in the sample are within $b \leq 300$ kpc of a NUV-bright QSO with *HST*/COS coverage, and each QSO field has VLT/MUSE, and deep imaging and spectroscopic coverage from the twin Magellan telescopes allowing for detection limits down to $L \leq 0.01L_*$. The nine papers published from CUBS have shown that (1) the $z \sim 1$ CGM has multi-component kinematic structure from multiple ionization states including C II, Mg II, Si III, and O VI, spread over hundreds of km s^{-1}, (2) the $z \sim 1$ CGM has dynamically cold gas $T \sim 2 \times 10^4$ K and $b_{\mathrm{turb}} \sim 5$ km s^{-1}, (3) the metallicity of CGM gas can vary significantly on a component-by-component basis by over 2 dex (Cooper et al., 2021; Zahedy et al., 2021), (4) non-thermal broadening dominates line widths (compared to thermal broadening) (Qu et al., 2022), (5) complexity and incidence of CGM metals are increased in galaxy groups compared to individual galaxies (Qu et al., 2023), (6) star-forming and low-mass galaxies show elevated presence of warm-hot gas as seen in O VI and Ne VIII, (7) low-mass/dwarf galaxies frequently show H I and O VI absorption but seldom show low- and intermediate-ionization absorption, and (8) CGM gas is seldom gravitationally unbound (within $R_{\rm vir}$).

The BASIC survey (Bimodal Absorption System Imaging Campaign) is a galaxy-absorber survey focused on investigating the bimodality seen in $z \sim 1$ LLS and SLLS (Lehner et al., 2022). The survey consists of 23 QSO fields and 36 p/LLS, which resulted in 23 absorber-associated galaxies. They found that the higher-metallicity absorbers were much more likely to have a galaxy associated with them ($\sim$ 80%) compared to the low metallicity absorbers ($\sim$ 40%), and the stellar mass of the galaxy was correlated with both metallicity and detectability of an associated galaxy.

At higher redshift is the MAGG survey (MUSE Analysis of Gas around Galaxies), a large VLT/MUSE survey of 28 QSO fields resulting in 127 LAEs and a detection rate of $\sim$ 82% with 61 pLLS (and higher column density) absorbers (Lofthouse et al., 2020). Their main findings on the high-z CGM showed that (1) it is common to find multiple galaxies associated with a single absorber, (2) the CGM accounts for almost all optically thick gas at this redshift (Galbiati et al., 2023), (3) C IV has a high covering fraction that increases with absorber multiplicity and extends farther than cooler gas traced by Mg II, and (4) there is no strong evolution with covering fraction of metals in the CGM from $z \sim 3$ to $z \sim 2$.

The MUSEQuBES survey (MUSE Quasar-field Blind Emitters Survey) found results similar to MAGG. The survey used MUSE to find host galaxies of absorbers using a blind sample of 8 QSOs (with HIRES or VLT/UVES coverage) at $z \sim 3.3$ (Muzahid et al., 2020). They found 96 low-mass LAEs ($M \sim 10^{8.6} \mathrm{M}_{\odot}$) and found (1) excess H I and C IV absorption out to $b \sim 250$ kpc (Muzahid et al., 2021), (2) C IV has a 65% covering fraction above $\log N = 16.5$ with no strong trend with impact parameter, (3) H I covering fraction is 100% in groups but $\sim$ 86% for isolated galaxies, and (4) the majority of galaxies with O VI (60/96) show that the gas is gravitationally bound with no strong trend with stellar mass but 4/6 galaxy groups show no O VI at all, which is attributed to passive galaxies being the closest absorber-hosts.

The Keck Baryonic Structure Survey (KBSS) aims to connect $z \sim 2.3$ star-forming galaxies to the exquisite CGM information provided by Keck/HIRES spectra of 15 hyperluminous QSOs (Steidel et al., 2010). The QSOs have near continuous spectral coverage from $\sim 0.35 - 1\mu m$, allowing for detection of both H I and metal absorption for galaxies with redshifts $1.8 \gtrsim z > z_{\rm QSO}$ from the ground. At the time of this thesis, KBSS has hundreds of galaxies with spectroscopic redshifts that could be cross-referenced with absorbers detected in the HIRES spectra.

Rudie et al. (2012) analyzed the largest sample of $z \sim 2$ H I absorbers to investigate the connection between CGM/IGM baryons and galaxies in the KBSS fields. They performed a semi-automatic Voigt-profile decomposition of the Lyα forest, which allowed them to answer many open questions about the $z \sim 2$ CGM (and IGM) such as (1) there is strong enhancement of H I within a projected distance of $D_{\mathrm{Tran}} \sim$ 300 kpc from a KBSS QSO, and a line-of-sight velocity $|\Delta v| \pm 300 - 700$ km s^{-1} of galaxy systemic redshifts, giving a clear bound of the ~ 2 CGM, (2) H I enhancement plummets outside of ~ 2 Mpc, giving a bound of the IGM, (3) the complexity of H I components or "clouds" increases with proximity to galaxies, and (4) similarly, a H I line widths increase with galaxy proximity which could be attributed to either turbulence or temperature (metal absorption is required to disentangle the two).

Though hundreds of galaxies were included in R12's analysis, there were few galaxies within R_{vir} of a KBSS QSO. Within this radius one would expect strong correlations between galaxy properties and CGM absorption due to the close proximity to the ISM-CGM transition. Rudie et al. (2019) analyzed eight $z \sim 2$ galaxies within R_{vir} of a KBSS QSO by performing a Voigt-profile decomposition of their metal absorption. Due to the presence of multiple ions of different masses but similar ionization energy (usually Si IV and C IV) they were able to decompose the Doppler width to determine turbulence (non-thermal broadening, b_{turb}) and temperature T of individual CGM absorbers following the form $b_{\mathrm{d}}^2 = b_{\mathrm{turb}}^2 + 2kT/m$ where b_{d} is the Doppler width, b_{turb} is the turbulent velocity, k is the Boltzmann constant, T is the temperature, and m is the mass of the ion. They found that the inner CGM of $z \sim 2$ typical star-forming galaxies: (1) is kinematically complex requiring at least 10 components to adequately model the absorption, (2) is multiphase showing that low- and intermediate-ionization metal absorption (e.g., C II, Si III, C IV) share the same structure and broadening but differ strongly from high-ionization metal absorption (O VI), (3) almost all of the galaxies (6/8) showed that a fraction of their metal-enriched CGM was unbound corroborating previous observations that $z \sim 2$ galaxies ubiquitously drive galactic outflows, (4) thermal broadening dominates over turbulent broadening (thermal energy dominates the energy budget), and (5) the CGM holds a significant mass of metals $M_{\mathrm{CGM,Metals}} \geq 0.25 M_{\mathrm{ISM}}$.

Figure 1.1 shows a summary of the total numbers of galaxies within R_{vir} for each sample and redshift bin discussed earlier. Each of the investigations had samples

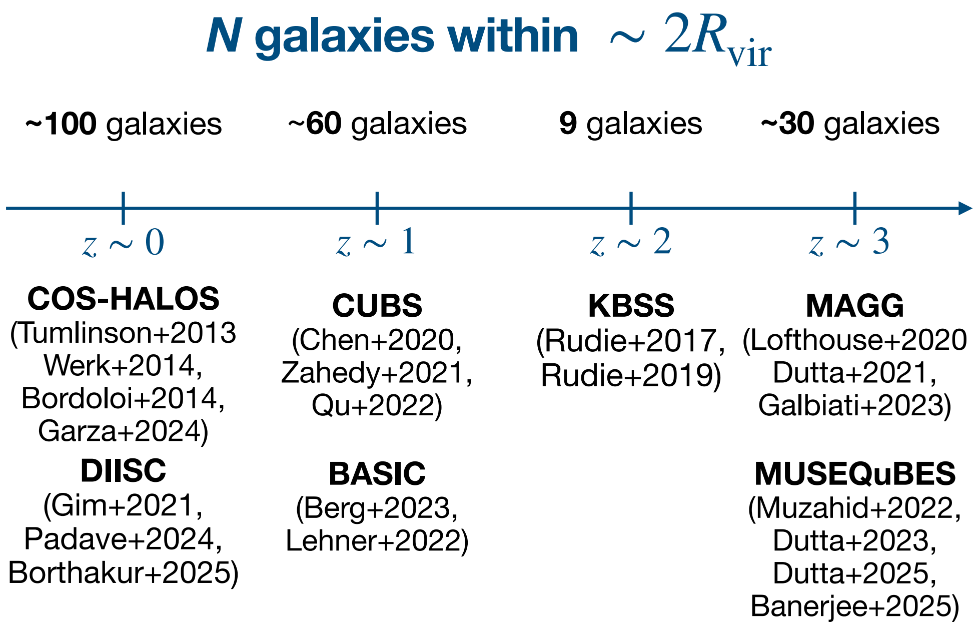

Figure 1.1: The number of galaxies whose CGM have been have analyzed within a couple $R_{\rm vir}$ of a QSO for each of the surveys discussed in this section. We need more galaxies at $z \sim 2$ and follow-up of the $z \sim 3$ galaxies because they generally lack both rest-optical spectra and deep images.

greater than ~ 30 *except* at $z \sim 2$. It is by no coincidence that at every other redshift there has been an optical IFU survey targeting its redshift. I address this lack head-on with this thesis and discuss in depth the practical steps and promise of the survey in the next section.

1.3 The Necessity, Novelty, and Nuance of This Thesis

I have shown that studies at redshifts surrounding "cosmic high noon" have exploded in sample size, and so has our their understanding of the CGM at those z. *Furthering our understanding of how the $z \sim 2$ CGM varies with impact parameter, stellar and halo mass, star-formation rate, and nebular metallicity* ***necessitates*** *a large sample* to smooth over the stochasticity of individual sightlines probed with the QSO absorption.

In my thesis I address the lack of a large, statistically significant sample of $z \sim$

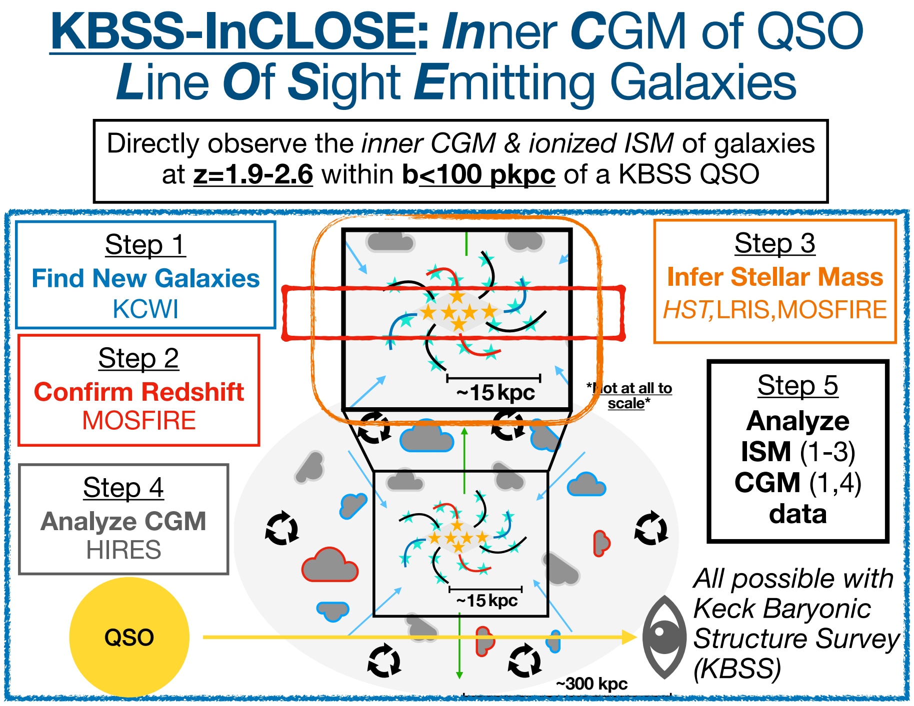

Figure 1.2: Summary of the workflow of KBSS-InCLOSE. Steps 1 and 2 represent all of the new data required for the survey. KBSS-InCLOSE would not be possible without the ancillary data provided by KBSS.

2 galaxies within $R_{\rm vir}$ of a QSO. Such a sample would dramatically increase our understanding of the $z \sim 2$ CGM by sampling impact parameter and stellar mass, which have been found to correlate most strongly with CGM properties. As discussed previously, this is the only redshift range with a sample size of fewer than 10 galaxies. It is no coincidence that there has not been a dedicated IFU survey at this z that targets QSOs to find close-in galaxies. As implied in the previous section, such samples require a significant amount of resources: observational resources including abundant telescope time, a diverse set of instruments, and planning and conducting the observations; data resources including reduction, combining/collating data, and then bookkeeping; and finally analyzing, interpreting, and then publishing the data.

To address this gap in our knowledge of the inner CGM at $z \sim 2$, I am leading a survey called KBSS-InCLOSE that will provide the first statistically significant sample of $z \sim 2$ star-forming galaxies with which we can probe their inner CGM ($R < R_{\rm vir} < R_{\rm CGM}$; $R_{\rm vir} \sim 80 - 90$ kpc, $R_{\rm CGM} \sim 300$ kpc).

Figure 1.2 shows the general workflow and main instruments used for the survey which builds on the Keck Baryonic Structure Survey (KBSS) that focuses on the Inner CGM of QSO Line Of Sight Emitting galaxies (InCLOSE). KBSS-InCLOSE relies on optical IFU data (rest-frame FUV) from the Keck Cosmic Web Imager (KCWI; Morrissey et al. (2018)), NIR spectra (rest-frame optical) from the Multi-Object Spectrometer For InfraRed Exploration (MOSFIRE; McLean et al. (2012)), deep ground- and space-based optical and NIR images from a variety of ground-based instruments (Keck/MOSFIRE, Keck/LRIS; Oke et al. (1995)) and the *Hubble Space Telescope* (WFC3-IR/F140W,F160W), and high resolution optical spectra of background QSOs from the HIgh Resolution Echelle Spectrograph (HIRES; Vogt et al. (1994)).

The first and most important step of KBSS-InCLOSE is finding new galaxies by acquiring deep KCWI pointings ($t_{exp} \geq 1.5\ hr$) of the KBSS QSOs and surrounding field ($b \leq 12''$, $b \leq 100$ kpc at $z \sim 2.3$). KBSS is fairly incomplete within this radius due to the bright wings of the hyperluminous QSOs point-spread function (PSF) which affects the typical continuum photometry selection (U_n, G, R_s). We must still deal with the PSF of the QSO, especially within $b = 3 - 5'' = 24 - 40$ kpc at $z \sim 2.3$ where the PSF dominates and where the most interesting galaxies would reside. To illustrate this problem more explicitly, the QSOs have $R_{s,\mathrm{QSO}} \sim 17 - 18$ while the galaxies have $R_{s,SFG} \sim 23 - 24$! This is a large dynamic range, requiring us to remove the bright QSO emission while preserving the faint emission from the underlying galaxy.

I refined and developed methods to remove the QSO emission while preserving the faint galaxy emission under the QSO PSF from both the images and IFU data. Point source removal in images is fairy straightforward compared to IFUs in that the PSF is "static" and imprinted on every point-source in the field. So long as a relatively isolated point source of comparable brightness to the QSO can be characterized in the field, the PSF can be modeled and subtracted. Ideally, multiple point sources are used to construct an "effective PSF" to capture the true shape of the PSF and mitigate flux contribution from unrelated nearby objects to the PSF. I used a tool written for this exact purpose, resulting in well-subtracted images.

However, PSF subtraction from IFU datacubes is significantly more complicated. With IFU data, the PSF is "dynamic" in that it changes with wavelength. A different approach must be taken because each object has a unique, spectrally varying PSF (i.e., each object has a unique spectrum). There are two ideal solutions to this problem: 1) treat the IFU data as an image and remove the QSO as such, and 2) treat IFU data as an array of spectra perform a model decomposition to remove the QSO.

Method 1, which I refer to as "QSO Continuum Subtraction", has been used in the literature for years and is fantastic for detecting narrow-line emission (Cantalupo et al., 2019). In this method a pseudo-narrowband image of some $\Delta\lambda$ (usually $\Delta\lambda \sim 250 - 400$) is constructed for each wavelength slice. The most important part of this process is normalizing each PSF to the average (or medium) flux of the $\Delta\lambda$. This ensures that only continuum is extracted but that narrow-line emission is left untouched. As such, this method is fast and used to analyze the Lyα halo of high-z QSOs. For this thesis, it is used to find preliminary redshifts for galaxy candidates in the KCWI cubes.

Method 2, which I refer to as "QSO Spectral Subtraction", is not as well known but has had a presence in the literature for a comparable amount of time as method 1 (Rupke et al., 2017). This method assumes that each spaxel can be decomposed into a linear combination of emission contribution from the QSO and some "excess." For example, in modeling a spaxel that contains a faint galaxy, the "excesss" is galaxy light. Mathematically this takes the form $S(x, y)_{\text{spaxel}} = A(x, y) * S_{\text{QSO}} + S_{\text{galaxy}}$ where S_{QSO} is flux from the QSO, A is the constant that scales the QSO spectrum, and S_{galaxy} is the flux from the galaxy.

I modified the algorithm of the "QSO Spectral Subtraction" from its original nine-step implementation to ensure that all of the QSO continuum light was removed, and that the QSO Lyα halo was removed as well. Procedurally, this was simple because only two steps of the nine-step process needed to be invoked, though I added two extra steps to remove the Lyα halo. Both methods are robust against model dependencies because the *datacube itself* is the only input for each model.

Altogether, I have "QSO-free" datacubes that allow for the detection of star-forming galaxies at $b \gtrsim 1''$. Indeed, the galaxy in the sample with the lowest impact parameter has $b = 1.25'' = 10.5$ kpc ($z = 1.9$). The decontaminated cubes are used to find new galaxies within $b \leq R_{\text{vir}}$, measure a preliminary redshift from Lyα emission (or absorption), and extract their rest-FUV spectrum. The spectra have interstellar absorption and can be used to measure inflow/outflow kinematics and strength.

Next, MOSFIRE is used to acquire follow-up rest-optical spectra of the galaxies to, at minimum, measure a nebular redshift z_{neb} using strong nebular emission lines e.g., [O III]$\lambda\lambda 4960, 5008$ which fall in the H-band. Nebular redshifts are better tracers of the systemic redshift $z_{\rm sys}$ compared to $z_{\rm Ly\alpha}$ due to the resonant nature of Lyα. Instantaneous star-formation rate is then inferred following a detection of Hα (K-band) ideally, but a lower-limit can be placed if only Hβ is detected (H-band). Dust attenuation can be inferred by measuring the Balmer decrement Hα/Hβ. Finally, electron density and ionization parameter can be inferred from detecting [O II]$\lambda\lambda 3727, 3729$.

KCWI and MOSFIRE are the new data required for KBSS-InCLOSE. These are supplemented with extant KBSS data. QSO-free ground- and space-based images are used to construct contaminant-free SEDs, which we model using state-of-the-art SED models that account for the high fraction of binarity in massive star populations. The most influential parameter in the SED models is stellar mass. Typically, constant SFH well describes $z \sim 2$ star-forming galaxies.

At this point, the minimum information needed to reasonably characterize the ISM and stellar population of each galaxy has been acquired through the FUV datacubes, rest-optical spectra, and rest-FUV through rest-optical images.

The information on the sightline is further supplemented by the CGM absorption of each galaxy as seen in the HIRES QSO spectra. The spectra are visually inspected for H I and metal absorption within $\pm 1,000$ km s^{-1} of $z_{\rm sys}$ of the galaxy. Then, a "by hand" component-by-component Voigt-profile decomposition is performed to measure the redshift, column density, and Doppler width of each absorber, starting with H I, then metals (though H I is not tied to the metals). For galaxy halos with multiple ions of different metals the Doppler width can be decomposed into non-thermal broadening $b_{\rm turb}$ and thermal broadening $\sqrt{2kT/m}$ to extract temperature and turbulence.

Finally, the CGM and ISM analyses are coupled to better contextualize the CGM absorption. There have been decades of $z \sim 2$ QSO absorber and star-forming galaxy investigations but few instances where galaxy-QSO pairs are associated with certainty. *The true **novelty** of this thesis (and survey) is the inclusion of the rest-optical spectra and deep ancillary images (ionized ISM and stellar populations) of the galaxies* because they are almost entirely lacking in the high-z CGM literature. For example, the MAGG and MUSEQuBES survey (as of the date of this thesis) lack rest-optical images and properties.

It is useful to think of the limits of the survey. In particular, what minimum ISM information is required to perform the ISM-CGM coupling? Indeed, it is already the case that some galaxies have had multiple observations with MOSFIRE with marginal and/or non-detections (likely due to their faintness). There are also some galaxies (10% of the sample) that have no counterparts in the KBSS ground- or space-based images (also likely due to their faintness). *The **nuance** of the survey is that not all galaxies will have fully characterized ionized ISM or stellar populations.* Nonetheless, every galaxy in the sample will have (1) a confident KCWI detection and therefore a FUV redshift z_{FUV} from either Lyα and/or IS absorption lines which can be converted to z_{sys} and (2) a HIRES QSO spectrum that contains CGM absorption. Further, non-detections can still give limits on the physical properties of the galaxies, which will be useful for future follow-up because it is likely that this subset galaxies are very low-mass. In other words, not all galaxies will have fully characterized ionized ISMs or stellar populations, but they can still be useful to the survey.

The connecting theme of this thesis is the use QSO absorbers to further our understanding of galaxy evolution. Chapter 2 shows how metal poor DLAs can be used to constrain the abundance ratios of the yields from CCSNe. Chapter 3 describes the first results from KBSS-InCLOSE, which focus on two known DLA-host galaxies that serve as a proof-of-concept for the survey. Chapter 4 describes the second results of KBSS-InCLOSE that focus on the first low-mass galaxies analyzed in the survey. Chapter 5 analyzes the whole sample and discusses preliminary results and future considerations for the survey. Chapter 6 summarizes this thesis.

Chapter 2

EMPIRICAL CONSTRAINTS ON CORE COLLAPSE SUPERNOVA YIELDS USING VERY METAL POOR DAMPED LYMAN ALPHA ABSORBERS

Nuñez Evan H., Kirby Evan N., Steidel Charles C. Empirical Constraints on Core-collapse Supernova Yields Using Very Metal-poor Damped Lyα Absorbers // . III 2022. 927, 1. 64.

2.1 Abstract

We place empirical constraints on the yields from zero- and low-metallicity core collapse supernovae (CCSNe) using abundances measured in very metal-poor (VMP; [Fe/H] ≤ -2) Damped Lyman Alpha Absorbers (DLAs). For some abundance ratios ([N,Al,S/Fe]), VMP DLAs constrain the metal yields of the first SNe more reliably than VMP stars. We compile a large sample of high-S/N VMP DLAs from over 30 years of literature, most with high resolution spectral measurements. We infer the IMF-averaged CCSNe yield from the median values from the DLA abundance ratios of C, N, O, Al, Si, S, and Fe (over Fe and O). We assume that the DLAs are metal-poor enough that they represent galaxies in their earliest stages of evolution, when CCSNe are the only nucleosynthetic sources of the metals we analyze. We compare five sets of zero- and low-metallicity theoretical yields to the empirical yields derived in this work. We find that the five models agree with the DLA yields for ratios containing Si and S. Only one model, Heger, Woosley (2010, hereafter HW10), reproduced the DLA values for N, and one other model, Limongi, Chieffi (2018, hereafter LC18), reproduced [N/O]. We found little change in the theoretical yields with the adoption of a SN explosion landscape (where certain progenitor masses collapse into black holes, contributing no yields) onto HW10, but fixing explosion energy to progenitor mass results in wide disagreements between the predictions and DLA abundances. We investigate the adoption of a simple, observationally motivated Initial Distribution of Rotational Velocities for LC18 and find a slight improvement.

2.2 Introduction

Core Collapse Supernovae (CCSNe) play a vital role in the evolution of the universe. They drive, and/or substantially contribute to, many astrophysical processes including the creation of metals, the dispersal of enriched gas, the injection of large amounts of energy into the interstellar medium, the chemical evolution of galaxies, and the launching of galactic outflows (Pettini, 2011; Woosley et al., 2002). In other words, CCSNe connect the largest and smallest scales of the universe.

The nearby universe no longer has any CCSNe from zero-metallicity or extremely metal-poor progenitor stars because the timescales associated with CCSNe are much shorter than the timescale for galactic chemical evolution. Although there is debate on the initial masses—and hence lifetimes—of Population III (PopIII) stars (e.g., Greif et al., 2011; Stacy et al., 2016) we have yet to observe a truly metal-free star. Most PopIII candidates have turned out to be extremely metal-poor PopII stars (e.g., Aguado et al., 2018). The indirect way to estimate yields of low-metallicity CCSNe is galactic archaeology, i.e. by observing the abundances of metal-poor stars found in pristine environments that condensed from the gas enriched by these CCSNe. Such observations can test theoretical models of CCSN nucleosynthesis.

Modeling the yields of CCSNe is a challenge that is fraught with many uncertainties (Heger, Woosley, 2010; Nomoto et al., 2006; Romano et al., 2010; Woosley, Weaver, 1995). These uncertainties compound with one another in ways that can drastically affect the resulting yield prediction. Uncertainties are introduced in, but are not limited to, the pre-supernova evolution of the star, the adopted nuclear reaction rates, the explosion mechanism, the rotational velocity of the progenitor, and the explosion energy (Limongi, Chieffi, 2018; Nomoto et al., 2006; Romano et al., 2010; Woosley, Weaver, 1995). Because of these uncertainties, observational data are sometimes integrated into models, e.g., light curves observed in nearby SNe, the compact remnants of those SNe, and the abundances observed in metal-poor stars (e.g., Perego et al., 2015; Woosley et al., 2002).

Galactic archaeology can help estimate CCSN yields. Metal-poor stars in the galactic halo and in dwarf galaxies are PopII stars that condensed from gas that was near primordial and therefore likely to be primarily enriched by nucleosynthetic events with short delays, like CCSNe. Their photospheric abundances may reflect the yields of PopIII CCSNe. This method has been used to place empirical constraints on CCSNe. For example, Kirby et al. (2019), de los Reyes et al. (2020), and Ishigaki et al. (2021) used the abundances of metal poor stars in Local Group dwarf galaxies to estimate the yields of both CCSNe and Type Ia SNe.

However, galactic archaeology has some drawbacks. The abundances measured from stellar atmospheres can depend critically on assumptions that are adopted to interpret their spectra (e.g., LTE). Some elements are more sensitive to this assumption than others. For example, non-LTE (nLTE) corrections to Al abundances can be as large as +1 dex (Nordlander, Lind, 2017), and 3D nLTE corrections for O and C can be as large as -0.6 dex and -0.3 dex respectively (Amarsi et al., 2019b). Stellar evolution can also alter the atmospheric abundances of some elements. For example, dredge-up on the red giant branch can deplete C and enhance N. In this way, stars act more as a middle-man to the "true" abundances from the near primordial gas out of which they formed. Our aim in this work is to measure this primordial gas directly to avoid the complications and corrections required to accurately map from the stellar spectra to atomic abundance.

Very Metal-Poor (VMP) Damped Lyman Alpha Absorbers (DLA) offer a unique way to investigate nearly primordial gas without the need for stellar spectroscopy. VMP DLAs are effectively the gas from which PopII stars formed. Therefore, measuring DLA abundances is the same as measuring the near-primordial gas. DLAs are QSO absorbers classified by their large column density $N_H > 2 \times 10^{20}\ cm^{-2}$ and therefore have damping wings in their Lyman-alpha absorption. DLAs account for up to ~90% of the neutral hydrogen content of the universe at their redshift (Lanzetta et al., 1995a; Prochaska, Wolfe, 2009; Sánchez-Ramírez et al., 2016; Zafar et al., 2013).

VMP DLAs at high redshift ($z \geq 2$) have a chemical enrichment history dominated by CCSNe (Cooke et al., 2017). This can be seen in their [α/Fe] evolution with respect to [Fe/H], which exhibits a knee at $[Fe/H] \sim -2$, preceded by a plateau (Berg et al., 2015a; Cooke et al., 2015; Prochaska, Wolfe, 2002a; Rafelski et al., 2012). This is qualitatively similar to evolution seen in dwarf spheroidal galaxies, where the plateau is indicative of CCSNe dominating the chemical evolution because they produce both α and Fe-peak elements, then Type Ia supernovae (SNe Ia) dominating after the knee because they primarily produce Fe-peak elements (e.g., Berg et al., 2015a; Cooke et al., 2015; Skúladóttir et al., 2018). Cooke et al. (2015) and Welsh et al. (2019) also showed that winds from AGB stars do not significantly affect the enrichment of VMP DLAs for almost any elements except carbon.

Deriving abundances from VMP DLAs is relatively straightforward compared to stars. One can map directly from line strength to abundance for most elements of interest. This is primarily due to the fact that lines used to measure metal abundances in VMP DLAs (excluding hydrogen and very strong metal lines, e.g., O I and C II) are weak at almost all wavelengths, such that line strength is proportional to column density and hence abundance. Even so, multiple ionization states and dust depletion (both discussed below) could lead to systematic errors in measuring DLA abundances.

Multiple ionization states of elements in DLAs could lead to overestimating, or underestimating, the "true" abundance of a system depending on whether the transition measured is the dominant ionization state. This leads to a discrepancy between the "true" abundance and what is measured, which must be corrected when converting to abundance. In general, the ionization corrections for DLAs are low due to their high H I column density, which allows the gas to self-shield from the UV background emitted from quasars and galaxies (Cooke, Pettini, 2016; Cooke et al., 2011b; Prochaska et al., 2002a; Wolfe et al., 2005; Zheng, Miralda-Escudé, 2002). Therefore ionization corrections are not a significant source of uncertainty in VMP DLA abundances because there is usually only one dominant ionization state detected.

Dust depletion can lead to an underestimate of DLA abundance (Berg et al., 2015a; De Cia et al., 2016; Wolfe et al., 2005). Refractory elements (e.g., Si, Mg, Fe) could condense onto dust grains, removing their signature from the detectable gas phase which results in an underestimate of the "true" abundance. It has been shown that DLAs in the VMP regime need little to no dust corrections (Cooke et al., 2011b, 2017; Pettini, 2011; Wolfe et al., 2005). Therefore, dust depletion is not a significant source of uncertainty in VMP DLAs. Retiring the major possible sources of systematic errors in DLAs makes them superior to PopII stars as sites to examine early nucleosynthesis.

The goal of this paper is to use the abundances measured from VMP DLAs to place empirical constraints on the yields of zero- or low-metallicity CCSNe. With the empirical constraints in hand, we attempt to quantify the differences between the empirical yields and the most widely adopted zero- and low-metallicity theoretical yields to offer insights into the most important input physics in the various models.

This paper is organized as follows. In Section 2.3 we discuss the sample of VMP DLAs. In Section 2.4 we place empirical constraints on the abundance ratios of zero- to low-metallicity CCSNe and compare them to metal poor stars. In Section 2.5 we compare theoretical yields of zero- and low-metallicty CCSNe to our empirical estimates, taking realistic explosion physics into account and reducing free parameters in a couple of the models in Section 2.5. In Section 3.7 we discuss the different input physics in the various theoretical yields that seem to reproduce our empirical yields. We summarize our results in Section 2.7.

2.3 Data

We compiled a large sample (79 total) of VMP DLAs that were available in the literature. We required that each system has both an Fe measurement ([Fe/H] $\lesssim -2$) and a measurement of at least one of C, N, O, Al, Si, and S. Our sample spans a wide range of redshifts ($z_{abs} = 1.8 - 5.9$), neutral hydrogen column densities ($\log N_{HI} = 20.1 - 21.9$ in cm^{-2}), and metallicities ($-3.5 < [Fe/H] < -1.9$). We re-normalized some of the solar abundances the datasets used to the Asplund et al. (2009) solar scale from older scales (e.g., Lodders (2003) or Asplund (2005)).

The majority ($\sim 60\%$) of sources in our sample have high-resolution spectroscopic measurements. The observations were mainly split between the High Resolution Echelle Spectrometer (HIRES) (Vogt et al., 1994) on Keck I and the Ultraviolet and Visual Echelle Spectrograph (UVES) (Dekker et al., 2000) on the Very Large Telescope (VLT) UT2 at the European Southern Observatory. HIRES typically covers a spectral range of 4000–8000 Å with a resolution $R > 30,000$. UVES has a spectral range of 3000–8000 Å between its red and blue configuration with a spectral resolution of R $\geq 40,000$.

The other $\sim 40\%$ of our sample have medium-resolution spectroscopic measurements. Their spectra were obtained using the Echelle Spectrometer and Imager (ESI) (Sheinis et al., 2002) on Keck II at a resolution of $R \approx 5000$ spanning a spectral range of 3900–10900 Å.

Additionally, two sources in our sample had spectra obtained by the MIKE (Bernstein et al., 2003) echelle spectrograph on the 6.5 m Magellan Clay telescope at Las Campanas with $R = 22,000 - 28,000$ covering a spectral range 3221–7420 Å, and the XSHOOTER Vernet et al. (2011) spectrograph on VLT UT2 with $R \sim 8500$ covering a spectral range 3000 Å – 2.5μm.

The majority of our sample has appeared in multiple surveys. The first DLA survey was conducted in 1986 by Wolfe et al. (1986), who compiled QSO candidates from the literature and followed them up at Lick Observatory. These sources, among others, were subsequently followed up by several authors once HIRES was commissioned in 1994 (e.g., Lu et al., 1998; Prochaska, Wolfe, 2002b; Prochaska et al., 2001b). More sources were followed up, and discovered, following the commissioning of UVES in 2000 (e.g., Centurión et al., 2003; Dessauges-Zavadsky et al., 2001, 2003; Ellison, Lopez, 2001; Levshakov et al., 2002; Lopez et al., 2002; Molaro et al., 2000, 2001; Pettini et al., 2002). In 2000 the Sloan Digital Sky Survey (SDSS) began operation and its first QSO sample target list was released by Richards et al. (2002). These sources were later followed up by SDSS low resolution spectroscopy, allowing an easy and automated way to search for VMP DLA candidates. One method, adopted by Cooke et al. (2011b), searched for candidates by requiring that only three metal lines be measurable for a system in their SDSS spectra. The other surveys included in our sample are the UCSD HIRES DLA Survey (Prochaska et al., 2007b), the Keck ESI MP DLA Survey (Penprase et al., 2010), and the ESO UVES Advanced Data Products Quasar Sample (Zafar et al., 2014c). The rest of the sources are compiled from the following authors and references therein: Berg et al. (2016); Cooke et al. (2013, 2012, 2011a,b); Cooke, Madau (2014); Cooke et al. (2015, 2017); D'Odorico et al. (2018); Ellison et al. (2010); Petitjean et al. (2008); Pettini et al. (2008); Srianand et al. (2010); Welsh et al. (2019, 2020).

Many ($\sim 40\%$) systems in our compilation were observed by different authors resulting in multiple abundance measurements for individual systems. We defaulted to measurements from high resolution spectra, then those with the smallest reported uncertainties. In cases when the uncertainties were comparable we chose abundances derived/compiled in Cooke et al. (2013, 2012, 2011a,b); Cooke, Madau (2014); Cooke et al. (2015, 2016, 2017); Welsh et al. (2019, 2020). The abundances used in our analysis are summarized in Table 2.1 and will be available as an electronic table.[1]

Table citations: 1: Lu et al. (1996); 2: Prochaska, Wolfe (1997); 3: Prochaska, Wolfe (1999); 4: Molaro et al. (2000); 5: Prochaska, Wolfe (2000); 6: Dessauges-Zavadsky et al. (2001); 7: Molaro et al. (2001); 8: Prochaska et al. (2001b); 9: Prochaska et al. (2001a); 10: Prochaska, Wolfe (2002b); 11: Dessauges-Zavadsky et al. (2001); 12: Ledoux et al. (2003); 13: Prochaska et al. (2003b); 14: Prochaska et al. (2003a); 15: O'Meara et al. (2006); 16: Noterdaeme et al. (2007); 17: Prochaska et al. (2007b); 18: Noterdaeme et al. (2008); 19: Petitjean et al. (2008);

[1]The full compilation, which includes all abundance measurements for a system (including the measurements that were not used in our analysis), is available at [https://github.com/evanhazey/CCSNe-Constraints-via-VMP-DLAs]https://github.com/evanhazey/CCSNe-Constraints-via-VMP-DLAs.

Table 2.1: Metal Summary of VMP DLAs (Partial table)

QSO	z_{abs}	log N_{HI}	[Fe/H]	[C/H]	[N/H]	[O/H]	[Al/H]	[Si/H]	[S/H]	Instrument	Ref
B0027-1836	2.402	21.75±0.1	-2.28±0.02[d]					-1.59±0.03[e]	-1.64±0.1	UVES	16
B1232+0815	2.3377	20.9±0.08	-1.96±0.08[d]					-1.35±0.05[e]	-1.21±0.12	UVES	18,24
BR0951-04	4.2029	20.4±0.1	<-2.6					-2.59±0.03		HIRES	3,8
BR1202-07	4.3829	20.6±0.14	-2.22±0.12					-1.78±0.02		HIRES	1
BR2237-0607	4.0803	20.52±0.11	-2.17±0.12					-1.84±0.02		HIRES	1
BRI1108-07	3.6076	20.5±0.1	-2.15±0.01					-1.77±0.001		HIRES	5,8
BRI1346-03	3.736	20.72±0.1	<-1.91					-2.28±0.01[e]		HIRES	8
BRJ0426-2202	2.9831	21.5±0.15	-2.78±0.06					<-2.0		ESI	13
CTQ247	2.6215	20.47±0.1	-2.4±0.02					-2.01±0.06		ESI	13
HS0741+4741	3.017	20.48±0.1	-1.93±0.01[d]					-1.64±0.01[e]	-1.6±0.1	ESI,HIRES	10,8
HS1132+2243	2.7835	21.0±0.07	-2.5±0.01					-2.05±0.14		ESI	13
J0035-0918	2.3401	20.55±0.1	-3.04±0.12	-1.51±0.18	-2.87±0.12	-2.28±0.13	-3.26±0.11	-2.65±0.11		HIRES,UVES	25, 31,29
J0140-0839	3.6966	20.75±0.15	-3.45±0.24	-3.05±0.17	<-4.20	-2.75±0.15	-3.37±0.16	-2.75±0.17	<-2.54	HIRES,UVES	21,25
J0255+00	3.9146	21.3±0.05	-2.08±0.09						-1.71±0.01	HIRES	8
J0307-4945	4.46658	20.67±0.09	-1.93±0.19		-2.93±0.15	-1.45±0.19	-1.75±0.11	-1.5±0.11		UVES	6
J0311-1722	3.734	20.3±0.06	<-2.01	-2.71±0.1	<-3.06	-2.29±0.1		-2.5±0.09		UVES	26
J0831+3358	2.30364	20.25±0.15	-2.39±0.16		<-3.30	-2.01±0.16	-2.5±0.16	-2.01±0.16		HIRES	26,22
J0903+2628	3.0776	20.32±0.05	<-2.81	-3.43±0.03[h]		-3.05±0.05		-3.21±0.02[i]		HIRES	34
J0953-0504	4.20287	20.55±0.1	-2.98±0.21	-3.05±0.1	<-2.84	-2.55±0.1		-2.7±0.1	<-1.78	HIRES,UVES	29
J1001+0343	3.07841	20.21±0.05	-3.18±0.15	-3.06±0.05	<-3.54	-2.65±0.05		-2.86±0.05		HIRES,UVES	26,31
J1037+0139	2.70487	20.5±0.08	-2.44±0.08		-3.06±0.09	-2.13±0.09	-2.62±0.09	-2.04±0.09		UVES	26
J1111+1332	2.27094	20.39±0.04	-2.27±0.04	-2.1±0.11[g]		-1.92±0.08		-1.95±0.02[f]		HIRES,UVES	31
J1113-1533	3.2665	21.23±0.05	-2.08±0.03[d]						-1.73±0.07	HIRES,UVES	30
J1337+3152	3.1735	21.3±0.09	-1.93±0.05[d]					-1.37±0.08[e]	-1.34±0.17	UVES	23
J1337+3153	3.16768	20.41±0.15	-2.74±0.3	-2.86±0.16	<-3.44	-2.67±0.17	-2.85±0.16	-2.68±0.16		UVES	23
J1340+1106	2.50792	20.09±0.05	-2.07±0.05		-3.12±0.06	-1.76±0.06	-2.26±0.05	-1.85±0.05	-1.81±0.05	HIRES,UVES	25,26
J1358+0349	2.853054	20.27±0.02	<-3.25		-3.58±0.11	-2.804±0.015	<-2.95	<-2.764	<-2.64	HIRES	32
J1358+6522	3.067295	20.47±0.07	-2.84±0.03	-2.25±0.1	-3.68±0.14	-2.22±0.05	-2.99±0.03	-2.58±0.03	-2.5±0.09	HIRES	27
J1419+0829	3.04973	20.4±0.03	-2.33±0.04		-2.95±0.04	-1.92±0.04		-2.08±0.03		UVES	26
J1558-0031	2.70262	20.67±0.05	-2.03±0.05		-2.04±0.05	-1.5±0.05		-1.94±0.05		HIRES,MIKE	15
J1558+4053	2.55332	20.3±0.04	-2.7±0.07	-2.51±0.07	-3.47±0.08	-2.45±0.06	-2.82±0.07	-2.49±0.04		UVES	20
J2310+1855[j]	5.938646	21.05±0.1	-3.08±0.12					-2.86±0.14		XSHOOTER	35

20: Pettini et al. (2008); 21: Ellison et al. (2010); 22: Penprase et al. (2010, hereafter P10); 23: Srianand et al. (2010); 24: Balashev et al. (2011); 25: Cooke et al. (2011b); 26: Cooke et al. (2011a); 27: Cooke et al. (2012); 28: Cooke, Madau (2014); 29: Dutta et al. (2014); 30: Zafar et al. (2014c, hereafter Z14); 31: Cooke et al. (2015, hereafter C15); 32: Cooke et al. (2016); 33: Morrison et al. (2016); 34: Cooke et al. (2017, hereafter C17); 35: D'Odorico et al. (2018, hereafter D18); 36: Welsh et al. (2019, hereafter W19); 37: Welsh et al. (2020)

2.4 Empirical Constraints on CCSN Yields

We place empirical constraints on the IMF-averaged yields of zero to low-metallicity core-collapse supernovae by analysis of the observed abundances of VMP DLAs. Specifically, we find the values of the low-metallicity plateaus in abundance ratios for the most readily measurable elements (C, N, O, Al, Si, S, and Fe). The first enriching events of system are CCSNe, followed by delayed enriching events, such as winds from AGB stars and Type Ia SN (SNe Ia). These processes can be disentangled in the space of [X/Fe] vs. [Fe/H] because [Fe/H] can be assumed to monotonically increase with time (assuming a relatively smooth star formation history), especially at low metallicity. At the earliest times, or lowest [Fe/H], the ratios should reflect the yields from CCSNe alone. The abundance ratios appear constant (a plateau in [X/Fe] vs. [Fe/H]) at low metallicities because there is only one type of enrichment (CCSNe, though not necessarily a single CCSN). At later times, or higher [Fe/H], the ratios reflect a combination of yields from CCSNe and delayed processes. The introduction of a new enrichment source leads to a change in [X/Fe] (a "knee" in [X/Fe] vs. [Fe/H]) at the value of [Fe/H] when the new sources turn on. In the case of the [α/Fe] ratio, CCSNe produce both α-elements and Fe-peak elements whereas SNe Ia produce mainly Fe-peak elements and little to no α-elements. Therefore, locating the [X/Fe] plateau gives the abundance ratio of CCSNe.

DLAs have been shown to exhibit a [α/Fe] knee at [Fe/H] ≈ -2 (Cooke et al., 2015) preceded by a plateau, implying that the VMP ($[Fe/H] \leq -2$) DLAs in our sample are in this plateau. To identify [X/Fe] values of these plateaus, and hence to obtain the abundance ratio of CCSN yields, we take the median of the abundance ratios observed in VMP DLAs, shown in Figure 2.1. We chose to use medians rather than means for several reasons. First, the mean is different depending on whether it is taken in logarithmic space (e.g., bracket notation like [O/Fe]) or linear space (e.g., mass ratios like $M(O)/M(Fe)$). The median is the same in either space. More importantly, the median is less sensitive to outliers, which might result from systematic uncertainties that are difficult to correct for (e.g., spurious instrumental errors, inconsistencies in abundance determinations, ionization corrections).

The median calculations begin by first finding the median for sources that are doubly bounded (i.e., no upper or lower limits). Then, using this preliminary median, we find all upper limits that are below it and all lower limits that are above it. Finally, we recalculate the median, and associated 68% confidence intervals (in log space), using the doubly bounded sources and the aforementioned meaningful upper/lower limits. The medians are shown as the colored horizontal lines in Figures 2.1 and 2.2. The figures also contain the abundance ratios of metal-poor stars, which we discuss in Section 2.4.

Abundances measured from medium resolution spectra, $R < 10,000$, can contain uncertainties not present in high resolution spectra such as line blending and/or hidden saturation, which can result in their abundances being inaccurate. To account for this, we calculate the median of each abundance ratio twice. First, we use all sources in the sample (i.e., with abundances measured from both high resolution spectra and medium resolution spectra; purple horizontal line(s) in Figures 2.1 and 2.2). Second, we use abundances measured only from high resolution spectra (blue horizontal line(s) in Figures 2.1 and 2.2). The differences between the medians were always <0.1 dex and as small as 0.01 dex. The 1-σ uncertainties decreased by about 0.1 dex when culling the sample to high resolution sources only. The uncertainty

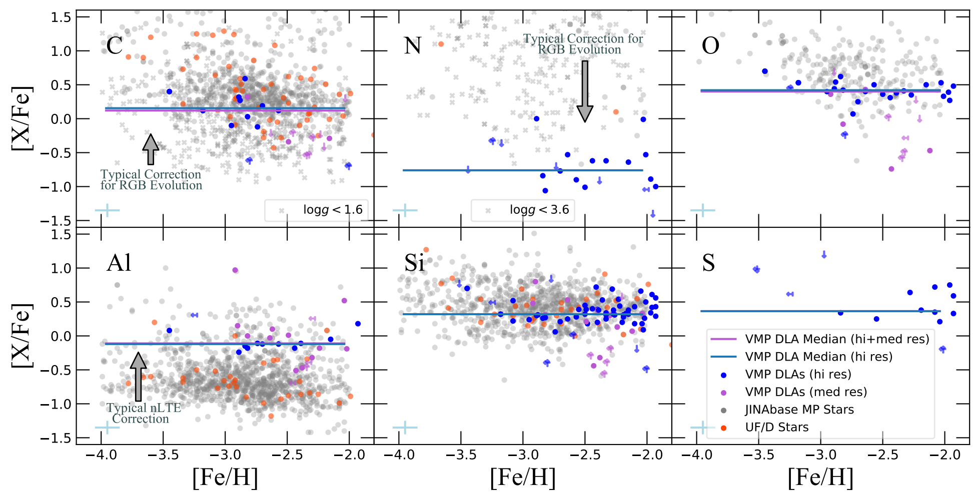

Figure 2.1: C, N, O, Al, Si, and S abundance ratios as a function of [Fe/H]. The blue (purple) points are VMP DLAs whose abundances were measured from high (medium) resolution spectra. The blue horizontal bars are the medians of the VMP DLA abundance ratios from high resolution sources, and the purple horizontal bars are the medians of the VMP DLA abundance ratios from high+medium resolution sources. Typical VMP DLA uncertainties (0.1 dex) are shown in the bottom left corner of each subplot. The grey smaller points are metal-poor stars from the JINA database (Abohalima, Frebel, 2018); the small gray x's are giants whose surface abundances have been altered by RGB evolution. The red smaller points are from the ultra-faint/dwarf galaxy star compilation from Alexander Ji (see Section 2.4). The gray arrows in the subplots show the typical corrections (Nordlander, Lind, 2017; Placco et al., 2014) for the stated physical processes, to scale (see Section 2.4 for discussion). The corrections vary widely from star to star. UFD Compilation References: Chiti et al. (2018); Feltzing et al. (2009); François et al. (2016); Frebel et al. (2010, 2014); Gilmore et al. (2013); Hansen et al. (2017); Ishigaki et al. (2014); Ji et al. (2016a,b, 2019); Kirby et al. (2017); Koch et al. (2013, 2008); Lai et al. (2011); Marshall et al. (2019); Nagasawa et al. (2018); Norris et al. (2010); Roederer, Kirby (2014); Roederer et al. (2016); Simon et al. (2010); Spite et al. (2018).

for [Al/O] decreased by 0.2 dex.

The [O/Fe] and [Si/Fe] abundance ratios contain a subset of sources between [Fe/H]~-2.5– -2 whose abundances are >0.5 dex below the bulk trends. The majority (~70%) of the sources come from Penprase et al. (2010, hereafter P10), were measured from medium resolution spectra, and have only upper limits on [Fe/H]. There are five sources who have both low [O/Fe] and [Si/Fe] (compared to the bulk trends) and three of them come from P10. These were among the most oxygen poor sources ([O/H]<-2.6) and silicon poor sources ([Si/H]<-2.5) in the sample.

Dust depletion has been shown to be minimal in DLAs at low-metallicity (see previous Section 2.2; Cooke et al., 2011b; Wolfe et al., 2005). While we cannot prove that there is no dust depletion in the VMP DLAs, we point to our work and that of others to argue that it is negligible. Figure 2.1 shows the observed abundance ratios of [S/Fe] and [Si/Fe]; S is an alpha element that is volatile (i.e., it does not easily condense onto dust grains similar to C, N, O, and Al, so its gas phase abundance is the same as its true abundance), and Si and Fe are both refractory elements (i.e., easily condense onto dust grains, Fe more so than Si). If dust depletion is appreciable there should be a trend between [Si/Fe] and [S/Fe] with metallicity; we observe no trend implying that the relative dust depletion between S, Si, and Fe is negligible. Further, the stellar abundance ratio—which is not subject to dust corrections—at low metallicities in the Milky Way is [Si/Fe] = 0.37 ± 0.15 (Cayrel et al., 2004); we observe [Si/Fe] = 0.32 ± 0.16. Finally, in recent work from De Cia et al. (2018), the dust depletion of Si and Fe in DLAs was shown to be effectively zero at [Fe/H] ~ -2 but as large as 1 dex at [Fe/H] ~ 0. Other studies have shown the same trend of dust depletion decreasing as metallicities approach 1/100 solar (Akerman et al., 2005; Pettini et al., 1997; Vladilo, 2002; Vladilo et al., 2018; Wolfe et al., 2005). All suggest minimal effects of dust on the abundance ratios measured in the gas phase.

In order to separate nucleosynthesis during the pre-SN evolution of the progenitor stars and during the explosion of the stars, we show the VMP DLA abundance ratios with respect to oxygen in Figure 2.2. Oxygen provides insight into the pre-SN evolution of the star because it is synthesized primarily during hydrostatic burning. On the other hand, Fe is synthesized during the SN explosion. Intermediate elements, such as Si, are produced significantly in both hydrostatic and explosive nucleosynthesis. This distinction will play an important role in our comparison to theoretical yield models in Section 2.5.

There should be a constant trend in the abundance ratios with respect to oxygen because oxygen is synthesized hydrostatically, the majority of the elements in Figure 2.2 are synthesized hydrostatically, and there is only one source of nucleosynthesis at the low metallicites that we are probing. In other words, most of the elements, except Fe, and perhaps Si and S, should be produced roughly in the same proportion in CCSNe.

There is evidence suggesting that [C/O] (vs. [O/H]) decreases for VMP DLAs until a minimum is reached at [O/H] ~ -1.5 (Cooke et al., 2011b; Penprase et al., 2010;

Pettini et al., 2008). This finding is based on extrapolating the behavior seen in red giants in the Milky Way halo whose [C/O] (vs. [O/H]) shows a decrease at low [O/H], a minimum at [O/H] $\sim$ -1.5, and an increase to solar at high [O/H] (e.g., Akerman et al., 2004; Fabbian et al., 2009). This rise in [C/O] at low oxygen abundance has been interpreted as a PopIII signature owing to C enhancements from zero metallicity stars. But the C abundances for red giants can be uncertain due to the astration corrections necessary to infer their abundance (e.g., Kirby et al., 2015; Placco et al., 2014; Smith, Briley, 2006). Also, C and O also could have 3D nLTE corrections as large as -0.3 dex and -0.6 dex respectively. Recently, Amarsi et al. (2019a,b) calculated 3D nLTE corrections for C and O abundances in metal-poor stars and found that the downturn in [C/O] (at low oxygen abundance) is no longer present; an increase is seen instead. Interestingly, if one were to observe [C/O] (vs. [O/H]) from the VMP DLAs in isolation, a strong trend with [O/H] is not apparent; a weak trend may be present (Berg et al., 2021; Cooke et al., 2017; Poudel et al., 2020).

Nitrogen is also affected by astration but it has been shown that [N/O] (vs. [O/H]) does not vary with oxygen abundances below [O/H] ~ -0.7 for DLAs and instead reaches a plateau (Petitjean et al., 2008; Pettini et al., 2008; Zafar et al., 2014a). This behavior is similar to what is found for [N/O] in local dwarf galaxies at the lowest [O/H] where for [O/H] $\lesssim -0.7$ there is a primary nitrogen plateau ([N/O]~ -0.65) then a rapid rise with increasing [O/H]; for DLAs the plateau at low [O/H] is more than 0.3 dex lower (Berg et al., 2019).

For these reasons, we use the same approach, rationale, and calculation to find the medians of these ratios with respect to oxygen, and interpret the medians as the yield ratios of CCSNe.

The medians of the abundance ratios with respect to oxygen in Figure 2.2 (and with respect to Fe), and their 1-σ (68% confidence interval) uncertainties, are listed in Table 2.2. These medians reflect the median IMF-averaged CCSN yield for zero- and low-metallicity massive stars.

Kirby et al. (2019, hereafter K19) placed empirical constraints on CCSNe using a method similar to what is presented here, except based on metal-poor stars in dwarf galaxies. We compare the empirical yields they derived to our empirical yields in Section 2.5.

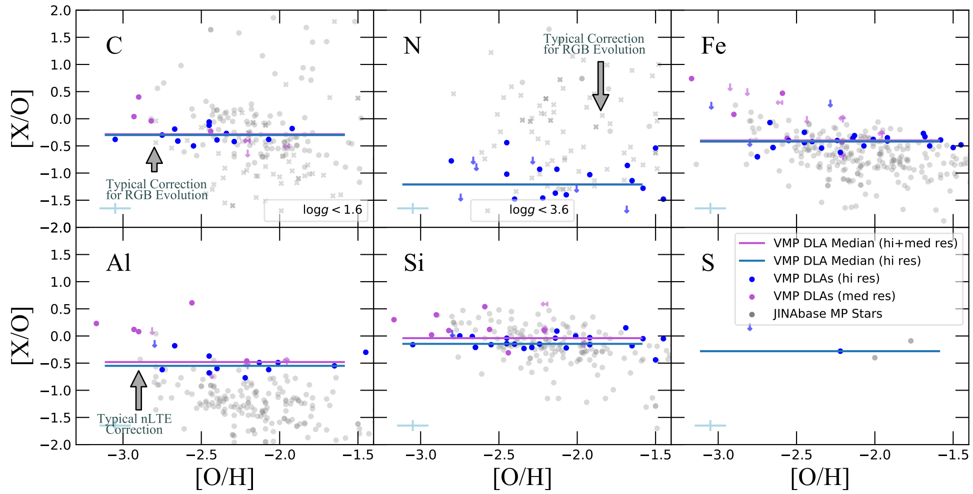

Figure 2.2: C, N, Fe, Al, Si, and S abundance ratios as a function of [O/H]. Same symbols as Figure 2.1.

Table 2.2: Median Abundance Ratios of VMP DLAs

Element	$[X/Fe]$	$[X/O]$
C	0.16±0.20	-0.30±0.13
N	-0.76±0.34	-1.21±0.33
O	0.42±0.13	
Al	-0.11±0.11	-0.55±0.16
Si	0.32±0.16	-0.14±0.12
S	0.36±0.18	-0.27
Fe		-0.41±0.13

Comparison Between VMP DLAs and VMP Stars

We compare the abundance ratios of VMP DLAs to VMP stars in order to understand the robustness of these ratios. The grey background points in Figures 2.1 and 2.2 are metal-poor stars compiled from the JINAbase database with $-4 < [Fe/H] < -2$ from the MW halo, MW bulge, ultra-faint dwarf (UFD) galaxies, and classical dwarfs (Abohalima, Frebel, 2018). The x's in the C and N panels are stars with surface gravity ($\log g$) small enough to necessitate corrections for evolution of surface abundances on the giant branch. All of the stellar abundances are subject to some nLTE correction, but the corrections for Al are particularly large. The grey arrows in the figures show, to scale, the typical corrections needed to properly infer the abundance ratios; [C/Fe]~+0.5 dex (Placco et al., 2014) for log g <1.6, [N/Fe]~-1 dex (Placco et al., 2014) for log g <3.6, and [Al/Fe]~+0.8 dex (Nordlander, Lind, 2017) for stars with $-4 < [Fe/H] < -2$ and $[Al/Fe] \sim -1$. The exact values of the corrections depend on temperature, surface gravity, metallicity, and for C and N, detailed abundances.

The red background points are a compilation of metal poor giants in ultra-faint dwarf and classical dwarf (UF/D) galaxies compiled by Alexander Ji[2] (references in Figure 2.1).

Figure 2.1 shows that the VMP DLA abundance ratios for N and Al (i.e., [N/Fe] and [Al/Fe]) exhibit a distinct difference (up to $\sim$ 1 dex) from VMP stars, whereas for the others ([C/Fe], [O/Fe], and [Si/Fe]) show general agreement between the samples. [Al/Fe] specifically show a systematic offset of -0.5 and can be explained by the nLTE corrections needed to infer their abundances. Importantly, measuring abundances from the cool dense gas from the DLAs is less susceptible to systematic effects than measuring abundances in stellar atmospheres. Sulfur is under-represented in the stellar sample because it has very few optical absorption lines.

Figure 2.2 shows similar trends as the previous figure. There is a systemic offset between the VMP stars and VMP DLAs in [N/O] and [Al/O]. [C/O], [Fe/O], [Si/O] show general agreement between the samples.

Taken together, Figures 2.1 and 2.2 give another quantitative, visual affirmation for using VMP DLAs as a complementary set to VMP stars to constrain the yields of zero- and low-metallicity CCSNe (e.g., Cooke et al., 2017; Prochaska, Wolfe, 2002b; Rafelski et al., 2012). For C, O, and Si, the abundances are complementary, whereas for N, Al, and S, VMP DLAs offer the ability to constrain yields without the effects of stellar astration (N), nLTE effects (Al), or observationally challenging wavelengths (S).

The empirical CCSN yields in Table 2.2 can be used as inputs in galactic chemical evolution models. Specifically, they could be an empirical guide to the first enriching events of the system being modeled.

2.5 Theoretical Yield Comparison

In this section we compare the zero- and low-metallicity yields calculated by Woosley, Weaver (1995, hereafter WW95); Kobayashi et al. (2006) and Nomoto et al. (2006, together referenced hereafter as KN06); Heger, Woosley (2010, hereafer HW10); Limongi, Chieffi (2018, hereafter LC18); and Ebinger et al. (2020, hereafter EC20) to the empirical yields we derived in the previous section.

[2] https://github.com/alexji/alexmods/data/

Synopsis of the Theoretical Yields

We discuss the relevant aspects of the physical models and input parameters that would affect the resultant yield predictions for the models below. For detailed discussions of each model we refer the reader to the cited manuscripts.

Woosley, Weaver (1995)

WW95 calculated the nucleosynthetic yields from massive stars as a function of mass and metallicity for elements through Zn. They computed 78 models that differed in explosion energy (usually 1.2×10^{51} erg (1.2 B); B is a Bethe, or 10^{51} erg.), metallicity (0–1 solar), and initial progenitor mass (11–40 $M_{\odot}$). We use the 'Z' models, which have zero-metallicity, e.g., a pre-supernova progenitor with a Big Bang composition.

WW95 evolved each star through the supernova explosion. The explosion was achieved by means of a mass piston located at the edge of the iron core modeled in 1-D (modeling in 1-D is common to all the models hereafter). The piston was moved inward at constant acceleration until it reached 500 km where it was moved rapidly outward (bounce) at a velocity tuned such that the final kinetic energy of the ejecta typically reached an energy of $\sim 10^{51}$ erg (1 B). The resultant shock decelerated in the mantle of massive stars, which, among other effects, led to significant fallback of Fe-peak elements. WW95's nucleosynthesis yields account for this fallback.

The models included the effects of neutrino irradiation, which had a major effect on the nucleosynthesis due to changes in the composition of the star before the shock wave from the mass piston caught up to the material. Neglected processes that could have affected the nucleosynthesis include neutrino capture processes, stellar rotation, and a model of the explosion physics more realistic than a mass piston.

The piston was tuned to ensure an explosion. Some modern 3-D supernova models explode without the need for a piston or thermal bomb by modeling the collapse and explosion phase of the star (e.g., Burrows et al., 2019), though there still is no consensus in the field as to a preferred method of explosion.

We explore the effects that an "explosion landscape" (wherein some supernovae collapse into black holes without contributing to nucleosynthesis) on IMF-averaged theoretical yields in Section 2.5. Also, we use the WW95 yields as a qualitative reference only and perform our analysis (i.e., compare theoretical abundance ratios to VMP DLA abundance ratios) to their successor (see Section 2.5).

Kobayashi et al. (2006) and Nomoto et al. (2006)

KN06 calculated the nucleosynthetic yields for elements up to Zn as a function of initial mass, composition, and explosion energy. We use their zero-metallicity yields over their total progenitor mass range (13–40 $M_{\odot}$) and compare their two available explosion energies: (1) 1×10^{51} erg (1 B), corresponding to a normal Type II supernova and (2) $10 - 30 \times 10^{51}$ erg (10–30 B), corresponding to a hypernova (HN). The authors found that a HN contribution of 50% was optimal to match the observed [α/Fe] trends in the Milky Way, but we vary the contribution from 0–100% for our computed IMF-averaged yields (see Section 2.5).

KN06 evolved the star from pre-supernova to explosion. Their explosion mechanism is a "thermal bomb"; when a critical density is reached in the core, the star is promptly exploded with the specified energy for SNe and HNe. The authors used light curves and spectral fitting from individual SNe to set the mass of ^{56}Ni ejected, 0.3–0.5 $M_{\odot}$. They also used the abundance ratios observed in EMP stars, specifically [O/Fe]=0.5, to set the amounts of mixing and fallback, which are otherwise free parameters in the calculations.

Included in their calculations were metallicity-dependent mass loss and neutron-capture processes. They did not include any neutrino processes, stellar rotation, or natural explosion physics (as opposed to a thermal bomb).

Heger, Woosley (2010)

HW10 computed nucleosynthetic yields for zero-metallicity stars as a function of mixing (0.0-0.25; explained in the next paragraph), explosion energy ($0.1 - 10$ erg; 0.1-10 B), mass cut (S4 or Y_e; also explained in the next paragraph), and progenitor mass (10–100 $M_{\odot}$). Several model combinations matched the abundances observed in different EMP stars adequately. One such model, as an example, had an explosion energy of 1.2 B, standard mixing of 0.1, and an S4 mass cut. These models are the successors to zero-metallicity models of WW95.

HW10 modeled their stars from main sequence to explosion using the KEPLER code, which was also used by WW95. They found that the density and structure of the zero-metallicity stars were the same as solar metallicity stars, implying a common central engine for single stars. The mixing of heavy elements deep in the star to outer layers was simulated by series of boxcar runs whose mass is set to be some fraction (0.0–25.1%) of the He core mass. A mass piston was then used to

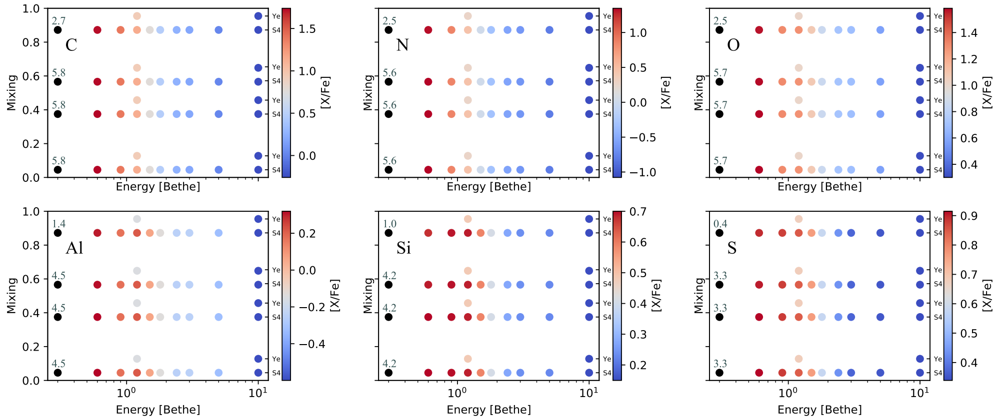

Figure 2.3: The IMF-averaged yields from HW10 as a function of mixing parameter and explosion energy. The color bar on the right of the figure denotes the [X/Fe] for each mass cut, which are labeled on the right side of each panel. The Y_e values are vertically offset from the $S4$ mass cut for clarity. The lowest explosion energy (0.3 B) points have their [X/Fe] value annotated above the point; they are all off the color bar scale.

explode the stars. There were two locations that the piston was placed: (1) near the base of the oxygen shell (where the entropy per baryon is $S/N_A = 4.0\ k_B$; S4 model) or (2) deeper in the star near the edge of the iron core (where the electron fraction Y_e becomes discontinuous; 'Y_e' model). Following this mass cut, each mass piston was moved to give the ejecta a final kinetic energy ranging from 0.3–10 $\times 10^{51}$ erg (0.3–10 B).

The models include neutrino irradiation and fallback. Neglected physics included stellar rotation (though the authors added a "mixing" term that mimics the effect of stellar rotation), neutrino winds (which would affect r- and some s-process elements), and more realistic explosion physics (as opposed to a piston).

To see how the numerous parameters affect the resultant yields, and to pick a preferred mass cut (S4 or Y_e) and mixing value (0.0–0.25), we show in Figure 2.3 the IMF-averaged (Salpeter) yields as a function of mixing, explosion energy, and mass cut for the entire modeled mass range. The yields stay constant with mixing but vary significantly ($\geq$ 3.5 dex) with explosion energy. The insensitivity to mixing is expected because the mixing is performed after all explosive nucleosynthesis and fallback are computed. Because the Y_e mass cut has only two explosion energies, its predicted [X/Fe] range is more tightly constrained than the S4 cut. Even so, the Y_e range is always within the wider values predicted by the S4 cut so we elect to use the S4 cut in our comparison. The yields from the lowest modeled energy in the S4 models (0.3 B) differ significantly ($1-3$ dex) from the higher energy models, so we neglect the low-energy models in our comparison. After this culling, the yields are comparable regardless of mixing, so we choose a mixing value of 0, which leaves explosion energy and mass as the only free parameters in our comparison.

Limongi, Chieffi (2018)

LC18 calculated the yields of elements up to Bi as a function of metallicity ([Fe/H] = −3, −2, −1, 0), progenitor mass (13–120 $M_{\odot}$), and initial rotational velocity (v = 0, 150, 300 km s^{-1}). We use their $[Fe/H] = -3$ model and masses from 13-100 $M_{\odot}$. We discuss the choice of rotation velocity below.

LC18 modeled the evolution of their stars from pre-main sequence to presupernova. The initial metallicity given to the stars for their $[Fe/H] = -3$ models were scaled from the solar composition (Asplund et al., 2009) for most elements (e.g., Al, N) but abundance ratios (with respect to Fe) observed in metal-poor stars were used for some elements (C, O, Si, and S). They exploded their star via a thermal bomb with three different calibrations. Their preferred calibration (the one used in this work) requires that (1) stars from 13–25 $M_{\odot}$ have a mixing and fallback scheme by requiring that the edges of the mixing region are fixed and that the mass cut is placed such that 0.07 $M_{\odot}$ of ^{56}Ni is produced and (2) stars more massive than 25 $M_{\odot}$ fully implode and therefore any yields are from the pre-SN stellar wind. The explosions energies that the authors calculated, which we infer from their quoted binding energy of mass above the Fe core, ranged from 0.65–15 $\times 10^{51}$ erg (0.65–15 B) for their 13–80 $M_{\odot}$ progenitors with the larger explosion energies corresponding to the more massive progenitors. We fully decayed the isotopes in our yield comparison to their final stable isotopes assuming 100% conversion.

LC18 included stellar rotation and mass loss but neglected realistic explosion physics (as opposed to a thermal bomb).

Stars are known to have varying rotation velocities so there likely exists some preferred Initial Distribution of ROtation Velocities (IDROV; analogous to mass and the IMF), that is a function of mass and metallicity (Limongi, Chieffi, 2018; Prantzos et al., 2018). At present, there has not been a detailed study of the IDROV and its properties coupled with the IMF. Still, we construct a simple, observationally motivated IDROV (see Section 2.5), alongside the yield predictions when all stars are rotating at a single velocity (see Section 2.5).

Ebinger et al. (2020)

EC20 of the PUSH collaboration (Perego et al., 2015) used an engine to self-consistently explode stars and obtain nucleosynthetic yields for isotopes up to ^{211}Eu as a function of metallicity ($Z = 0 - 10^{-4}\ Z_{\odot}$) and mass (11-75 $M_{\odot}$). We use their zero-metallicity models, which have a smaller mass range of 11–40 $M_{\odot}$.

The authors used pre-SN models from Woosley et al. (2002). The explosion, which relies on the delayed neutrino-driven mechanism, of the pre-SN progenitor was simulated by following the core collapse, bounce, neutrino heating, and resultant explosion (or implosion) of the stars in increments of 1 $M_{\odot}$ assuming spherical symmetry. The neutrino heating term, the most important term for the explosion, has two free parameters that were calibrated such that the models reproduced properties observed from SN 1987A.

The authors did not force the stars to explode but instead relied on the physical outputs from their simulation to determine if an explosion was successful or not. An explosion was deemed successful if the final explosion energy of the simulation was positive. An explosion was deemed as a failure if the final explosion energy was negative at the end of the simulation. From this criteria they found that stars from 11–23 $M_{\odot}$ and 27–31 $M_{\odot}$ successfully exploded whereas the other masses failed, i.e., imploded into a black hole. The exploding stars contributed to yields whereas direct-collapse stars did not. The resultant explosion energies ranged from ~0.3–1.6×10^{51} erg (0.3–1.6 B) with no uniform trend with progenitor mass.

Only explosive nucleosynthesis was considered in the yields published by EC20, so we added the contribution from the preSN progenitors (i.e., hydrostatic nucleosynthesis) to get the total yield (S. Curtis, private communication, Woosley et al., 2002). This primarily affected the abundance of light elements (C, N, O) that are created in small quantities during explosive nucleosynthesis. We could not compute a total yield for Al because the pre-SN progenitors did not track it. We do not include the Al predictions from EC20 in our subsequent analysis.

The authors included realistic explosion physics but neglected neutrino irradition and stellar rotation.

Comparison Between Yield Tables

In Figure 2.4 we show the theoretical [X/Fe] predictions from the models described in the previous section and compare them to empirical yields from VMP DLAs (see

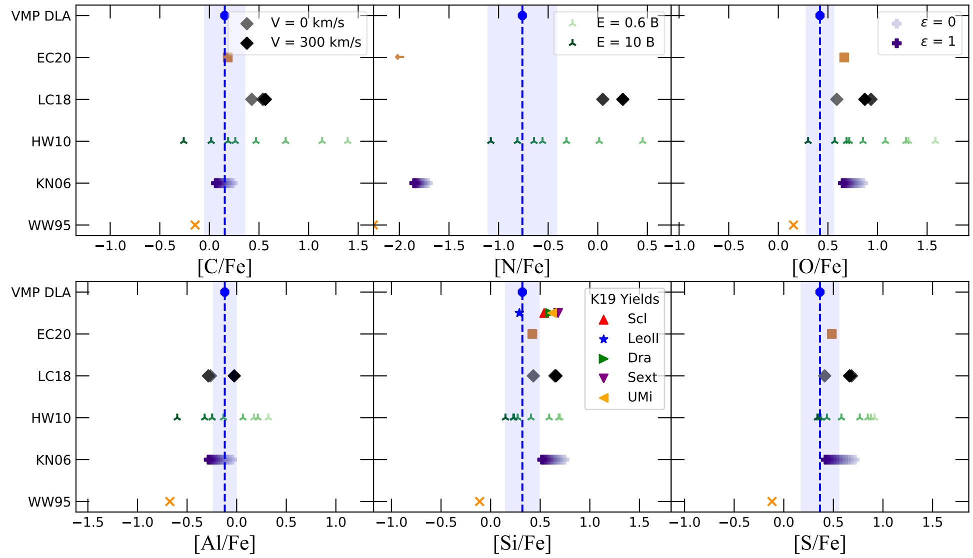

Figure 2.4: Predicted [X/Fe] for each yield table compared with the median [X/Fe] from VMP DLAs. The dashed vertical blue line is the median of the VMP DLAs, the blue shaded region shows the 1-σ uncertainties. The colored stars are empirical yields derived by K19 from metal-poor stars in the respective dwarf galaxies (see end of Section 2.4). EC20 predictions are shown as orange squares, LC18 as black/dark grey diamonds (varying rotational velocities), HW10 as green tripoints (varying explosion energy), KN06 as blue pluses (varying HN contribution), and WW95 as orange X's.

Section 2.4). The [X/Fe] values were calculated by integrating the model yields under a Salpeter IMF from a mass range of 10–100 $M_{\odot}$. We interpolate the yields to achieve steps of 0.25 $M_{\odot}$ but did not extrapolate the yields outside of their modeled masses (see mass ranges above). For [Si/Fe] we also compare the empirical yields derived by K19 using metal-poor stars in the dwarf galaxies Sculptor (Scl), Leo II, Draco (Dra), Sextans (Sext), and Ursa Minor (UMi) (see end of Section 2.4).

There is general agreement between the empirical yields and the theoretical [X/Fe] predictions for the majority of elements. Each model reproduces the empirical yields (within $1-\sigma$) for a subset of elements. [Si/Fe] and [S/Fe] are consistently reproduced by all models. [C/Fe], [O/Fe], and [Al/Fe] show similar agreement (EC20 did not track the total Al yields; see Section 2.5). [N/Fe] is a notable exception, it showed the largest spread between models. Only one, HW10, reproduced the empirical [N/Fe] yields. The [N/Fe] differences between the empirical yields and theoretical predictions exceeded 0.5 dex for all other models.

The various models' overall agreement in their [S/Fe] and [Si/Fe] predictions with

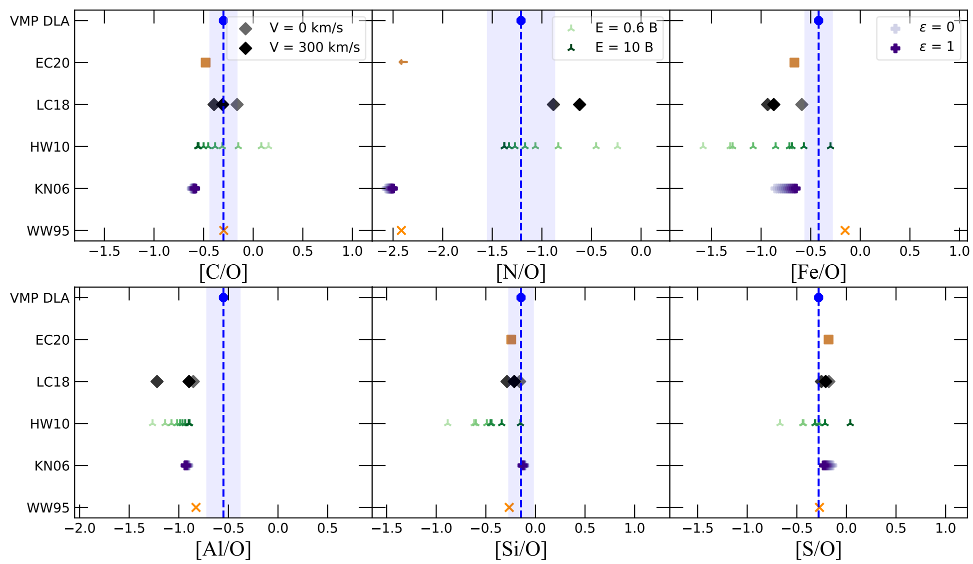

Figure 2.5: Median [X/O] for VMP DLAs and predicted [X/O] for each of the yield tables. Same symbols as Figure 2.4.

the VMP DLA data can be used to further argue that there is minimal dust depletion in VMP DLAs. If this were not true, one would expect systematic discrepancies between the nucleosynthetic predictions and the observed ratios in VMP DLAs, just as one would expect some trend in [Si/Fe] and [S/Fe]. But neither is seen, further suggesting that there is negligible dust depletion in VMP DLAs.

The majority of the yields derived by K19 fall just outside of our uncertainties, except for Leo II. After accounting for K19's yield uncertainties (0.02–0.08 dex), Scl and Dra also become consistent with the DLA estimates. Note that K19 measured Si in red giants in a spectral range ~6300–9100 Å. The only available Si lines in this spectral range are weak due to their high excitation potentials, making it difficult to measure Si in low-S/N spectra. This means there could be a bias toward higher Si abundances for very metal-poor stars because lower Si abundances would result in undetectably weak lines. In fact, extremely-metal poor Milky Way halo stars have a plateau at $[Si/Fe] = 0.4$ (e.g., Frebel, Norris, 2015), which is consistent with the VMP DLA abundances.

In Figure 2.5 we compare the theoretical [X/O] to the empirical yields. The theoretical [X/O] values were calculated using the same method as above for [X/Fe].

There is general agreement between the inferred empirical yields and the models for a subset of elements, Si and S. We see near unanimous agreement between models in their predictions for [C/O], [Fe/O], [Si/O], and [S/O].(There is only one VMP DLA data point available for [S/O].) Wide disagreement is seen in [N/O] where only two models reproduced the empirical yields, HW10 and LC18. No model reproduces [Al/O].

Explosion Landscape and IDROV

All of the models discussed thus far had their parameters tuned to ensure that the star exploded, except EC20. This was also true for LC18, though they ensured that stars above 25 $M_\odot$ fully imploded. There is strong evidence that massive stars in certain regions of mass–metallicity space will collapse directly to a black hole, resulting in zero metal yield, other than any yields from pre-SN winds (Adams et al., 2016; Smartt, 2015; Sukhbold et al., 2016; Woosley, 2017). This so called SN explosion landscape describes the ability of stars to explode or not by assigning one of two outcomes to ranges of stellar mass (at fixed metallicity): (1) explosion potentially with fallback or (2) direct collapse into a black hole. Fallback onto the dense remnant during/after explosion has been shown to be rare in recent studies (Ertl et al., 2020; Sukhbold et al., 2016). Still, given its importance, all of the models we described previously (Sections 2.5–2.5) include fallback in their calculations. We add the yield contributions for exploding stars (i.e., the yields with fallback included) and remove 100% of the yields from the imploding stars.

Because there has not been a recent SN explosion landscape for zero- or low-metallicity stars that accounted for the full mass range (10–100 $M_\odot$), we use results computed by EC20 for the mass range 10–40 $M_\odot$. They found that stars exploded in the mass ranges 11–23 and 27–31 $M_\odot$ (in steps of 1 $M_\odot$) but did not explode otherwise (see Section 2.5 for discussion of the EC20 models). We summarize the explosion landscapes from EC20 and LC18 in Table 2.3.

Table 2.3: SN Explosion Landscapes

Model Range ($M_\odot$)	Step ($M_\odot$)	Explosion ($M_\odot$)	Authors
10–40	1	11–23; 27–31	EC20
13–120	2, 5, 10, 20	13–25	LC18

To understand how the inclusion of realistic explosion physics changes the predicted yields, we show in the top panel of Figure 2.6 abundance ratios from HW10 modified by the SN explosion landscape from EC20 (i.e., only adding the yields from stars that the authors found to explode and removing the yields from those that do not) and as-published LC18 and EC20 yields, along with the empirical DLA abundances. We chose not to adapt this SN explosion landscape to the other yield models because they used different stellar evolutionary codes. The landscape is sensitive to the final core structure of the star, which itself is sensitive to all prior modeling assumptions (e.g., stellar evolutionary code, interaction cross sections, adopted reactions rates, convection criteria, etc.) such that two authors using different assumptions will likely have different landscapes. The progenitors used in HW10 and EC20 used the same formalism, based on the KEPLER code for stellar evolution, as were the the progenitors from Woosley, Weaver (1995) and Woosley et al. (2002). Even though there are differences present between the the progenitors of HW10 and EC20, they are closer to direct comparisons than the other models, who used their own stellar evolutionary code. We calculate the yields in the same manner as the previous section except that we do not interpolate between the modeled masses to ensure that only the stars that explode contribute to the yields. We compared this method with the interpolation method of Section 2.5 and found that they are comparable, with differences < 0.01 dex.

Similar to the SN explosion landscape, one can analogously construct an explosion energy landscape that maps progenitor mass to explosion energy (i.e., remove explosion energy as a free parameter). EC20 predicted explosion energies ranging from 0.3–1.6 B with a peak of ~1.6 B for the 25 $M_{\odot}$ progenitor, and a minimum of 0.3 B for the 31 $M_{\odot}$ progenitor. We adapt this explosion energy landscape to HW10 alongside their explosion landscape (i.e., we ensure that only stars that explode contribute to the yields, and that the energy for each progenitor reflects the energy calculated by EC20 for the progenitor mass), and show the IMF-averaged yields in the bottom panel of Figure 2.6.

We discussed briefly in Section 2.5, that there likely exists a preferred IDROV which one can map from progenitor mass to rotation velocity. There is strong evidence for a bimodal velocity distribution among young massive stars in the local universe in which there are slow rotators (40–60 km s^{-1}) and fast rotators (150–300 km s^{-1}) (Kamann et al., 2020; Milone et al., 2018; Ramírez-Agudelo et al., 2015). Whether a massive star is a fast or slow rotator does not strongly depend on its mass or its membership in a binary system (Bastian et al., 2020; Bouvier, 2013; Kamann et al., 2020). We construct a simple, observationally motivated IDROV that we apply to the LC18 yields in which we require that all stars below a mass cutoff (15, 25, 30, or 40 $M_{\odot}$) are slow rotators with $v_{rot,low}$ = 50 km s^{-1}, and stars above the

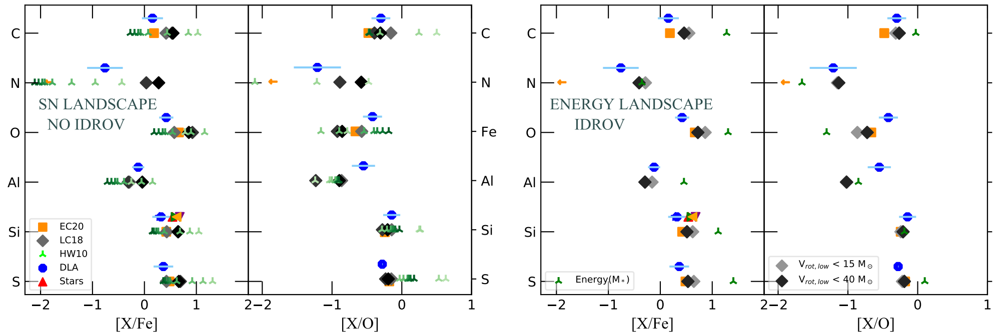

Figure 2.6: Theoretical yield ratios compared to the empirical abundance ratios [X/Fe] on the *left* and [X/O] on the *right*. Same symbols as Figure 2.4 unless noted otherwise. The empirical yields and uncertainties (from DLAs and stars ([Si/Fe])) are vertically offset for clarity. *Top:* Predicted yields from HW10 when imposing a SN explosion landscape, and as-published LC18 and EC20 yields. *Bottom:* HW10 yields when imposing both the explosion landscape and explosion energy landscape (i.e., fixing explosion energy), and LC18 yields when imposing an IDROV such that all stars up to a given mass (e.g., 15 $M_{\odot}$; light grey diamond) rotate with a low initial rotation velocity (50 km s^{-1}) while stars more massive rotate at 250 km s^{-1} (dark grey diamond).

cutoff are rapid rotators with $v_{rot,high}$ = 250 km s^{-1}. We show the IMF-averaged, IDROV-modified LC18 yields in the bottom panel of Figure 2.6.

This IDROV is based on observations of local, solar-metallicity, massive stars. The IDROV might be different at low metallicity. Because there is little to no observational evidence on how rotational velocity or binarity changes at low metallicity (Moe, Di Stefano, 2017), we adopt the IDROV mentioned above with the acknowledgement that it will likely need to be modified when the necessary data is present.

The inclusion of the explosion landscape into HW10 does not make a significant difference in the predicted abundance ratios (less than 0.2 dex for most elements). The behavior seen here is similar to that in Figures 2.4 and 2.5, where for every element HW10 has at least a few explosion energies (typically between 3–10 B) that fall within the range of the empirical constraints, LC18 reproduces most of the abundances, and EC20 is well within the empirical estimates for some elements and differs by more than 1 dex for others.

Imposing the explosion energy landscape onto the HW10 yields results in widespread disagreement with the empirical yields; more than half of the predicted abundance ratios fall well outside the empirical yield uncertainties. The largest disagreement is for [X/Fe], where only one empirical ratio is reproduced, [N/Fe]. Similarly for

[X/O], only one ratio is reproduced, [Si/O].

The IDROV-modified LC18 yields nearly unanimously reproduce the empirical yields (except [Fe/O] and [Al/O]), an improvement compared to the simpler cases shown in the top panel of Figure 2.6 (and Figures 2.4 and 2.5) where all stars are assumed to rotate at the same velocity. The mass cutoffs in the range 25–40 $M_{\odot}$ predict comparable yields, whereas the 15 $M_{\odot}$ cut-off differed by a small amount (< 0.2 dex).

2.6 Lessons from VMP DLAs

In this section we discuss the physical reasons that could explain why each set of yields matched (or did not match) the VMP DLA abundance ratios.

The large variation in explosion energy of HW10 ensured that at least one energy was able to reproduce the empirical yields for most abundance ratios (except [Al/O]) when no explosion landscape or energy landscape was adopted. The energy range that best fit the data varied between 3–10 B. Although we cannot place any constraints on a preferred mixing treatment (because they all predict comparable abundance ratios; see Figure 2.3), we focus on the S4 mass cut over the Y_e mass cut because of the larger range of explosion energies that were modeled. KN06 modeled a similarly wide energy range (1–30 B), but their yields did not reproduce the empirical abundance ratios for as many ratios as HW10. One reason for this could be the calibrations used by KN06 of the amount of ^{56}Ni that each star had to produce. This observational constraint has the effect of restricting the predicted abundance ratios to a smaller range of values than HW10, who did not impose such constraints in their models. When we applied the SN explosion landscape calculated by EC20 in two different ways onto HW10 we found 1) comparable yield predictions when energy is left as a free parameter, but 2) wide disagreement when energy is constrained to be a function of mass. Both points are consistent with the main HW10 result (without the landscape constraints), that higher-energy explosions ($\geq$ 3 B) were needed to reproduce the data. The disagreement in [X/Fe] with the fixed, lower energies can be explained by the resultant low Fe yield from these models, which systematically increased the [X/Fe] ratios for the light and intermediate mass elements (i.e., those synthesized hydrostatically).

LC18, similar to HW10, consistently reproduced the VMP DLA yields with at least one of their models (varying initial rotational velocity) falling within the empirical estimates for each abundance ratio except [N/Fe] and [Al/O]. Similar to KN06, LC18 tuned their models to reproduce observational constraints on the amount of ^{56}Ni produced in the supernova. They achieved this tuning by varying the location of the mass cut for their pre-SN progenitor. The initial rotation velocity that reproduces the empirical yields for most ratios was 0 km s^{-1} (exception to this was [N/O], where the higher rotation velocities reproduced the data). When a simple IDROV is adopted, in which stars below a certain mass threshold were considered slow rotators (50 km s^{-1}) and stars above that mass cut were considered fast rotators (250 km s^{-1}), we found near unanimous agreement between the predicted yields and the empirical yields (exceptions were [Fe/O] and [Al/O]). We acknowledge that this is a simple parameterization that could be improved with better data on the rotation velocities and binarity of low-metallicity massive stars, and/or when binary stellar evolution is modeled in more detail. Even so, our findings may suggest that adopting some observationally motivated IDROV is helpful in matching observed abundance ratios of VMP DLAs.

KN06 reproduced the empirical yields of most abundance ratios to within ~ 0.1 *dex* of the 1-σ confidence interval. A HN contribution of $\gtrsim 50\%$ was required to reproduce more than half of the empirical yields. Exceptions to this agreement were [N/Fe], [N/O], [C/O], and [Al/O]), which were $\sim 0.3 - -1$ *dex* discrepant with the empirical yields. Because N is synthesized hydrostatically during H burning, and is therefore not sensitive to the explosion mechanism of the star, one explanation for this discrepancy could originate in the pre-SN evolution of the star. In contrast, there the Fe yield could also be the cause of the discrepancy.

EC20 reproduced the empirical yields for more than half of the ratios we studied (C, O, Si, and S with respect to O and Fe). N disagreed with the empirical yields by up to a few orders of magnitude (Figures 2.4, 2.5, and 2.6), and Al did not have a prediction for its total yield, so it was not included in our analysis. EC20 uniquely modeled the collapse and explosion phase of the SN for each of the stars they modeled, but they did not model the MS evolution of the stars and instead used pre-SN progenitors from the literature (see Section 2.5). Nitrogen, which is synthesized hydrostatically, showed the largest discrepancy between the EC20 yields and the DLAs. As argued previously, this discrepancy likely originates in the pre-SN evolution of the stars. Another (less plausible) explanation could be that the explosion landscape itself causes the discrepancy. Perhaps the combined mass of N that was lost to implosion, if allowed to contribute to the yields, could account for the differences between the predictions and the data (but see Griffith et al. (2021b)).

EC20's predicted abundance ratios for the intermediate-mass and heavy elements studied here (S, Si, and Fe) consistently reproduced the empirical yields. This suggests that the explosion mechanism employed by the authors is consistent with the data.

There is an interesting discrepancy between HW10 (when the explosion energy landscape is applied) and EC20. One would expect agreement between the two models because they are based on similar progenitors, have the same explosion landscape, and have the same energy constraints. But the bottom panels of Figure 2.6 show that there is still an average difference of 1 dex between them. Specifically, the EC20 [X/Fe] ratios agree with the DLAs for most of the elements including the intermediate-mass elements ([Si/Fe] and [S/Fe]). In contrast, HW10 shows systematically high [X/Fe] for all ratios. EC20 has low [N/O], but they reproduced the empirical [X/O] for all other elements, contrasted by HW10 which only reproduced [Si/O]. As mentioned previously, HW10 produced very little Fe in these low explosion energy models, and EC20 conversely produced a lot of Fe in their lowest explosion energy models. The low iron yields from HW10 are explained by increased fallback of iron-group elements with decreasing explosion energy. Therefore, fallback treatment is likely causing the large discrepancy between the two models.

A common feature in the models that reproduced the data were high explosion energies. We showed in Figures 2.4 and 2.5 that the models that best reproduced the empirical yields were those with explosion energies exceeding 2 B, namely KN06, HW10, and LC18. For calibrated neutrino-driven explosions it is difficult to exceed this threshold, as seen in the peak energy explosion of 1.6 B calculated by EC20 (See also Ertl et al., 2016, 2020; Perego et al., 2015; Sukhbold et al., 2016). As discussed in Section 2.5, it has been shown (Heger, Woosley, 2010) that the core structures for solar metallicity stars and metal-free stars are similar, so it should be the case that the explosion and explosive nucleosynthesis in these models should be similar. Our work adds more evidence to suggest that the energetics of the explosion, and potentially the underlying explosion mechanism, must be modified to allow for higher energies if one is to match the abundances measured from VMP stars and VMP DLAs. An interesting point of contention for this is the fact that EC20, which had comparatively low explosion energies, consistently reproduced the abundance ratios of half of the light elements (C and O) and all of intermediate-mass elements. This suggests that that there may be no need for HN class explosion energies if one properly models the explosion phases of the delayed neutrino-driven mechanISM.

We do not have much observational data on how binarity of massive stars changes at low-metallicity (Moe, Di Stefano, 2017), and are just starting to theoretically explore the effects of binarity on their evolution and final outcomes (Ertl et al., 2020; Vartanyan, Burrows, 2020). A potential solution for the low explosion energies of neutrino-driven explosions would be to invoke a rotationally powered explosion (Mösta et al., 2015) from stars that have evolved in binary configurations where the progenitor gains a substantial rotational energy through its companion. These rotationally powered explosions could achieve explosion energy comparable to HN ($\sim$ 10 B).

2.7 Conclusions

We have placed empirical constraints on the CCSN yields of zero- and low-metallicity stars using the abundances measured from VMP ([Fe/H] < -2) DLAs available in the literature from the past 30 years. The majority of this compilation is based on high-resolution spectroscopic measurements (Section 2.4). We equated the median of the VMP DLA abundances with the IMF-averaged CCSN yield by assuming that the VMP DLAs are at the earliest stages of galactic chemical evolution, where CCSNe dominate the nucleosynthesis.

We show that our approach is complementary, and at times superior, to using VMP stars for the same work (Section 2.4; e.g., Berg et al., 2015a; Welsh et al., 2019). In particular, for elements whose stellar photospheric abundances depend on the assumption of LTE (O, Al), astration corrections (N), or difficult-to-measure atomic transitions (O, S), VMP DLAs are superior because measuring abundances from their cool, mostly neutral gas relieves the need for such corrections or considerations.

We compare the empirical yields to the most widely adopted theoretical yields in the literature and find that all models can reproduce the empirical yields for a subset of abundance ratios studied here by varying only a single parameter (e.g., explosion energy, HN contribution, or initial rotation velocity). The yields calculated by HW10 (Section 2.5) consistently reproduce the empirical yields with explosion energies ranging from 3–10 B, even when a relevant SN explosion landscape is adopted (Section 2.5). However, when fixing explosion energy for a given progenitor mass with a functional form derived by EC20 (i.e., imposing an explosion energy landscape) the theoretical yields disagree widely with the DLA observations. LC18 (see Section 2.5) reproduced most of the empirical yields with their 0 $km\ s^{-1}$

initial rotation velocity models, though some of the empirical yields were only reproduced by the higher rotation velocity models. When we apply a simple IDROV that mimics the bimodal velocity distribution of young massive stars in the local universe, there is near unanimous agreement between the predicted abundance ratios and empirical yields. KN06 (Section 2.5) adequately reproduced the empirical yields when contributions from HNe were $\gtrsim 50\%$ for most ratios, reinforcing the ability for high-energy explosions to match the DLA observations.

We found that the inclusion of realistic explosion physics (i.e., taking into account ranges of initial stellar mass that fail to explode) in the theoretical yields does not result in a quantitatively better fit to the empirical yields. Interestingly, models from the PUSH collaboration or EC20 (see Section 2.5), show the largest discrepancies in light element production (N) compared to the empirical yields, even though these models take into account the explosion landscape with initial stellar mass. These discrepancies likely originate in the pre-SN evolution of the star and not the modeling of the explosion (see Section 2.5). This assertion is supported by EC20 consistently reproducing the empirical ratios containing intermediate mass and heavy elements (e.g., Si, S, and Fe), which are more sensitive to the explosion mechanism, but not reproducing the ratios containing N.

Models that frequently reproduced the VMP DLAs abundance ratios had high explosion energies (≥ 2 B). This finding adds more observational evidence to suggest that higher energies are helpful, perhaps necessary, in reproducing abundances measured from near pristine gas. However, these energies are believed to be unattainable with neutrino-driven explosions (e.g., Ertl et al., 2020; Sukhbold et al., 2016). There is some evidence that rotationally powered explosions, in which the progenitor gains rotational energy from its companion, could provide the necessary explosions energies (Mösta et al., 2015). However, the close match between the empirical yields and the predictions from EC20 of the intermediate mass elements (whose abundances are more sensitive to the explosion of the star) supports the opposite conclusion: HNe are not needed to explain the abundance patterns if the explosion of the CCSN is modeled properly. A more detailed analysis of the Fe-peak element production between these different models could answer this question definitively.

VMP DLAs have allowed for an empirically driven approach to quantify the abundances of metals ejected from the first stars. They are complementary to using VMP stars for the same purpose (e.g., Griffith et al., 2021a; Grimmett et al., 2018; Ishigaki et al., 2018, K19). Improvements that would benefit future work using VMP DLAs include increasing the number of elemental abundances measured from VMP DLA spectra so that more abundance ratios can be constrained, and increasing the sample size of VMP DLAs to improve the statistics of the empirical constraints. Even with our current constraints (Table 2.2), an interesting avenue of inquiry would be to quantify how the results of galactic chemical evolution models (e.g., Kirby et al., 2011, de los Reyes (submitted)) change when theoretical input yields are replaced with our empirically estimated yields from VMP DLAs.

Acknowledgements

We thank Tuguldur Sukhbold for their in-depth comments and correspondence that significantly improved this work. We thank Ryan Cooke, Louise Welsh, Donatella Romano, Carl Fields, Lynne Hillenbrand, and Sanjana Curtis for thoughtful conversations and for sharing information and data that improved the quality of this work. We thank our referee for helpful comments that improved this paper. E.H.N. acknowledges the support of the NSF Graduate Research Fellowship Program. This material is based upon work supported by the National Science Foundation under Grant No. AST-1847909. E.N.K. gratefully acknowledges support from a Cottrell Scholar award administered by the Research Corporation for Science Advancement.

Astropy (Astropy Collaboration et al., 2018, 2013)

Chapter 3

KBSS-INCLOSE I: DESIGN AND FIRST RESULTS FROM THE INNER CGM OF CLOSE QSO LINE OF SIGHT EMITTING GALAXIES AT $z \sim 2-3$

Nuñez Evan Haze, Steidel Charles C., Kirby Evan N., Rudie Gwen C., Prusinski Nikolaus Z., Chen Yuguang, Zhuang Zhuyun, Strom Allison L., Erb Dawn K., Pettini Max, Welsh Louise, Rupke David S. N., Cooke Ryan J. KBSS-InCLOSE. I. Design and First Results from the Inner Circumgalactic Medium of QSO Line-of-sight Emitting Galaxies at z ∼ 2–3 // . XI 2024. 976, 1. 41.

3.1 Abtract

We present the design and first results of the Inner Circumgalactic Medium (CGM) of QSO Line of Sight Emitting galaxies at $z \sim 2-3$, KBSS-InCLOSE. The survey will connect galaxy properties (e.g., stellar mass M_*, interstellar medium ISM metallicity) with the physical conditions of the inner CGM (e.g., kinematics, metallicity) to directly observe the galaxy-scale baryon cycle. We obtain deep Keck/KCWI optical IFU pointings of Keck Baryonic Structure Survey (KBSS) QSOs to discover new star-forming galaxies at small projected distances $b \lesssim 12$" (98 kpc, $\overline{z} = 2.3$), then obtain follow-up Keck/MOSFIRE NIR spectra to confirm their redshifts. We leverage KBSS images and Keck/HIRES QSO spectra to model stellar populations and inner CGM absorption. In this paper, we analyze two QSO fields and discover more than 15 new galaxies with KCWI, then use MOSFIRE for two galaxies Q2343-G1 ($z = 2.43$; G1) and Q2233-N1 ($z = 3.15$; N1), which are both associated with Damped Lyman Alpha absorbers. We find that G1 has typical M_*,UV/optical emission properties. N1 has lower M_* with very strong nebular emission. We jointly analyze neutral phase CGM and ionized ISM in N/O (for the first time at this z), dust extinction, and high-ionization CGM finding that G1's CGM is metal poor and less evolved than its ISM, while N1's CGM and ISM abundances are comparable; their CGM shows ~ 1 dex less dust extinction than the ISM; and G1's CGM has direct evidence of hot, metal-rich galactic outflow ejecta. These findings support that metals and dust are driven into the CGM from outflows, but may also be, e.g., stripped ISM gas or satellite enrichment. The full KBSS-InCLOSE sample will explore these scenarios.

3.2 Introduction

Connecting galaxy properties and the physical conditions of the inner circumgalactic medium (CGM) of $z \sim 2-3$ star-forming galaxies is necessary to understand the evolution of baryons in the galaxy. There have been many statistical analyses of the $z = 2-3$ ISM (e.g., Kriek et al., 2015; Shapley, 2011; Shapley et al., 2005; Steidel et al., 2003; Strom et al., 2017) and CGM absorption properties (e.g., Lehner et al., 2014, 2022; Péroux, Howk, 2020; Prochaska et al., 2007b; Rudie et al., 2012; Simcoe et al., 2006; Turner et al., 2014; Wolfe et al., 1986, 2005) but it is difficult to make confident ISM-CGM connections of the same galaxy.

This redshift range lies close to the peak of star formation rate density in the universe (sometimes called "Cosmic Noon") when many galaxies were rapidly assembling (i.e., heavily star-forming). It has been shown that rapidly star-forming galaxies ubiquitously exhibit strong galaxy-scale outflows with occasional evidence for inflows/accretion (e.g., Prusinski et al., 2021; Shapley, 2011; Steidel et al., 2010).

Strong outflows suggest that a significant amount of gas is being ejected into the CGM (and/or intergalactic medium; IGM). Similarly, the presence of inflows may indicate that previously-ejected gas—possibly mixed with primordial gas— falls back onto the galaxy, providing fuel for further star formation and chemical enrichment (e.g., Anglés-Alcázar et al., 2017; Tumlinson et al., 2017). The process by which baryons transition through different phases (e.g., T, ρ) during a galaxy's star formation history (SFH) is known as the "baryon cycle." Such strong outflows suggest that most of the baryons associated with a galaxy reside in the CGM during the peak epoch of galaxy formation, and therefore it *must* be included in our understanding of the galaxy formation and evolution process.

Even though there is a significant amount of mass in the CGM, the gas is very diffuse and difficult to observe directly in emission due to its intrinsically low surface brightness (e.g., Tumlinson et al., 2017). We must instead rely on unrelated bright background sources (e.g., QSOs) to provide absorption signatures. A high resolution spectrum of the background QSO provides a detailed, albeit singular, view of the galaxy's CGM at a particular projected distance, or impact parameter (b), with the caveat that the pencil beam sightline might not be representative of the entire CGM (e.g., Cooke et al., 2010; Rudie et al., 2019). This suggests that when using galaxy-QSO pairs, one we must build a large statistical sample of galaxies with similar properties (e.g., stellar mass M_*, star formation rate SFR, metallicity, etc.) with background probes sampling a range of impact parameters.

Galaxy-QSO pairs with small impact parameters (i.e., within the galaxy's viral radius or $R_{\rm vir}$) offer the best chance of seeing (1) CGM gas that is directly associated with the galaxy, and (2) a causal connection between the galaxy's ISM and CGM properties, where ongoing star formation and AGN activity – and resultant feedback processes – are likely to be reflected in the physical properties of the CGM (e.g., Mintz et al., 2022; Pratt et al., 2018; Prochaska et al., 2017; Turner et al., 2014; Zahedy et al., 2021).

Work over the past decade using galaxy-QSO pairs has increased our understanding of the CGM at low redshift ($z \sim 0.3$; e.g., Prochaska et al., 2017; Tumlinson et al., 2017, 2013; Werk et al., 2014), intermediate redshift ($z \leq$0.3–1; e.g., Chen et al., 2023, 2020a; Qu et al., 2023, 2022; Zahedy et al., 2021), $z \sim 2-3$ (Nielsen et al., 2022; Rakic et al., 2012; Rudie et al., 2019, 2012; Turner et al., 2014, 2015, e.g.,), and $z \sim 3-4$ (e.g., Galbiati et al., 2023; Lofthouse et al., 2023, 2020).

However, only at low-z and intermediate-z is there a large statistical sample (N$\gtrsim$50) of similar galaxies (e.g., with $L \sim L_*$) with CGM gas probed within the virial radius ($b \leq R_{\rm vir}$). To date there are about two dozen $z \sim 2-3$ galaxies that are thought to be associated with QSO absorption systems of various $N_{\rm HI}$ densities and metal line detections at $b < 100$ kpc in the literature (e.g., Krogager et al., 2017; Rudie et al., 2019; Weatherley et al., 2005). Of these, less than a dozen have well-characterized ionized ISM and stellar populations (i.e., far ultraviolet FUV and optical nebular emission spectra, FUV–Optical SEDs; Rudie et al., 2019).

Rudie et al. (2019) used a sample of 8 $z \sim 2.3$ KBSS galaxy-QSO pairs with known galaxy properties and found that the $b \lesssim R_{\rm vir}$ high-z CGM is multiphase (with singly, doubly, and triply ionized species sharing the same component or "cloud" structure), kinematically complex (requiring more than 10 components to model the absorption), contains a significant amount of metals (high covering fraction of metal ions, and a large estimated metal halo mass compared to the ISM), has a high occurrence of gravitationally unbound gas (70% of the galaxies have absorber components with velocities in excess of the escape velocity $v_{\rm esc}$ ~450-550 km s^{-1}), and is thermally supported (thermal broadening dominates over turbulent/non-thermal broadening). These first results must be explored further to understand how and if they correlate with galaxy properties such as stellar mass, SFR, nebular metallicity and ionization, Lyα halo properties, etc. To accomplish this, we must build a larger sample of $z \sim 2-3$ galaxy-QSO pairs probing $b < R_{\rm vir}$.

KBSS-InCLOSE (an extension to KBSS-KCWI; Chen et al. (2021)) is an ongoing campaign to connect galaxy properties with the physical conditions of the Inner CGM of QSO Line Of Sight Emitting (InCLOSE) galaxies at $z \sim 2-3$. InCLOSE will leverage the approach (and ancillary data) employed (gathered) by the original KBSS survey (e.g., Rudie et al., 2012; Steidel et al., 2014; Turner et al., 2014) to connect galaxies to the exquisite information provided by signal-to-noise ratio $S/N \sim 50-100$ HIRES spectra of QSOs carefully selected to lie just "behind" the galaxy survey volume. In spite of years of effort obtaining LRIS and MOSFIRE spectra of more than 3,000 galaxies in the redshift range $2 \leq z \leq z_{\mathrm{QSO}} \sim 2.8$, the census of galaxies in KBSS was known to be highly incomplete at very small angular scales ($\theta \lesssim 8-10$ arcsec), or impact parameters of $b \lesssim 100$ physical kpc (pkpc) due to the "glare" of the PSF of the very bright ($V \sim 16-17$) QSOs. As a result, there were only 8 spectroscopically identified galaxies with $b < 100$ pkpc (1 of which with $b < 50$ pkpc, Rudie et al. (2019)) – and yet these are the only systems in KBSS where the QSO spectrum is probing gas within the virial radius of the galaxies ($\sim 80-90$ kpc; e.g., Trainor, Steidel (2012)), where the response of CGM gas to ongoing star formation and resultant feedback processes will be most evident.

InCLOSE will address the incompleteness of the original KBSS survey at small impact parameters to expand the sample reported in Rudie et al. (2019). Specifically, Keck Cosmic Web Imager (KCWI; Morrissey et al., 2018) optical IFU pointings of all the KBSS QSOs is used to find previously "missed" galaxies. Then follow-up NIR spectra using the Multi-Object Spectrometer for InfRared Exploration (MOSFIRE; McLean et al., 2012) will be obtained to spectroscopically confirm and characterize the ionized ISM of newly found galaxies. Each KCWI pointing focuses on the regions within $10-12''$ (82-98 pkpc at z ~2.3) of the QSO sightline, specifically configured to discover previously unseen absorbing galaxies within projected distances of ≤ 100 pkpc. This "discovery" phase is critical and relies on KCWI's blue sensitivity for detections of Lyα emission (and FUV continuum) in the redshift range of interest, $z \sim 2.08-2.61$. Additionally, the data cubes allow for accurate subtraction of the QSO PSF which is required for detecting these near QSO line-of-sight (nLOS) galaxies.

This redshift range is optimized to allow for observations of a large suite of strong nebular emission lines in the observed-frame near-IR atmospheric bands with MOSFIRE including Hα, Hβ, [O III], [O II], [S II], and [N II] at $z \sim 2.3$, all with resolving power $R \sim 4000$. Rest-frame optical nebular spectra enable the measurement of ionized gas-phase physical conditions (H II regions) in the inner regions of galaxies, allowing for a direct comparison of the galaxy ionized ISM properties with those measured in the CGM. More explicitly they provide: (1) precise galaxy systemic redshifts (uncertainties $|\delta v| < 20$ km s^{-1}) from strong non-resonant emission lines (e.g., [O III]λ5008, Hα), (2) gas-phase oxygen abundance (and, for a subset, abundances of N, and S), (3) measurements of star formation rates (SFRs) derived from the dust-corrected Hα luminosity (or limits from Hβ luminosity), and (4) dynamical mass measurements, from nebular line widths when combined with *HST* sizes, etc.

Importantly, these critical diagnostics are almost entirely lacking in the literature because the inclusion of the rest-optical spectrum of absorption-bearing nLOS galaxies has been done only a handful of times at this z (e.g., Christensen et al., 2004; Christenson, Jorgenson, 2019; Møller et al., 2002; Neeleman et al., 2018; Rudie et al., 2019; Weatherley et al., 2005).

Each KBSS-InCLOSE galaxy will have (assuming $\bar{z} \sim 2.3$): (1) a rest-FUV spectrum from KCWI blue covering 1060-1665 Å in the rest frame, (2) a rest-optical spectrum from MOSFIRE covering 3650-6800 Å in the rest-frame, (3) deep imaging from ground- and space-based observatories covering 0.1-1.4 μm in the rest-frame, including at least one band observed with *HST*/WFC3-IR, (4) a Lyα emission and velocity map (from KCWI blue), and (5) a HIRES spectrum of the background QSO with average S/N$\sim 50-100$ covering absorption systems from 970-3045 Å in the rest-frame. Using products (1)–(3) we will characterize the ionized ISM and stellar populations of the galaxies, measuring or inferring properties such as systemic redshift, star formation rate SFR, nebular metallicity, stellar mass, etc., and using product (4) we will characterize the global view of the cold emitting CGM via Lyα and (5) analyze a highly detailed view (at $b < R_{\rm vir}$) of the CGM via background QSO absorption, measuring or inferring H I and metal abundance, kinematic properties, and thermal properties. Altogether by combining (1)–(5) for a large sample of galaxies we aim to explicitly connect galaxy and CGM properties of star-forming galaxies at $z \sim 2-3$.

In this paper, we focus on two galaxies toward two QSOs – Q2343+1232 ($z_{\rm QSO}$ = 2.573) and Q2233+1310 ($z_{\rm QSO}$ = 3.295; which is not part of KBSS) – for which we have added extensive new optical IFU data from KCWI (Christensen et al., 2004; Trainor, Steidel, 2012). These fields have a rich history in the literature and are known to have at least one nLOS star-forming galaxy per field. One of the galaxies, toward Q2343+1232, was missed from the KBSS survey due to its proximity to the QSO (e..g., Strom et al., 2018) but was found recently by Nielsen et al. (2022) using KCWI. The other galaxy is towards Q2233+1310. It was discovered using rest-FUV color selection and was found by early optical IFU observations to be very bright in Lyα (e.g., Christensen et al., 2007; Steidel et al., 1996, 1995).

We selected these two galaxies because their brightness and proximity to QSO sightlines allowed us to develop methods to discover and analyze new galaxies. They should not necessarily be taken as representative of the broader InCLOSE population. Rather, they are systems with high-quality data useful for refining our methodology. These methods will be applied to future observations where we will have little a priori knowledge about $z \sim 2-3$ nLOS galaxies surrounding the KBSS QSOs. The workflow, techniques, and analysis presented here will be applied to the growing KBSS-InCLOSE sample in future papers.

The main results of this paper can be found in Section 3.6. The paper is organized as follows. In Section 3.3, we discuss our observations and data reduction, how we remove the bright background QSOs from our datacubes and images, then we analyze the galaxies' ionized ISM emission via rest-FUV spectra, rest-optical spectra, and rest-FUV to rest-optical SED. In Section 3.5, we analyze the inner CGM of the galaxies via H I CGM emission (i.e., Lyα halo, and background QSO absorption. In Section 3.6, we discuss insights into the galaxy scale baryon cycle by explicitly comparing ISM and CGM properties. In Sections 3.7 and 3.8, we discuss our findings and caveats, then summarize the paper. We adopt solar abundances from Asplund et al. (2009). We adopt the following ΛCDM cosmological parameters: $H_0 = 70\ km\ s^{-1}\ Mpc^{-1}, \Omega_m = 0.3, \Omega_\Lambda = 0.7$.

3.3 Data and Observations

Discovering nLOS Galaxies with KCWI

Obtaining KCWI pointings of the KBSS QSO fields is crucial for discovering new nLOS galaxies. Our primary KCWI configuration uses the Medium slicer (slice width= $0\farcs69$) and large blue (BL) grating to provide an optimal compromise between field of view (FoV≃ $16\farcs5 \times 20\farcs3$, or ≃ 135×166 physical kpc (pkpc) at z∼2.3), wavelength coverage (3500−5500 Å), and spectral resolution (2.5 Å, or $R = 1400 - 2240$) across the band.

A summary of the observations are shown in Table 3.1. For Q2233+1310, the data comprise a total of 5 hours integration time taken with the same observational approach, in which each of 15 individual 1200s exposures was obtained with a different position angle of the IFU on the sky, with small ($\lesssim 1''$ moves of the center position of the pointing, in order to achieve reasonable spatial sampling and minimize pixel covariance in the final data cube.

Table 3.1: New Observations Summary

Object	Type	Instrument (Config.)	RA (J2000.0)	Dec (J2000.0)	t_{exp} (hr)	Date (Y/M/D)	PI	P/ID
Q2343+1232	Optical IFU	KCWI	23:46:28.30	+12:48:57.8				
		Med/BL	-	-	5.2	2018/11/10	Steidel	C305
	Optical Images	LRIS	23:46:28.42	+12:48:57.4				
		U_n,G,R	-	-	1.9,0.7,2.2^a	2022/08/23	Steidel	C409
	NIR Spectra	MOSFIRE	23:46:28.42	+12:48:57.4				
		J,H,K	-	-	1.4,1.0,2.0^b	2022/09/17	Steidel	C409
Q2233+131	Optical IFU	KCWI	22:36:19.21	+13:26:19.3				
		Med/BL	-	-	2.0	2021/09/05	Steidel	C249
		Med/BL	-	-	3.0	2021/08/11	Erb	R349
	NIR Spectra	MOSFIRE	22:36:19.27	+13:26:16.9				
		H,K	-	-	0.9,1.0^c	2022/09/17	Steidel	C409

a) U_n, G, R band exposure times.
b) J, H, K band exposure times.
c) H, K band exposure times.

For Q2343+1232 we combined our own KBSS-KCWI data set, with a total exposure time of 18700 s (5.2 hours) centered at a position 8″.7 NE of the QSO (such that the QSO falls in the SW corner of the final mosaic, where the net integration time is closer to 17500 s), with additional data retrieved from the Keck Observatory Archive[1] (KOA) (see Nielsen et al. (2022)) composed of two partially overlapping footprints taken at the same PA, where the region of overlap is centered on the QSO position with a total exposure time of ~ 5670 s (1.6 hours). In the region of full overlap of between the two observations [2], the total exposure time is ~ 24400 s (6.8 hours), but the region SW of the QSO has received significantly less integration time (0.8 hours).

We reduced the KCWI data using a custom version of the publicly available KCWI DRP[3], with modifications as described by Chen et al. (2021) including a second-pass correction to the background subtraction.

Reduced data cubes from each individual 1200 s exposure were combined into a final mosaic using a custom post-DRP pipeline[4] (Prusinski, Chen (2024); implementation described in Chen et al. (2021)) that projects each exposure onto an astrometrically-

[1]https://koa.ipac.caltech.edu/cgi-bin/KOA/nph-KOAloginhttps://koa.ipac.caltech.edu/
[2]This includes the position of galaxy Q2343-G1.
[3]https://github.com/Keck-DataReductionPipelines/KCWI$_DRP$
[4]https://github.com/yuguangchen1/KcwiKit.git

correct grid with spatial sampling of $0\farcs3 \times 0\farcs3$ or $0\farcs2 \times 0\farcs2$ and wavelengths sampled with 1 Å/pixel.

The same procedures were used to re-reduce the archival KCWI data (in the case of the Q2343 field) and incorporate them into the final mosaic.

Need for QSO PSF Subtraction

Galaxies with small impact parameters will have varying levels of "contaminant" emission from the bright background QSOs that must be removed. The QSO contamination affects all derived physical properties of the galaxy deduced from the datacubes, extracted spectra, and images.

The difficulty of QSO subtraction from the IFU cubes is exacerbated by our goal of detecting the nebular line emission *and* stellar continuum emission of the galaxies in the rest-FUV, e.g., to measure kinematics and flux of spatially extended Lyα emission and interstellar absorption lines.

In the following sections, we present two methods for subtracting QSOs from the KCWI cubes. The first method recovers only extended line emission from the galaxy and is used first to detect new line emitting objects, then for analyzing extended line emission, e.g., Lyα in the emitting CGM. The second method recovers the full rest-FUV spectrum of the galaxy (FUV continnum+Lyα halo) and is used to detect nLOS continuum-emitting sources, then measure line flux, line centroids, and equivalent widths of nebular emission and interstellar absorption lines.

QSO PSF and Continuum Source Subtraction, and Halo Extraction using CubePSFSub

CubePSFSub is a routine within the package CubExtractor (Cantalupo et al., 2019, hereafter C19) that removes QSO emission using an empirical PSF model constructed from the cube itself. It provides an efficient means to discover new line emitting galaxies and extract physical properties of their Lyα halos. The package is described in detail in C19 but we summarize it here. The inputs for the program include the position of the QSO, an inner radius (R_{in}) to set the normalization constant for the subtraction, an outer radius (R_{out}) within which the subtraction is performed, a spectral width ($\Delta\lambda$) to define the PSF size, and number of spectral bins to divide the cube (N_{bins}).

CubePSFSub makes pseudo-narrowband images using the mean flux across the spectral width $\Delta\lambda$ (for each spaxel) using R_{in} (usually a cirular aperture with a radius of 2 pixels which is the typical two-dimensional 2D Gaussian full width at half maximum (FWHM) of the QSO ∼4 spaxels) to set the peak value of the image. It then subtracts a flux scaled, pseudo-narrowband image from each wavelength slice of the data cube. We ran the routine with no spectral binning i.e., a running filter. We mask wavelength layers where we expect there to be line emission to reduce oversubtraction.

We varied the spectral width from 50 Å to 750 Å and found that values between 250–500 Å were preferable. We tested this explicitly by fixing all other parameters (R_{in}, R_{out}), then extracting the resultant extended emission from Q2233-N1's Lyα halo using CubEx (assuming spatial and spectral filtering of 1 pixel, and a S/N=1.5). We found that PSF sizes between 250–400 Å resulted in comparably extended emission, while values below (above) this threshold resulted in 6% (2%) less detected emission. Additionally, values below this threshold left the cube with significantly increased instances of over-subtraction. Values above the threshold increased the overall residuals. We used a spectral width of 350 Å for Q2343+1232 and 300 Å for Q2233+1310.

Finally, after PSF subtraction we removed all continuum sources from the cube using the CubeBKGSub package (in CubExtractor) to ensure that neither QSO continuum nor other continuum sources were left in the cube. We use the same parameters as C19 by setting the median filtering to a bin size of 50-100 Å with a spatial and spectral smoothing of 1 pixel (0.3”, 1Å).

We are left with a continuum subtracted datacube that contains only extended line emission, which we use to find new line emitters, then characterize the physical properties of the emitting CGM (e.g., physical size, flux, kinematics) in Section 3.5. We refer to these cubes as “QSO+continuum subtracted.”

Spatially extended line emission maps were extracted from these cubes using a combination of CubExtractor and a custom script to find peaks of Lyα emission per spaxel. CubExtractor was used to make segmentation masks to highlight the voxels (RA, Dec, Wavelength) that are within ±3000 $km\ s^{-1}$ of the emission line of interest (i.e., Lyα) and have a signal-to-noise ratio greater than 3.5 after the cube is spatially and spectrally filtered by 1 spatial bin (0.2″ –0.3″) and 1 spectral bin (1 Å), which are typical values (e.g., Cantalupo et al., 2019; Langen et al., 2023). The 3D mask is then flattened to 2D by summing all spaxels to a single value (i.e., collapsing over wavelength) and keeping pixels with values >1 (i.e., we ensure that there is a detection in each spaxel; discussed more later). The segmentation mask is then applied to the 3D cube and (1) all of the surface brightness (SB) within each spaxel is summed to create spatial distribution maps, then (2) the peak wavelength of each spaxel is located and converted to velocity using the systemic redshift measured from Section 3.5.

We compared our methodology to the maps that can be generated from CubEx and find that they are comparable. We used our custom script due to its flexibility to more easily remove the QSO residuals from the SB and velocity maps.

QSO Spectral Subtraction using IFSFIT

IFSFIT (Rupke, 2014; Rupke et al., 2017) uses a purely spectral approach to subtract QSOs from data cubes. This approach can disentangle the spatially and spectrally varying contributions of the QSO in *each* spaxel so as to remove only the QSO light but preserve nLOS galaxy light.

Rupke et al. (2017) described the method in detail but here we summarize the main differences in our implementation. We want to remove all emission related to the QSO including its host galaxy so we modified the method to rely solely on the input QSO spectrum. Our method can be broken down into four steps: 1) QSO continuum extraction, 2) QSO subtraction, 3) QSO halo extraction, and 4) and QSO halo subtraction.

Step (1) is to extract the QSO continuum spectrum from the KCWI data cube. We use a circular aperture centered on the QSO position with a diameter equal to the FHWM (seeing) of the pseudo-broadband cube (2D collapsed by summing from 3500-5500 Å) i.e., where the QSO dominates the spectrum. The QSO centroid and the seeing were determined from a 2D Gaussian fit performed on the pseudo-broadband image.

Step (2) is to feed the extracted QSO continuum spectrum into IFSFIT without stellar population synthesis models or emission line modeling (steps 1 and 2 from Rupke et al. (2017)). Algorithmically, the program extracts the spectrum of each spaxel and models it as two components such that

$$S_{SPAXEL}(x,y) = A(x,y) \times S_{\mathrm{QSO}} + S_{Cont}(x,y) \tag{3.1}$$

where $S_{SPAXEL}(x,y)$ is the extracted spectrum from location x, y, $A(x,y)$ is a constant that scales the input QSO spectrum according to a series of exponential functions (which keeps the QSO spectrum positive-definite and accounts for changes in seeing and spectral sensitivity) based on the x, y location in the cube, S_{QSO} is the input QSO spectrum, and $S_{Cont}(x, y)$ is the featureless additive continuum model. For example, if there is a galaxy present in the spaxels at (x, y) then $S_{Cont} = S_{Galaxy}$. In all cases, both A and S are fit to minimize the residuals between the data (S_{SPAXEL}) and model ($A \times S_{\mathrm{QSO}} + S_{Cont}$).

The output is a QSO-continuum-subtracted cube, i.e., the difference between the S_{SPAXEL} and $A \times S_{\mathrm{QSO}}$, expressed as

$$S_{cont} = S_{SPAXEL} - A \times S_{\mathrm{QSO}} \tag{3.2}$$

In Figure 3.1 we show the results of this procedure before and after being applied to the KCWI cubes towards Q2343+1232 and Q2233+1310.

Previously known galaxies Q2343-G1 and Q2233-N1 are clearly visible in the subtracted data cube along with more than seven new galaxies per field.

In order to ensure that the continuum and spectral lines detected in the extracted galaxy spectra were minimally affected by residual contamination from the QSO, we varied the radius of the circular aperture used to define the QSO spectrum and examined the resultant extracted galaxy spectra.

We found that the galaxy spectra extracted from the QSO-subtracted data cubes were insensitive to the aperture size used to define the QSO "basis spectrum"; in general, the aperture radius does not affect the strength or centroid of galaxy emission or absorption features or the overall shape of the galaxy continuum (see Appendix A for more details). We used the aperture that fully sampled the QSO PSF (i.e., an aperture with a 2-spaxel radius) as our default.

Steps (3) and (4) of the spectral cube subtraction are concerned with extracting and subtracting extended nebular emission associated with the QSO because it could affect the extracted spectra of nLOS galaxies, e.g., elevating the continuum surrounding nebular emission, and interstellar absorption lines. The Lyα emission is generally more narrow (spectrally) than the emission from the broad-line region meaning it is not completely removed in Step (2). To remove the extended narrow-line QSO halo emission, we first visually identified spaxels that contained extended Lyα emission in the QSO continuum-subtracted cube. We extracted the average Lyα spectrum ensuring that no spaxels were spatially coincident with emission from other objects in the field (Step 3). In other words, we assume that we can represent the

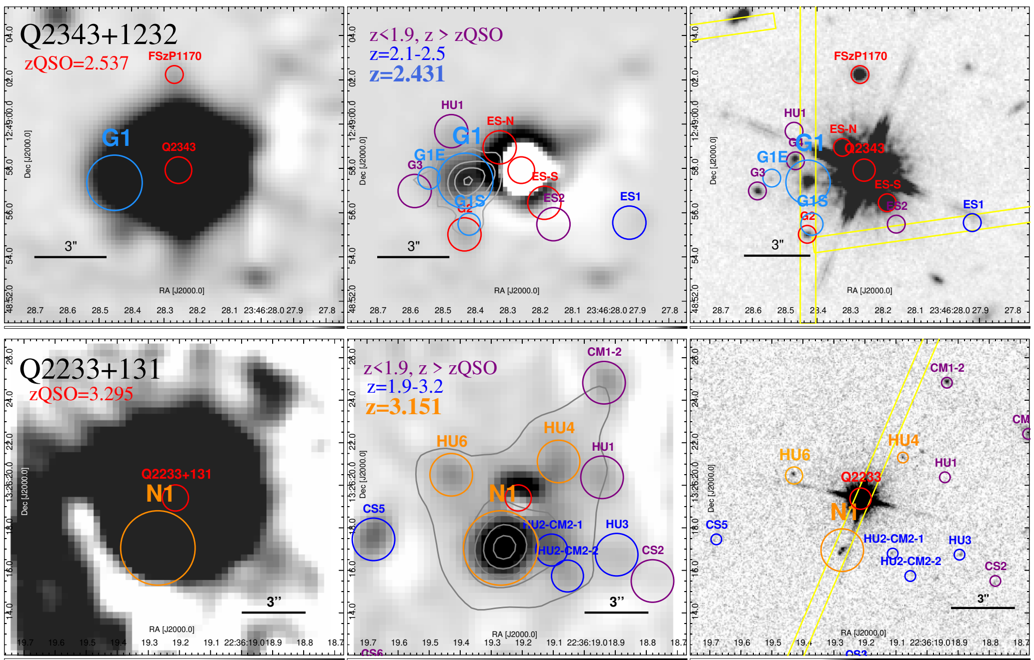

Figure 3.1: Rest-FUV and rest-Optical images of the QSO sightlines. *Left column:* Keck/KCWI pseudo-broadband (3500–5500 Å) images before and after (*Middle column*) QSO subtraction; the images are on the same scale and stretch, showcasing the effectiveness of the subtraction (see Section 3.3). The grey contours in the post subtracted images show constant Lyα surface brightness ($v_{\mathrm{Ly}\alpha} \sim \pm 1000\,\mathrm{km\ s^{-1}}$; discussed in Section 3.5) *Right column: HST* images of the QSO sightlines. Objects at a similar redshift have the same color and are summarized in Section 4.3. *Top row:* The small red circle shows QSO Q2343, the large blue circle shows galaxy Q2343-G1, the Lyα contours show 0.35, 0.06, 0.01, 0.0012 $\times 10^{-17}\mathrm{erg\ s^{-1}\ cm^{-2}}\ arcsec^{-2}$ for the galaxy, and the *HST*-IR/WFC3 F160W image shows all objects at higher resolution. *Bottom row:* The red circle shows QSO Q2233, the large orange circle shows galaxy Q2233-N1, the Lyα contours show 0.06, 0.04, 0.02, 0.002 $\times 10^{-17}\mathrm{erg\ s^{-1}\ cm^{-2}}\ arcsec^{-2}$ for the galaxy, and the *HST*/WFPC2 F702W image shows all objects at higher resolution. Both galaxies lie at small impact parameter $b \sim 20kpc$ (see Table 3.2). More than 15 new galaxies were discovered from the KCWI cubes. North is up and east is left.

QSO Lyα halo peak flux and line shape using an average one-dimensional (1D) spectrum, which should be adequate to remove the most luminous portions of the halo.

We fed the 1D Lyα halo spectrum into IFSFIT where it was run on the QSO continuum-subtracted cube in the same two-component mode described above[5]. The resultant cube is QSO continuum+halo subtracted that can be used to extract the spectrum of continuum-detected objects at very small impact parameters with minimal flux from the QSO continuum or Lyα halo.

We show the effects of all four steps on the extracted spectra of galaxies Q2343-G1 and Q2233-N1 in Appendix A.

We refer to the resultant cube as "QSO-spectrally subtracted." With this cube we were able to find continuum emitting nLOS galaxies and measure their emission/absorption line properties (see Section 3.3). We also used the cubes to verify the extent and flux of Lyα emission from the galaxies, finding that they are comparable (i.e., Figure 3.7 is the same regardless of using the QSO-spectrally subtracted cube or the QSO+continuum subtracted cube)

The 1D rest-FUV spectra of the galaxies were extracted from the QSO-spectrally subtracted KCWI cubes (see Section 3.3) by averaging all of the spaxels that contained continua of the galaxy as seen from the pseudo-broadband images (summed from 3500–5500 Å). We preferred this method over, e.g., weighting the spaxels based on their flux, because the extracted spectrum was otherwise noisier, likely due to to a combination of object faintness and increased noise residuals from the QSO subtraction process.

At the top of Figures 3.2 and 3.3 we show the smoothed (3 pixels/Å; for clarity) rest-FUV spectra of G1 and N1 with IS lines overplotted at the galaxies systemic redshift (Section 3.3). The quality of the KCWI spectrum is such that average IS lines have $S/N \gtrsim 2$, which is adequate for checking preliminary redshift; Lyα has $S/N \geq 50$.

New Objects Toward Q2343+1232 & Q2233+131

We identified previously uncatalogued objects using the deep KCWI cubes. We started classification by making pseudo-broadband images from the non-QSO sub-

[5]The QSO's Lyα halo spectrum is featureless (i.e., effectively zero) at all wavelengths besides the QSO peak, because the cube has already been QSO continuum subtracted.

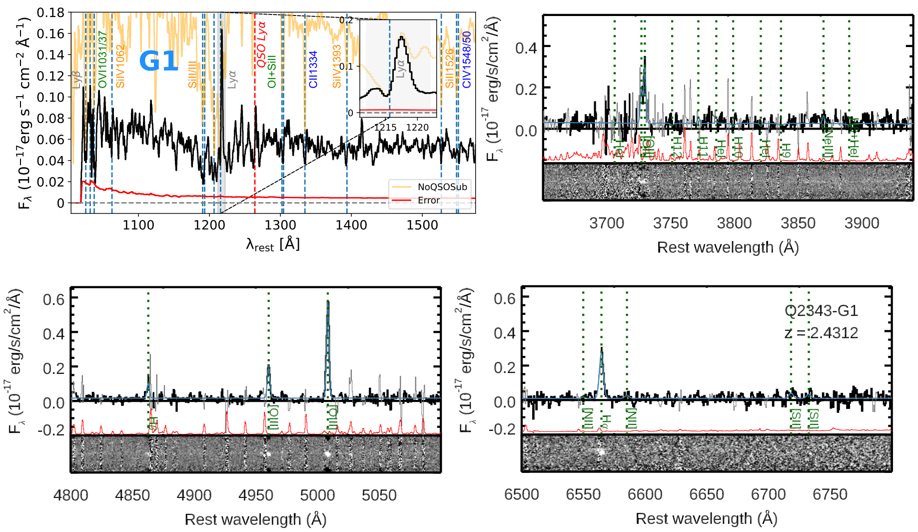

Figure 3.2: Keck/KCWI and Keck/MOSFIRE spectra of G1. *Top left:* Smoothed FUV spectrum from the QSO-spectrally subtracted cube (black), non subtracted cube (yellow-orange), and error spectrum (red). Vertical colored lines show emission and absorption based on G1's systemic redshift. *Other panels:* Optical spectrum. The top of each panel shows the 1D spectrum (black), offset error spectrum (red), and modeled emission lines (green dashed). The bottom shows the 2D spectrogram.

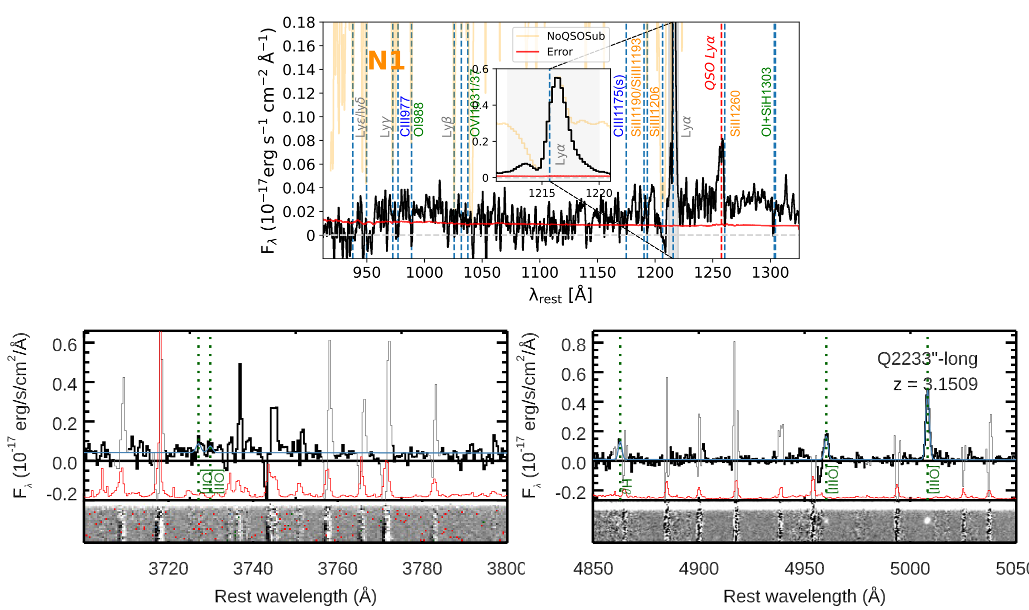

Figure 3.3: Keck/KCWI and Keck/MOSFIRE spectra of N1. Hα is not accessible from the ground at N1's redshift. Same lines and colors as Figure 3.2.

tracted cubes where we catalogued new "Continuum Serendipitous" sources, which we call CS#; these sources are always found at b ≥3–5". There were sources that would not have been possible to detect without QSO subtraction because they were "Hidden Under" the QSO PSF. We call these objects HU#; they are always found at b ≤3–5" and have continuum detections as seen in images made from the QSO-spectrally subtracted cubes (see Section 3.3). Finally, faint line emitting sources were catalogued as "Emission Serendipitous," which we call ES#; these sources are found at all impact parameters by scanning through the QSO+continuum subtracted cubes via narrow bandpasses (~10–20 Å); ES# sources have no continuum detection in the QSO-spectrally subtracted cubes. We catalog the object IDs, their sky position, preliminary FUV redshifts, and some notes in Table 3.2. Several objects are omitted from the table and will be discussed in future work.

In field Q2343+1232 (Q2343 hereafter) we discover seven new objects and recover three objects, the main one being Q2343-G1 (G1 hereafter). G1 was missed by Wang et al. (2015) who searched for Hα emission around high metallicity high-H I absorbers (i.e., Damped Lyman Alpha Absorbers, DLAs) at z ~2.4 due their small footprint of only ~12.5 kpc. G1 was one of three galaxies (G1, G2, G3) discovered by Nielsen et al. (2022) (N22 hereafter) with KCWI who were searching for host galaxies of strong Mg II absorption at $z \sim 2$. Our new cube confirms their main finding that G1 is at the same redshift as the DLA ($z_{DLA} \sim 2.431$) but shows that galaxies G2 and G3 are not. They appear as bright continuum emitting objects in the QSO-spectrally subtracted cubes but show no Lyα or IS lines at the DLA redshift. However, we find two new objects at the same redshift of G1 from their Lyα emission which we call G1-E (east; towards G3) and G1-S (south; towards G2). It is likely that these are the galaxies that N22 originally catalogued. We discuss these new galaxies in detail in Section 3.6.

In field Q2233+131 (Q2233 hereafter), we discover 12 new objects and recover four objects, the main one being Q2233-N1 (N1 hereafter). N1 is a well-studied Lyman Break Galaxy (LBG; e.g., Christensen et al., 2007; Christenson, Jorgenson, 2019; Møller et al., 2002; Sargent et al., 1989; Steidel et al., 1996) that was discovered in a search for hosts of optically thick absorbers near QSO sightlines from its UGR continuum photometry (Steidel et al., 1995); the first optical IFU observations were acquired by Christensen et al. (2004, 2007) and the first NIR IFU observations were by Christenson, Jorgenson (2019).

Recently, Ogura et al. (2020) acquired ALMA Band 8 (600-800 μm) observations of the Q2233+1310 sightline and surrounding field to search for $[CII]\lambda158$ μm emission from N1. No significant emission from N1 was detected, but two other galaxies with significant dust continuum emission were identified, located at angular distances of 4.″7 and 8.″1 from the QSO, respectively.

We report a significant detection of object Q2233-CS3 which has a previous detection (and photometry) from Steidel et al. (1995, object #1), and a recent detection in the sub-mm from Ogura et al. (2020, SMG 2). These are all likely the same source because their coordinates are consistent, the F702W and KCWI pseudo-broadband image show a similar morphology, and its colors are consistent with a Lyman break for a galaxy at Lyα redshift $z_{\mathrm{Ly}\alpha}$ = 2.077 (G-R=0.65; U$_n$-G=1.33; Steidel et al., 1995).

We report a significant detection of object Q2233-CS4 which has a previous detection (and photometry) from Steidel et al. (1995, object #7). CS4 is bright in FUV continuum, and has colors that are consistent with the $z_{\mathrm{Ly}\alpha}$ = 2.088 we measure from KCWI (G-R=0.26; U$_n$-G=0.82; Steidel et al., 1995).

We report a significant detection of Q2233-CS5 and have marginal evidence that it might have been detected recently in the sub-mm by Ogura et al. (2020, SMG 1). The uncertainty arises from its published coordinates and the ensuing $\sim$1″ difference that we measure from its position with KCWI. However, we measure $z_{\mathrm{Ly}\alpha}$ = 2.078 which is typical of sub-mm galaxies with no continuum detection in non sub-mm bands (e.g., Chapman et al., 2005; Danielson et al., 2017).

Since Q2233 is not a part of KBSS it lacks crucial ancillary data so we do not include it in the InCLOSE sample. Nonetheless, it serves as an excellent example of using KCWI to find new nLOS galaxies. We have at least three objects per field that are at redshifts appropriate for rest-optical follow-up. Namely G1, Q2343-G1E, Q2343-G1S, Q2343-ES1 N1, Q2233-HU4, and Q2233-HU6.

MOSFIRE

All NIR spectra used in this work were obtained using Keck/MOSFIRE (McLean et al., 2012). MOSFIRE uses a cryogenic configurable slit unit (CSU) to form single-slit or multi-slit masks in the telescope focal plane. The integration times and program IDs are summarized in Table 3.1.

In the case of G1 , the object was included as part of a multi-slit mask that also targeted a number of other galaxies of interest in the Q2343 KBSS survey field. The observations were obtained using the same CSU mask configuration in the J, H, and

Table 3.2: New KCWI Objects

KCWI-ID	RA (J2000.0)	Dec (J2000.0)	z_{KCWI}	b (")	b (kpc)	Notes
Q2343+1232						
$1.9 < z < z_{\rm QSO}$						
Q2343-G1	23:46:28.4278	+12:48:57.440	2.4343	2.57	20.8	Nielsen et al. (2022)
Q2343-G1E	23:46:28.5397	+12:48:57.561	2.4335	4.17	33.9	Same z_{Lya} as G1, towards G3
Q2343-G1S	23:46:28.4160	+12:48:55.480	2.4359	3.39	27.5	Same z_{Lya} as G1, towards G2
Q2343-ES1	23:46:27.9218	+12:48:55.550	2.097	5.42	45.1	H I but no metals in HIRES
$z < 1.9$ *or* $z \geq z_{\rm QSO}$						
Q2343-G2	23:46:28.4303	+12:48:55.020	?	3.83		Nielsen et al. (2022)
Q2343-G3	23:46:28.5839	+12:48:56.980	?	4.84		Nielsen et al. (2022)
Q2343-HU1	23:46:28.471	+12:48:59.68	3.0449	3.31		$z_{\rm Ly\alpha}$ and Lyb
Q2343-ES2	23:46:28.156	+12:48:55.48	2.661	2.86		Marginal in f110w,f140w,f160w,No H I in HIRES
Q2343-ESN	23:46:28.3218	+12:48:58.951	z_{qso}	1.41		Seen in KCWI Lya maps centered at z_{qso}
Q2343-ESS	23:46:28.1840	+12:48:56.448	z_{qso}	1.78		Seen in KCWI Lya maps centered at z_{qso}
Q2233+131						
$1.9 < z < z_{\rm QSO}$						
Q2233+131-N1	22:36:19.2733	+13:26:16.950	3.1537	2.55	19.3	Steidel et al. (1995)
Q2233+131-CS3	22:36:19.2296	+13:26:11.329	2.0773	8.03	66.9	#1 in Steidel et al. (1995), SMG2 (Ogura et al., 2020)
Q2233+131-CS4	22:36:19.5772	+13:26:06.951	2.0888	13.4	113	#7 in Steidel et al. (1995)
Q2233+131-CS5	22:36:19.6789	+13:26:17.458	2.0781	7.02	58.5	May be SMG1 (Ogura et al., 2020),Faint in 702w, H I in HIRES
Q2233+131-HU4	22:36:19.0827	+13:26:21.122	3.1460	2.61	19.8	Similar z_{Lya} as N1
Q2233+131-HU6	22:36:19.4286	+13:26:20.497	3.144	3.31	25.1	Similar z_{Lya} as N1,near multiple sources in F702W
$z < 1.9$ *or* $z \geq z_{\rm QSO}$						
Q2233+131-CM1-1	22:36:18.6267	+13:26:22.225	0.4124	9.01		z_{OII},1/2 in Complex1,Large spiral galaxy
Q2233+131-CM1-2	22:36:18.9364	+13:26:24.828	0.4124	6.81		z_{OII},2/2 in Complex1,Same z as CM1-1
Q2233+131-CS2	22:36:18.7803	+13:26:15.500	?	7.37		
Q2233+131-CS6	22:36:19.6848	+13:26:10.131	?	11.5		
Q2233+131-CS7	22:36:20.2202	+13:26:16.619	0.1466	14.7		
Q2233+131-HU1	22:36:18.9428	+13:26:20.377	?	4.06		May be part of HU4 complex
Q2233+131-HU3	22:36:18.8957	+13:26:16.737	?	5.29		Faint in 702w,marginal HI and FeII in HIRES

K bands, using the same approach described in previous KBSS work (Steidel et al., 2014; Strom et al., 2018, 2017). The sky position angle of the instrument field of view was chosen so that G1's $0\farcs7 \times 15\farcs0$ slit would also include galaxy Q2343-G2 and Q2343-G4. Total integration times of 1.4, 1.0, and 2.0 hours were obtained in J, H, and K bands, respectively, over the course of the nights of 2022 September 14-16, under variable seeing conditions ($0\farcs5$-$0\farcs8$ FWHM).

In the case of Q2233-N1, spectra in the H and K bands were obtained using MOSFIRE with a $0\farcs7$ longslit oriented to include both galaxy Q2233-N1 and the QSO, using a 2-position nod sequence and a nod offset of $20\farcs0$ instead of the $3\farcs0$ used for multislit masks.

The data were reduced using the publicly-available MOSFIRE DRP[6], which produces background-subtracted, flat-fielded, wavelength-calibrated, telluric-absorption corrected, heliocentric-velocity shifted, rectified, and stacked 2D spectrograms for each slit on the CSU mask. We refer the reader to Steidel et al. (2014) for more details on the data acquisition and reduction, and to Strom et al. (2017) for details on the flux calibration and slit loss corrections.

[6]https://keck-datareductionpipelines.github.io/MosfireDRP/https://keck-datareductionpipelines.github.io/MosfireDRP/

We use MOSPEC (Strom et al., 2017)[7] to extract 1D spectra from the 2D spectrograms. For Q2343-G1, the spatial profile of the galaxy was modeled as a Gaussian and used to perform optimal extraction of the 1D spectrum for each band. Slit loss corrections were determined separately for the J, H, and K band spectra using a method described by Strom et al. (2017), which combines information from the spectrum of the calibration star included on the slitmask with comparison to independent measurements (on other KBSS masks) of emission line fluxes of objects that were also observed on the CSU mask. The slit loss corrections for G1 are 1.72 ± 0.05 (J), 1.61 ± 0.03 (H), 1.33±0.2 (K). Slit loss corrections for N1 are 1.85±0.1 (J,H).

We show the MOSFIRE spectra of G1 and N1 in in the bottom panels of Figures 3.2 and 3.3. G1's rest-optical spectrum (Figure 3.2) shows significant detections (S/N> 6.5σ) of most of the major diagnostic emission lines including [O II]$\lambda\lambda 3727, 3729$, H$\gamma$, H$\beta$, [O III]$\lambda\lambda 4960, 5008$, H$\alpha$, and marginal detections (S/N> 2σ) of [Ne III]$\lambda 3829$, [N II]$\lambda\lambda 6549, 6585$, [S II]$\lambda\lambda 6718, 6732$. We measure a nebular redshift of $z_{neb} = 2.4312 \pm 0.0005$ and adopt this redshift as the systemic redshift for the remainder of the paper (i.e., $z_{sys} = z_{neb}$).

The MOSFIRE spectra of N1 (Figure 3.3) shows significant detections (S/N> 4σ) of [O III]$\lambda\lambda 4960, 5008$ and Hβ, and marginal detections (S/N> 2.2σ)) of [O II]$\lambda\lambda 3727, 3729$, [Ne III]$\lambda 3869$. H$\alpha$ was not observed because it was shifted out of the NIR atmospheric bands. We measure a nebular redshift $z_{neb} = 3.1509 \pm 0.0005$ and adopt it as z_{sys}. We analyze the MOSFIRE spectra in Section 3.4.

Images & Photometry

We use extant and archival images, and archival photometry to construct spectral energy distributions (SED) of the galaxies. For Q2343, new ground-based UV and optical images (U_nGR; see e.g. Steidel et al. (2003)) were obtained on August 28, 2022, from *Keck*/LRIS (Oke et al., 1995; Steidel et al., 2004), Table 3.1 shows integration times and dates. Ground-based JH images (published by e.g., Steidel et al., 2014; Strom et al., 2017) were taken using *Magellan*/FourStar (Persson et al., 2013). Ground-based K_S images were taken using *Palomar*/WIRC (data published in e.g., Steidel et al., 2004) (Wilson et al., 2003). Finally, space-based NIR images were taken with *HST*/WFC3IR-F140W (Trainor PID#14620 2016October05) and *HST*/WFC3IR-F160W (Law PID#11694 2010June13), and a reduced and science-

[7] https://github.com/allisonstrom/mospechttps://github.com/allisonstrom/mospec

ready F110W image was pulled from the Hubble Legacy Archive (HLA Lindsay et al., 2010) *HST*/WFC3IR-F110W (Forster Schreiber PID#12578 2017August21).

For N1, reduced and science-ready images were pulled from the HLA, including *HST*/WFPC2IR-702W (Macchetto PID#6307 19997May09) and *HST*/NICMOS-F160W (Warren PID#7824 1998Aug07). UGR photometry is from Steidel et al. (1995), based on images taken from the William Herschel Telescope (U*n*,R) and *MDM*/Hiltner (G,R), and K_s band photometry is from Steidel et al. (1996) based on images taken from *Keck*/NIRC1 (Matthews, Soifer, 1994). Our photometry measurements are discussed in detail in Section 3.3.

In the right panels of Figure 3.1 we show G1, N1, background QSOs Q2343 and Q2233, the newly identified and reobserved KCWI objects (Table 3.2), the MOSFIRE slits, and the surrounding foreground and background objects (relative to the QSOs).

Image QSO Subtraction and Photometry

To subtract the QSOs from the ground-/space-based images, we construct effective point spread functions (ePSF Anderson, 2016; Anderson, King, 2000) for each imaging band (U, G, R, J, H, and K). We find field stars of comparable brightness to the QSOs using IMEXAM (Sosey et al., 2022)[8]. Using at least one field star, we build the ePSF using the EPSFBuilder class in the PHOTUTILS package (Bradley et al., 2022), which is based on the formalism described in detail by Anderson (2016); Anderson, King (2000). We set all parameters to 1. Finally, we fit and scale (centroid and peak flux) the ePSF to the QSO using a Levenberg-Marquardt fitter, then subtract it.

We measure the photometry of the galaxies using PHOTUTILS by placing circular apertures at x and y offsets from the centroid of the QSO. We take the average median of two separate nearby circular apertures of the same size for background sky subtraction. As expected we find very large differences of up to 2.5 mag between QSO-subtracted and non-subtracted images.

We compared the QSO-subtracted ground-based magnitudes to space-based magnitudes in similar bands (e.g., *HST*/F160W and H-band) because the higher spatial resolution of HST reduces the contribution of the QSO's PSF wings. We generally found good agreement between the magnitudes 0.1–0.3 mag. Additionally, this was

[8]https://github.com/spacetelescope/imexamhttps://github.com/spacetelescope/imexam

useful for placing limits on the photometry error introduced from the QSO subtraction process. We adopt 0.2 magnitude for all photometry measured from QSO subtracted images.

SED Fitting

We use a custom SED fitting routine (Reddy et al., 2012; Theios et al., 2019) that uses pre-computed grids of SED models (Binary Population and Spectral Synthesis models version 2.2, Stanway, Eldridge (2018, hereafter BPASS)) with a Kroupa initial mass function (IMF (Kroupa, 2001)), an upper IMF mass of 100 $M_{\odot}$, low stellar metallicity Z_{*}=0.002 ($Z_{*}/Z_{\odot} \sim 0.14$) an SMC-like extinction curve, and a constant SFH. These default parameters were informed by past work on SED fitting of $z \sim 2-3$ galaxies (e.g., Erb et al., 2006a; Reddy et al., 2015, 2012; Shapley et al., 2005; Strom et al., 2017). Specifically, Theios et al. (2019) found that this stellar metallicity was required to reconcile the FUV and optical spectra of a sample of $z \sim 2$ KBSS star-forming galaxies; this stellar metallicity also well described a sample of $z \sim 3$ LBGs (e.g., Keck Lyman Continuum Survey; Pahl et al., 2023; Steidel et al., 2018). Similarly, the resultant nebular metallicities are consistent with previous results (Steidel et al., 2016; Strom et al., 2022, 2018) and recent direct T_e-based nebular metallicities from *JWST* (e.g., Rogers et al., 2024; Sanders et al., 2024). We run an additional model that forces the stellar ages to be ≥50 Myr to more realistically model young stellar populations whose SED ages were younger than the inferred dynamical time estimated from their sizes and nebular line widths (e.g., Reddy et al., 2012).

HIRES

We use extant and archival optical high-resolution spectra of background QSOs from Keck/HIRES (Vogt et al., 1994) to probe CGM absorption from the nLOS galaxies.

Q2343 was observed as part of the original KBSS program (e.g., Rudie et al., 2012; Steidel et al., 2014; Turner et al., 2014)). We refer the readers to Rudie et al. (2012) for details on the observations and reduction of the spectra but note that the final spectrum includes data obtained from both HIRES and VLT/UVES on UT2 (Dekker et al., 2000). The spectra were reduced, continuum normalized, and coadded, resulting in a spectral resolution of $R \simeq 45,000$ ($FWHM = 6.7$ km s^{-1}), an average $S/N \sim 40-70$ per resolution element, and spectral range $\lambda \sim 3150-10,090$

(Rudie et al., 2012).

Q2233 was observed a couple of years after HIRES's commissioning (PI: Sargeant, PID: C15H 1996A, Date: 1996-07-21) and was recently included in the KODIAQ survey (O'Meara et al., 2017, 2015, 2021). We pulled the fully reduced, continuum-normalized, 1D spectrum from KOA/KODIAQ. The spectrum has a resolution of $R \simeq 48,000$ ($FWHM = 6.3$km s^{-1}), average $S/N \sim 15-25$ per resolution element, and spectral range $\lambda \sim 4900 - 7300$.

We analyze the CGM absorption spectra in Section 3.5.

3.4 Ionized ISM and Stellar Population Properties

In this section we analyze the ionized ISM and stellar population of galaxies G1 and N1 from their rest-FUV spectra, rest-optical spectra, and SEDs to infer systemic redshift, nebular linewidths, star formation rates, metallicity, ionization, dynamical and stellar mass, and dynamical and stellar age.

FUV Continuum

The FUV spectrum of galaxies is dominated by emission from massive OB stars and contains information about the warm-hot ISM. Interstellar absorption (IS) lines seen in the FUV could arise from anywhere between the observer and the ISM. Indeed, previous studies have used FUV IS lines to place constrains on metal absorption in the CGM (e.g., Chen et al., 2020b; Steidel et al., 2010). In our case, the main utility of the rest-FUV spectrum is to measure a preliminary redshift to determine priorities for rest-optical follow-up. Additionally, we measure Lyα emission flux, Lyα halo morphology and size, and use IS absorption lines to estimate z_{sys} and corroborate $z_{\mathrm{Ly}\alpha}$.

To measure Lyα flux and equivalent width we directly integrated over the lines, assuming that the continua on either side of the line was representative of the continuum underlying the emission. We measured the line center by finding the peak flux. We tabulate the Lyα measurements for G1 and N1 in Table 3.3 referring to them as "Continuum Aperture".

G1's FUV spectrum (top panel of Figure 3.2) shows strong emission from Lyα and IS absorption from e.g., Lyβ, O6, Si2, Si3, O1+Si2, C2, Si4, and C4. It has a single red peaked Lyα emission profile. We measure a Lyα velocity difference (from z_{sys}) of $\Delta v \sim +271$ km s^{-1}, $F(\mathrm{Ly}\alpha)_{G1} = (0.94 \pm 0.02) \times 10^{-17}$ erg s^{-1} cm^{-2}, using z_{sys} we convert to a luminosity $\log{(L_{\mathrm{Ly}\alpha}/erg\ s^{-1})} = 41.64$, and a rest-equivalent width

$W_{rest} = (-6.19 \pm 0.4)$ Å. These values are typical of $z = 2-3$ star-forming galaxies of comparable mass to G1 (Prusinski et al., 2021; Steidel et al., 2010, 2016).

N1's FUV spectrum (top panel of Figure 3.3) shows strong emission from Lyα and IS absorption from, e.g., higher order Lyman series lines, C2, O1, Lyβ, Si2, Si3, O1+Si2, Si4, and C4. It has a strong, double peaked Lyα emission profile with a peak separation of $v_{red} - v_{blue} \sim 600$ km s^{-1}, blue to red peak ratio of 0.07, and a red peak equivalent width $W_r = -39.5$ Å. These values place N1 in the lower quartile of $z \sim 3$ LBG continuum-selected galaxies (e.g., Reddy, Steidel, 2009; Steidel et al., 2014; Trainor et al., 2015). Interestingly, N1 appears to have properties in between $z \sim 2.7$ faint, low mass narrow-band selected LAEs (KBSS-LAEs) and higher-mass $z \sim 3$ Lyman Continuum LBGs (LyC-LBGs) analyzed by Trainor et al. (2015). N1's $EW_{\mathrm{Ly}\alpha}$ and red-peak velocity offset are consistent with KBSS-LAEs ($EW_{LAE} \sim$ 44 Å, $v_{red,LAE} \sim +200$ km s^{-1}) while its Lyα flux and red-blue peak velocity separation are more consistent with LyC-LBGs ($F_{LyC-LBG} \gtrsim 7\times10^{-17}$erg s^{-1} cm^{-2}, $v_{red-blue,LyC-LBG} \sim +300$ km s^{-1}). Though there are exceptional sources in each sample that have properties that overlap with N1, this comparison suggests that N1 is not necessarily a typical $z \sim 3$ LBG or $z \sim 2.7$ LAE. We discuss this more in Section 3.4.

Optical Line Emission

We aim to infer the physical quantities associated with the ionized gas (e.g., H2 regions) in G1 and N1. Rest-optical emission line properties were measured from the MOSFIRE NIR spectra (discussed in Section 3.3) using simultaneous 1D Gaussian fits to all lines in a single band using MOSPEC (Strom et al., 2017).

The first three sections of Table 3.4 tabulate measured emission line properties including redshift, linewidth, inferred dynamical mass, slit loss- (Section 3.3) and extinction-corrected (Section 3.4) line fluxes, and common strong line ratios. The typical S/N for the brightest emission lines are >20 (>2.5 for marginal detections).

We adopt the $FWHM$ of the 1D Gaussian fits as the nebular line widths and account for the spectral resolution of the instrument (~ 30 km s^{-1} McLean et al., 2012). We measure $\sigma_{\mathrm{H}\alpha,G1} \sim 81$ km s^{-1} *and* $\sigma_{[OIII],N1} \sim 51$ km s^{-1}.

We estimate the dynamical masses of G1 and N1 using their nebular line widths following the same approach as Erb et al. (2006b):

$$M_{dyn} = \frac{C\sigma^2 r}{G} \tag{3.3}$$

Table 3.3: Lyα Line Measurements

	G1	N1
Kinematics[†]		
z_{red}	2.4343 ± 0.0008	3.1533 ± 0.0008
Δv_{red} (km s^{-1})	271 ± 72	171 ± 59
z_{blue}		3.1450 ± 0.0008
Δv_{blue} (km s^{-1})		-423 ± 59
Continuum Aperture[*]		
F_{red} (10^{-17} erg s^{-1} cm^{-2})	0.94 ± 0.02	4.48 ± 0.03
F_{blue} (10^{-17} erg s^{-1} cm^{-2})		0.30 ± 0.02
F_{tot} (10^{-17} erg s^{-1} cm^{-2})	0.94 ± 0.02	4.78 ± 0.05
$\log(L_{tot}/\text{erg s}^{-1})$	41.64 ± 0.02	42.62 ± 0.01
$W_{red,rest}$ (Å)	-6.19 ± 0.97	-39.45 ± 0.97
$W_{blue,rest}$ (Å)		-2.66 ± 0.59
$(\text{Ly}\alpha/\text{H}\alpha)_{cont}$	0.17 ± 0.16	0.96 ± 0.08
$f_{\text{Ly}\alpha\ esc,cont}$	$0.020^{+0.028}_{-0.020}$	$0.110^{+0.014}_{-0.014}$
Halo Aperture[+]		
F_1 (10^{-17} erg s^{-1} cm^{-2})	2.94 ± 0.01 (G1)[a]	12.50 ± 0.01 (N1)[d]
$\log(L_1/\text{erg s}^{-1})$	42.14 ± 0.01	43.04 ± 0.01
$(\text{Ly}\alpha/\text{H}\alpha)_{halo}$	0.54 ± 0.16	2.50 ± 0.08
$f_{\text{Ly}\alpha\ esc,halo}$	$0.06^{+0.02}_{-0.02}$	$0.29^{+0.01}_{-0.01}$
F_2 (10^{-17} erg s^{-1} cm^{-2})	0.32 ± 0.01 (G1-E)[b]	0.36 ± 0.01 (HU6)[e]
F_3 (10^{-17} erg s^{-1} cm^{-2})	0.46 ± 0.03 (G1-S)[c]	1.15 ± 0.02 (HU4)[f]

†) $Redshiftandvelocityhavethesameerror \pm$ 1 Å.
*) Extracted from spaxels showing continuum flux in the QSO-spectrally pseudo-narrowband KCWI images; see Fig. 3.1.
+) Extracted from spaxels showing extended Lyα flux in the narrowband KCWI images; see Fig. 3.7.
a) G1: projected area of 5.08 $arcsec^2$.
b) G1-E: projected area of 1.40 $arcsec^2$.
c) G1-S: projected area of 1.12 $arcsec^2$.
d) N1: projected area of 14.40 $arcsec^2$.
e) HU6: projected area of 4.41 $arcsec^2$.
f) HU4: projected area of 7.11 $arcsec^2$.

where C is a constant related to the galaxies' mass distributions, velocity fields, assumed geometries, and inclination angles; σ is the line width taken from Hα for G1 and [O3] for N1 (see Table 3.4); and r is the radius that we measure from the *HST*/F160W images. More specifically, the radii are the half width at half maximum ($HWHM$) of a 2D Gaussian fit to their continua yielding $r_{G1} = 1.56$ kpc and $r_{N1} = 1.23$ kpc. The value of C in principle ranges between 1 and 5 (face on to edge on) but we adopt $C \simeq 3.4$ owing to limited information on the galaxies' morphology (average inclination and velocity correction $\pi/(2v_{obs})$) and not measuring the true circular velocity ($v_{obs} = 2.35\sigma/2$). Their resulting dynamical masses are typical for galaxies at their redshift with log $(M_{dyn,G1}/\mathrm{M}_{\odot}) = 9.9\, and$ log $(M_{dyn,N1}/\mathrm{M}_{\odot}) = 9.2$ but N1 is more towards the low-mass end of KBSS-MOSFIRE sample (Steidel et al., 2014; Strom et al., 2017) and in the lower quartile of the $z \sim 3$ LBG mass distribution (KLCS; Pahl et al., 2023; Steidel et al., 2018).

Christenson, Jorgenson (2019) acquired adaptive optics-assisted, high spatial resolution NIR IFU data using Keck/OSIRIS to construct [O3]+$H\beta$ emission line maps of N1 in the observed K-band window. They detected [O III]λ5008 with flux $F([\mathrm{O\ III}]\lambda 5008) = 2.4 \pm 0.5 \times 10^{-17}$ erg s^{-1} cm^{-2} and marginally detected [O III]λ4960 and Hβ. The line kinematics and spatial extent were used to infer a dynamical mass of $\sim 3.1 \times 10^{9}\ M_{\odot}$ and a SFR $\sim 7.1 - 13.6\ M_{\odot} yr^{-1}$ based on their marginal detection of Hβ. These values are all consistent with what we have found.

G1's spectrum appears to be blended with a foreground galaxy at $z_{\mathrm{H}\alpha}$ =1.589. We call the galaxy G1fg (foregound), its trace can be seen a few pixels above G1's emission peaks in the J (top) and H (middle) spectra; its Hα emission is just blueward of G1's [O3]λ4960 emission line (Figure 3.2), and there are marginal detections of [O3] in the J band (top) spectra. We discuss the implication of this on the SEDs in Section 3.4.

Additionally, the MOSFIRE slit centered on G1 was oriented such that it included G2 and G4 (partially). We detect diffuse emission near G2 at the observed wavelength of the QSO's Hα peak (see the bottom row of Figure 3.2) and did not detect optical line emission from G4. This suggests G2 is at the same redshift as the QSO, and that G4 is not at the redshift of G1 and/or that it has weak line emission.

The emission line ratios will be used to infer dust attenuation (Hα/Hβ), instantaneous SFR (Hα), ionization parameter (O3, O32, Ne3O2), and nebular metallicity (R23,O32,N2,N2O2) in the following sections.

Dust and Instantaneous SFR

We calculate instantaneous SFR (SFR(Hα)) following the method described in Theios et al. 2019 (hereafter Theios et al. (2019)). Briefly, Theios et al. (2019) updated the calibration constant used to convert Hα luminosity ($L_{\mathrm{H}\alpha}$) to $SFR(\mathrm{H}\alpha)$ by modeling the SEDs of a representative sample of $z \sim 2-3$ KBSS galaxies using stellar population synthesis models that self consistently reproduced the joint

Table 3.4: Rest-Optical Measurements (Partial)

	G1	N1
Line Measurements		
$z_{[OIII]}$	2.4312 (± 5.3014 $km\ s^{-1}$)	3.1509 (± 4.4409 $km\ s^{-1}$)
$Linewidth$	81.31 ± 4.03 $km\ s^{-1}$ (Hα)	50.99 ± 1.06 $km\ s^{-1}$ ([OIII])
$\log M_{dyn}$	9.85 ± 0.01 ($M_\odot$)	9.22 ± 0.01 ($M_\odot$)
Flux Measurements*	$10^{-17} erg\ s^{-1}\ cm^{-2}$	$10^{-17} erg\ s^{-1}\ cm^{-2}$
$H\alpha$	5.468 ± 0.865	
$H\beta$	1.912 ± 0.174	1.758 ± 0.400
$H\gamma$	0.898 ± 0.138	
$[O\ II]\lambda3727$	2.811 ± 0.244	0.536 ± 0.224
$[O\ II]\lambda3729$	3.617 ±0.421	0.463 ±0.132
[O III]λ4960	3.554 ± 0.100	2.997 ± 0.178
[O III]λ5008	10.655 ± 0.300	8.973 ± 0.519
Line Ratios#		
$H\alpha/H\beta^{|}$	3.05 ± 0.56	
$H\gamma/H\beta^{|}$	0.45 ± 0.08	
$O3^a$	0.75 ± 0.04	0.71 ± 0.10
$O32^b$	0.34 ± 0.03	1.08 ± 0.11
$R23^c$	1.03 ± 0.05	0.87 ± 0.10
$O3N2^d$	1.77 ± 0.17	
$N2^f$	-1.02 ± 0.17	
Nebular Inferences@		
A_V	$0.21^{+0.73}_{-0.21}$ mag	
$E(B-V)_{neb}$	$0.07^{+0.17}_{-0.07}$	
SFR(Hα)	5.82 ± 0.92 M$_\odot$ yr^{-1}	
SFR(Hβ)	>4.67 M$_\odot$ yr^{-1}	>10.01 M$_\odot$ yr^{-1}
Strong Line Metallicities+		
Oxygen Abundance	$12 + \log(O/H)$ ($[O/H]^\$$)	$12 + \log(O/H)$ ($[O/H]^\$$)
$O/H_{R23\&O32}$	8.39 ± 0.10 (-0.30)	7.82 ± 0.17 (-0.87)
O/H_{O3N2}	8.38 ± 0.04 (-0.31)	
Nitrogen Abundance	$\log(N/O)$ ($[N/O]^\$$)	$\log N/O$ ($[N/O]^\$$)
N/O_{N2}	-1.20 ± 0.23 (-0.34)	
N/O_{N2O2}	-1.21 ± 0.13 (-0.35)	

*) Slit loss and extinction corrected Cardelli et al. (1989) , R$_V$=3.1.
#) The notation $\lambda\lambda$ refers to the sum of the two lines. (|) Before extinction correction.
a) O3=log ($[O\ III]\lambda5008/H\beta$).
b) O32=log ($[O\ III]\lambda\lambda4960, 5008/[O\ II]\lambda\lambda3727, 3729$).
c) R23=log ($([O\ III]\lambda\lambda4960, 5008 + [O\ II]\lambda\lambda3727, 3729)/H\beta$).
f) N2=log ($[N\ II]\lambda6585/H\alpha$).
@) Calibrations from Theios et al. (2019).
+) Calibrations from Strom et al. (2018) and McGaugh (1991).

rest-FUV and rest-optical spectra of the galaxies. The SFR follows the form

$$\log(SFR_{H\alpha}/M_\odot yr^{-1}) = \log(L_{H\alpha}/erg\ s^{-1}) - C \tag{3.4}$$

where Theios et al. (2019) found C to be 41.64, leading to SFRs almost a factor of 2 lower than the canonical values at $z \sim 0$ (Kennicutt et al., 1994).

To correct $L_{\mathrm{H}\alpha}$ for dust extinction we use the Balmer decrement ($F(\mathrm{H}\alpha)/F(\mathrm{H}\beta)$) to infer nebular dust attenuation assuming Cardelli et al. (1989) extinction (R_V=3.1) and case B recombination at 10^4 K in the low density limit 10^2 cm^{-3} ($I(\mathrm{H}\alpha)/I(\mathrm{H}\beta)$=2.86; Brocklehurst, 1971; Osterbrock, 1989). We correct the Hα line flux for dust attenuation, use z_{sys} to convert to luminosity, and then convert to SFR(Hα) using Equation 3.4.

N1 is at a higher redshift such that Hα is not accessible from the ground so we place a lower limit on the instantaneous SFR by assuming no dust and converting Hβ to Hα under the same assumptions as above (Hα = 2.86× Hβ), convert to luminosity then SFR; we call this quantity SFR(Hβ). The lack of a [C2]$\lambda 158\mu m$ nor sub-mm (dust) continuum emission supports that N1 has relatively low dust attenuation (Ogura et al., 2020).

We tabulate SFR(Hα), SFR(Hβ), Hα extinction, A_V extinction, and nebular reddening in Table 3.4. The SFR(Hα) and SFR(Hβ) of both galaxies is within a factor of 2 the median SFR of the KBSS-MOSFIRE sample (Steidel et al., 2014). G1's Balmer decrement, extinction, and nebular reddening are also typical. We infer a SFR surface density for both galaxies using the effective radius used to calculate dynamical mass in Section 3.4. Assuming a disk geometry at an average inclination angle ($\pi/4$) yields $\Sigma_{SFR(\mathrm{H}\alpha),G1} = 0.48$ M$_\odot$ yr^{-1} kpc^{-2} and $\Sigma_{SFR(\mathrm{H}\beta),N1} \gtrsim 1.34$ M$_\odot$ yr^{-1} kpc^{-2}, which are well above the typical threshold found in galaxies that drive galactic outflows at lower redshift ($\Sigma_{SFR} \sim 0.1$ Heckman et al., 2015).

Nebular Excitation and Metallicity

The metal content in the ISM gives insights on recent star formation and feedback sources (e.g., core collapse supernovae CCSNe, asymptotic giant branch AGB stellar winds) present in HII regions. In practice, usually only hydrogen, nitrogen, oxygen, and sulfur abundances are reliable because they are bright and therefore often detected at high z. It is a non-trivial task to map from emission line flux to abundance (even abundance ratios) due to varying ionizing state, inhomogenities in the gas density and temperature, and dust extinction present in galaxy environments. In the past, authors would use calibrations found at low-z (where most of the degeneracies can be broken) and apply them to high-z. Recently, close attention has been paid to the so called "strong line" metallicity calibrations specifically for $z \sim 2-3$ galaxies, which we discuss and adopt in this paper.

We use strong line calibrations provided by Strom et al. 2018 (hereafter, Strom et al. (2018)) to infer $12 + \log O/H$, $\log N/O$, and $\log U$. Strom et al. (2018) developed the calibrations by using photoionization models that account for the chemistry, ionization, and excitation of nebular gas for a representative sample of KBSS-MOSFIRE galaxies. We tabulate the values in the last two sections of Table 3.4. Under each of the metallicities we show their logarithmic abundances with respect to solar values.

Both galaxies are in (near) the low-metallicity branch of the O/H vs R23 space based on their R23 ratios ($R23_{N1} = 0.87$ and $R23_{G1} = 1.03$) but Strom et al. (2018) only calibrated $12 + \log O/H$ for the high-metallicity branch. Therefore we use the calibrations by McGaugh (1991, shown explicitly by Steidel et al. 2016) to map from R23 (and O32) to O metallicity ($O/H_{R23\&O32}$), which we show in the first row of the Oxygen Abundance section of Table 3.4.

The inferred $12 + \log{(O/H)}$ values for G1 are internally consistent regardless of ratio used. For G1 we adopt $12{+}\log{(O/H)}_{G1,O3N2} = 8.39$ ($[\mathrm{O/H}]_{G1} = -0.30$). This metallicity is typical of KBSS star-forming galaxies. We have only one appropriate O inference for N1, which yields $12{+}\log{(O/H)}_{N1,R23\&O32} = 7.82$ ($[\mathrm{O/H}]_{N1} = -0.87$), making it low-metallicity compared to the KBSS-MOSFIRE sample.

The inferred $\log{(N/O)}$ values for G1 are also internally consistent. We adopt $\log{(N/O)}_{G1,N2O2}$=-1.21 ($[\mathrm{N/O}]_{G1} = -0.35$). We do not calculate (N/O) for N1 because [N2] was not observable from the ground.

The inferred $\log U$ for both galaxies are fairly consistent regardless of ratio used.

Overall, both galaxies ionization parameters are typical of star-forming galaxies at their z. G1's gas-phase nebular metallicity as seen in $\log{(O/H)}$ and $\log{(N/O)}$ is also typical whereas N1's metallicity is low.

SED Properties

We want to model and infer physical properties of the galaxies underlying stellar populations. In Section 3.3 and 3.3 we constructed QSO-subtracted SEDs. However, bright line emission (e.g., Lyα, [O3], Hα) can affect the continuum photometry, which can result in inaccurate SED modeling.

We use the line fluxes measured from the KCWI spectra (from continuum spaxels; see Section 3.4) and slit-loss corrected MOSFIRE spectra (see Section 3.4) to subtract strong line emission from the measured photometry. The corrections had the form $\Delta M = -2.5 \log{((F(Phot\ Flux) - F(Line\ Flux))/F(Phot\ Flux))}$. For

G1 we correct F110W, J, and F140W band photometry for line emission from [O2]$\lambda\lambda 3727, 3729$ and [Ne3]$\lambda 3869$, F140W and F160W band from H$\beta$and Hγ, and K$_S$ band from Hα, [N2]$\lambda\lambda 6549, 6585$, and [S2]$\lambda\lambda 6718, 6732$. The corrections were the largest for J and K$_S$ at 0.1 mag, but small for F110W, F140W, and F160W at 0.03-0.05 mag, smaller than the photometry error. G band requires no line correction because Lyα falls outside of the bandpass, and U and R bands contain no bright emission lines (as seen in the KCWI rest-FUV spectra).

For N1, we correct G band from Lyα, K$_S$ band from [O3]$\lambda\lambda 4960, 5008$, and H$\beta$, and F160W band from [O2]$\lambda\lambda 3727, 3729$ and [Ne3]$\lambda 3869$. The correction for K$_S$ was very large at 1.2 mag, but small for G and F160W band at 0.1 and 0.08 mag, respectively. U and R bands contain no bright emission lines.

G1's SED has an additional complication because it is blended with foreground galaxy G1fg ($z_{\mathrm{H}\alpha}$ =1.589; see Section 3.4). The foreground galaxy has a detected trace in J and H band, but does not have strong emission lines in any band, and no detected trace in K band (Figure 3.2). The J and H band trace suggests that there is elevated flux in R, F110W, and F140W mags that will affect the reddening determination from the SED. The lack of a trace in K band suggests that the K$_S$ band photometry is negligibly affected and will therefore not significantly affect the mass determination (which relies strongly on K$_S$ photometry).

We ran each galaxy's QSO-subtracted and emission line-corrected photometry through the SED fitting routine discussed in Section 3.3. From the best-fit BPASS v2.2 SED models we infer stellar mass M_*, stellar age t_*, dust attenuation (continuum color excess) $E(B-V)_{SED}$, and star formation rate SFR_{SED}.

We show the best-fit SED models in Figure 3.4 and tabulate the best-fit values in Table 3.5. We can see that the QSO- and emission line-corrected photometry (black points) are well fit by their respective models.

G1 has a stellar mass and age that is consistent with its dynamical time and dynamical mass, its SFR(SED) is within a factor of 2.5 of SFR(Hα), and it has similar SED and nebular reddening. This agreement shows a consistency between the two independent methods and is evidence that the foreground galaxy G1fg had a small effect on its SED.

For N1, we adopt the model that constrains the age to be ≥50 Myr because the best fit BPASS model with no age constraint preferred an age $t_* \sim 10\ Myr$ which is about ~20 Myr *younger* than the dynamical time inferred from its size and nebular line

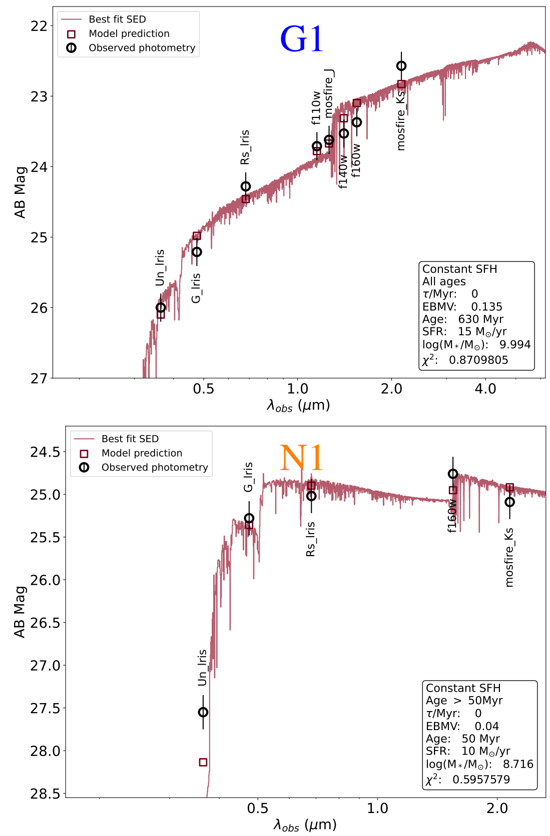

Figure 3.4: Best fit SEDs from BPASSv2.2 for galaxies G1 (*top*) and N1 (*bottom*). Black points show observed AB magnitudes (after QSO subtraction and bright emission line correction) and red points/curves are from the best fit model. The best fit parameters for the galaxy are shown at the bottom right of plot and are tabulated in Table 3.5. *Top:* G1 and *Bottom:* N1.

width $\tau_{N1,dyn} \sim 30$ Myr. With the new age-constrained model, the dynamical mass and SED mass differ by 0.5 dex ($\log{(M_{SED}/\mathrm{M}_{\odot})} = 8.7$ *and* $\log{(M_{dyn}/\mathrm{M}_{\odot})} = 9.2$), stellar age and dynamical time are within 0.3 dex, and SFR$_{SED}$ is consistent with the lower limit set by SFR(Hβ), and it has negligible reddening (E(B-V$_{SED}$=0.04; which is consistent with N1's lack of a [C2]$\lambda158\mu m$ nor sub-mm (dust) continuum emission (Ogura et al., 2020).). These masses are low, but not necessarily atypical, when compared to the $z \sim 3$ Keck Lyman Continuum Survey (KLCS) which has a mean stellar mass and standard deviation of $M_{*} \sim 9.6 \pm 0.6$ (Pahl et al., 2023; Steidel et al., 2018). This all suggests that N1 is a young, low dust, lower mass, moderately star-forming galaxy.

Table 3.5: BPASSv2.2 Best-Fit SED Parameters

Parameter	G1	N1^{+}
$\log{(M_*/M_\odot)}^*$	9.99	8.72
t_* (Myr)	630	50
$E(B-V)_{SED}$	0.135	0.04
SFR$_{SED}$ $(M_\odot/yr)^*$	15	10

*) Typical uncertainty of ~30%.

+) Due to age constraint, values could vary by ~ 50%.

Comparing ISM and Stellar Population Properties

We now combine the ionized ISM and stellar population properties and put them in context with the KBSS-MOSFIRE sample of $z \sim 2-3$ star-forming galaxies and AGN (Steidel et al., 2014; Strom et al., 2017, with a $> 2\sigma$ measurement of O3 and N2), and low-z galaxies from SDSS-DR8 (Aihara et al., 2011) taking emission line measurements and inferred physical properties from the MPA-JHU[9] catalogs. As noted by Strom et al. 2017 (Strom et al. (2017) hereafter), this particular set of SDSS galaxies was chosen due to their similar detection properties to KBSS-MOSFIRE. They have $0.04 \leq z \leq 0.1$, $> 50\sigma$ Hα detections, $> 3\sigma$ detection's of Hβ, [O3], a good redshift measurement and "reliable" flag from the MPA-JHU pipeline. The reported M_*, SFR, sSFR, are the median estimates from the "total" value probability distribution functions.

Figure 3.5 shows the galaxies on the N2- (Baldwin et al., 1981) and S2-BPT (Veilleux, Osterbrock, 1987) diagrams compared to KBSS-MOSFIRE and SDSS star-forming galaxies. Both galaxies have typical O3 ratios compared to KBSS-MOSFIRE that are well above the SDSS galaxies. G1 in particular sits close to both N2- and S2-BPT locus fits by Strom et al. (2017).

The top panel of Figure 3.6 shows the Mass–Excitation (M_*–O3; (Juneau et al., 2011)) diagram. We use the SED derived mass for G1 (which is within 0.1 dex of the dynamical mass) and use a logarithmic average of the dynamical and SED mass for N1 ($\log \mathrm{M}_\odot \sim 9.0 \pm 0.25$). Both galaxies reside within the majority of the KBSS-MOSFIRE sample which itself is vertically offset from z ~0 galaxies indicating higher excitation per unit stellar mass. G1 is in the upper quartile of the distribution towards higher excitation. N1 falls on the low-mass end of the median fit from Strom et al. (2017).

The bottom panel of Figure 3.6 shows the galaxies' specific star formation rate

[9][https://www.sdss4.org/dr17/spectro/galaxy_mpajhu/]https://www.sdss4.org/dr17/spectro/galaxy_mpajhu/

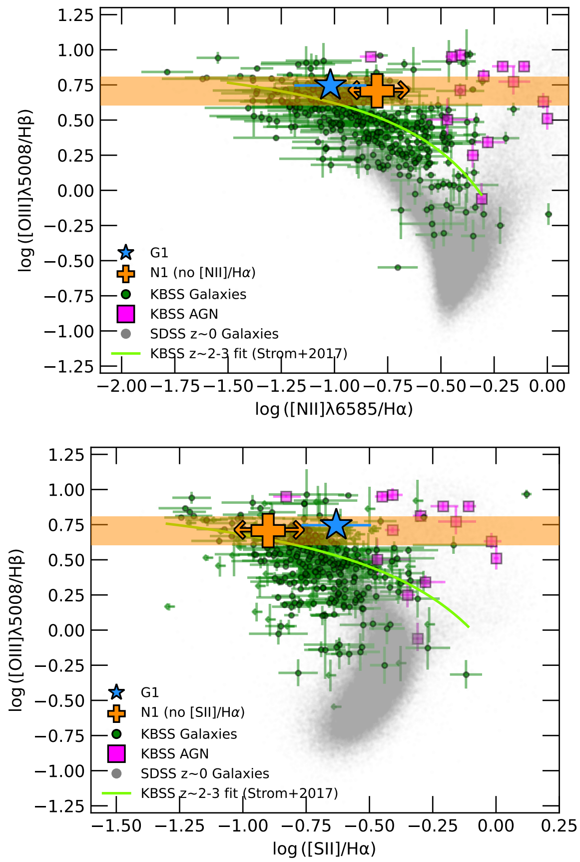

Figure 3.5: BPT diagrams showing G1 (blue filled star) and N1 (orange filled plus). Green points are $z \sim 2-3$ KBSS star forming galaxies, magenta points are KBSS AGN, and grey points are $z \sim 0$ SDSS star-forming galaxies. Light green lines are fits to the KBSS galaxies from Strom et al. (2017). Note that N1 does not have an observation of [N2], Hα, or S2 so we show it is an unbound point and orange horizontal bar whose width is equal to its O3 error. *Top:* N2-BPT diagram. *Bottom:* S2-BPT diagram.

(sSFR) and excitation (O3). We show sSFR calculated from SFR(SED), and SFR(Hα) (or SFR(Hβ) for N1; see section 3.4). The Hα and SED SFRs for both galaxies are fairly consistent with one another, suggesting a consistent picture between the nebular emission spectra and SED modeling.

Altogether, G1 and N1 have similar O3 ratio and $\log U$ but otherwise appear to be on different ends of the $z = 2-3$ star-forming galaxy distribution. G1 has a typical stellar mass, sSFR (instantaneous and SED), dust attenuation, Lyα continuum flux, Lyα equivalent width, and N2- and S2-BPT diagram location when compared to KBSS-MOSFIRE. N1 on the other-hand is a lower mass (dynamical and SED), high sSFR (SED(SFR) and SFR(Hβ), relatively dust-free, and strong Lyα and O3 emitting

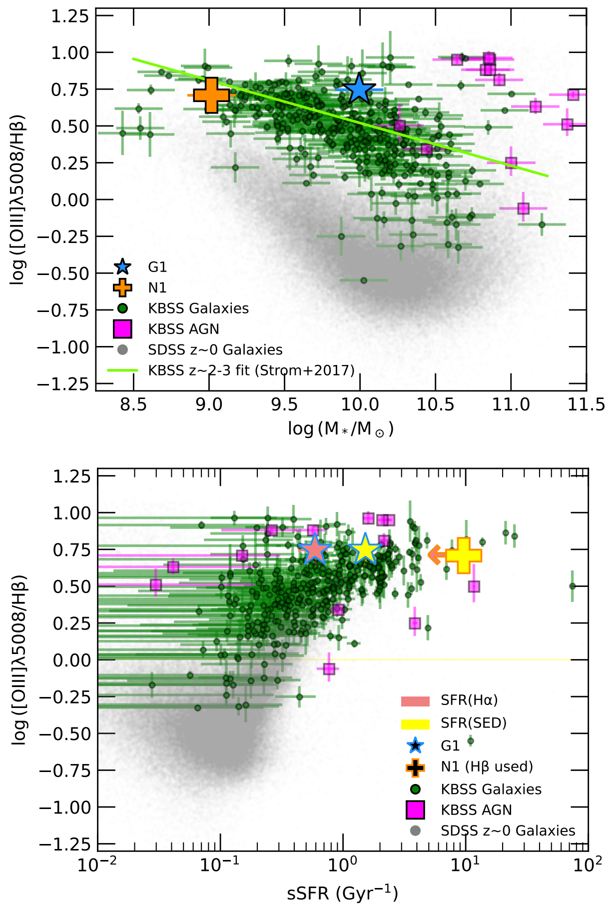

Figure 3.6: Combined rest-optical and SED properties of G1 (blue outlined star) and N1 (orange outlined cross). The symbols and colored lines are the same as Figure 3.5. *Top:* Stellar Mass–Excitation plot. *Bottom:* sSFR–Excitation plot. Light red filled points show sSFR calculated from SFR(Hα) (Hβ for N1), and yellow filled points are calculated from SFR(SED). N1s Hβ SFR(Hβ) (lower limit) and SFR(SED) are roughly the same and so appear as one point.

LBG that is in the lower quartile of $z \sim 3$ LBG continuum-selected population.

3.5 CGM Properties

Most of the baryons in high-redshift galaxies reside in their CGM (e.g., Mitchell et al., 2018). Therefore, it is necessary to analyze the CGM to completely study galaxy evolution at the peak epoch of star formation in the universe.

In this section we analyze the CGM properties of the galaxies from their extended Lyα halo emission in the KCWI cubes and by H I and metal absorption of background QSOs from HIRES. Specifically, we analyze Lyα halo morphology, Lyα velocity maps, and Lyα physical size, then perform component-by-component Voigt profile decomposition of CGM absorption to measure the gas physical properties.

Lyα Halo Emission

Extended Lyα halo emission is common in z ~2-3 star-forming galaxies (e.g., Chen et al., 2021; Erb et al., 2023; Steidel et al., 2010). Lyα is useful because it is bright, indicative of star-formation and other FUV photon sources, such as AGN, and traces cold ($T \sim 10^4$ K) gas in the CGM. Due to the resonant nature of Lyα (i.e., instantaneous absorption and emission that scatters photons *and* changes their wavelength), modeling Lyα profiles to extract physical properties is non-trivial. Physical quantities such as H I column density, temperature, dust content, 3D spatial distribution, intrinsic gas kinematics, etc., are exceedingly difficult to derive unambiguously and independent of model assumptions. Nonetheless, the observational constraints that we compile in this section are vital for context and literature comparisons, and future efforts.

In Figure 3.7 we show Lyα surface brightness spatial distribution maps and velocity distribution maps for G1 and N1. The surface brightness maps show that both galaxies possess extended Lyα halos that are at least ten times the extent of their continuum (as measured from *HST*/F160W images; e.g., Figure 3.1), and that there is complex (simple) structure in N1's (G1's) velocity distributions.

In Table 3.3 we show the Lyα flux for each kinematic component detected and its corresponding area. We calculate the Lyα fluxes by creating a narrowband image that includes all of the emission of a given component using the QSO+continuum subtracted cubes generated from CubEx (Section 3.3). We compute the average SB of the component, then convert to flux using the bandpass and projected area (number of spaxels and spatial scale of the cubes 0.2–0.3$''$).

We calculate (or place limits on) the total Lyα escape fraction by assuming that all of the Lyα photons originate from the HII regions that we detected in Hα emission (Section 3.4; Table 3.4), and that Lyα/Hα=8.7 (assuming $T \sim 10^4$ K and $n_e \sim 350$ cm^{-3} (Langen et al., 2023; Osterbrock, 1989)). We calculate this for both the total Lyα from the continuum apertures and from the halo apertures.

G1's morphology is typical compared to other KBSS galaxies with Lyα halos (e.g., Chen et al., 2021) in that it is circular (perhaps spherical), and is more extended than its continuum with a peak size of $s_{halo} \sim 28$ kpc (3.5"); $s_{cont} = 3.12$ kpc). The two protrusions to the east and south of the halo are the new galaxies G1-E and G1-S. G1's velocity map shows a simple kinematic structure with $v \sim +250$ km s^{-1}. We

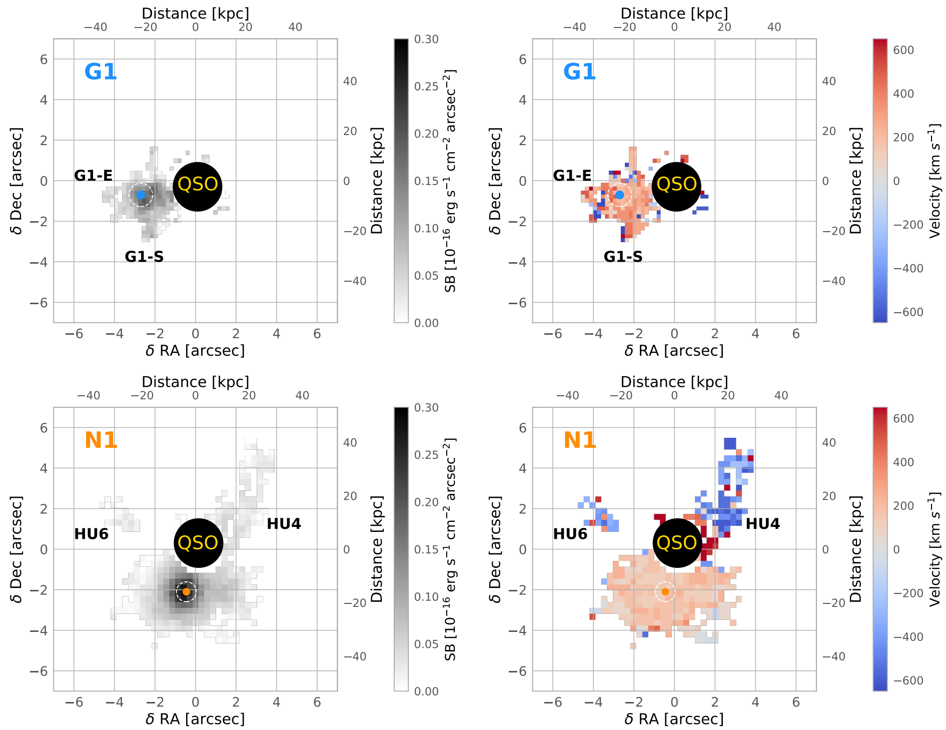

Figure 3.7: Lyα halos of G1 (*top*) and N1 (*bottom*). The colored dots are the galaxy continuum size and location as measured from *HST*/F160W ($s_{cont,G1}$ = 3.12 kpc, $s_{cont,N1}$ = 2.26 kpc), the white dashed circle highlights the continuum location. We show newly discovered objects as black labels. *Left:* Lyα surface brightness spatial map. *Right:* Lyα velocity map showing the peak of Lyα emission in each spaxel in velocity space with respect to the systemic redshifts z_{G1}=2.4313 and z_{N1}=3.1509. Red shows redshifted gas and blue shows blueshifted gas.

measure a Lyα halo flux $F_{G1,\mathrm{Ly}\alpha,halo} = (2.94 \pm 0.01)\ \times 10^{-17}$erg s^{-1} cm^{-2}, which gives $(\mathrm{Ly}\alpha/\mathrm{H}\alpha)_{G1,halo} = 0.54 \pm 0.16$ and $f_{G1,\mathrm{Ly}\alpha\ esc,halo} = (6 \pm 2)$ %. These values are comparable to other star-forming galaxies at $z \sim 2-3$, and the low $(\mathrm{Ly}\alpha/\mathrm{H}\alpha)$ fraction indicates that the Lyα emission mechanism is not dominated by collisional excitation, predicted $(\mathrm{Ly}\alpha/\mathrm{H}\alpha) > 100$ (e.g., Langen et al., 2023).

N1's halo morphology is unique in that it has three distinct components that are very extended. The main complex (south) has the highest SB and is spatially coincident with N1, the secondary complex (northwest) has a tapered morphology that widens towards N1 and is spatially coincident with newly discovered galaxy HU4, and the detached complex (east) is small and coincident with new galaxy HU6. The velocities of the complexes are also distinct: $v_{N1} \sim +170$ km s^{-1} for N1, $v_{HU6} \sim -350$ km s^{-1} for HU6, and $v_{HU4} \sim -500$ km s^{-1} for HU4, all with respect to the $z_{sys,N1}$.

N1's Lyα halo (main complex) has both a red and blue component that is is spatially extended (s_{halo} = 46 kpc) compared to s_{cont} = 2.46 kpc. We measure a total Lyα halo flux $F_{N1,\mathrm{Ly}\alpha,halo} = (12.50 \pm 0.01) \times 10^{-17}$erg s^{-1} cm^{-2}, which gives $(\mathrm{Ly}\alpha/\mathrm{H}\alpha)_{N1,halo} = 2.50 \pm 0.08$ and $f_{N1,\mathrm{Ly}\alpha\ esc,halo} = (29 \pm 1)$ % (assuming negligible dust, which is consistent with its SED). As seen before, N1's small (Lyα/Hα) fraction indicates that collisional excitation is not the dominant emission mechanism for its Lyα halo. Its large Lyα equivalent width, moderate red peak velocity, high Lyα escape fraction, and large $F_{\mathrm{Ly}\alpha}/F_{\mathrm{H}\alpha}$ are similar to low mass KBSS-LAEs, while its bright $F_{\mathrm{Ly}\alpha}$ and large red-blue peak velocity separation are similar to LyC-LBGs. Additionally, the combination of its lower-mass, continuum colors, nebular excitation, low dust extinction, strong Lyα properties (flux, equivalent width), and its complex and very extended Lyα halo morphology ($\sim$ 100 kpc) make it reminiscent of $z \sim 2$ Lyαemitting extreme emission line galaxies (EELGs) (e.g., Erb et al., 2023, 2016). The sample analyzed by Erb et al. (2023) all showed double-peaked Lyα profiles, extended halos ($\gtrsim$ 50 kpc), typical peak separations $v \sim 600$ km s^{-1}, and median Lyα escape fraction $f_{\mathrm{esc}} \sim 0.3$.

As a summary, both galaxies show extended Lyα emission in their CGM. Their Lyα is kinematically dynamic (with respect to z_{sys}), spatially extended (more than 10x their continuum size), bright ($F_{\mathrm{Ly}\alpha} > 3 \times 10^{-17}$erg s^{-1} cm^{-2}, and is not dominated by collisional excitation. G1 shows a simple velocity distribution (v_{peak} ~+250 km s^{-1}), whereas N1 shows three distinct velocity components that span a large velocity range $v \sim -600$ - +250 km s^{-1}(discussed more in Section 3.6). G1 has a typical Lyα escape fraction whereas N1's is very large. This suggests that G1 is a typical Lyα emitting star-forming galaxy at its z. N1 on the other-hand is in the tail distribution of $z \sim 3$ LBG continuum-selected galaxies, and analogous to $z \sim 2$ EELGs.

QSO Absorption

Using an unrelated background source (e.g., QSO) to probe the CGM is an ideal method to obtain a very high quality *but* highly localized view. It is difficult to draw galaxy-wide conclusions from these localized views given the patchy/clumpy nature of the CGM but at small impact parameters, we might be more likely to see trends with galaxy properties (e.g., M_*, SFR, Z_{ISM}) (e.g., Rudie et al., 2019, 2012; Tumlinson et al., 2017; Werk et al., 2014).

We use HIRES spectra of the KBSS QSOs to search for CGM absorption at the systemic redshifts of G1 and N1. As noted in the literature, both galaxies are at the same redshifts as DLAs and show detections of metals of varying ionization states. The DLA towards Q2343 was first identified by Sargent et al. (1988), and has been analyzed using high-resolution VLT/UVES and Keck/HIRES spectra by several groups over the past 20 years (D'Odorico et al., 2002; Dessauges-Zavadsky et al., 2004; Nielsen et al., 2022; Wang et al., 2015). Similar attention has been paid to the sub-DLA towards Q2233 which was analyzed using Keck/HIRES by many groups (Lu et al., 1997, 1998; Sargent et al., 1989; Steidel et al., 1995).

In Figures 3.8 and 3.9 we show representative neutral (e.g., H I, N I, O I), low-ionization (e.g., C II, Si II, S II, Fe II), intermediate-ionization (C IV, Si IV) and metal transitions. The metals extend more than 400 $km\ s^{-1}$, and for G1 extend from $v \sim -800 - +200$ km s^{-1}! The darkest grey shaded region shows the metal components that are self-shielded by the DLA; this was determined by the velocity spread of the low-ionization Fe-peak elements (e.g., Mn II, Fe II, Zn II) which require dense, self-shielded gas for detection due to their low ionization potentials.

Voigt Profile Fitting

We inferred physical properties of inner CGM gas absorption via Voigt profile decomposition. To fit the complexes, we used a series of individual Voigt profiles of a single redshift z, Doppler parameter b (i.e., single temperature), and column density N_Z. We use two Voigt profile fitting programs for this task: VoigtFit (Krogager, 2018) for quick interactive initial guesses, and ALIS (Absorption LIne fitting Software[10]; Cooke et al., 2014) for the main fitting.

The HIRES spectra are of high enough quality that we identified absorption components by visual inspection. We started by assigning a component to each absorption trough using the interactive version of VoigtFit, assuming the smallest Doppler parameter that we could realistically resolve $b \sim 5\ km\ s^{-1}$ (given the spectral resolution of 7 km s^{-1}).

We fit the first guesses with ALIS, then visually inspected the residuals between the best-fit model and data. We used locations of peaks and troughs in the residuals to add or remove components. We continued this process iteratively until the residuals showed no clear peaks and troughs (i.e., residual deviations were below that of the error spectrum). Finally, once the components showed no strong residual deviations

[10][https://github.com/rcooke-ast/ALIS]https://github.com/rcooke-ast/ALIS

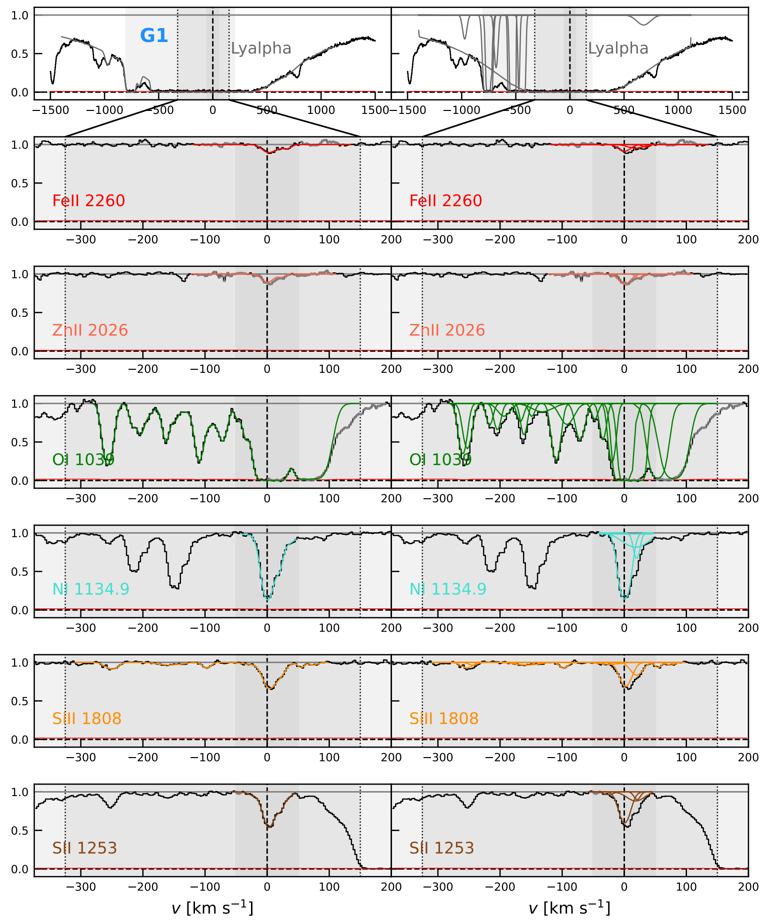

Figure 3.8: G1's CGM absorption and best fits centered at z_{G1}=2.4312. Best fit models are shown as colored lines, and contamination from intervening absorption is shown as light gray lines. Note that H I (top) is on a different velocity scale. The darkest gray region shows the velocity range associated with the DLA which is defined by the Fe-peak elements velocity range, the lighter gray shaded region shows the full extant of the low-ionization metal absorption, and the lightest gray regions shows the velocity of the intermediate- and high-ionization absorption (discussed in Section 3.6). *Left panel:* The product of the individual Voigt profiles. *Right panel:* The decomposed Voigt profiles. The error spectrum is shown at the bottom as a red solid line.

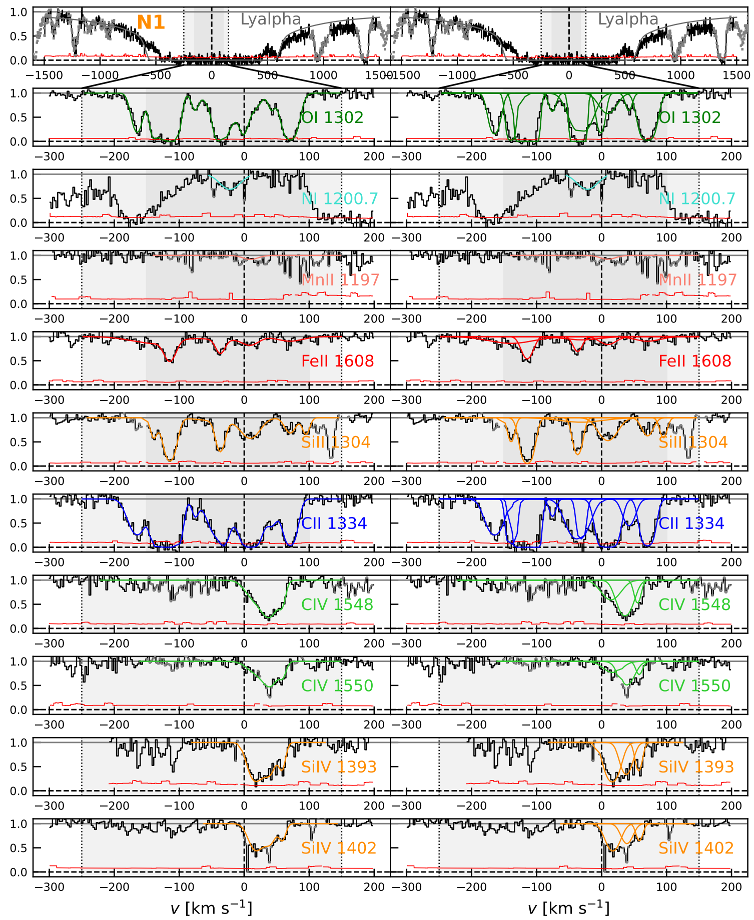

Figure 3.9: N1's CGM absorption centered at its systemic redshift z_{N1}=3.1509. The lines and colors are the same as Figure 3.19.

we checked that $\chi^2/DOF \sim 1$. There were instances where fits achieved this but multiple components gave large errors that were comparable to or greater than the best-fit value. In these cases, we removed the component, then refit, and usually the fit statistic stayed the same.

We assumed that ions of similar ionization state arise from the same gas so we tie their redshifts (velocities) to one another, and allow column density and Doppler width to vary. We fit one metal transition at a time (e.g., all Fe II transitions) then copy the best-fit component structure to to the next transition (e.g., copied Fe II, to Si II), run the fit, check the residuals, *then* add and remove components as needed. This procedure resulted in $\sim 90\%$ of the best-fit components being tied with at least one component from another metal transition with the same ionization state. We did not tie any components to H I (or vice versa) due to the difficulty of separating single from blended components.

G1 and N1's low ionization transitions (e.g., O I, Si II, Fe II) always had a similar structure that was distinct from their higher ionization transitions (e.g., C IV, Si IV, O VI) which is typical in DLAs due to self-shielding. We discuss the intermediate- and high-ionization transitions in Section 3.6. In practice, all of the low ions had their z tied to strong non-saturated transitions (e.g., Si II, Ai II, Fe II), and the higher ions were tied to each other (e.g., C IV, Si IV; O VI).

To derive column densities of saturated transitions (e.g., C II, O I, Ai II) we froze b in the strongest (saturated) components to that of the b of an unsaturated ion of similar mass (usually Si) to place a lower limit on the column density. For G1 this included O I and Ai II, and for N1 this included C II and O I. There are other more heavily saturated transitions we did not fit (e.g., C II, Mg II for G1).

After determining the tied component parameters, we refit the spectrum by shifting the components together in z while allowing $\log N$ and b to vary (unless the absorption was saturated). Once again, we checked the errors and residuals to ensure a good fit a fit statistic $\chi^2/DOF \sim 1$.

We use the $\log N_{H\ I}$ catalog from Rudie et al. (2012, hereafter R12) to determine the H I component structure and total H I column for systems that were covered in their work, which includes G1. R12 was interested in the H I absorption systems toward the 15 KBSS QSO sightlines whose redshifts were (1) not proximate to the QSO redshift ($\lesssim 1000\ \ km\ s^{-1}$), and (2) allowed for Lyβ to fall on the detector. In practice, we froze H I to R12's best fit z_{R12}, b_{R12}, and $\log N_{R12}$ for G1, and we used literature values for N1.

R12's H I catalogs were also useful in fitting transitions that were contaminated with Lyα/Lyβ absorption such as O VI$\lambda\lambda 1031, 1037$. The H I catalog allowed us to remove Lyβ absorption from higher redshift systems. Specifically, we divided out the best-fit R12 absorption components from the entire spectrum, saved it, and used it to fit the contaminated species. It is still possible that there is Lyα contamination and unresolved components so we quote lower limits on these column densities $\log N$. We did not use the H I-removed spectrum for all systems because the large residual spikes that surrounded well-fit H I systems were difficult to work around for some transitions [11]. More importantly, the H I-removed spectrum would have made

[11]Most absorbers with $\log N_{H\ I} \gtrsim 14.5$ are well fit.

our results dependent on R12's modeling. This would add an unnecessary source of uncertainty because most transitions have little to no contamination.

In Figures 3.8 and 3.9 we show the results of the best-model fits and H I fits from R12 for some representative transitions of G1 and N1 . We show all of the fits in Appendix B.

The top three panels of Figure 3.8 show representative H I and Fe-peak metal transitions for G1. The HIRES spectral coverage allows measurements of Lyα through Lyζ giving strong constraints on b and $\log N_{H\ I}$. The Fe-peak transitions have a simple structure that is fit well with two or three components. The systems only span ±50 $km\ s^{-1}$. We use these elements to estimate dust depletion in Section 3.5.

The bottom four panels of Figure 3.8 show representative neutral and low-ionization metal transitions for G1. The component structure for each of the ions is very similar and well fit, and almost every component is tied with at one other metal transition. The strongest components (H I and metals) are all near the systemic redshift of G1 ($\Delta v \sim -8\ km\ s^{-1}$), but there is still weak metal absorption out to velocities exceeding $\sim -500\ km\ s^{-1}$. This high-velocity absorption has the same structure as intermediate- and high-ionization ions and is discussed in Section 3.6 (Figure 3.20).

In Figure 3.9, we show all of the best-fit H I and metal transitions for N1. All of the neutral and low ionization metal transitions share a similar component structure, more than 85% of their components are tied to another. The dominant H I component is offset from $z_{sys,N1}$ by $\sim 7\ km\ s^{-1}$, but the dominant metal absorption complex appears to be blueshifted by ~ -100 km s^{-1}. The low ions span a velocity range of $\sim -200 - +100\ km\ s^{-1}$ and might all be associated with the main DLA (H I) component. The intermediate-ionization ions (C IV and Si IV) have a simpler kinematic structure and smaller velocity range compared to the low ions with an average velocity offset of $\sim$ 50 km s^{-1} spread over $\sim$ 100 km s^{-1}. C IV and Si IV share no common components with the low ions.

Column Densities and Kinematics

In this section, we analyze the total column density and component structure of the best-fit model parameters found in Section 3.5.

In Table 3.6, we report the total column summed over ±1000 $km\ s^{-1}$ from the systemic velocity for the given ions.

Due to the difficulty of associating extended metal components with a parent H I absorber, we report the total column densities, not total metallicities. Indeed, even in ideal scenarios where there are strong constraints on the location of H I components, large ionization corrections are necessary for absorbers with low log $N_{\rm HI}$ gas making metallicity determination non-trivial (e.g., Zahedy et al., 2021).

Table 3.6: CGM Absorption Column Density

Galaxy	z_{sys}	$D_{\rm Tran}$	$\log(\Sigma N_X)[cm^{-2}]^{a,b}$															
		(pkpc)	HI	CII	NI	OI	AlII	SiII	SII	CrII	MnII	FeII	NiII	ZnII	AlIII	CIV	SiIV	OVI
G1	2.4313	20.8	20.40		14.70	>16.72	>13.91	15.31	14.73	12.82	12.26	14.45	13.25	12.07	13.26	14.74	14.03	>15.39
N1	3.1509	19.3	20.00	>15.55	>13.99	>16.05	13.33	14.56			>12.57	14.28				13.90	13.59	

a) Column density summed over ± 1000 $km\ s^{-1}$.
b) Typical uncertainty of 0.1–0.2 dex.

The total column densities we measured are comparable or larger than the highest column densities reported by R19 for ions we have in common (e.g., Si II, C III, C IV, O VI. For some saturated ions e.g., O VI, we report lower limits on the column density meaning they could be even larger.

Table 3.7 shows the number of components required to fit each ion. Note that the Si II structure for G1 is slightly misleading because we report only the weak non-saturated transition (Si II λ1808). There are many components for stronger, saturated Si II transitions. The metal absorption for N1 requires $\gtrsim$ 5 components, and up to 31 components and for G1. This complicated kinematic structure for z ~2-3 galaxies has been noted before by Rudie et al. (2019).

Table 3.7: Component Structure

Galaxy	$\#^{a,b}$									
	HI	CII	OI	AlII	SiII	FeII	AlIII	CIV	SiIV	OVI
G1	9		19	29	9^c	20^c	10	31	23	29
N1	1	9	10	6		6		3	3	

a) Total number of single Voigt components required for the composite fit.
b) N I, S II, Cr II, Ni II, and Zn II have ≤ 3 components and are omitted from this table.
c) Does not include saturated components.

The total column density and kinematic structure of the components add more evidence that the z ~2–3 CGM (within $R_{\rm vir}$) is kinematically complex requiring at minimum 10 components (for neutral and low ions) with some transitions requiring up to 31 components (for intermediate and high ions), and column densities exceeding the largest found by R19 seen in C II, Si II, C IV, Si IV, and O VI, suggestive of a high covering fraction of metals within $R_{\rm vir}$ at $z \sim 2-3$ CGM.

CGM Metallicity

We derive CGM metallicity using metal components that are self-shielded by the DLA gas, which reduces ionization effects. For G1, we use the velocity range of the Fe-peak components $v \pm 50\ km\ s^{-1}$ to estimate the extent of the DLA self-shielding. For N1, we the location of the strongest Fe II component ($v \sim$ -150 km s^{-1}) and Mn II (50 km s^{-1}) $-150 - 50\ km\ s^{-1}$ to estimate the extent of the DLA self-shielding. Additionally, all of the absorption components that we sum over have O I and N I in common, suggesting that the gas is mostly neutral based on their low ionization potentials (Field, Steigman, 1971; Steigman et al., 1971). We sum the metal columns, normalize by the H I column, then normalize by solar values (Asplund et al. (2009)), and report the values in Table 3.8. For ions where the main components are saturated we quote lower limits on the metallicity.

The α-element metallicities are consistent with one another for G1 (O, S, Si; within 0.1 dex) and N1 (O, S; within 0.2 dex). The Fe-peak element abundances for both galaxies are fairly consistent with one another (within 0.3 dex) with the largest discrepancy found in Mn II.

Table 3.8: CGM Metallicity[a]

Galaxy	[C/H]	[N/H]	[O/H]	[Al/H]	[Si/H]	[S/H]	[Cr/H]	[Mn/H]	[Fe/H]	[Ni/H]	[Zn/H]
	(N_{CII})	(N_{NI})	(N_{OI})	(N_{AlII})	($N_{\mathrm{Si}II}$)	($N_{\mathrm{Si}I}$)	(N_{CrII})	(N_{MnII})	(N_{FeII})	(N_{NiII})	(N_{ZnII})
G1[a]		-1.49	>-0.85	>-1.11	-0.73	-0.79	-1.22	-1.50	-1.39	-1.35	-0.89
	()	(14.74)	(16.24)	(13.74)	(15.18)	(14.73)	(12.82)	(12.33)	(14.51)	(13.27)	(12.07)
N1[b]	>-0.92	>-1.84	>-0.72	-1.12	-0.92			<-0.86	-1.22		
	(15.51)	(13.99)	(15.97)	(13.33)	(14.59)	()	()	(12.57)	(14.28)	()	()

a) Column density of the gas self-shielded by the G1 DLA: $\pm 50\ km\ s^{-1}$.
b) Column density of the gas self-shielded by the N1 DLA: $-150 - 100\ km\ s^{-1}$.

The top row of Figure 3.10 shows a summary of the abundance ratios of G1 and N1. The Fe-peak elements (Cr, Mn, Fe, Ni; top left) are consistent with one another for both galaxies. Mn appears to be underabundant for G1, which is commonly found in DLAs and related to its nucleosynthetic origin (e.g., SNeIa; Konstantopoulou et al., 2022; Nomoto et al., 1997; Pettini et al., 2000; Vladilo, 1998). We place an upper limit on Mn for N1 due to the weakness of the line and difficulty locating the continuum. The [α/Fe] ratios show α-enhancement for both galaxies. Carbon and the odd elements show similar deviations from solar. Additionally for G1, there is a clear offset in the Zn abundance compared to the rest of the Fe-peak elements that we discuss in the next section.

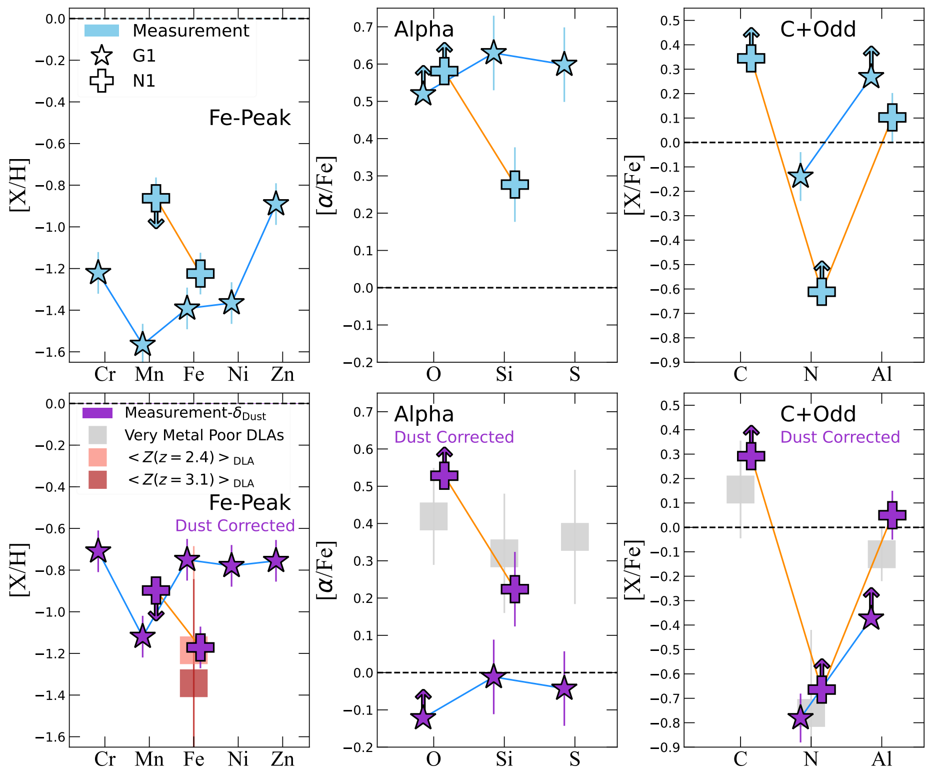

Figure 3.10: CGM abundance ratios for G1 (star) and N1 (plus). *Top row: Blue filled* symbols are direct non-dust corrected metallicity measurements. *Bottom row: Purple filled* symbols have been dust-corrected following empirical prescriptions from De Cia et al. (2016). The *left column* shows Fe-peak abundance; the *middle column* panel shows [α/Fe] ratios; and the *right column* show Carbon and odd number elements. The light red and dark red squares show the DLA mean metallicity (and typical dispersion) from a compilation/analysis by Rafelski et al. (2012) (references therein), the gray squares show the median abundance ratios for very metal poor DLAs compiled by Nuñez et al. (2022).

Dust Depletion

It is well known within the literature that DLAs experience dust depletion analogous to that seen in the MW ISM (e.g., Calura et al., 2003; De Cia et al., 2016, 2018; Jenkins, 2009; Khare et al., 2007; Konstantopoulou et al., 2022; Péroux, Howk, 2020; Ramburuth-Hurt et al., 2023; Vladilo et al., 2006). We are interested in the total metallicity of the DLAs (CGM gas), so we must account for metals in all phases, i.e., gas and dust. We must rely on ratios of refractory elements (easily condense onto dust grains) and volatile elements (easy to keep in the gas phase), to gauge the amount of dust depletion in DLAs with the important condition that the elements track each other nucleosynthetically. The dust depletion correction δ_d can be used to correct metallicity and place limits on the amount of dust (e.g., A_V or $E(B-V)$) in the CGM.

G1 shows detection's of the volatile element Zn, and refractory elements Cr, Mn, Fe, and Ni, which are all near the Fe-peak. For N1, there are no detection's of volatile elements but a few detection's of refractory elements Mn, Fe, and Si. We can use Si to place limits on dust depletion because it is not as easily depleted as Mn and Fe.

We estimated the dust depletion corrections using a couple of methods. The simplest approach used the difference (linear ratio) between the Zn and Fe-peak abundances (see Section 3.5). In practice, this meant setting all Fe peak elements abundances to match that of [Zn/H]. We then computed the dust depleted ratios [X/Fe]$_d$ = [X/(Fe-δ_{Zn})] where δ_{Zn} is the difference between [Zn/H] and [Fe/H]. The equivalent expression is [X/Fe]$_d$=[X/Zn]. The advantage of this method is that it is straightforward, completely empirical, and specific to this absorber. Importantly, it does not account for potential depletion effects of Zn and cannot be used in systems that do not have detections of Zn.

The other method uses the relations derived by De Cia et al. (2016, 2018, hereafter DC16) and later improved by Konstantopoulou et al. (2022), who used an ensemble of abundances measured from DLAs, Galactic absorbers, and SMC and LMC absorbers to predict the average dust depletion of a system given an [Zn/Fe]. The unknown intrinsic abundances of an individual absorber make it difficult to calibrate from one system, but with a large enough sample one could find bulk trends that can be used to find an average dust depletion correction. The critical assumption that the authors made was that the depletion correction δ_d =0 at [Zn/Fe]=0. We refer the reader to Section 3 of DC16 for a complete description of the method but note that the updated relations published by De Cia et al. (2018) allowed dust depletion to be predicted with either [Zn/Fe], [Si/Fe], or [S/Fe]. They also computed relations for elements besides Fe (e.g., N, O, S, Al, N) but we correct only the Fe-peak elements because (1) they likely dominate the depletion (they have much higher condensation temperatures than e.g., O, N (Lodders, 2003)), (2) the other relations rely on the predicted curves from the [Zn/Fe] abundances i.e., a model based upon another model, and (3) the other relations have a significant amount of scatter and much fewer measurements than that used for [Zn/Fe] and [Si/Fe].

Both methods result in dust corrected Fe abundances that were consistent with one another for G1 $[Fe/H]_{Zn} = -0.89 \pm 0.1$, $[Fe/H]_{DC16} = -0.76 \pm 0.15$. We use the depletion corrections from DC16 because its predicted values were consistent with our simpler empirical approach and because it allows us to estimate depletion for N1, which has no detection of Zn. Konstantopoulou et al. (2024) recently analyzed cosmic dust evolution using a large sample of DLAs (and MW, SMC, and LMC absorbers) that included G1. We find comparable depletion.

We use the [Si/Fe] ratio to infer N1's dust depletion correction, which is small (δ_d = 0.05 dex).

The bottom row of Figure 3.10 show the dust depletion-corrected abundances for G1 and N1; red and pink squares show the DLA mean metallicity from a sample of H I-selected DLAs at high-z (analyzed by Rafelski et al. (2012)) at G1's and N1's redshift; and grey squares show the median abundance ratios of one of the largest samples of very metal-poor (VMP; $[Fe/H] \leq 2$) DLAs compiled by Nuñez et al. (2022). The CGM metallicity for both G1 and N1 are comparable to that of the DLA mean metallicity at their redshifts (we discuss this more in Section 3.5). The Fe-peak elements for both galaxies are consistent after applying the dust depletion correction, and comparable to what we inferred empirically (i.e., [Zn/H] in the upper plot or δ_d = 0.6 dex for G1). The [α/Fe] abundance patterns (lower middle plot) show a striking difference: G1's CGM [α/Fe] is solar and consistent across the three α tracers, and N1's CGM shows α-enhancement similar to VMP DLAs. Interestingly, both of their [C,N,Al/Fe] abundance patterns (right bottom plot) are consistent with the VMP DLAs. There could be a few reasons for this consistency that are related to the nucleosynthetic origin of the elements. Nitrogen, which is produced abundantly by AGB stars, might increase in lockstep with Fe, suggesting that the VMP DLA ratios include some enrichment from delayed events.

Altogether, G1's CGM has a moderate-high metallicity with a moderate amount of dust depletion reminiscent of a chemically evolved absorber, but has a C and odd-element abundance pattern similar to less chemically evolved absorbers. Interestingly, G1 has not been recently enriched, as evidenced by its solar $[\alpha/Fe] \sim 0$ ratio. This suggests that the abundance patterns for individual absorbers are hard to predict and caution must be used if assuming any abundance pattern for analysis (e.g., photoionization modeling).

N1's CGM has a low-moderate metallicity with C, odd-element, and [α/Fe] abundance ratios consistent with VMP DLAs. This suggests that it was recently enriched by CCSNe.

Comparison with the DLA Literature

In this section we compare our measured/inferred DLA properties with those in the literature in terms of H I column density and metallicity (we assume [Fe/H]$_d$=[M/H]). We discuss dust depletion in Section 3.6. We refer to the DLA associated with G1 at z = 2.41 as G1DLAz2, and the DLA associated with N1 at z = 3.15 as N1DLAz3.

N1DLAz3 has previously been found to have $\log N_{H\ I}$ = 20.00 ± 0.1 at z$_{abs}$=3.153 ($\delta v_{ISM} < 60\ kms^{-1}$), $[Fe/H] = -1.4 \pm 0.1$ (Lu et al., 1997, 1998; Sargent et al., 1989). Our H I is the same as the authors and Fe abundance is within 0.2 dex (regardless of dust correction).

We compare the metallicity of both DLAs to the cosmic DLA mean metallicity (and dispersion) at their redshift using the linear relation computed by Rafelski et al. (2012), who analyzed a large sample of DLAs across a wide redshift range (z∼1.5-5) with little metallicity bias (H I selected sample). Using the relation at N1's redshift yields $Z(z = 3.1509) = -1.34 \pm 0.5$ making N1DLAz3 comparable to the mean metallicity at its redshift ([Fe/H]$_d$ ∼-1.1±0.1). Even though the mean relation is not a physical model and the scatter is large, it is interesting that N1DLAz3 is not obviously metal-poor because its abundance ratios are similar to that seen in VMP DLAs, which are systematically below the DLA cosmic mean by 1 dex between $z \sim 2-3$ (i.e., [M/H]=[Fe/H]<-2 by definition).

The H I column density of N1DLAz3 ($\log N_{H\ I}$ = 20.0) is at the boundary between sub-DLAs ($19 \leq \log N_{H\ I} < 20.3$; also known as Super Lyman Limit Systems or SLLS) and DLAs ($\log N_{H\ I} \geq 20.3$). It would therefore be useful to compare it to a survey of sub-DLAs. The KODIAQ-Z (Lehner et al., 2022) and HD-LLS surveys (Fumagalli et al., 2016; Prochaska et al., 2015) analyzed the metallicity distribution of a large number of H I absorbers with $\log N_{H\ I}$ =14.6–20.3. Among their many findings was an increase in metallicity with $N_{H\ I}$ from sub-DLA to DLA, which is consistent with our findings for N1DLAz3 and G1DLAz2, though there is large scatter in these relations ($\Delta[M/H] > 0.5$). Additionally, the authors found that the median/mean (standard deviation) metallicity of sub-DLAs is $< Z >_{SLLS}$=-1.90/-1.93±0.89 putting N1DLAz3 well above the median/mean. As mentioned before, this is puzzling given that its abundance ratios are similar to that of VMP DLAs.

Berg et al. (2015a) analyzed a large sample of metal-rich DLAs that we will compare with G1DLAz2. Almost half of their sample had $\log N_{H\ I} > 21$ meaning G1DLAz2 is on the low end of the distribution ($\log N_{H\ I}$ = 20.4). The median metallicity of their sample is [M/H]~0.7 which is comparable to the metallicity of G1DLAz2 ([Fe/H]$_d$=-0.75). Finally, the DLA mean metallicity at this redshift is $Z(z = 2.4312) = -1.18 \pm 0.5$ placing G1DLAz2 well above the mean. This all suggests that it is a relatively low H I, metal-rich DLA.

G1DLAz2 was recently studied in detail by N22. Their absorption analysis was based on a component by component ("cloud-by-cloud") multiphase Bayesian modeling scheme that extracted the kinematic structure and physical conditions for each of the components ("clouds") independently but self consistently (each component per ion had its own model that folded in multiphase components when necessary) (Sameer et al., 2021). Photoionization grids were used to infer the physical conditions of the gas associated with low $\log N_{\rm HI}$ gas ($\log{(N_{\rm HI}/cm^{-2})} < 19$ typically; the majority of the metals components). Importantly, the grids assume a solar abundance pattern, which we found is likely not representative of the true intrinsic abundance pattern of the DLA (Section 3.5). Nonetheless, their analyses presents an opportunity for us to compare our flexible "by hand" method with their statistically robust method.

One of the most straight-forward comparisons that we can make is the overall quality of fit and total column density, since neither of these should be significantly affected by model assumptions. A visual comparison of both our fits to Lyα/β, $/\gamma$, Fe IIλ2344, and C IV$\lambda\lambda$1548,1550 show that the fits are comparable in terms of fit statistics and the kinematic structure (see Fig. 4 in N22). However, a visual comparison of Si IV$\lambda\lambda$1393,1402, show that we were able to obtain a better fit. When comparing the derived total column densities of Si IV though, we obtain similar columns: $\log{(N_{\rm Si\mathit{IV}}/cm^{-2})}_{This\ work}$ = 14.04±0.05, $\log{(N_{\rm Si\mathit{IV}}/cm^{-2})}_{N22}$ = 14.12 ± 0.01. Indeed, for almost all of the column densities that we have in common (H I, Si II, S II, N I) our measurements are within 0.2 dex.

One exception to our agreement is the lower limit that we measure for O I being 1.5 dex larger than their reported values. N22 separately measure O I from their main fit and achieve a similar column as ours. They acknowledge that their main fit is unable to reproduce this O I column and might be explained as either the assumed abundance pattern (solar scale from Grevesse et al. (2010)) or additional unseen neutral components superimposed on the O I complex.

Finally, they find a total $N_{H\ I}$ weighted metallicity of $log(Z/Z)_{\odot}$ =-0.68, and find a wide distribution of metallicties per cloud from effectively pristine gas ($\log Z/Z_{\odot} < -2$) to super solar metallicity gas ($\log Z/Z_{\odot} > 0$). We infer a similar dust-corrected metallicity [Fe/H]$_d$=-0.75 and find components that may have high metallicities (see Section 3.6).

This comparison with N22 has shown that the flexible fitting method we use is quantitatively and qualitatively comparable to their statistical method.

3.6 Insights into the Galaxy-Scale Baryon Cycle at z~2-3

Here we compare the CGM and ISM analyses presented in Sections 3.4 and 3.5 to place constraints on the galaxy-scale baryon cycle of galaxies G1 and N1. We will summarize what we have learned about each of the galaxies thus far.

G1 is a typical, Lyα emitting star-forming galaxy at z_{sys} = 2.4312. From the KCWI cube we found it possesses a Lyα halo that extends to more than five times its continuum size (28 kpc), has a simple velocity distribution that peaks at $v_{\mathrm{Ly}\alpha}$ = +271 km s^{-1}, and appears to have small objects that are connected to its Lyα halo, G1-E and G1-S. From the MOSFIRE spectra and SEDs we found that its stellar mass ($\log(M_*/\mathrm{M}_\odot) = 9.9$), gas-phase oxygen abundance ($12 + \log(O/H) = 8.39$), gas-phase N/O ($\log(N/O) = -1.51$), star formation rate (SFR=6-15 M$_\odot$), ionization parameter ($\log U = -3.0 - -2.5$), and dust extinction (A_V=0.21) are all typical of $z \sim 2.3$ star-forming galaxies. From the HIRES spectrum we found that G1's CGM (as probed by DLA absorption) has a high occurence of metal absorption across many ionization states with large column densities, is kinematically complex (requiring more than 10 components to fit the absorption – metal absorption across $\Delta v \sim 1000$ km s^{-1}), a moderate–high metallicity ([Fe/H]=-0.76, dust-corrected) with an abundance pattern that seems to deviate from solar, and moderate dust depletion (δ_d=0.6 dex) inferred from line-of-sight extinction.

N1 is a lower-mass star-forming galaxy at z_{sys} = 3.1509 with properties in the tail distribution of $z \sim 3$ LBG population and analogous to $z \sim 2$ EELGs. From the KCWI cube we found it posses a complex Lyα halo with three components that extends to more than fifty times its continuum size (100 kpc); the main components is double peaked with velocities at $v_{\mathrm{Ly}\alpha,b} = -439$ km s^{-1} and $v_{\mathrm{Ly}\alpha,r}$ = +171 km s^{-1}, and appears to include small objects that are connected to its Lyα halo, HU4 and HU6. From the MOSFIRE spectra and SEDs we found that N1 has a stellar mass that places it in the bottom quartile of UV-selected galaxies in spectroscopic samples ($\log(M_*/\mathrm{M}_\odot) = 8.7 - 9.2$), low gas-phase oxygen abundance ($12 + \log(O/H) = 7.82$), moderate star formation rate (SFR>10 M$_\odot$), strong Lyα ($F_{\mathrm{Ly}\alpha} = 12.5 \times 10^{-17}$erg s^{-1} cm^{-2}) and strong [O III] ($F_{[\mathrm{O\ III}]} = 14.1 \times 10^{-17}$erg s^{-1} cm^{-2}), and a large $f_{\mathrm{esc,Ly}\alpha}$ = 29%. From the HIRES spectrum we found that N1's CGM shows metallic absorption with high column densities across multiple stages of ionization, kinematically complex gas (requiring more than 6 components to fit the absorption), metal absorption across hundreds of km s^{-1}, a moderate metallicity ([Fe/H]=-1.1, dust-corrected) with an abundance pattern that is similar to chemically young absorbers, and has low CGM dust depletion (δ_d=0.05 dex).

Potential Satellites of G1 and N1

We define a galaxy group as two or more galaxies of comparable mass (ΔM ~50%) with projected distances smaller than the $z \sim 2-3$ galaxy autocorrelation length r_0^{GG} = (6.0 ± 0.5) Mpc (Peebles, 1980). The virial radii of the two galaxies are informed by previous KBSS studies and ranges from $R_{vir,G1}$ ~80–90 kpc for G1 (based on the clustering of KBSS L_* galaxies with $M_h \sim 10^{12}$ M$_\odot$, assuming an NFW dark matter halo profile (Rudie et al., 2019; Trainor, Steidel, 2012)), and $R_{vir,N1}$ ~60–70 kpc based on the virial radius determined for the median stellar mass $M_* \sim 10^9$ M$_\odot$ (implied $M_h \sim 10^{11.5}$) of $z \sim 2$ low-mass EELGs (Erb et al., 2023). The potential satellites are well within the virial radii of G1 and N1; the projected distances between the objects are at most 40 kpc, which is about the same distance as the SMC and LMC from the MW.

N22 suggested that the origin of the DLA towards Q2343+1232 is the intragroup medium of a galaxy group at the same redshift. We found from our deep KCWI cube, which includes N22 exposures, that only G1 is at the same redshift as the DLA. However, we find evidence for two satellites of G1: G1-E (east), and G1-S (south). Both sources are visible in the *HST* image of the Q2343 sightline (Figure 3.1) but only G1-E appears to be associated with a continuum source. Both objects appear in Lyα narrow-band images (irrespective of QSO subtraction technique) centered around $z \sim z_{\mathrm{Ly}\alpha,G1}$ (Fig. 3.7). We argue that they are lower mass than G1 based on their photometry and Lyα fluxes. Specifically, their rest-frame optical photometry (*HST-IR*/F160W; QSO-subtracted) is small (compared to G1 $m_{G1,F160W} = 23.37 \pm 0.2$), $m_{G1-E,F160W} = 25.90 \pm 0.2$, and $m_{G1-S,F160W} > 25.96$, and their Lyα fluxes are also small compared to G1, $F_{G1-E}/F_{G1} \sim 0.11$ and $F_{G1-S}/F_{G1} \sim 0.15$ (see Table 3.3). Both galaxies may be resonantly scattering the Lyα from G1's halo because their spaxels connect/overlap in the pseudo-narrow band images. Additionally, G1-S has no optical emission lines detected in the MOSFIRE spectra. Therefore, G1 is likely not part of a galaxy group but instead is a massive galaxy with two detected satellites.

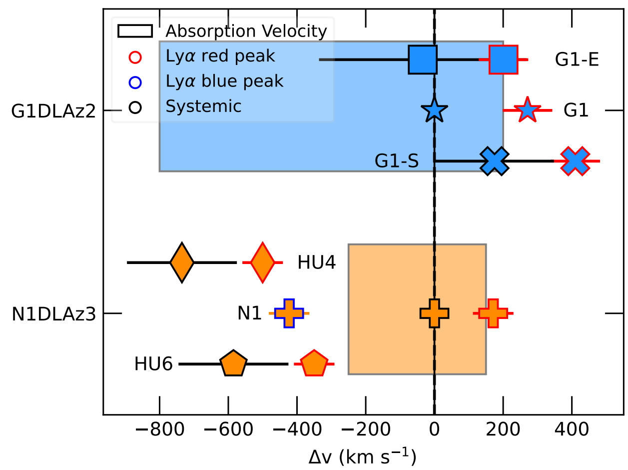

Figure 3.11: Lyα emission kinematics (filled points) compared to CGM absorption kinematics (shaded regions) for the DLA associated with G1 (*top*; blue shaded region) and the DLA associated with N1 (*bottom*; orange shaded region). Red outlined markers show the Lyα red peak velocity (Section 3.5,3.3), black outlined markers are the systemic velocity (Section 3.3,3.5), and blue outlined markers show blue peak velocity, all with respect to z_{sys} (nebular emission) of G1 and N1. Each marker is labeled in the center of the figure.

In Figure 3.11 we compare the kinematics of G1-E and G1-S to explore their potential effects on the dynamics (and perhaps abundances) measured in the DLA. We measure $z_{\mathrm{Ly}\alpha,G1-E} = 2.4335 \pm 0.0008$ ($\Delta v_{\mathrm{Ly}\alpha,G1-E} = 201 \pm 72$ km s^{-1}) and $z_{G1-S,\mathrm{Ly}\alpha} = 2.4359 \pm 0.0008$ ($\Delta v_{sys} = 410 \pm 72$ km s^{-1}). Non-resonant transitions would provide more reliable redshifts but applying the typical $z_{\mathrm{Ly}\alpha} - z_{sys}$ velocity offset to the galaxies ($\Delta v_{\mathrm{Ly}\alpha} = -235 \pm 101$ km s^{-1} (Steidel et al., 2018; Trainor et al., 2015)) gives $\Delta v_{G1-E,sys} = -34 \pm 72$ km s^{-1} and $\Delta v_{G1-S,sys} = 175 - \pm 72$ km s^{-1}. Their estimated systemic velocities coincide with metal absorption in the HIRES spectrum between -100 – +200 km s^{-1}, making it possible that they could be contributing to the absorption.

N1's Lyα halo appears to have three distinct kinematic components (see Fig.3.7). Interestingly, each component is coincident with continuum source(s) in the *HST*/702W image (Figure 3.1), the redshifted component with N1, the intermediate component with HU6 (east of N1), and the blueshifted component with HU4 (and perhaps even more uncatalogued continuum sources; northwest of N1).

In Figure 3.11 we compare the Lyα kinematics of N1, HU4, HU6, and the DLA at the bottom of the figure. The components have velocities that are similar to N1's blue peak (extracted from spaxels that contain the continuum of the galaxy i.e., there is little chance of contamination from the other sources).

The estimated systemic velocities are fairly large when compared to the escape velocity of z ~2 halo with virial mass $\log(M_{\rm vir}/{\rm M}_{\odot}) = 11.7$ at 20 kpc (Rudie et al., 2019; Trainor, Steidel, 2012): $v_{\rm esc}$ ~450 km s^{-1}(when assuming a NFW profile). This velocity is an upper limit for N1 because it is low stellar mass ($\log M_{*} \sim 8.7 - 9.2$) compared to more massive KBSS star-forming galaxies. Due to the complexities of Lyα radiative transfer, it is difficult to determine whether these Lyα velocities are dominated by bulk gas motion or resonant scattering, but the lack of a velocity gradient in all of the objects suggests that there is no gas acceleration/rotation. Indeed, all of the objects have a simple velocity structure with a small velocity dispersion of $\sigma \sim 50 - 100$ km s^{-1}. Additionally, we showed in previous sections that the dominant emission mechanism of Lyα in N1 is not collisional excitation given its low Lyα/Hα.

Both HU4 and HU6s velocities do not overlap with the DLA absorption, suggesting that they do not significantly affect the CGM absorption seen in the DLA. Though, it is still possible that they could have interacted with N1 in the past and/or ejected metals from a previous starburst to the DLA.

The objects are likely lower mass than N1, considering their small Lyα fluxes ($F_{HU4,{\rm Ly}\alpha}/F_{N1,{\rm Ly}\alpha} = (2.88 \pm 0.1)\%$), $F_{HU6,{\rm Ly}\alpha}/F_{N1,{\rm Ly}\alpha} = (9.2 \pm 0.1)\%$, and fainter F702W magnitudes: $m_{HU6} = 25.65 \pm 0.3$ and $m_{HU4} = 25.85 \pm 0.3$, compared to $m_{N1} = 24.45 \pm 0.3$.

Altogether, the combination of the *HST* images, KCWI, MOSFIRE, and HIRES spectra suggest that the new objects discovered towards G1 and N1 are likely satellites. The *HST* images showed that the objects are at projected distances well within the virial radius of G1 and N1, and that they are lower mass based on their photometry. The KCWI spatial and velocity maps showed that the objects have small Lyα fluxes ($F < 0.1 F_{{\rm Ly}\alpha}$) and velocities consistent with G1 and N1, though if a systemic velocity correction is applied to N1 only one of the objects is at a consistent velocity. The KCWI spatial maps and MOSFIRE spectra suggest that the objects near G1 may be scattering photons from its Lyα halo based on their low Lyα/Hα and their Lyα emission appearing spatially connected to the halo. The KCWI velocity maps and HIRES spectra show: for N1, that the satellites' presence may not significantly affect the DLA absorption because their Lyα emission velocities are much larger than the absorption velocity range; for G1 the satellites have similar velocities to strong metal absorption in its CGM and may affect the kinematics and abundances.

Chemical Enrichment

One of the most straightforward methods to trace the galaxy-scale baryon cycle is to compare metallicity differences between the ISM and CGM. Metals are formed via nucleosynthesis and are liberated via supernovae (CCSNe and Type Ia SNe) and other less energetic processes, e.g., the winds from AGB stars. Metals that are found in the CGM therefore likely originated from the ISM. In Section 3.4 we calculated ISM bulk metallicity using strong line calibrations, and in Section 3.5 we inferred the metallicity of self-shielded, neutral phase CGM gas (where ionization effects are minimal) using Voigt profile decomposition. Since different elements can have different channels of production (e.g., hydrostatic vs. explosive nuclesynthesis, αproduction, thermonuclear explosions) it is useful to compare similar metals. In this case, O and N can be reliably measured from both the ISM and CGM.

For the first time at this z (to our knowledge), Figure 3.12 shows the N/O as a function of O/H for G1 and N1. We color coded the symbols to show metals from the CGM (blue) and from the ISM (red) compared to nearby H II regions analyzed by Pilyugin et al. (2012), a sample of metal-rich ($[M/H] > -1.0$) high-z DLAs compiled by Berg et al. (2015a), moderate-low metallicity ($[M/H] < -1.6$) high-z DLAs compiled by Pettini et al. (2008), and very metal poor ($[M/H] < -2$) DLAs compiled by Cooke et al. (2011b). Unfortunately, [N II] was not accessible for N1's ISM, so we show an unbound point (in N/O) at the O/H abundance that we were able to measure, which places it in the low-metallicity regime. Although the O CGM absorption lines are saturated, we nonetheless represent the [O/H] as a point and not a limit because both galaxies α-element abundances were within 0.2 dex; we adopt this difference as its error.

The CGM gas lies in the "primary nitrogen" plateau where the majority of the N is liberated from CCSNe, which has been observed before in high redshift DLAs (e.g., Centurión et al., 2003; Pettini et al., 2002, 1995, 2008; Zafar et al., 2014b). Indeed, we can see that neither the high-, moderate-, or low-metallicity DLA samples populate the secondary nitrogen rise. G1's ISM gas is in the "secondary nitrogen" rise where more delayed enriching events have commenced (e.g., winds from AGB stars, Marigo, 2001). This shows that the ISM of G1 is more chemcially evolved, similar to the KBSS-LM1 galaxy stack (an effective average of the KBSS-MOSFIRE sample). More explicitly, this result suggests that the CGM metals (probed from this sightline) were ejected earlier in G1's SFH when it was in the primary nitrogen plateau or that the CGM has been enriched by SN winds with minimal entrainment of AGB-enriched gas. In the latter scenario, the high-velocity (high-energy; CCSNe and SNeIa) SN winds escaped the galaxy and enriched the CGM whereas the low-velocity (low-energy) winds stayed within the ISM in the recent past.

This positive metallicity gradient (Z_{ISM}-Z_{CGM} > 0) seen in G1 is common in other galaxy-QSO studies (e.g., Battisti et al., 2012; Berg et al., 2023; Chen et al., 2005; Péroux et al., 2011; Prochaska et al., 2007b) and aligns well with the picture of the ISM being the main driver of metals into the CGM *and* the presence of inefficient mixing of outflow ejecta with ambient gas. More specifically, if the ISM is the origin of the bulk of metals seen in the CGM with non-instantaneous mixing, one would expect most sightlines to show $Z_{ISM} \gg Z_{CGM}$ with some sightlines (or components) being metal rich.

N1 shows a flat metallicity gradient (Z_{ISM}-Z_{CGM} ∼ 0), i.e., it has similar O abundance in both its CGM and ISM. This is not common (but see e.g., Péroux et al., 2011; Schady et al., 2024). Unfortunately, we do not have any constraints on the N/O ratio in the ISM and only a lower limit in the CGM, so it is difficult to make inferences on its enrichment history. But its O abundance suggests that both the ISM and CGM lie in the primary nitrogen plateau which is consistent with the findings thus far that it has a young stellar population. Indeed, N1's stellar mass is small, its SED is blue, and its sSFR is high, all of which point to a young stellar population with an ongoing/recent starburst (Figs. 3.4 and 3.6).

There are a few ways that one could explain N1's flat metallicity gradient (1) The QSO is intersecting a particularly metal-rich sightline. This would be consistent with the patchy nature of the CGM. (2) We are seeing stripped ISM from HU6. This could be consistent with the Lyα kinematics (v_{HU5} ∼-500 km s^{-1}) and tapered morphology that narrows away from near N1, but is inconsistent with the DLA absorption velocities (v_{DLA} ∼-200 - +150 km s^{-1}) and lack of velocity gradient. (3) The satellites of N1 (HU4 and HU6) are driving galactic outflows so that the DLA metallicity (and all other properties) is a combination of two or more of the galaxies. The kinematics of the Lyα from the satellites do not fully support this interpretation because neither of the satellites are at velocities with DLA absorption (v_{DLA} ∼-200 - +150 km s^{-1}). (4) N1 ejected very metal-rich (super-solar) gas that efficiently mixed into the CGM such that the metallicity is now similar to the ISM. This is the least likely scenario as the CGM is not well mixed (e.g., Faucher-Giguère, Oh,

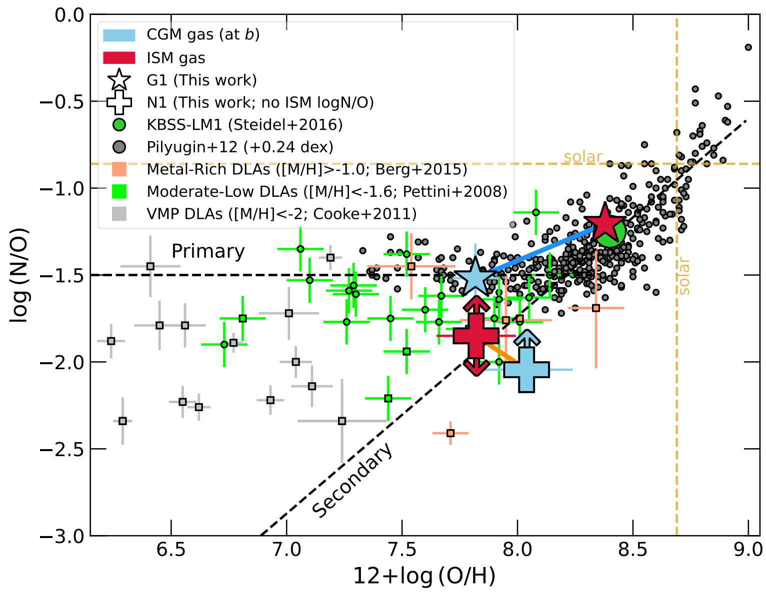

Figure 3.12: Comparison of gas-phase N/O as a function of oxygen abundance in G1's (star) and N1's (plus) CGM (light blue filled; Section 3.5) and ISM (red filled; Section 3.4) gas. This is the first time this explicit comparison has been made at this z (to our knowledge) and shows that G1's CGM is less chemically evolved than its ISM, and that N1's ISM and CGM are comparable in oxygen abundance. An effective average of the KBSS-MOSFIRE sample is plotted as a green circle (KBSS-LM1; Steidel et al., 2016); pink squares show metal-rich DLAs compiled by Berg et al. (2015a); light green squares are moderate–low metallicity DLAs compiled by Pettini et al. (2008) where the pentagons show points where S was converted to O assuming $(O/S)_{\odot}$=1.57 Asplund et al. (2009)); gray squares show very metal poor DLAs compiled by Cooke et al. (2011b); grey points show nearby HII regions in SDSS galaxies from Pilyugin et al. (2012); dashed black lines show the approximate locations of the primary N plateau and the secondary N rise with similar locations and slopes as Pettini et al. (2008); and dashed yellow lines show solar values from Asplund et al. (2009). REFERENCES. Metal-rich compilation by Berg et al. (2015a): Berg et al. (2013, 2015b); Centurión et al. (2003); Dessauges-Zavadsky et al. (2007, 2001, 2006); Dutta et al. (2014); Erni et al. (2006); Henry, Prochaska (2007); Ledoux et al. (2006, 1998); Levshakov et al. (2002); Lopez, Ellison (2003); Lopez et al. (2002, 1999); Lu et al. (1996); Noterdaeme et al. (2008, 2012); Petitjean et al. (2008); Pettini et al. (2008); Prochaska et al. (2001a, 2003b, 2002b); Prochaska, Wolfe (1999); Prochaska et al. (2007a, 2001b); Srianand et al. (2012, 2005); Zafar et al. (2014c). Moderate–low metallicity compilation by Pettini et al. (2008): Centurión et al. (2003); D'Odorico et al. (2002); Dessauges-Zavadsky et al. (2004, 2006); Ellison, Lopez (2001); Henry, Prochaska (2007); Ledoux et al. (2006); Lopez, Ellison (2003); Lopez et al. (2002); Lu et al. (1998); Petitjean et al. (2008); Pettini et al. (2002); Very metal poor compilation by Cooke et al. (2011b): Cooke et al. (2011a); Dessauges-Zavadsky et al. (2001); Ellison et al. (2010); Molaro et al. (2000); O'Meara et al. (2006); Penprase et al. (2010); Petitjean et al. (2008); Pettini et al. (2008); Prochaska, Wolfe (2002a); Srianand et al. (2010).

2023), but it is possible drive such high metallicity winds (Chisholm et al., 2018; Martin et al., 2002; Strickland, Heckman, 2009).

Altogether we were able to see that the ISM-CGM metalliciity between the galaxies were very different. G1's CGM was more metal poor and less chemical evolved than its ISM while N1 CGM and ISM had comparable metallicity. Expanding the number of galaxies that we can map onto this space will help answer questions about the metal enrichment of the CGM.

Dust Abundance and Depletion

Explicit comparisons between the dust content in the CGM and ISM of individual galaxies are almost entirely lacking in the literature, especially at $z \sim 2$. There is work describing cosmic dust content (e.g., De Cia et al., 2018; Konstantopoulou et al., 2023; Ledoux et al., 2015; Péroux, Howk, 2020; Pontzen, Pettini, 2009) using DLAs, but the explicit connection to singular galaxies is not common (but see, e.g.; Boettcher et al., 2021; Rudie et al., 2017).

We quantify the amount of dust in the ISM in Section 3.4) using the Balmer decrement ($F(H\alpha)/F(H\beta)$), then again in Section 3.4) from the best-fit SED parameters. We calculated CGM dust depletion corrections δ_d in Section 3.5 using the empirical scaling relations from DC16. We convert the CGM depletion corrections to extinction by scaling the galactic A_V to $N_{H\ I}$ conversion by metallicity (equation 8 from DC16):

$$A_V = DTM \times \left(\frac{A_V}{N_{HI}}\right)_{Gal} \times N_{HI} \times 10^{[M/H]} \tag{3.5}$$

where DTM is the dust to metal ratio equal to $(1 - 10^{\delta_d})/dtm(Gal)$ where $dtm(Gal)$=0.98 (the dust-to-metal ratio of the Milky Way; De Cia et al., 2013) and δ_d is the depletion correction derived in Section 3.5; $\left(\frac{A_V}{N(H\ I)}\right)_{Gal} = 0.45 \times 10^{-21}\ mag\ cm^{-2}$ (Watson, 2011) is the galactic conversion from H I column to extinction, $N(H\ I)$ is the linear neutral hydrogen column density, and [M/H] is the metallicity, which we equate to the dust corrected iron abundance $[Fe/H]_d$ (see Section 3.5).

In Figure 3.13 we show the dust content of G1 and N1 expressed as extinction from H II regions (Balmer decrement), continuum photometry (SED), and CGM (using Equation 3.5). We do not have a nebular extinction for N1 because Hα was accessible from the ground. We compare the extinction to that of a typical DLA from the large samples analyzed by De Cia et al. (2016); Konstantopoulou

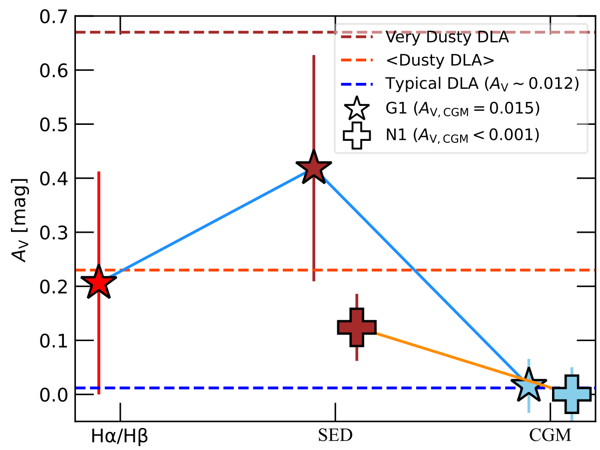

Figure 3.13: Dust extinction of G1 (blue outlined star) and N1 (orange outlined plus) in the ISM (red fill) and CGM (light blue fill). Extinction measurements using (1) the Balmer decrement are denoted as "$H\alpha/H\beta$," (see Section 3.4), (2) the best-fit SED models as "SED," (see Section 3.4) and (3) from the CGM as "CGM" (see Section 3.5). We show typical DLA dust extinction as a blue horizontal dashed line from (De Cia et al., 2016; Konstantopoulou et al., 2023), average dusty DLA extinction (Heintz et al., 2018), and a very dusty DLA that was analyzed by Konstantopoulou et al. (2024). We use R_V=3.1 (Cardelli et al., 1989).

et al. (2023); Ramburuth-Hurt et al. (2023), the average extinction of a sample of dusty DLAs ($A_V \gtrsim$0.2; Heintz et al., 2018), and a very dusty DLA (J1056+1208; Konstantopoulou et al., 2024). Regardless of the method employed to determine the dust in the ISM, there is at least an order of magnitude less inferred line-of-sight extinction in the CGM (light blue filled symbols).

It is possible that we are underestimating the depletion of N1 because we could only use the [Si/Fe] ratio to determine its dust depletion correction. We note that if we were to use the empirical CGM depletion correction for G1 instead of the DC16 relations, the A_V would not change significantly.

This trend is consistent with dust being driven from the ISM to the CGM. It seems likely that the dust was formed in the ISM and was expelled via SN winds, just like the metals. Along with dust creation and expulsion, it is also possible that dust was destroyed during this process (e.g., Otsuki, Hirashita, 2024). There could be a few ways in which the depletion patterned formed. Either the depletion pattern was always there, or it took time for refractory elements to deplete onto dust grains.

Regardless of the origin of the dust depletion pattern, we have shown that the inferred line-of-sight extinction is more than ten times smaller in the CGM as compared to the galactic H II regions.

Unbound Gas in the CGM

In Figure 3.14, we show all best-fit intermediate- and high-ionization metal transitions, a representative low-ionization transition, and the best-fit H I from R12 for G1. The intermediate- and high-ionization transitions (C IV, Si IV, O VI) have a very similar structure, and share $\sim$ 90% of their components. Their structure is different from that of the low ionization metals which is typical in DLAs due to the self-shielding.

Some of the absorbers in G1's CGM have radial velocities $v_r \gtrsim$500 km s^{-1} relative to the systemic redshift. These velocities are lower limits on the true (three dimensional) velocity of the gas. Absorbers at smaller velocities might also be unbound, but we cannot tell from the current data. At these large velocities, the absorbers are *unambiguously* gravitationally unbound to the galaxy, given the escape velocity of a typical KBSS L_* star-forming galaxy $v_{\rm esc}$ ~500 km s^{-1}at b ~20 kpc and $M_h \sim 10^{12}$ M$_\odot$, assuming an NFW dark matter halo profile (Rudie et al., 2019; Trainor, Steidel, 2012). Additionally, the impact parameter is a lower limit on the distance from the galaxy, so some absorbers near (or below) the escape velocity may actually be unbound since a farther distance would reduce the escape velocity. N1 might also have unbound gas in its CGM but its absorbers' radial velocities range between -200 – +100 km s^{-1} which is well below its likely escape velocity $v_{{\rm esc},N1} \sim$ 400 km s^{-1} ($M_h \sim 10^{11.5}$ M$_\odot$), so we can conclude only that there is no *unambiguously* unbound gas and do not discuss it in this section (Erb et al., 2023; Rudie et al., 2019). The sightline to Q2343 has two absorption complexes that, if associated with G1, would have velocities equal to or exceeding its escape velocity: one near v ~-500 km s^{-1}which we refer to as "Complex500", and the other near v ~-750 km s^{-1}which we refer to as "Complex750".

Complex500 (magenta dash-dot lines) is seen across all ionization states observed in the HIRES spectra, including neutral (H I, O I, N I), low (C II, Ai II, Si II), low-intermediate (C III, Al III, Si III), intermediate (C IV, Si IV), and high (O VI) ionization metal species. The ions share the same kinematic structure even though they differ significantly in their column densities. For example, $\log{(N_{H\ I}/cm^{-2})}$ = 15.86 ± 0.1, $\log{(N_{Al\ II}/cm^{-2})}$ = 11.65 ± 0.1, $\log{(N_{{\rm Si}\ IV}/cm^{-2})}$ = 12.43 ± 0.2, $\log{(N_{C\ IV}/cm^{-2})}$ = 13.58 ± 0.2, and $\log{(N_{O\ VI}/cm^{-2})}$ = 14.82 ± 0.2 (found by summing over ~-550 – -450 km s^{-1}). We can see that the low-ion metal columns

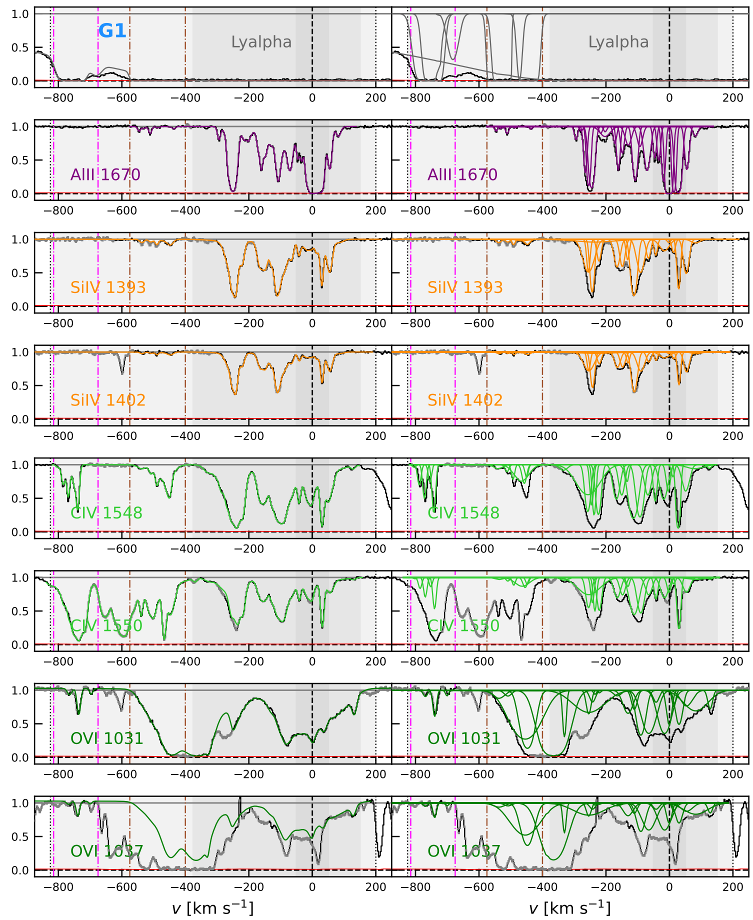

Figure 3.14: G1's intermediate- and high-ionization metal CGM absorption and and best-fit Voigt profiles centered at z_{G1}=2.4312. The magenta dashdot lines shows a metal absorption complex at $v \sim -750$ km s^{-1} and brown dashdot lines show metal absorption at $v \sim -500$ km s^{-1}. The lines and colors are the same as Figure 3.8.

(e.g., Al III) are small compared to the intermediate- and high-ionization metals (e.g., C IV). Complex500 is reminiscent of the CGM absorbers analyzed by R19, who found that most absorption complexes (within $R_{\rm vir}$ at z ∼2–3) had low- to intermediate-ionization (and some high-ionization) ions with the same kinematic structure, with many of the absorbers at velocities that exceeded the galaxies gravitation potential. This suggests that Complex500 is more typical of the $z \sim 2$ CGM compared to the $v \sim 0$ km s^{-1} absorbers that are self-shielded by the DLA that allow for much larger columns of low-ionization gas.

Complex750 (brown dashdot lines) is seen only in H I (two components), C IV (five components), and O VI (three components) spread between -800 – -700 km s^{-1}. They are the fastest moving absorbers detected in G1's CGM.

Their column densities are more comparable to each another (in contrast to Complex500). Specifically, $\log{(N_{H\ I}/cm^{-2})} = 14.89{\pm}0.1$, $\log{(N_{C\ IV}/cm^{-2})} = 13.61 \pm 0.1$, and $\log N_{O\ VI}/cm^{-2} = 13.40 \pm 0.1$. Their ratios are $\log{(N_{C\ IV}/N_{H\ I})} = -1.28 \pm 0.2$, $\log{(N_{O\ VI}/N_{H\ I})} = -1.49 \pm 0.2$, and $\log{(N_{C\ IV}/N_{O\ VI})} = 0.21 \pm 0.2$. The strongest component of Complex750 is found at $v \sim 766$ km s^{-1}.

These two complexes are associated with low $\log N_{H\ I}$ gas and relatively high columns of metals, suggesting that the gas is either highly ionized, metal-rich, or both. The high velocities associated with the two complexes, especially that of Complex750, point to an energetic origin. The combination of the column densities and velocity suggests that the absorbers were ejected via energetic galactic outflows. Indeed, N22 found that the metallicities of the clouds in Complex500 are super-solar, possibly indicating that these absorbers are the products of undiluted CCSNe. This is likely also true for Complex750 given its column density ratios.

These results are similar to previous studies where enhancement of H I, C IV, and O VI was found within 180 kpc of KBSS galaxies, at column densities and velocities that would suggest metal-rich (or highly ionized) gas that originated from a galactic outflow, and that unbound absorbers were usually associated with low $\log N_{H\ I}$ (Adelberger et al., 2003; Pratt et al., 2018; Rudie et al., 2019; Simcoe et al., 2006; Turner et al., 2014, 2015). Indeed, enhanced O VI absorption (and C IV) have been found to favor a scenario where the ions arise from metal-rich ($Z > -0.1$) hot ($T > 10^5\ K$) gas (Simcoe et al., 2004, 2006; Turner et al., 2015).

We now place limits on the timescales associated with the ejection of the absorbers using their measured velocities as a sanity check. Starburst driven galactic superwinds are known to have velocities of v_{winds} ~200 - >1000 km s^{-1}from $z = 0 - 1$ (Heckman et al., 2015, 1990; Prusinski et al., 2021). Indeed, the average velocities of the two complexes are consistent with this range. Using the lower and upper limit for galactic superwind velocity over 20.8 kpc gives an ejection time between $\lesssim$21-104 Myr ago. That is ample time for the proposed galactic outflow to have launched and made its way to b given the stellar age of G1 (~600 Myr).

Altogether, these complexes appear to provide direct evidence of metal enrichment of the CGM (and/or IGM) from galactic outflows based on their velocities, H I and metal column densities, multiphase nature of the absorbers, and limits on the timescales of ejected absorbers.

3.7 Discussion and Caveats

Are We Actually Probing CGM Gas?

One can never prove that an absorber is associated with a particular galaxy because there are multiple explanations for the presence of gas at the same redshift as the galaxy: ejected/stripped gas from another galaxy, chance alignment of a satellite galaxy intersecting the QSO LOS, intragroup medium of an unresolved galaxy group, etc. Therefore, we must rely on the ensemble of overlapping physical properties of the galaxy and absorber to argue whether it is *reasonable* to assume that they are physically associated with one another.

The velocity offset between the systemic redshift acquired from the rest-optical non-resonant nebular emission and the best-fit DLA HI component for both G1 and N1 are $|\Delta v| < 10$ km s^{-1}. One would expect a larger velocity offset if the objects were truly not physically in the same vicinity.

The impact parameters of the QSO sightlines are well within the virial radius of the galaxies ($b \ll 100$ kpc) where one would expect large column densities from CGM gas absorption detectable within a single sightline. The occurrence rate of high H I column gas decreases steeply with impact parameter (Krogager et al., 2017; Rudie et al., 2012; Werk et al., 2014).

The metallicity difference seen between the ISM (12+log (O/H)) and CGM ([O/H]) fits well with the picture of the DLA arising from CGM gas that has been enriched by metal products from the ISM with non-instantaneous mixing for G1. However, N1's flat metallicity difference is puzzling but could be explained by a more complex interplay between N1 and its satellite galaxies e.g., the origin of the DLA could be the stripped ISM of HU6 or the satellite galaxies are driving outflows that are enriching the DLA.

An interesting argument against a galactic origin of the DLA gas towards G1 is related to its metal abundance pattern. After accounting for dust depletion, we found that the DLA has moderate-metallicity $[Fe/H]_d = -0.76$ but has no α-enhancement ($[\alpha/Fe] \sim 0$), suggesting that it has not seen recent enrichment from galactic outflows dominated by CCSNe like that seen in VMP DLAs ($[\alpha/Fe] \sim 0.5$). These two points seem to contradict G1's apparent ability to drive galaxy-scale outflows, deduced from the instantaneous SFR (and SFR$_{SED}$), ionization, and optical line ratios. After all, galaxy-scale outflows are ubiquitous at $z \sim 2-3$. Nonetheless, we know that the CGM is patchy, so the sightline we are probing might have been "missed" by the most recent outflow events *or* G1s abundance pattern deviates from solar values.

Finally, it is possible that the DLA arises in the ISM of a (physically) small satellite galaxy that has not yet been identified; this possibility is difficult to rule out, but the level of enrichment attained by the gas would make it implausible to associate the absorption with a very faint host. We have leveraged very deep IFU cubes and the natural masking of the QSO by the DLAs to show that there is no faint/diffuse Lyα emission on top of the QSO other than emission directly associated with the galaxies. Our 3σ detection limit corresponds to a surface brightness of $SB \geq 1.5 \times 10^{-19}$ erg s^{-1} cm^{-2} arcsec^{-2}. Unfortunately, our QSO subtraction technique only allows us to probe $b \geq$1.25" from the QSO center, so future improvements to our technique may result in discoveries of new galaxies. The HST images contain no detectable continuum sources within 0.7$''$ of the QSOs, which places a limit on the hypothetical projected radius $r \lesssim$2.8 kpc at both galaxies' redshifts. With more sensitive IFUs on larger telescopes with longer integration times, we will be able to probe lower limits of flux (stellar mass) until either a galaxy is found or the limiting stellar mass is less than that corresponding to log $N_{H\ I}$.

Altogether, it is reasonable to interpret the DLAs as the CGM of the galaxies due to the small CGM-ISM velocity offset ($< 10\ km\ s^{-1}$), small impact parameters (b <21 kpc, well within $R_{\rm vir}$), and the positive ISM-CGM metallicity gradient (for G1). Some puzzles remain: the CGM abundance pattern (for G1) and the flat CGM-ISM metallicity gradient (for N1).

Comparison with other Absorber-Galaxy Systems

In this section we compare G1 and N1 to several works that analyzed absorber-host galaxies at z≥2. One caveat to this comparison is that the two galaxy-absorber pairs presented in this paper do not represent a homogeneous selection and thus should not be used to infer properties of some underlying population.

Krogager et al. (2017) analyzed a sample drawn from two decades of searches for $z > 2$ DLA host galaxies. Their new search focused on metal-rich DLAs under the assumption that their hosts would follow the mass-metallicity relation, i.e., the hosts would be more likely to be detected (e.g., Fynbo et al., 2011, 2008). Similarly, a very recent survey was conducted by Oyarzún et al. (2024) who searched for Lyα emission of metal-rich DLA hosts using KCWI. This sample was unique because of the inclusion of galaxies with CO detections associated with DLAs. Both studies report a galaxy detection rate (Lyα and/or CO detection) close to $\sim$ 50%, well above the typical blind detection rate of $\sim$ 10 – 15% (i.e., no metal selection), adding more evidence that metal-rich DLAs are more likely to have detectable host galaxies (Fumagalli et al., 2015; Krogager et al., 2017). This is consistent with our findings that neither G1 nor N1 is associated with a metal-poor DLA. Interestingly though, the DLA metallicities of the detected galaxies ranged from low–moderate to metal–rich ([M/H]=-1.39 – -0.27) putting G1 in the middle of the distribution.

Comparing further, we see that the H I column density of the DLAs were comparable to that of G1 (log $(N_{H\ I})\sim 20.6$); the impact parameters spanned b=0 – 70 kpc, the majority (4/6) of which being $b < 12$ kpc, which is about 1.5× smaller than G1 and N1; and the Lyα fluxes ranged from 0.5 – 17 $\times 10^{-17}$erg s^{-1} cm^{-2}, comparable with the fluxes we measured for N1 and G1 (3, 13 $\times 10^{-17}$erg s^{-1} cm^{-2}).

The MUSE Analysis of Gas Around Galaxies (MAGG; Lofthouse et al., 2020) survey and the MUSE Quasar-field Blind Emitters Survey (MUSEQuBES; Muzahid et al., 2020) have recently searched for $z \gtrsim 3$ LAEs at the same redshift as H I absorbers. Both samples are galaxy-selected (via Lyα emission detection) and MAGG additionally focuses on QSOs with strong H I-absorbers (LLS, and higher). Both samples discovered a large number ($N \gtrsim 100$) of LAEs within $b \sim 10$ – 300 kpc of QSOs and $\pm$1000 km s^{-1} of a mix of LLS, sub-DLAs, and DLAs (log $(N_{H\ I}/cm^{-2}) > 16.5$) that have moderate to low metallicities ([M/H]~-3.5 – -1.5). The novelty of N1 compared to these samples is threefold: first, its impact parameter is almost an order of magnitude smaller than a typical detection ($b_{N1} \sim 20$ kpc vs. $b_{MAGG,median} \sim 165 - 200$ kpc); second, it is associated with a (sub-)DLA whereas the majority of the MAGG LAEs are associated with LLSs; third, N1 was a continuum-selected galaxy as opposed to the Lyα selection from MUSEQuBES and MAGG.

MAGG has found more than 120 LAEs but only six (confident) detections are found at $b < 50$ kpc, whereas MUSQuBES discovered 96 LAEs, 5 of which have $b < 50$ kpc. Interestingly, the LAEs with the smallest impact parameter in their sample are not found to be associated with DLAs but instead LLS (or lower), suggesting the CGM of N1 may not be typical, although larger samples at small impact parameters would be required for this statement to be made with high confidence. The closest (confident) LAE-DLA hosts are typically found at $b > 50$ kpc while the brightest (confident) LAEs are found at $b > 100$ kpc. Though seemingly uncommon, there have been discoveries of $z \sim 3$ DLA host galaxies (see e.g., Fumagalli et al., 2017).

Finally, we compare N1 to dwarf-galaxy CGM studies given its lower mass $M_* \sim 10^9 M_\odot$. MUSEQuBES probes a lower stellar mass ($M_* \sim 10^{8.6} M_\odot$) and lower Ly$\alpha$ luminosity ($L_{\mathrm{Ly}\alpha} \sim 10^{42}\ erg\ s^{-1}$) than N1. Among some of their findings is an excess of H I and C IV at line of sight (radial) velocities $v < 500$ km s^{-1}; they measure a range of $\log N(CIV/cm^{-2})$ ~11.4–14.3, placing N1 at the high end of their distribution ($\log N(CIV/cm^{-2})_{N1}$ =13.9); about 45% of the C IV absorbers were at velocities that were unbound to the halo, which is not the case for N1 which showed no unambiguously unbound absorbers (see Section 3.6).

At low-redshift there have been multiple dwarf-galaxy CGM studies that have found a low frequency of CGM metal absorption from low- (e.g., Si II) and intermediate-ions (e.g., C IV) but a high frequency of high-ionization gas O VI, all associated with low H I gas (Johnson et al., 2017; Qu, Bregman, 2022; Zheng et al., 2024) (but see Bordoloi et al., 2014). Therefore, N1 appears to support this trend that at high-z there is a large fraction of neutral–intermediate ionization metal absorption, though a larger sample of $z \sim 3$ lower mass galaxies will be required to more convincingly support this.

The full KBSS-InCLOSE sample will provide significantly improved statistics on the bulk properties of the inner CGM surrounding galaxies at $z \sim 2$, including the frequency of high-N(HI) absorption such as that seen in N1 and G1, herein.

3.8 Summary and Conclusions

We have presented the design and first results from the new KBSS-InCLOSE survey which focuses on the Inner CGM of QSO Line Of Sight Emitting (InCLOSE) galaxies at z ~2-3. KBSS-InCLOSE allows us to connect galaxy properties (e.g., stellar mass, interstellar medium ISM metallicity) with the physical conditions (e.g., kinematics, metallicity) of the inner circumgalactic medium to directly observe the galaxy-scale baryon cycle of $z \sim 2-3$ star-forming galaxies.

In this paper we focused on two QSO fields, Q2343+1232 and Q2233+1310, for which we have added extended optical IFU coverage with deep KCWI pointings. We leveraged the fact that these fields have $z \sim 2-3$ star-forming galaxies near the QSO line of sight (nLOS galaxies), Q2343-G1 (G1, z=2.4312; a typical $z \sim 2$ star-forming galaxy) and Q2233-N1 (N1, z=3.1509; a lower mass LBG with strong, extended nebular emission that makes it analagous to $z \sim 2$ EELGs), to develop observation strategies, QSO subtraction techniques, and coupled ISM-CGM analyses that will be applied to the remaining KBSS-InCLOSE fields.

We summarize our main findings below:

1. KCWI is an efficient and effective instrument for finding new nLOS galaxies. We discovered more than 15 new galaxies across the two QSO fields. The QSO subtraction techniques that we develop, use, and repurpose were key to this discovery process since the QSO point spread function (PSF) dominates emission in the wings, where new galaxies are likely to be found.

2. For the first time at this z, we explicitly compare the gas-phase N/O (vs O/H) in the CGM and ISM finding that *G1's* CGM is metal-poor and less chemically evolved than its ISM, suggesting that it was enriched by a previous starburst, perhaps when its ISM was in the low metallicity regime.

   N1's CGM has a comparable metallicity to its ISM ($\Delta[O/H]_{CGM-ISM}$ ~0) which may be a result of stripped ISM gas from a previous interaction with one of its satellite, or simultaneous enrichment from one or more of its satellite galaxies.

3. The inferred CGM line of sight dust extinction is an an order of magnitude less than the ISM for both galaxies, suggesting there is little dust in their CGM.

4. G1's CGM appears to have unbound, metal-rich, hot gas that may be the product of undiluted CCSNe ejecta driven by an energetic galactic outflow between $\sim 20 - 100$ Myr ago

5. Both galaxies' CGM absorption (HIRES) revealed: a high incidence of metal absorption showing detections of e.g., C, N, O, Al, Si, S, Fe, etc.; multiphase gas is common from neutral to quintuply ionized transitions with similar kinematic structure; kinematicatically complex absorbers, requiring at least 10 components (and up to 31 components!) to fit most metal transitions and spread out to ~ -800 $km\ s^{-1}$; there are low to moderate levels of dust depletion (δ_d = 0.6 dex for G1; δ_d = 0.05 dex for N1) ratios; and *G1* has a puzzling abundance pattern (chemically evolved by some ratios [α/Fe]~0 but chemically young in some ratios [N/Fe]~-0.8) that may deviate significantly from solar, and *N1* has an abundance pattern typical of chemically young absorbers.

6. Lyα surface brightness and velocity maps (KCWI) revealed that *G1* has a single-peaked Lyα profile (v_{red} = +271 km s^{-1}), an extended Lyα halo (28

kpc), and has two Lyα satellite galaxies in proximity to it. *N1* has a double-peaked Lyα profile ($v_b \sim -420$ km s^{-1}, $v_r \sim 171$ km s^{-1}), strong Lyα emission ($EW_{\mathrm{Ly}\alpha} \sim -40$), a very extended Lyα halo (s ~100 kpc), and has Lyα emitting satellite galaxies near it

7. Rest-optical spectra (MOSFIRE) and SED modeling of the galaxies revealed that *G1* is a typical $z = 2 - 3$ star-forming galaxy in terms of its stellar mass ($\log M_*/M_{\odot G1} = 9.9 \pm 0.1$,), star formation rate (SFR=6-15 M$_\odot$), dust extinction ($A_V = 0.21$), ionization parameter ($\log U \sim -2.7$), and Lyα escape fraction ($f_{\mathrm{esc,Ly}\alpha,G1} = 6\%$). *N1* is a lower mass ($\log M_*/M_{\odot G1} = 8.7 - 9.2 \pm 0.1$,), young ($t_*$=30-50 Myr), relatively low dust ($A_V \sim 0.1$) star-forming galaxy with strong nebular emission (Lyα [O III]), complex and extended Lyα halo morphology ($s \sim 100$ kpc), and high Lyα escape fraction ($f_{\mathrm{esc,Ly}\alpha,N1} = 30\%$) putting in the tail end of the $z \sim 3$ LBG population, and reminiscent of $z \sim 2$ EELGs.

The diversity of the two galaxies' CGM-ISM properties highlights the need to build a large sample of nLOS galaxy-QSO pairs to place global observational constraints on the $z \sim 2-3$ CGM. The complete KBSS-InCLOSE sample will accomplish this by analyzing e.g., the abundance of unbound gas, how CGM measurables vary as a function of galaxy property (e.g., M_*, SFR), metallicity distribution as a function of ion and impact parameter, the fraction of thermally vs. non-thermally supported gas a function of galaxy properties, further constrain the gas and metal mass of the CGM, etc.

Fundamentally, these first results show that the observational strategies, QSO subtraction techniques, and analyses that we have adopted/developed for KBSS-InCLOSE are well suited to expand our understanding of the $z \sim 2 - 3$ baryon cycle.

Acknowledgements

We thank Sebastiano Cantalupo for assistance, guidance, and troubleshooting with CubExtractor. We thank Holly Christenson and Regina Jorgenson for providing insights and sharing data of Q2233-N1. We thank Hsiao-Wen Chen, Sean Johnson, and Mandy Chen for useful discussions regarding datacube QSO subtraction.

This material is based upon work supported by the National Science Foundation Graduate Research Fellowship under Grant No. 2019286522. CCS has been supported, in part, by NSF grant AST-2009278 and by the Caltech/JPL President's and Director's program. E.N.K. acknowledges support from NSF CAREER grant AST-2233781. Z.Z. acknowledges the financial support from NASA FINESST grant 80NSSC22K1755. D.K.E. is supported by the NSF through Astronomy & Astrophysics grant AST1909198. RJC is funded by a Royal Society University Research Fellowship, and acknowledges support from STFC (ST/T000244/1, ST/X001075/1).

The authors wish to recognize and acknowledge the very significant cultural role and reverence that the summit of Maunakea has always had within the Native Hawaiian community. We are most fortunate to have the opportunity to conduct observations from this mountain.

This research has made use of the Keck Observatory Archive (KOA), which is operated by the W.M. Keck Observatory and the NASA Exoplanet Science Institute (NExScI), under contract with the National Aeronautics and Space Administration.

Some of the data presented in this work were obtained from the Keck Observatory Database of Ionized Absorbers toward QSOs (KODIAQ), which was funded through NASA ADAP grant NNX10AE84G.

Keck:II (KCWI) Keck:I (MOSFIRE) Keck:I (LRIS)

NUMPY (Harris et al., 2020), MATPLOTLIB (Hunter, 2007), Astropy (Astropy Collaboration et al., 2018, 2013), DS9 (Smithsonian Astrophysical Observatory, 2000), IMEXAM (Sosey et al., 2022), PHOTUTILS (Bradley et al., 2022), VoigtFit (Krogager et al., 2017), ALIS (Cooke et al., 2014), MOSPEC (Strom et al., 2017), CubExtractor (Cantalupo et al., 2019).

Appendix A: Impact of Quasar Spectral Cube Subtraction on the Individual Galaxy Spectra

In the section we wanted to show effects on the QSO subtraction from the KCWI cube using IFSFIT discussed in Section 3.3.

We wanted to ensure that the continuum and spectral lines detected in the extracted galaxy spectra from the QSO-spectrall subtracted cubes were not strongly dependent on the sampling of the input QSO spectrum to IFSFIT. To test this, we varied the radius of the circular aperture used to extract the QSO spectrum, then ran it through IFSFIT, and then extracted the spectra of G1 and N1.

We can see from both the plots in Figure 3.15 that the radius of the extraction aperture does not affect absorption line strength or centroid, emission line strength or centroid, or continuum shape. Even the smallest aperture size is sufficient to recover the main galaxy spectral features. Adding more pixels just removes flux from the galaxy continuum at the 5-10% level depending on the portion of the spectrum.

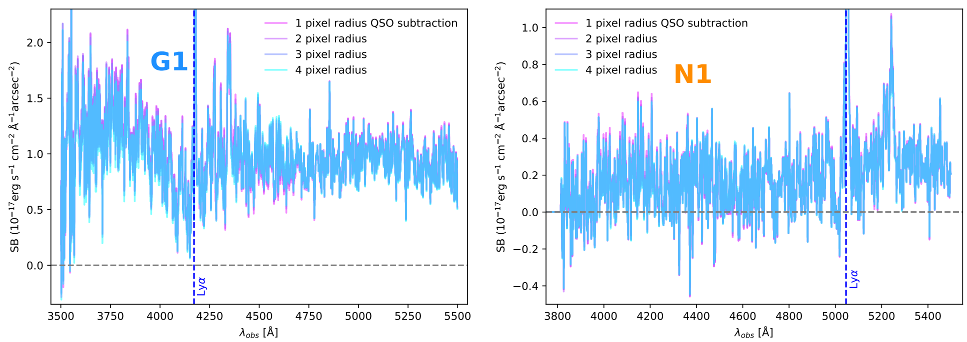

Figure 3.15: Extracted rest-FUV Keck/KCWI spectra as a function of extraction aperture size (used in the QSO subtraction input). Lyα emission peak is marked as a blue dashed line in each spectrum. *Left:* Sum of spaxels that contain galaxy G1. The blue end of the spectrum shows the largest difference (in flux) between the apertures size but are still $\lesssim$ 10% of one another while the shape stays identical. *Right:* Sum of spaxels that contain galaxy N1. Similar behavior is seen except the percent differences between the aperture sizes are $\lesssim$ 5%.

In Figure 3.16 we show the effects of steps 3 and 4 from the KCWI cube spectral subtraction (i.e., QSO Lyα halo subtraction; Section 3.3) on the extracted spectra of galaxies Q2343-G1 and Q2233-N1. The red spectrum show the results from the QSO continuum subtraction (steps 1 and 2), while the black lines show the results from the QSO continuum+halo subtraction (Steps 3 and 4). In both galaxies the QSO Lyα peak is reduced by more than 50% while the rest of the spectrum is unaffected.

Appendix B: Complete Voigt Profile Fitting Results

In Figures 3.17-3.20 we show the all of the best-fit Voigt profiles to G1s CGM absorption.

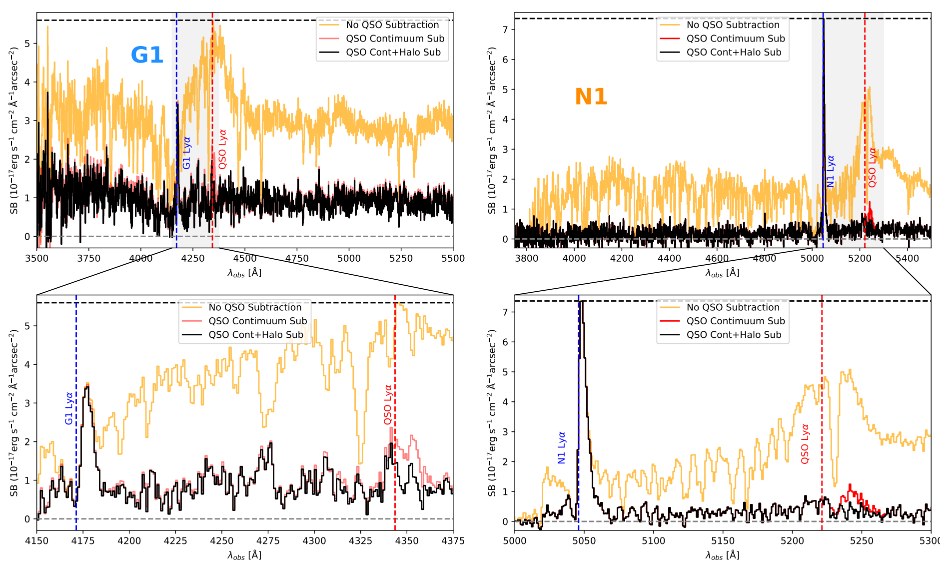

Figure 3.16: Extracted rest-FUV KCWI spectra during all stages of QSO subtraction for G1 (left two panels) and N1 (right two panels). *Top panels:* Orange shows the spectrum without subtraction, red shows the first subtraction (i.e., QSO continuum subtraction), and black shows the second/final subtraction (removal of QSO Lyα halo+QSO continuum removal). *Bottom panels:* Zoom-in showing the QSO Lyα halo removal.

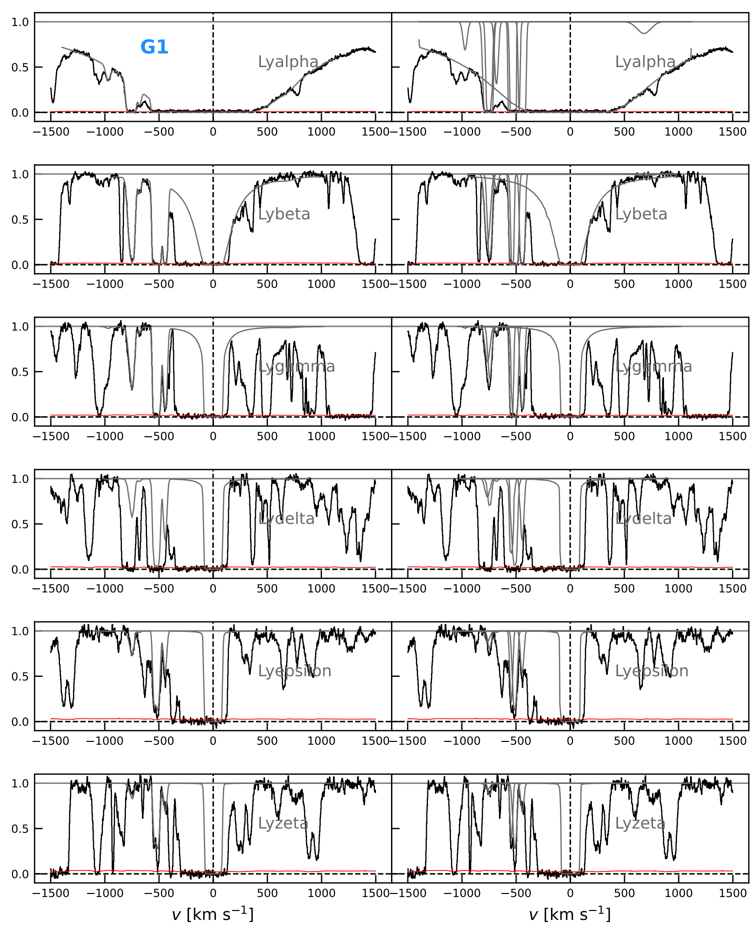

Figure 3.17: G1's H I CGM absorption fits from R12 centered at z_{G1}=2.4312. The lines and colors are the same as Figure 3.8.

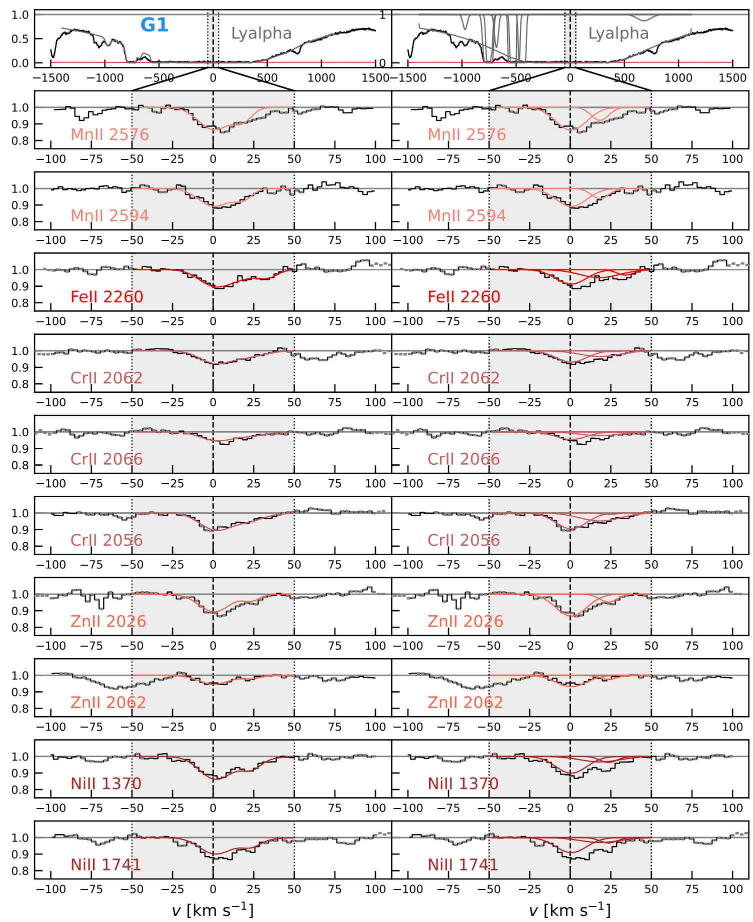

Figure 3.18: G1's Fe-peak element CGM absorption and best-fit Voigt profiles centered at z_{G1}=2.4312. The lines and colors are the same as Figure 3.8.

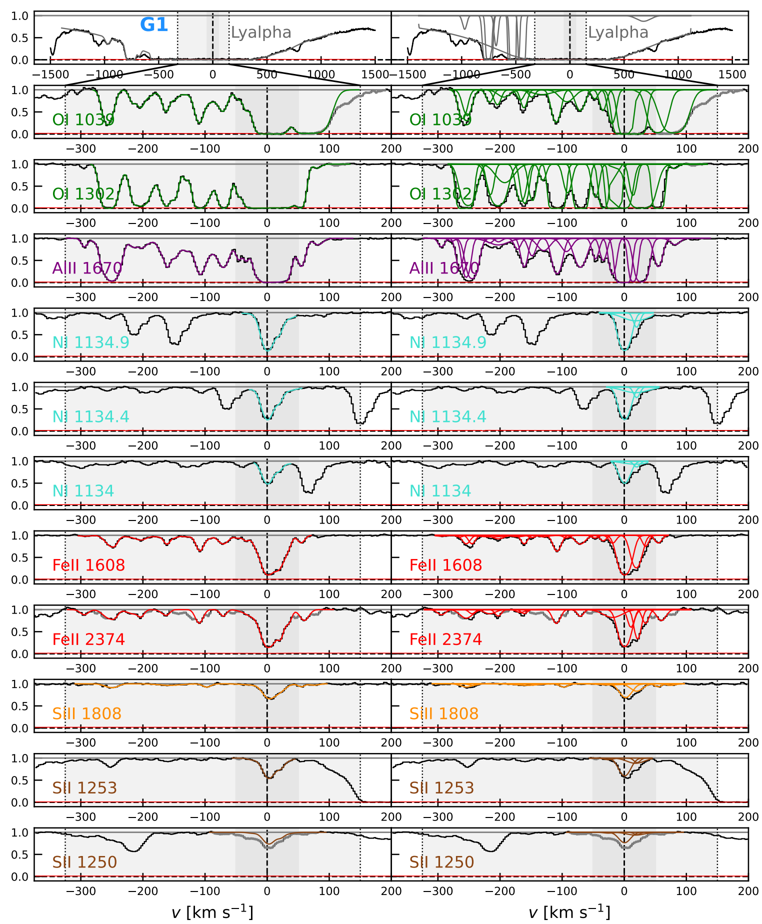

Figure 3.19: G1's neutral- and low-ionization metal CGM absorption and best-fit Voigt profiles centered at z_{G1}=2.4312. The lines and colors are the same as Figure 3.8.

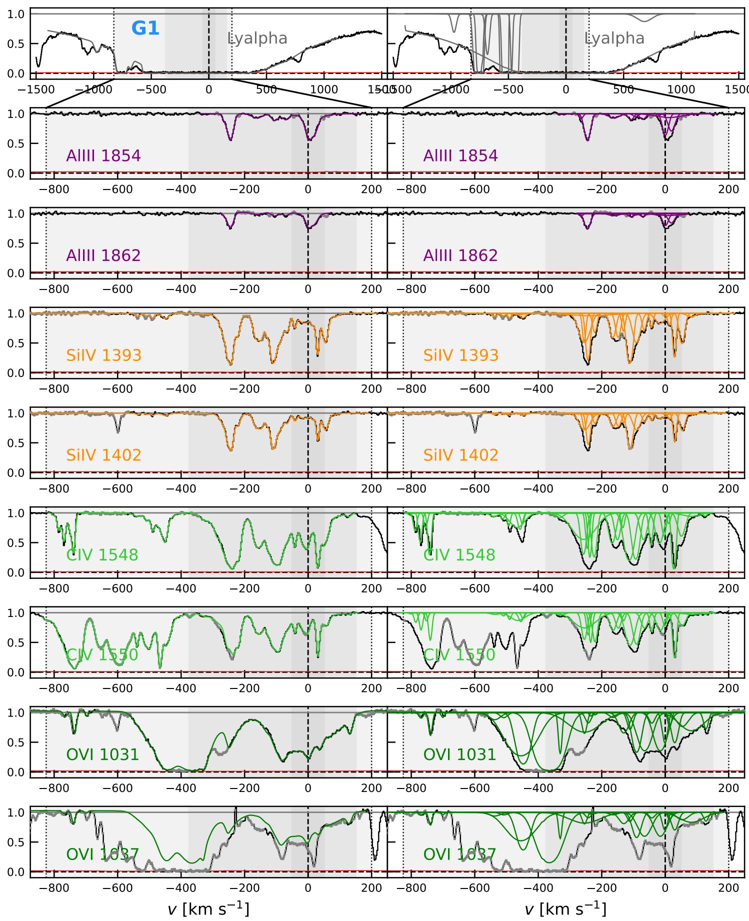

Figure 3.20: G1's intermediate- and high-ionization metal CGM absorption and best-fit Voigt profiles centered at its systemic redshift z_{G1}=2.4312. The lines and colors are the same as Figure 3.8.

Chapter 4

KBSS-INCLOSE II: THE CGM OF THREE LOW-MASS GALAXIES TOWARDS Q1623

4.1 Abstract

We present the second set of results of an extension to the Keck Baryonic Structure Survey (KBSS) that focuses on the Inner CGM of QSO Line Of Sight galaxies at $z \sim 2$ (InCLOSE). KBSS-InCLOSE II showcases three low-mass galaxies ($M_* < 10^{8.5}$ M$_\odot$), two galaxies are detected as Lyman Alpha Emitters (LAEs) seen in Keck/KCWI pointings, and one galaxy is detected as a serendipitous line emitter in a Keck/MOSFIRE spectrum. Each galaxy is within a projected distance of $b < 75$ kpc of a luminous QSO, and each QSO is separated by ~ 1.3 Mpc. FUV redshifts from Lyα and nebular redshifts from [O III] show that the galaxies are at the same redshift $z_{\rm sys} = 2.24$. SED fitting and analysis of *HST* images corroborate that the galaxies are low-mass based on their best-fit stellar masses ($\log \mathrm{M}_*/\mathrm{M}_\odot \leq 8.4$) and small projected sizes ($r_{1/2\ \rm light} < 0.89$ kpc), which are both consistent with measurements of local dwarf galaxies. Analysis of their CGM absorption as seen in Keck/HIRES QSO spectra shows a lack of low-ionization metal absorption, ubiquitous detections of intermediate- (e.g., C IV, Si IV) and high-ionization (O VI) metal absorption, kinematically complex absorption typically spread over ~ 500 km s^{-1}, temperatures that are consistent with photoionization $\log T_{\rm med} \sim 10^{4.03}$ K, and moderate detections of unbound gas. This work hints that the z$\sim$ 2 CGM may evolve strongly with z in terms of kinematic complexity and absorption strength, and with stellar mass in terms of abundance of low-ionization gas and fraction of unbound gas. Future KBSS-InCLOSE papers will investigate these preliminary findings by leveraging the growing sample.

4.2 Introduction

Low-mass ($M_* < 10^9$ M$_\odot$) galaxies are much more numerous than their more massive $M_* = 10^{10}$ M$_\odot$ galaxies (Reddy, Steidel, 2009) and likely play an important role in ionizing and enriching the CGM/IGM (Romano et al., 2023; Wetzel et al., 2015). However, it is difficult to observe these galaxies due to their intrinsic faintness. Specifically, the R band magnitude for a typical $z \sim 2$ star-forming galaxy is $R \sim 24$ (Steidel et al., 2004), while for low-mass Lyman Alpha Emitters (LAEs)

$R \sim 27$ (Trainor et al., 2015).

In the past, efficiently finding high-z low mass galaxies required deep narrowband (NB) images coupled with deep optical and/or NIR spectroscopy. The main limitation of this approach is its observational expense and the narrow redshift range to which it is restricted, i.e., the central wavelength chosen for the NB filter. Trainor et al. (2015) analyzed a sample of more than 300 faint $z \sim 2.7$ ($z_{\rm avg}$ for KBSS QSOs) LAEs in this manner. They found that compared to more massive $z \sim 3$ Lyman Break Galaxies (LBGs), the faint LAEs have significantly higher Lyα escape fractions ($f_{\rm esc} \sim 30\%$), significantly reduced low-ionization metal covering fraction, smaller outflow velocities ($v_{\rm FUV,avg} < 500$ km s^{-1}) that are (likely) larger than their escape velocity ($v_{\rm esc} \sim 200$ km s^{-1}) tracing hot, metal-rich outflows. Additionally, $z \sim 2-3$ faint LAEs are typically characterized by low stellar masses ($M < 10^{9.0}$ M$_\odot$), low dust content ($A_V < 0.1$), and extended Lyα halos ($s > 60$ kpc) (Oyarzún et al., 2017; Steidel et al., 2011; Trainor, Steidel, 2012).

Due to the difficulty of detection, we have few constraints on the physical properties of the circumgalactic medium (CGM; column density, ionization state, kinematics, and temperature) of low-mass galaxies at $z \gtrsim 2$. But at low-z it has been found that the $z \sim 0.3$ sub-$L*$ inner CGM systematically shows a lack of low-ionization gas (e.g., C II), but often shows intermediate-ionization (e.g., CIV), and almost always shows high-ionization (e..g, O VI) gas coupled with low HI column densities ($\log N_{\rm HI} \sim 10^{14}$ cm^{-2}; Dutta et al. 2020, 2025; Johnson et al. 2017; Mishra et al. 2024; Qu et al. 2022; Zheng et al. 2024). Interestingly, at $z \sim 3$ the CGM of faint LAEs also shows a lack of low-ionization gas, but exhibits intermediate-ionization gas coupled with low HI column density (Galbiati et al., 2023; Muzahid et al., 2020).

Targeting LAEs near bright QSOs is an efficient means of detecting low-mass galaxies with the benefit of probing their CGM via spectroscopy of the background QSO. The KBSS-InCLOSE survey is an extension of the Keck Baryonic Structure Survey (KBSS) that focuses on the Inner CGM of QSO Line of Sight Emitting (InCLOSE) galaxies at $z \sim 2$ that is discussed in detail by Nuñez et al. (KBSS-InCLOSE I hereafter 2024). Keck/KCWI is the driving instrument for the survey and is uniquely equipped to detect $z \sim 2$ faint LAEs due to its blue sensitivity.

In this chapter, we focus on the CGM of three low-mass star-forming galaxies discovered in deep KCWI IFU datacubes towards KBSS field Q1623. These galaxies represent the first low-mass galaxies analyzed in the KBSS-InCLOSE sample and serve as an important stepping stone for the rest of the sample. The Q1623 field includes three bright QSOs KP77 (z = 2.5353), KP76 (z = 2.2448), and KP78 (z = 2.2436) each within 2.8′ of one another, and each of the three galaxies is within a projected distance of $b < 75$ kpc $\sim 1.25\ R_{\rm vir}$ of one of the QSOs.

This chapter is structured as follows. In Section 4.3 we summarize the new observations, data reduction, data processing, and the identification of new objects. In Section 4.4 we analyze the galaxy properties in terms of their nebular emission, morphology, and stellar populations. In Section 4.5 we analyze the CGM absorption of each galaxy in terms of column density, Doppler width, and (for the first time for KBSS-InCLOSE) turbulent velocity and kinematic temperature. In Section 4.6 we discuss insights into the CGM of $z \sim 2$ low-mass galaxies gleaned from explicitly connecting the ISM properties to the CGM properties of each galaxy. Section 4.7 summarizes our findings.

4.3 KCWI as a Discovery Machine for Low Mass Galaxies

The data presented in this paper are part of the KBSS-InCLOSE survey. In summary, we use new Keck/KCWI and Keck/MOSFIRE observations to identity and confirm star-forming galaxies with $z = 1.9 - 2.6$ with impact parameters to one of the KBSS QSO sightlines of $b < R_{\rm vir} \sim 80 - 90$ kpc (Trainor, Steidel, 2012). We then use existing KBSS ground- and space-based images from Keck/LRIS, Keck/MOSFIRE, and *HST*/WFC3 to model their stellar populations, and KBSS Keck/HIRES QSO spectra to analyze the CGM absorption associated with the the newly identified galaxies along the sightlines.

Keck/KCWI is the driving instrument for KBSS-InCLOSE because of its efficiency in identifying galaxies projected very close to the LOS toward KBSS hyper-luminous QSOs. KCWI is particularly well-suited for finding low-mass LAEs due to its blue sensitivity ($\geq$ 3500 Å) that allows for the detection of Lyα emission down to $z_{{\rm Ly}\alpha} \geq 1.89$, which is unique among the other IFUs on 10-m class telescopes.

We used Keck/KCWI to acquire rest-FUV data cubes with each QSO centered in the field. We observed Q1623-KP77 on the nights of 2021 July 6, 2021 September 5, and 2024 September 2 for a total integration time of 2.36 hr. KP76 was observed on the nights of 2022 May 28, 2022 May 29, and 2024 September 04 for a total integration time of 1.20 hr. KP78 was observed on the nights of 2022 May 28 and 2024 September 04 for a total integration time of 1.36 hours. Conditions were good on all nights. Our primary configuration used the Medium slicer and BL grating to optimize spatial resolution, spectral resolution, and field of view (FoV). The medium

Table 4.1: Observations Summary

Type	Instrument	Object	RA	Dec	t_{exp}	Date	PI	P/ID
-	(Config.)	-	(J2000.0)	(J2000.0)	(hr)	(YYYY/MM/DD)	-	-
Optical IFU	KCWI							
	Med/BL	Q1623	16:25:48.83	+26:46:58.80	5.96	2021/07/06	Steidel	C300
						2021/09/05	Steidel	C249
						2024/09/02	Steidel	C355
	Med/BL	Q1623-KP76	16:25:48.11	+26:44:32.96	1.20	2022/05/28,29	Steidel	C263
						2024/09/02,04	Steidel	C355
	Med/BL	Q1623-KP78	16:25:57.40	+26:44:48.50	1.36	2024/09/02,04	Steidel	C355
NIR Spectra	MOSFIRE							
	H,K	HU1	16:25:48.65	+26:46:55.77	3.5,2.4^{a}	2022/08/17	Steidel	C205
	H					2023/09/18	Steidel	C409
	H					2024/03/30	Steidel	C381
	H					2024/04/25		
	H,K					2024/05/25		
	H,K	BX426b	16:25:47.92	+26:44:27.45	2.7,1.0^{a}	2022/08/17	Steidel	C205
	H	BX426b	16:25:47.92	+26:44:27.45		2023/09/18	Steidel	C409
Optical Images	LRIS							
	Un,G,R$_S$	Q1623	16:25:53.95	+26:46:26.70	3.5,2.4^{b}	2022/08/24	Steidel	C205

a) H, K$_S$ band exposure time.
b) Un, G, R$_S$ band exposure time.

slicer has a FoV of 16.5” × 20.3” or ~ 135 × 166 physical kpc (pkpc) at z~2.3 per pointing. The BL grating is the bluest grating with the widest spectral range 3500-5500 Å but lowest spectral resolution of R~1800 (2.5 Å or 166 km s^{-1}resolution, sampled at 1 Å).

For Q1623-KP77, we combined our data with the KBSS-KCWI data set (Chen et al., 2021) which had a total exposure time of 3.6 hours centered at a position 7.5” S of the QSO such that the QSO falls on the N (top) of the the final mosaic. In the region of full overlap between the two observations the total exposure time is 1.38 hours, while the region south of the QSO is much deeper, with total exposure time of 5.96 hours.

We reduced and stacked the KCWI data using the procedures described by Nuñez et al. (2024). In summary, data were reduced using a custom version of the publicly available KCWI DRP[1], after which each reduced cube was combined into a final mosaic using the custom post-DRP pipeline KCWIKit[2] (Prusinski, Chen 2024; implementation described by Chen et al. 2021). The final cubes have a spatial sampling of $0.3'' \times 0.3''$ and spectral sampling of 1 Å/pixel.

The reduced cubes have bright emission from the QSOs that must be removed in order to detect galaxies with small projected distances of $b \lesssim 3-5''$ or $b \lesssim 40$ kpc at $z \sim 2.3$. This “contaminant” emission affects the datacubes, spectra, and images.

[1] https://github.com/Keck-DataReductionPipelines/KCWI_DRP
[2] https://github.com/yuguangchen1/KcwiKit.git

Our procedure for QSO removal for each data type are explained in detail by Nuñez et al. (2024), but we summarize the main points here.

For the IFU data we have two methods of QSO subtraction. One method uses the CubePSFSub routine within the package CubExtractor (Cantalupo et al., 2019) that removes QSO emission by empirically constructing a pseudo-narrowband point spread function (PSF) of a specified mean filter of 250–400 Å, centered on each wavelength pixel that is then removed, i.e., a running mean filter. To reduce oversubtraction we mask wavelength layers with expected narrow line emission e.g., Lyα. We then used CubeBKGSub, a package in CubExtractor, to remove all continuum sources. We refer to these cubes as "QSO+continuum subtracted" and use them to search for and extract Lyα emitters.

The second method uses a spectral approach to subtract the QSOs using a modified version of IFSFIT (Rupke, 2014; Rupke et al., 2017). The program assumes that each spaxel can be modeled as a linear combination of the QSO spectrum and some additional light, e.g., a foreground galaxy. Our implementation of the program has four steps: 1) QSO continuum extraction (from the datacube), 2) QSO subtraction, 3) QSO Lyα Halo extraction (from the datacube), and 4) QSO Lyα Halo subtraction. We refer to these cube as "QSO-spectrally subtracted" and use them to recover continuum emitting galaxies, measure their emission/absorption line properties, and corroborate the LAEs found in the QSO+Continuum subtracted cubes.

We describe in detail how we remove QSOs from the ground-/space-based images in Nuñez et al. (2024). In summary, we construct an effective point spread function (ePSF Anderson, 2016; Anderson, King, 2000) using non-saturated field stars of comparable brightness to the QSO with the EPSFBUILDER in the PHOTUTILS software package (Bradley et al., 2022). This is done for each imaging band with all ePSF parameters set to 1.

We measure the photometry of each galaxy using PHOTUTILS with one circular aperture for the source and two background apertures for sky subtraction. For the galaxies at small impact parameters we adopt a photometric error of 0.2 magnitudes.

Keck/MOSFIRE and Keck/LRIS

All NIR spectra used in this work were obtained using Keck/MOSFIRE (McLean et al., 2012). Observations were conducted using MOSFIRE's configurable slit unit (CSU) to form multi-slit masks using the same approach described in previous KBSS work (Nuñez et al., 2024; Steidel et al., 2014; Strom et al., 2018, 2017). The integration times and program IDs are summarized in Table 4.1; each object has a minimum integration time of $\sim$ 1 hour.

Galaxy Q1623-HU1 (HU1 hereafter) and Q1623-BX426b (BX426b hereafter) were included as part of a multi-slit mask that also targeted a number of other galaxies of interest in the Q1623 KBSS field. The observations were obtained using slightly different CSU mask configurations in the H and K bands to center the several emission "knots" associated with HU1 (see Section 4.4). The sky position angle of the instrument FOV was chosen so that HU1's and BX426b's 0.7" $\times$ 15.0" slits would also include other KBSS galaxies. Total integration times of 3.5, and 1.0 hours were obtained in H and K bands, respectively, over the course of the nights of 2022 September 14-16, under variable seeing conditions (0.5"-0.8" FWHM).

The data were reduced using the publicly-available MOSFIRE DRP[3], which produces background-subtracted, flat-fielded, wavelength-calibrated, telluric-absorption corrected, heliocentric-velocity shifted, rectified, and stacked 2D spectrograms for each slit on the CSU mask. We refer the reader to Steidel et al. (2014) for more details on the data acquisition and reduction, and to Strom et al. (2017) for details on the flux calibration and slit loss corrections.

As described by Nuñez et al. (2024), we use MOSPEC (Strom et al., 2017)[4] for all post-processing of the spectra including extracting 1D spectra from the 2D spectrograms. For each galaxy, their spatial profile was modeled as a boxcar which was used to extract the 1D spectrum for each band. Slit loss corrections were determined separately for the H and K band spectra using a method described by Strom et al. (2017), which combines information from the spectrum of the calibration star included on the slitmask with comparison to independent measurements (on other KBSS masks) of emission line fluxes of objects that were also observed on the CSU mask. The galaxies projected sizes are smaller than the 0.7" slits and had small slit loss corrections.

KBSS Images, SED Fitting, and HIRES Spectra

We use extant KBSS ground-based images from Keck/LRIS, P200/WIRC, Magellan/Fourstar, and space-based images from *HST*/WFC3, to construct spectral energy distributions (SED) of the galaxies. New ground-based UV and optical images (U_nGR; see, e.g., Steidel et al. 2003) were obtained on 2022 Au-

[3]https://keck-datareductionpipelines.github.io/MosfireDRP/https://keck-datareductionpipelines.github.io/MosfireDRP/

[4]https://github.com/allisonstrom/mospechttps://github.com/allisonstrom/mospec

gust 28, from *Keck*/LRIS (Oke et al., 1995; Steidel et al., 2004). Table 4.1 shows integration times and dates. Ground-based H images (published by Steidel et al., 2014; Strom et al., 2017) were taken using Magellan/FourStar (Persson et al., 2013). Ground-based JK_S images were taken using P200/WIRC (Steidel et al., 2004; Wilson et al., 2003). Finally, space-based NIR images were taken with *HST*/WFC3-IR F140W (Erb PID#12471 2012March17) and *HST*/WFC3-IR F160W (Law PID#11694 2010August06). Archival, reduced, and science-ready *HST* images were pulled from the Hubble Legacy Archive (HLA Lindsay et al., 2010). Q1623-KP77 had coverage in *HST*/WFPC2 F450W (Beckwith PID#8085 1999May16), *HST*/WFPC2 F702W (Steidel PID#6557 1997May30), *HST*/WFPC2 F702W (Beckwith PID#6557 1999May16); only HU1 was captured in these images because the other QSOs, KP76 and KP78, were outside the field of view of pointings.

We use high-resolution spectra of the QSOs from Keck/HIRES (Vogt et al., 1994) to probe CGM absorption associated with the galaxies. Q1623-KP77, Q1623-KP76, and Q1623-KP78 were observed as part of the original KBSS program (Rudie et al., 2012; Steidel et al., 2014; Turner et al., 2014). We refer readers to Rudie et al. (2012) for details on the observations, reduction, continuum normalization, and coaddition of the spectra, which include data obtained from both HIRES and VLT/UVES on UT2 (Dekker et al., 2000). The final spectra have $R \simeq 45,000$ (FWHM = 6.7 km s^{-1}), an average $S/N \sim 28 - 48$ per resolution element, and spectral range $\lambda \sim 3126 - 10,090$ Å (Rudie et al., 2012).

The HIRES spectra of the QSOs contain CGM absorption of the galaxies which we analyze by performing Voigt-Profile decomposition using the same procedures described by Nuñez et al. (2024). In summary, the HIRES spectra are of high enough quality that we perform the fitting by hand by making initial guesses with VoigtFit (Krogager, 2018), then performing the final fit using ALIS (Cooke et al., 2014) by adding a minimum number of absorption components, fitting, adding components where residuals of $\gtrsim 3\sigma$ are present, then iterating until we achieve a reduced $\chi^2 \sim 1$.

The H I fitting for HU1 was performed by Rudie et al. (2012, hereafter R12) as part of their catalog of more than 6,000 Lyα absorbers towards all 15 KBSS QSOs. We adopt their best-fit H I column densities, Doppler widths, and redshift. For BX426b and CS13, their H I fitting was performed manually in the same way described earlier because KP76 and KP78 were not included in R12's H I absorber analysis.

We use the same SED fitting routine described by Nuñez et al. (2024). In summary, the custom SED fitting routine (Reddy et al., 2012; Theios et al., 2019) uses pre-computed grids of SED models (Binary Population and Spectral Synthesis models version 2.2, Stanway, Eldridge 2018, hereafter BPASS) with a Kroupa initial mass function (IMF, Kroupa, 2001), an upper IMF mass of 100 $M_{\odot}$, low stellar metallicity Z_{*}=0.002 ($Z_{*}/Z_{\odot} \sim 0.14$) an SMC-like extinction curve, a constant SFH, and a restriction that leaves the age of the stellar population as a free parameter or restricts it to $t_{\rm age} > 50$ Myr.

New Galaxies Towards Q1623

Figure 4.1 shows the Q1623 field and highlights the QSOs (black circles), the three galaxies analyzed in this paper (blue circles), galaxies that will be discussed in future work (cyan circles), and new galaxies with $z < 1.9$, $z > z_{\rm QSO}$, or unknown z detected in the KCWI datacubes (purple circles).

The top left image of Figure 4.1 shows hyperluminous QSO Q1623 (KP77), and luninous QSOs KP76 and KP78. The QSOs are separated by $\sim$ 1.3 Mpc (at $z = 2.24$) and have similar enough redshifts that they have been used to study the transverse proximity effect (effect of radiation field of foreground QSOs to background QSO sightlines), which can give insights into the duty cycle of QSO lifetimes (Gonçalves et al., 2008).

The rightmost image shows galaxy HU1 at $b = 31$ kpc from Q1623. HU1 is a bright LAE that was discovered while visually inspecting the KCWI cube of Q1623-KP77. HU1 was bright enough that it was detected *without* the need for QSO subtraction. It is therefore interesting that the only objects that appear to be spatially coincident with the Lyα emission are a faint object that appears to be either a clumpy/irregular galaxy and three separate objects, which we will refer to as "knots." This unique morphology is discussed in more detail in Section 4.4. The yellow boxes show slits that were included on multiple MOSFIRE slit masks that were designed to ensure that each of the emission knots were included in the slit. Each slit had slightly different coordinates measured from 1) the centroid of the Lyα emission peak (blue contours in the image), 2) the centroid position between the three emission knots seen in the *HST*/F140W image, and 3) the centroid of the brightest emission knot. "Missing" a galaxy is typically not an issue because most KBSS galaxies have projected sizes larger than the slit width (Strom et al., 2018).

The bottom right image in Figure 4.1 shows galaxy BX426b which is at a projected

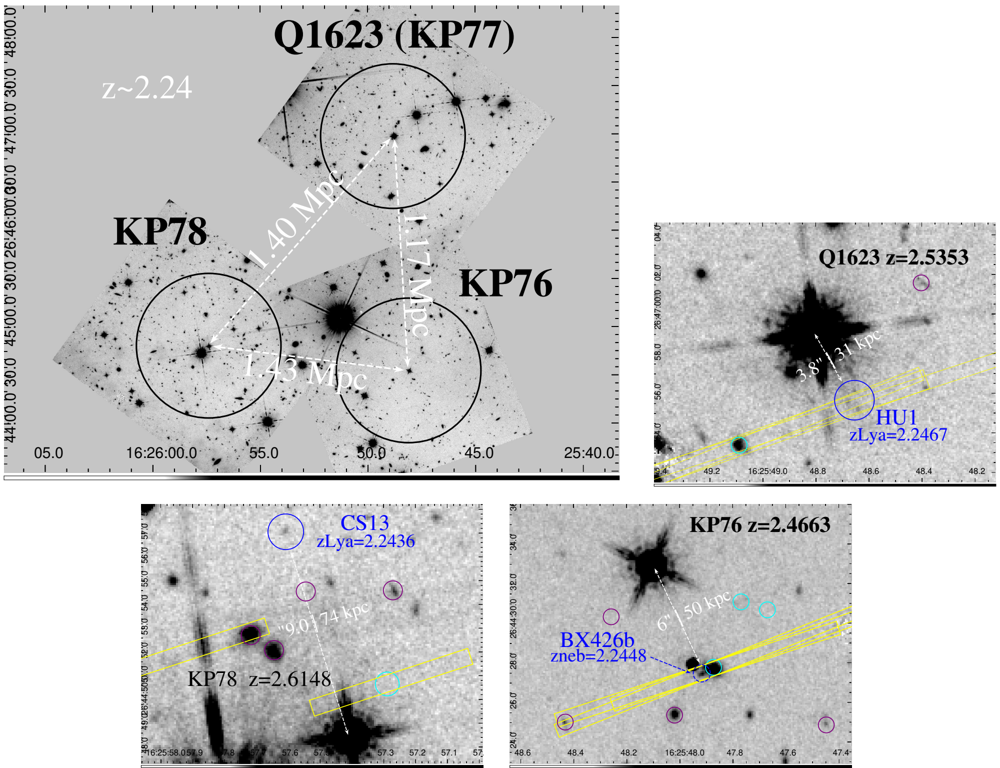

Figure 4.1: Summary of the three galaxies, three QSOs, and newly discovered objects in the Q1623-KP77 field as seen in *HST*-IR/WFC3 F160W images. *Top left:* Full view of the three QSOs and their transverse distances to one another (D_{Tran}) at $z = 2.24$. Their angular distances are $D(KP78 - KP77) \sim 170''$, $D(\mathrm{KP77} - \mathrm{KP76}) \sim 143''$, $D(\mathrm{KP76} - \mathrm{KP78}) \sim 173''$. The QSOs have an average projected distance from one another of $D_{\mathrm{Tran}} \sim 1.3$ Mpc. *Right:* Zoom-in to QSO Q1623-KP77 showing galaxy HU1 (blue circle) at a projected distance of $D_{\mathrm{Tran}} = 31$ kpc. Yellow boxes show slits from the multiple slit masks that included the the galaxy (see Section 4.3). *Bottom right:* Zoom-in to QSO KP76 showing galaxy BX426b (blue circle) at a projected distance of $D_{\mathrm{Tran}} = 50$ kpc. The galaxy shares the same slit as BX426 (cyan circle) which will be discussed in a future InCLOSE paper. *Bottom left:* Zoom-in to QSO KP78 showing galaxy CS13 (blue circle) at a projected distance of $D_{\mathrm{Tran}} = 74$ kpc. All three QSO sightlines exhibit at least one new galaxy added to KBSS-InCLOSE.

distance of $b \sim 50$ kpc from KP76. BX426b was discovered serendipitously while searching for rest-optical line emission from larger galaxy BX426 (which will be discussed in future work). These galaxies were not included in the original KBSS survey because contamination from a nearby foreground star significantly affected SEDs constructed from the KBSS ground-based images. BX426 was added to KBSS-InCLOSE after marginal Lyα absorption was detected in the blended continuum of the aforemention foreground star, BX426, and BX426b in new KCWI datacube. The yellow rectangles show the MOSFIRE slits that included both galaxies.

The bottom left image in Figure 4.1 shows galaxy CS13 which is at an projected distance of $b \sim 74$ kpc from KP78. CS13 was discovered in the new KCWI datacube via faint Lyα emission (SNR = 4.4σ). Another KBSS galaxy, BX511, is at a similar redshift as a strong C IV absorption system, but its large impact parameter ($b > 100$ kpc) made it unlikely that it was the sole galaxy responsible for the absorption. CS13 is about half the impact parameter of BX511 ($b_{\mathrm{BX511}} \sim 130$ kpc) making it a more likely host for the absorption system. CS13 will be included on a future MOSFIRE slit mask.

4.4 Ionized ISM and Stellar Population of the Galaxies

Nebular Emission

Rest-FUV spectra for each galaxy were extracted using a non-weighted approach from the QSO-free KCWI datacubes (see Nuñez et al. 2024). Only two of the galaxies have clear detections: HU1 and CS13. BX426b's small size and KCWI's spatial resolution make it near impossible to deblend the spaxels between the bright foreground star, and the larger galaxy BX426. Nonetheless, the two detections show clear Lyα emission at $z_{\mathrm{Ly}\alpha} = 2.24$.

Rest-optical 2D-spectrograms were obtained from MOSFIRE following the procedure described in Section 4.3. Only two of the galaxies, HU1 and BX426b, were included on a MOSFIRE slit. CS13 will be included on a future slit mask.

Figures 4.2, 4.3, and 4.4, show the rest-FUV and rest-optical spectra for galaxies HU1, BX426b, and CS13. The spectrum of each galaxy is typical of $z \sim 2$ star-forming galaxies in that it shows redshifted Lyα emission in the FUV, and/or [O III]λ5008 and Hα emission in the rest-optical.

The top panel of Figure 4.2 shows HU1's strong Lyα emission. It is the most luminous Lyα emitter in KBSS-InCLOSE thus far with $\log{(L_{\mathrm{Ly}\alpha}/\mathrm{erg\ s^{-1}})} = 41.94$

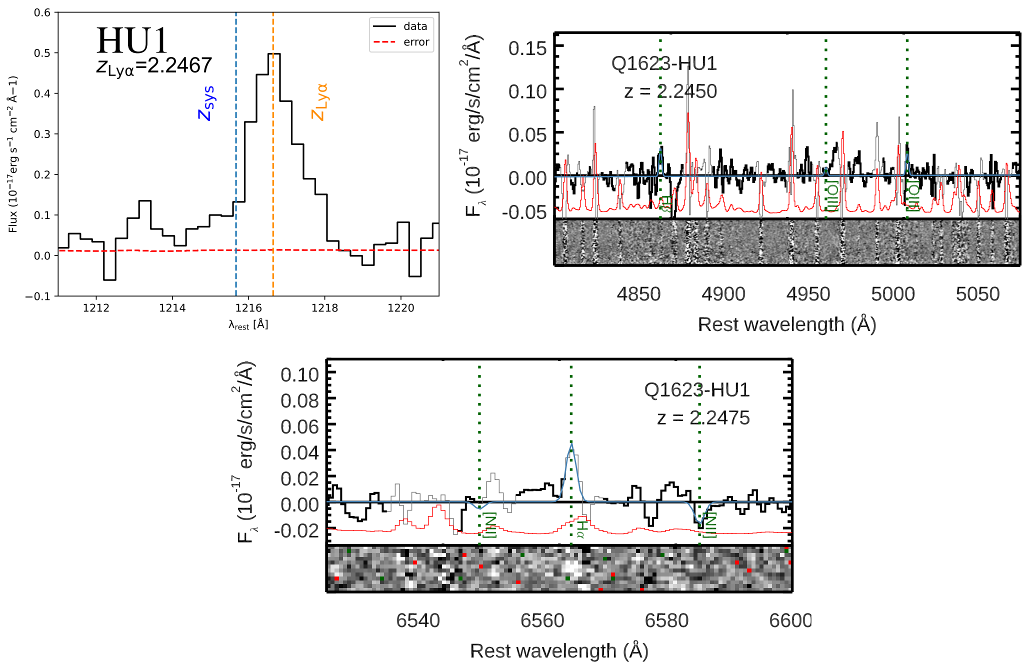

Figure 4.2: *Top left panel:* Extracted rest-frame FUV spectrum of Q1623-HU1 from KCWI after QSO subtraction. The dashed blue line shows the systemic redshift of HU1 while the orange line shows the Lyα redshift. *Top right panel:* H-band spectrum from MOSFIRE showing marginal detections of [O III] and Hβ. The top of the panel shows the extracted 1D spectrum (black), offset error spectrum (red), and modeled emission lines (green dashed). The bottom shows the 2D spectrogram. *Bottom panel:* K_s-band MOSFIRE spectrum showing a maginal detection of Hα emission at a slightly different redshift than [O III].

($F_{\mathrm{Ly}\alpha}$ = (23 ± 0.4) × 10^{-18} erg s^{-1} cm^{-2}). In stark contrast is its weak [O III] emission which is shown in the top right panel of Figure 4.2. We measure $F_{\mathrm{[O\ III]}}$ = (1.87 ± 0.56) × 10^{-18} erg s^{-1} cm^{-2}. This weak emission is not unexpected considering that its rest-optical counterpart in the *HST*/F160W image is faint m_{F160W} = 25.54 ± 0.1. Though weak, we are able to measure a nebular redshift for the galaxy $z_{\mathrm{[O\ III]}} = 2.2450$ which is $\Delta v = -160$ km s^{-1} from $z_{\mathrm{Ly}\alpha}$, consistent with Lyα of other LAEs (Trainor et al., 2015). There is a plausible detection of Hα at $z_{\mathrm{H}\alpha} = 2.2475$ with a flux $F_{\mathrm{H}\alpha} = (3.15\pm0.82)\times10^{-18}$ erg s^{-1} cm^{-2} which results in a velocity difference of $\Delta v = +74$ km s^{-1} from $z_{\mathrm{Ly}\alpha}$. The velocity difference between all of the redshifts are small; the largest velocity difference is between [O III] and Hα or $|\Delta z_{\mathrm{[O\ III]-H}\alpha}| = 231$ km s^{-1}. We decide to adopt $z_{\mathrm{sys}} = z_{\mathrm{neb}} = z_{\mathrm{[O\ III]}}$ because it is more consistent with the velocity range of the CGM absorption (see Section 4.5) and is more similar to the velocity offset between z_{neb} and $z_{\mathrm{Ly}\alpha}$ for bright $z \sim 2$ LAEs (Trainor et al., 2015). The Lyα to Hα ratio gives $F_{\mathrm{Ly}\alpha}/F_{\mathrm{H}\alpha} = 23.1/3.15 = 7.33$

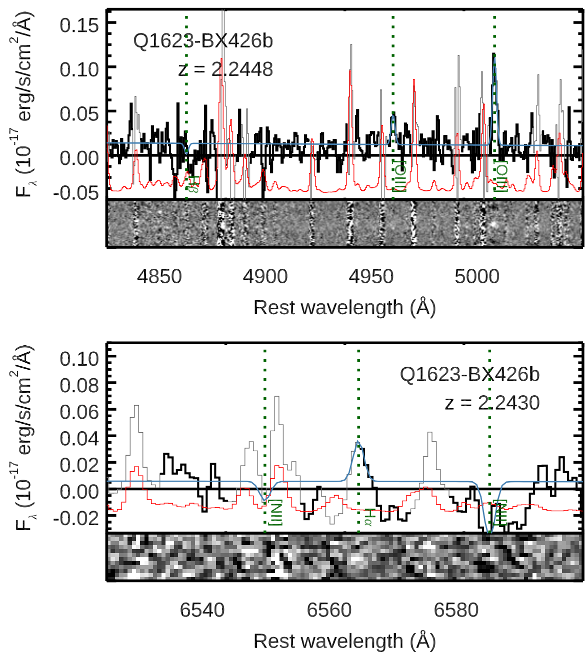

Figure 4.3: Rest-Optical spectra of BX426b from MOSFIRE. The same colors and symbols and panels as Figure 4.2. *Top panel:* H-band spectrum showing clear detections of [O III]$\lambda\lambda$4960, 5008 and Hβ. *Bottom panel:* K_s-band spectrum showing a marginal detection of Hα at a slightly different redshift than [O III].

which is close to Case B recombination ($I_{\mathrm{Ly}\alpha}/I_{\mathrm{H}\alpha}$ = 8.7 assuming $T \sim 10^4$ K and $n_e \sim 350$ cm^{-3}; Osterbrock 1989), leading to a high Lyα escape fraction $f_{\mathrm{esc,Ly}\alpha}$ = 0.84 that is consistent with bright, low-stellar mass LAEs analyzed by Erb et al. (2023).

The top and bottom panels of Figure 4.3 show the rest-optical spectrum of BX426b. There is a clear detection of the [O III]$\lambda\lambda$4960, 5008 doublet at $z_{[\mathrm{O\ III}]}$ = 2.2448 with a measured flux of $F_{[\mathrm{O\ III}]}$ = $(9.85 \pm 1.08) \times 10^{-18}$ erg s^{-1} cm^{-2}. There is a marginal detection of Hα at $z_{\mathrm{H}\alpha}$ = 2.2430 with a measured flux of $F_{\mathrm{H}\alpha}$ = $(2.7 \pm 0.89) \times 10^{-18}$ erg s^{-1} cm^{-2}. The velocity difference between the two redshifts is $|\Delta v|$ = 166 km s^{-1}. We adopt z_{neb} = [O III]λ5008 because it is a 10σ detection compared to the 2.6σ Hα detection. We were unable to detect BX426b in the KCWI datacube due to confusion with the bright foreground star and more massive galaxy BX426.

Figure 4.4 shows the Lyα emission from CS13 at $z_{\mathrm{Ly}\alpha}$ = 2.2459. CS13 is a weak emitter compared to HU1 with a flux $F_{\mathrm{Ly}\alpha}$ = $(3.21 \pm 0.91) \times 10^{-18}$ erg s^{-1} cm^{-2}. Since CS13 has not been included on a slit mask we apply an average correction to its

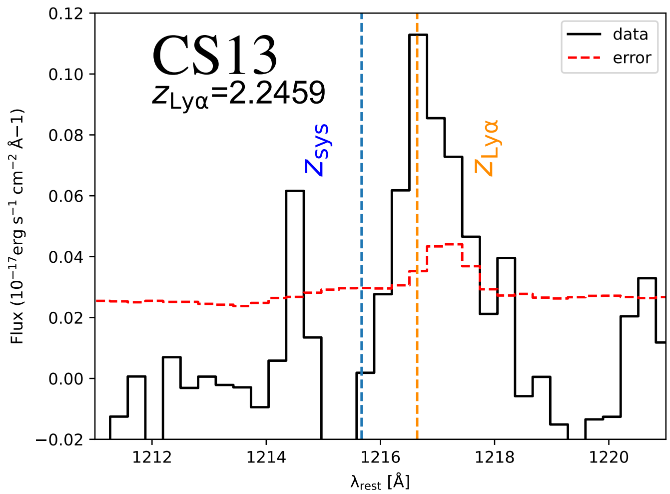

Figure 4.4: Extracted rest-FUV spectrum of CS13 from KCWI. Same colors and lines as the top left panel of Figure 4.2.

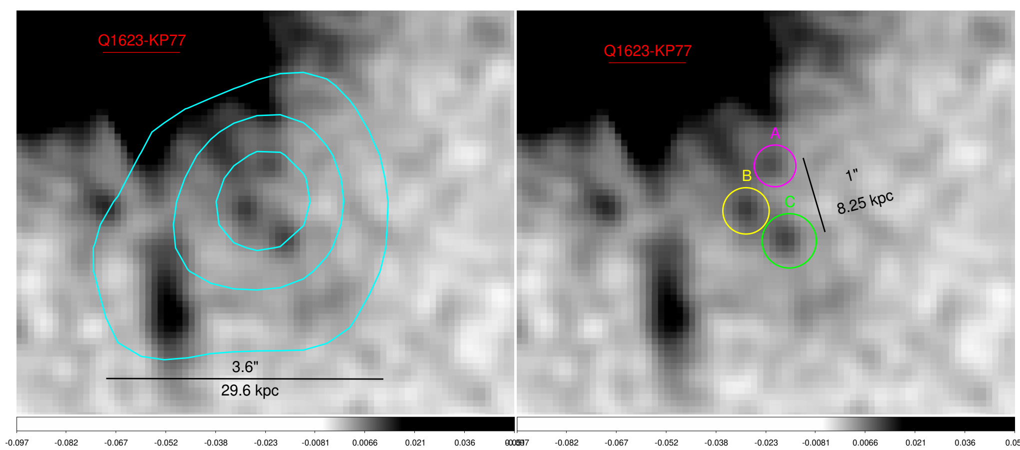

Figure 4.5: *HST*/F160W zoom in on the morphology of HU1. The scale and stretch between both images are the same. *Left panel:* Blue contours show Lyα emission created from a KCWI pseudo-narrowband image. The scale of the emission is shown at the bottom and extends to ~30 pkpc. The Lyα extends to the position of all of the emission knots. *Right panel:* Emission "knots" that may be responsible for the Lyα emission. The largest distance between the knots (A to C) is ~8 pkpc.

Lyα redshift assuming it has the typical velocity offset seen in other $z \sim 2-3$ galaxies $v = -235$ km s^{-1}. We adopt a new estimated systemic redshift $z_{sys,\mathrm{Ly}\alpha} = 2.2433$.

Stellar Populations and Morphology

Each galaxy is detected and resolved in the extant *HST*/F160W images. We use the images to measure their projected sizes and magnitudes. Visual inspection suggests that each galaxy has a small projected radius and is faint.

The bottom left panel of Figure 4.1 shows a zoom-in on galaxy CS13. The morphology of CS13 appears spheroidal, diffuse, and typical of low-luminosity objects. We estimate its half-light radius as half of the full width at half maximum (FWHM) of a two dimensional Gaussian fit to the galaxy after de-convolving the PSF of the F160W image by using the typical FWHM of stars in the field ($\mathrm{PSF}_{\mathrm{FWHM}} \approx 2.7$ pix $\approx 0.22''$). This results in a half-light radius for CS13 of $r_{1/2,\mathrm{CS13}} = 0.083'' = 0.69$ kpc.

The bottom right panel of Figure 4.1 shows a zoom-in of BX426b. The galaxy appears to be extended along the slit resembling a small disk. With the assumed geometry, the half-light radius of along the major axis of the galaxy is $r_{1/2,\mathrm{Major,BX426b}} = 0.13'' = 1.10$ kpc, the half-light radius along the length of the minor axis is $r_{1/2,\mathrm{Minor,BX426b}} = 0.03'' = 0.24$ kpc, and the average half-light radius is then $r_{1/2,\mathrm{BX426b}} = 0.67$ kpc.

Figure 4.5 shows a zoom-in on HU1. The left panel shows the Lyα halo contours overlaid on *HST* rest-optical image. The centroid of the emission is close to the center of three objects, which we will refer to as "knots." The distance between the emission knots are shown in the right panel with a maximum transverse distance of 8.25 kpc, while the half-light radius of the knots varies between $r_{1,2,\mathrm{HU1}} \sim 0.24 - 0.81$ kpc. It might be the case that one, or all, of the emission knots is responsible for the Lyα emission based on its centroid position. Deeper NIR spectroscopy is needed to disentangle these possibilities.

The projected sizes of each galaxy measured in this section are consistent with the range of half-light radii measured from local dwarf galaxies $r_{1/2,\mathrm{Local\ Dwarfs}} \sim 0.02 - 2.6$ kpc (McConnachie, 2012).

SEDs for each galaxy were constructed using ground-based images from Keck/LRIS, P200/WIRC, and Magellan/FourStar, and space-based images are from *HST*/WFC3-IR F140W, F160W, and *HST*/WFPC2 450W, F702W, and F814W (see Section 4.3).

All of the galaxies are faint ($m_{F160W} > 25.5$) and therefore are seldom detected in the ground- and space-based images including KBSS *HST*/F140W. This resulted in sparse SEDs with few constraints useful for the best-fit SED models. HU1 had coverage in many *HST* bands from rest-FUV to rest-optical. Using QSO-subtracted versions of the *HST* images, and ground-based K_s band images, we estimated HU1's stellar mass, star-formation rate, and reddening assuming a constant SFH for two age models (1) age is left as a free parameter and (2) age forced to be $t_{\mathrm{age}} > 50$ Myr.

Table 4.2 shows the range of best-fit SED properties for HU1 in the top row. The mass range $\log(\mathrm{M}/\mathrm{M}_{\odot}) = 7.9 - 8.4$ suggests that HU1 is a low-mass galaxy.

The stellar mass of BX426b would certainly overestimated if using the same approach for HU1 because in all of the ground-based images it is blended with the more massive galaxy BX426, which has a mass of $\log M_{*} = 9.6$. Unfortunately, both BX426b and CS13 only have *HST* coverage in F160W. To estimate their stellar masses, we assume that they have similar stellar populations as HU1 since their FUV and rest-optical spectra show that they are actively forming stars. We combine this assumption with the facts that the galaxies are at the same redshift as HU1, and that both galaxies are fainter than HU1 by at least half a magnitude $m_{\mathrm{F160W,HU1}} = 25.5 \pm 0.2$, $m_{\mathrm{F160W,BX426b}} = 26 \pm 0.2$, and $m_{\mathrm{F160W,CS13}} = 28 \pm 0.2$, to place upper limits on their stellar masses, SFR, reddening, and ages based on HU1's best-fit parameters. This implies that BX426b and CS13 have stellar masses of $\log(\mathrm{M}_{*}/\mathrm{M}_{\odot}) < 8.4$, which we show in Table 4.2.

The galaxies' inferred stellar masses are well within the range of masses of local dwarf galaxies $\log(\mathrm{M}_{*}/\mathrm{M}_{\odot})_{\mathrm{Local\ Dwarfs}} \sim 4 - 9$ (McConnachie, 2012). For reference, the SMC has a stellar mass of $\log(\mathrm{M}_{*}/\mathrm{M}_{\odot})_{\mathrm{SMC}} = 8.7$.

Table 4.2: Galaxy SED Properties

Galaxy	$\log M_{*}$ ($M_{\odot}$)	Age (Myr)	SFR_{SED} ($M_{\odot} yr^{-1}$)	E(B-V)
HU1	7.9-8.4	10-63	2-15	<0.09
BX426b[a]	< 8.4	< 63	< 15	< 0.09
CS13[a]	< 8.4	< 63	< 15	< 0.09

a) Upper limits based on HU1's best fit parameters.

Altogether, we showed that the three galaxies are at similar z ($z_{\mathrm{sys}} = 2.24$), actively star-forming (Lyα and/or [O III] emitters), have small best-fit SED stellar masses ($\log(\mathrm{M}_{*}/\mathrm{M}_{\odot}) \leq 8.4$), exhibit small projected sizes ($r_{1/2} < 0.89$ kpc), and are therefore the first $z \sim 2$ star-forming dwarf galaxies analyzed in KBSS-InCLOSE.

4.5 Inner CGM Properties

In this section we measure the physical conditions of the galaxies' CGM as seen in absorption in the background QSO spectra. The small projected distances from the QSOs ($b < 74$ kpc) and small masses stellar masses $\log(\mathrm{M}_{*}/\mathrm{M}_{\odot}) < 8.4$ of each galaxy show that we are seeing the first direct views of the CGM of $z \sim 2$ star-forming dwarf galaxies (to our knowledge). Each galaxy has a systemic redshift based on analysis of their nebular emission presented in the previous section (Section 4.4) that defines the zero-point velocity for the peculiar velocities presented henceforth.

Column Density and Gas Kinematics

Figures 4.6, 4.7, and 4.8 show ion velocity stackplots with best-fit Voigt profiles overlaid on the data (fitting described in Section 4.3) for each galaxy centered at $z_{\rm sys}$. Visual inspection of the stackplots shows that each galaxy has a detection of at least H I, C IV, and O VI.

Figure 4.6 shows HU1's CGM absorption. The total column densities of the best-fit models are shown in Table 4.3. The H I absorbers were included in the catalog of H I absorbers analyzed by Rudie et al. (2012), so we adopted their best-fit models. We also used the catalog to mitigate Lyα and Lyβ forest contamination by removing the best-fit H I components of all absorbers from the QSO spectrum. After removing the contamination, we can see clear H I, C IV, and O VI absorption in HU1's halo.

The H I column density $\log{(N_{\rm HI}/{\rm cm^{-2}})} = 15.13$ is consistent with Super Lyman Alpha Forest (SLYF) absorbers which are characterized by H I column densities $\log{(N_{\rm HI}/{\rm cm^{-2}})} = 14.5 - 16.2$. C IV and O VI column densities ($N_{\rm CIV}$, $N_{\rm OVI}$) are dominated by two components at $v = -50$ km s^{-1} from $z_{\rm sys}$ with $\log{(N_{\rm CIV}/{\rm cm^{-2}})} =$ 13.4 and $\log{(N_{\rm CIV}/{\rm cm^{-2}})} = 14.2$; the strongest H I component is at a similar velocity $\log{(N_{\rm HI}/{\rm cm^{-2}})} = 14.8$.

The kinematics of HU1's CGM absorption are complex in that the best-fit model requires eight components spread over $|\Delta v| \sim 450$ km s^{-1}. The fastest intermediate-ionization components are weak $\log{(N_{\rm CIV}/{\rm cm^{-2}})} \leq 12.1$. O VI exhibits the fastest velocity components $|v| = 300$ km s^{-1} and largest velocity spread $|\Delta v| \sim$ 450 km s^{-1}. Half of the C IV and O VI components were kinematically tied to one another, suggesting they may be in the same phase. We explore if the tied components can be modeled as a single phase gas in the next Section 4.5.

Figure 4.7 shows BX426b's CGM absorption. There is clear H I, Si III, C IV, Si IV, and O VI spread over $|\Delta v| \sim 150$ km s^{-1}.

The H I column density $\log{(N_{\rm HI}/{\rm cm^{-2}})} = 15.68$ is consistent with that of SLYF absorbers. Si III, C IV, and Si IV show the same kinematic structure and are tied to one another. The O VI component structure inhabits the same velocity range of H I and the intermediate-ions but is more broad and not kinematically aligned with the intermediate-ions.

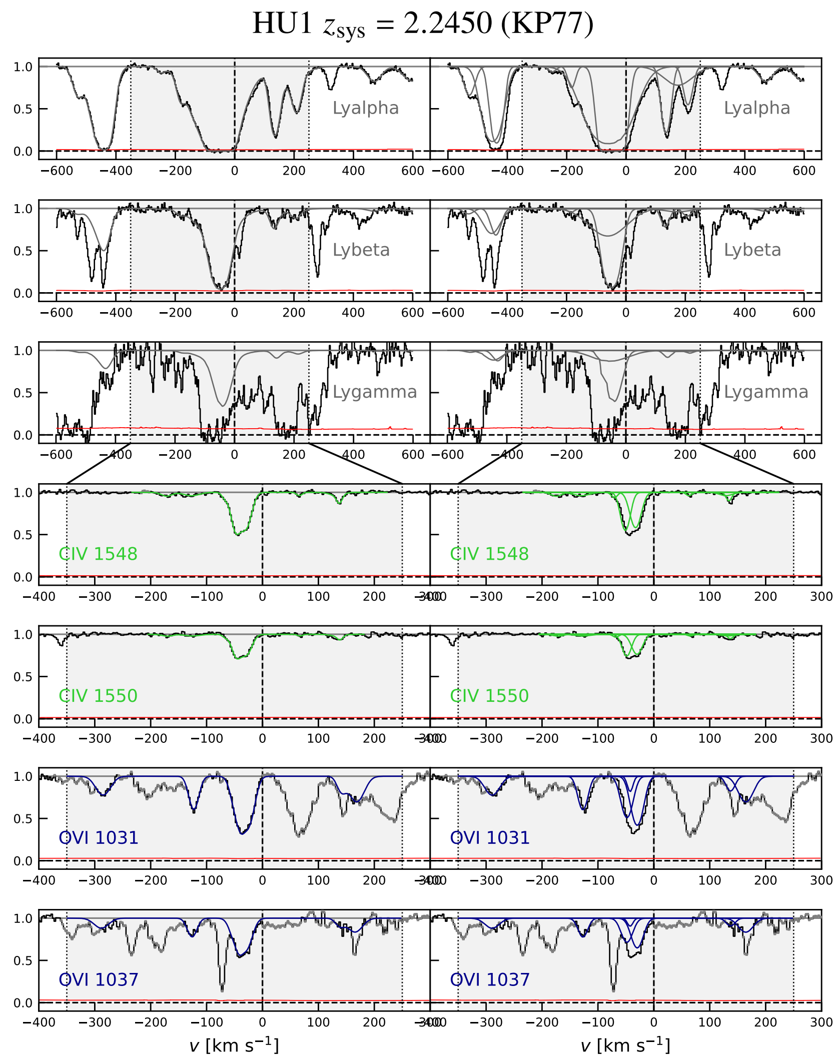

Figure 4.6: Ion velocity stackplot and best-Fit Voigt-profiles of HU1's CGM metal absorption centered at z_{sys} = 2.2450. The black lines show the data, the colored lines show the best-fit model(s), the red lines show the error spectrum, the light grey lines shows HI or intervening contamination, and the light grey shaded regions show the extent of the metal-line absorption. *Left:* Product of the individual Voigt profile components, i.e., total fit. *Right:* Individual Voigt-profile components.

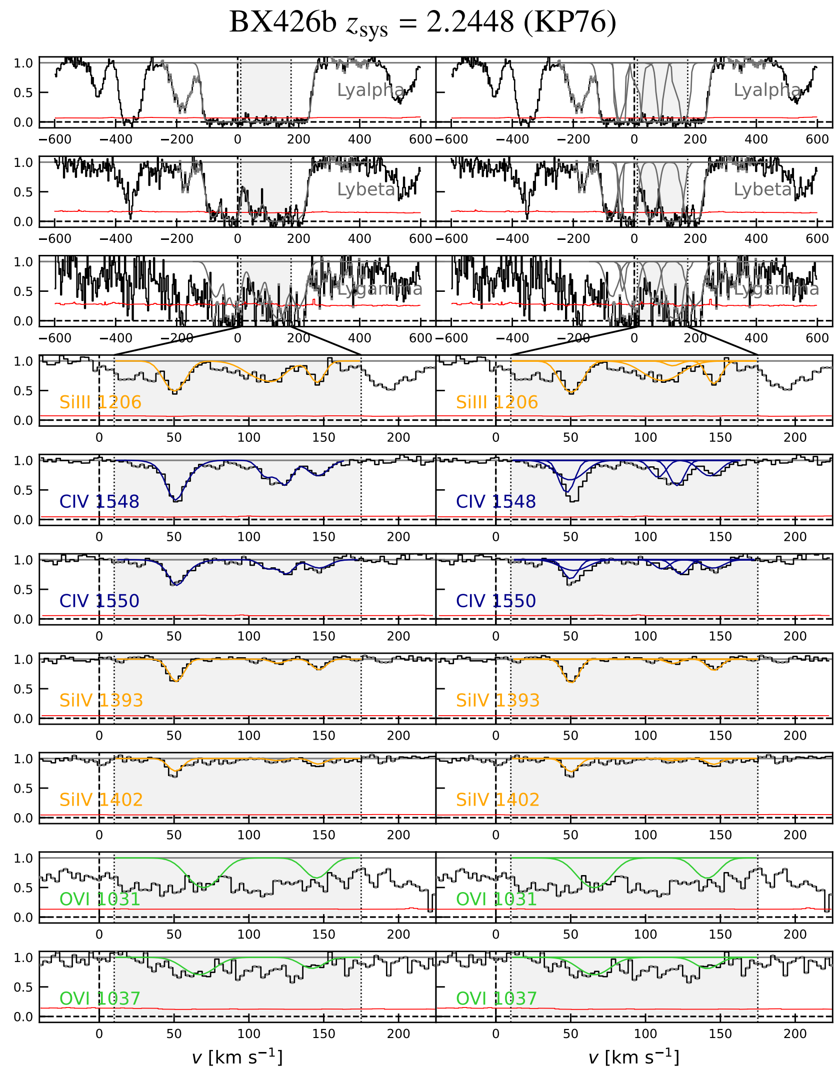

Figure 4.7: Ion velocity stackplot and best-Fit Voigt-profiles to BX426b's CGM metal absorption centered at (z_{sys} = 2.2448). Same colors and lines as Figure 4.6.

The kinematics of BX426b's halo as seen in intermediate-ionization absorption requires at most six components (5 unique to C IV and 1 unique component to SI IV) spread over a small velocity range $v \sim 150$ km s^{-1}. The high-ionization absorption as seen in O VI has only two components. The fastest components for the metal ions have a velocity of $v \sim 150$ km s^{-1} which is at a similar velocity as the strongest H I component $\log{(N_{\rm HI}/{\rm cm}^{-2})} = 15.3$ of the system. Interestingly, the strongest metal components have a velocity near $v \sim 50 - 75$ km s^{-1}, which corresponds to a weaker H I component with $\log{(N_{\rm HI}/{\rm cm}^{-2})} = 14.7$.

Figure 4.8 shows CS13's CGM absorption. Visual inspection of the stackplots shows strong absorption for the intermediate- and high-ionization species, but weak

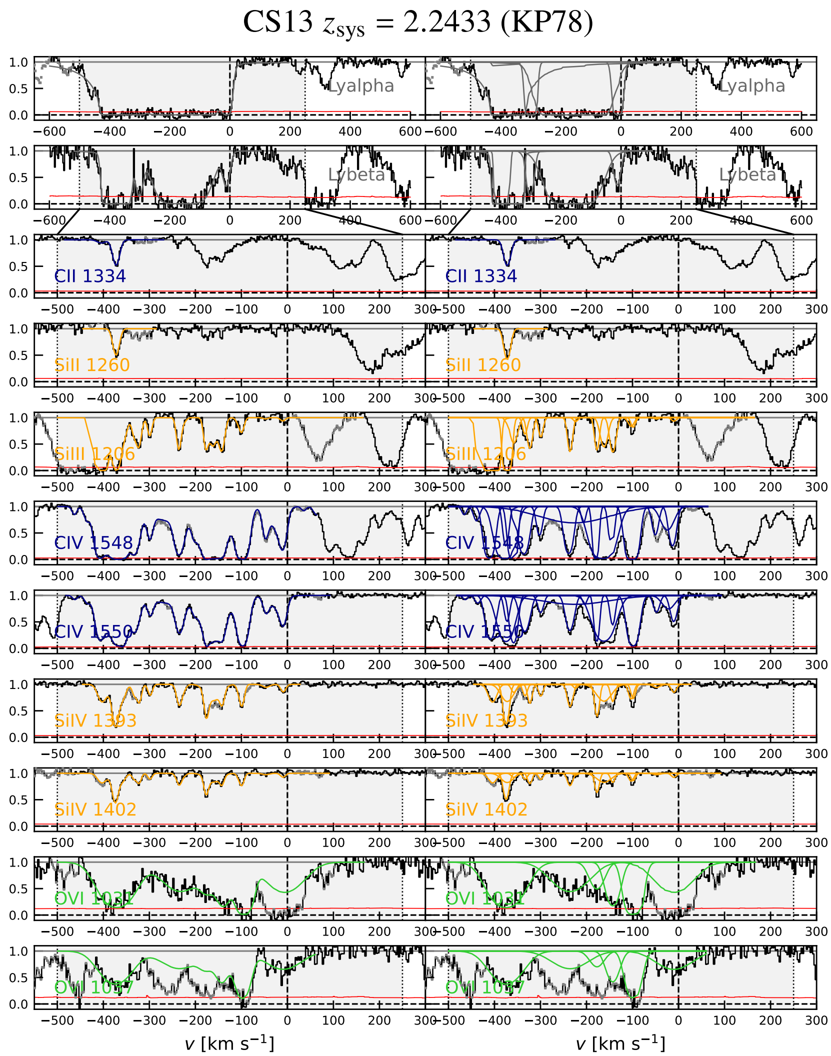

Figure 4.8: Ion velocity stackplot and best-Fit Voigt-profiles to CS13's CGM metal absorption (z_{sys} = 2.2433). Same colors and symbols as 4.6.

absorption for the low-ionization species (C II, Si II).

The column densities of H I, Si III, C IV, and O VI are larger by $> 1 - 1.5$ dex compared to the other galaxies in the sample. The H I column density $\log{(N_{\rm HI}/{\rm cm}^{-2})} = 17.95$ is consistent with that of Lyman Limit System (LLS) which are characterized by $\log{(N_{\rm HI}/{\rm cm}^{-2})} = 17.2 - 19$.

CS13's halo kinematics are very complex requiring up to 19 components and spread over $|\Delta v| \sim 550$ km s^{-1}. Si IV was used to establish the main component structure for all of the metal ions because of its strong, non-saturated, and narrow components. This was particularly useful for determining C IV components because it exhibited broad and saturated components. Si IV was also helpful for identifying O VI

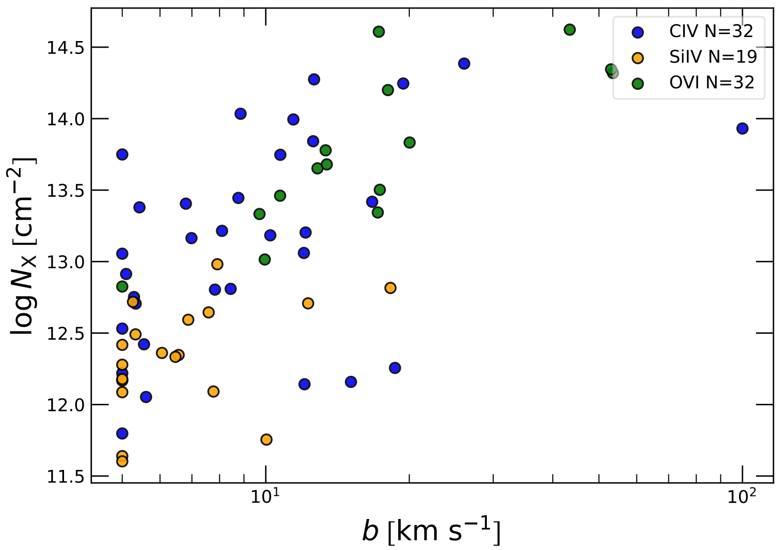

Figure 4.9: Best-Fit $\log(N/\mathrm{cm}^{-2})$ and b for C IV (red), Si IV (red), and O VI (blue) for all absorbers associated with HU1, BX426b, and CS13. The number of absorbers per ion are shown.

components due the severity of foreground Lyα and Lyβ contamination. Note that H I absorbers towards KP78 were not included in the catalog constructed by Rudie et al. (2012), so we were unable to remove this contamination. The low-, intermediate-, and high-ions share a similar kinematic structure spread over a similar velocity range. However, it is clear that O VI has fewer components and that each component is more broad.

Table 4.3: CGM Absorption

Galaxy	QSO	z_{sys}	D_{Tran} (pkpc)	log (ΣN_X) [(cm^{-2})] H I	C II	Si II	Si III	Si IV	C IV	O VI	N^a_{max}
HU1	KP77	2.2441	31.3	15.13	...	...	...	...	13.59	14.21	8
BX426b	KP76	2.2448	49.7	15.68	...	...	>12.76	12.68	13.63	13.84	6
CS13	KP78	2.2433	74.3	17.95	13.41	12.47	>14.01	13.72	15.09	15.18	19

a) Maximum number of unique components considering all ions.

Table 4.3 summarizes the best fit column densities (summed over $\pm 1,000$ km s^{-1}) for each ion in the halos of HU1, BX42b, and CS13. HU1 and BX426b have similar neutral-, intermediate-, and high-ionization metal column densities. CS13's CGM shows neutral-, low-, intermediate-, and high-ionization column densities that are more than 1-1.5 dex stronger than that of the the other galaxies in this sub-sample.

Figure 4.9 shows column density as a function of Doppler width for C IV, Si IV, and O VI, for each galaxy. C IV and O VI are detected in all of the halos. It is clear that there are many components with small b that reach the resolution limit of the QSO spectra but that the absorbers still vary by more than 1.5 dex in N. We can see that the majority of the absorbers have small Doppler widths $b < 10$ km s^{-1}. This is consistent with visual inspection of the absorbers being narrow and weak. There is a positive correlation between N and b with a modest ~ 0.5 dex scatter at large $b > 10$ km s^{-1}.

Temperature and Turbulence

We use the best-fit b_d components from Section 4.5 for tied ions, to determine their non-thermal broadening or turbulent velocity b_turb and temperature (T) using the following equation:

$$b_\mathrm{d}^2 = b_{nt}^2 + 2kT/m_\mathrm{ion} \tag{4.1}$$

where k is the Boltzmann constant, m_ion is the mass of the ion being fit, T is the temperature of the gas, and b_{nt} is the non-thermal broadening component, e.g., the non-thermal broadening will be dominate so we equate this to turbulent velocity b_turb (Rudie et al., 2019). This explicitly assumes that the gas in each absorber is isothermal and therefore each ion arises from the same gas. To ensure that each absorber's width was equal to or greater than the resolution of the QSO spectra, we set $\log{(T/\mathrm{K})_{min}} = 4$ and $b_\mathrm{turb} = 2.5$ km s^{-1} which ensures that the sum of Si widths match the resolution of HIRES $b_\mathrm{d} = \sqrt{b_\mathrm{turb}^2 + 2kT/m_\mathrm{Si}} \gtrsim 5$ km s^{-1}.

Each galaxy's halo shows clear detections of C IV and at least one other ion, Si IV or O VI, that has the same kinematic structure. Therefore these ions can be used to solve for Equation 4.1 since they have different masses. For BX426b's halo we tied C IV, Si IV, and Si III, for CS13's halo we tied C IV, Si IV, C II, and Si II, and for HU1 we tied C IV and O VI. We attempted to tie O VI with the other ions in BX426b's and CS13's halos but were unable to find physical single-phase solutions, which showed explicitly that the gas is multiphase.

For HU1 we tied four of its C IV and OVI components; C IV has eight total components and O VI has seven total components. The tied components exhibited the strongest absorption seen in H I, C IV, and O VI. Two out of three of the non-tied components were at the velocity extremes of the halo ($v_{\mathrm{min,O\ VI}} = -289$ km s^{-1}, $v_{\mathrm{max,O\ VI}} = 164$ km s^{-1}). The fact that we obtain satisfactory and physically reasonable results suggests that these ion components are single-phase and arise from the same gas. The two components that show the strongest absorption ($v \sim -50$ km s^{-1}, $v \sim -30$ km s^{-1}) have widths that are dominated by

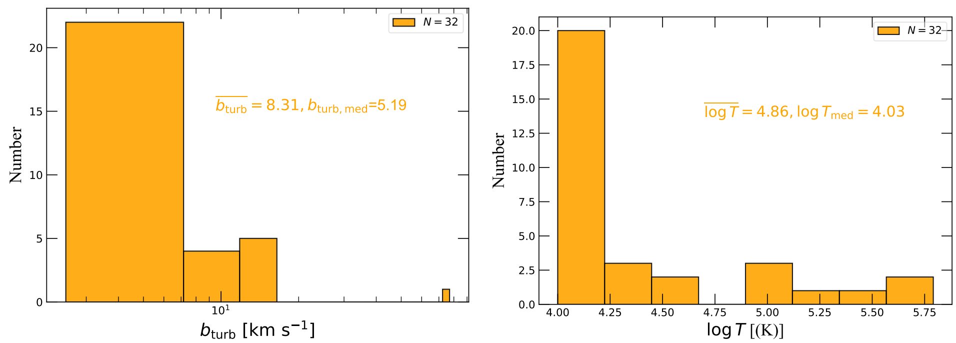

Figure 4.10: Best-Fit $\log T$ and $b_{\rm turb}$ distribution for all tied absorption components associated with HU1, BX426b, and CS13.

turbulence $b_{\rm turb} \sim 11.3$ km s^{-1} and $\log(T/{\rm K}) = 4$. The two other components ($v \sim -130$ km s^{-1}, $v \sim 150$ km s^{-1}) are dominated by thermal broadening with $\log(T/{\rm K}) = 5.16$, $\log(T/{\rm K}) = 5.78$ and small $b_{\rm turb}$ of $b_{\rm turb} = 2.5$ km s^{-1}.

Figure 4.10 shows $\log(T/{\rm K})$ and turbulent velocity width $b_{\rm turb}$ for all of the components tied with at least two ions from each galaxy. In the left panel we see similar behavior to Figure 4.9 where the majority of the absorbers are small ($b_{\rm turb} < 10$ km s^{-1}). Similarly, the right panel shows that the majority of the gas is cool and consistent with heating from photoionization ($\log T \sim 4$). Both of the panels occupy a similar range of $\log T$ and $b_{\rm turb}$ seen by Rudie et al. (2019). The only difference is that their temperature distribution peaked at $\log T_{med,R19} = 4.37$ whereas our median is a factor of 2 smaller at $\log T_{med} = 4.03$. However we caution that we have far fewer absorption components and it is possible that both $\log T$ and $b_{\rm turb}$ are piling up at the lower limit that we set for Voigt-profile fitting.

In Figure 4.11 we explore whether there is a correlation between the absorbers with $\log T_{min}$ and $b_{{\rm turb},min}$ by plotting each pair of $\log T$ and $b_{\rm turb}$.

There appears to be a degeneracy as opposed to a correlation between $b_{\rm turb}$ and $\log T$ suggesting that $\log T$(or $b_{\rm turb}$) can only be measured when $b_{\rm turb}$(or $\log T$) is small, i.e., similar to the specified lower limit for temperature ($T_{\rm min} = 10^4$ K) and turbulent velocity ($b_{\rm turbmin} = 2.5$ km s^{-1}).

4.6 Novel and Preliminary Insights on the Low-Mass CGM at $z \sim 2$

The sub-sample presented in this work allows for a preliminary investigation into how the CGM changes with stellar mass and redshift. To this end, we compare our results to two studies that investigated halo gas within $\sim R_{\rm vir}$ of a QSO for $z \sim 2$ massive

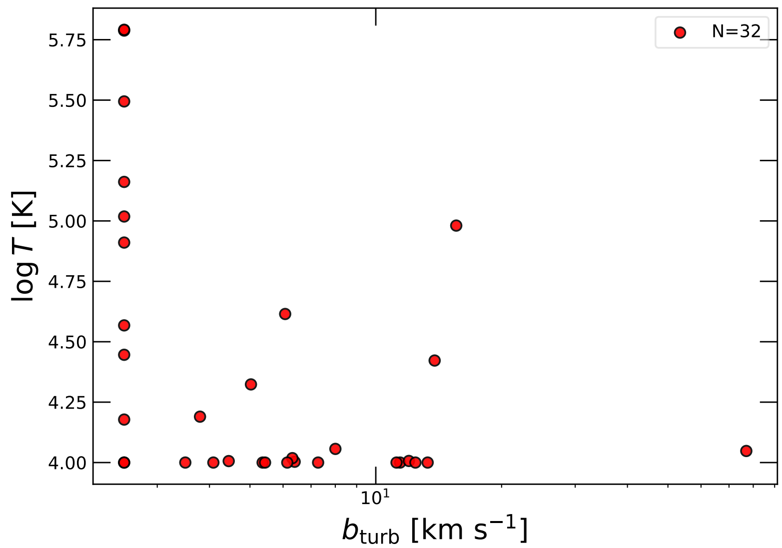

Figure 4.11: Best-Fit $\log T$ as a function of $b_{\rm turb}$ for all tied absorbers associated with HU1, BX426b, and CS13. The absorbers are tied with C IV and at least one other ion, Si IV or O VI (only 4 absorbers).

and $z \sim 0.3$ dwarf galaxies. Using the stellar mass inferred from Section 4.4 we estimate an upper limit on the virial radius and escape velocity of the galaxies using the $z \sim 2$ LAE literature with typical masses of $M_* = 1.5 \times 10^9$ M$_\odot$, corresponding halo mass of $M_h \sim 3 \times 10^{11}$ M$_\odot$, which corresponds to $R_{\rm vir} < 60$ kpc (Erb et al., 2023) and $v_{\rm esc} < 200$ km s^{-1} (Erb et al., 2023; Trainor et al., 2015). This implies that HU1 is at a projected normalized distance from KP77 of $D_{\rm Tran}/R_{\rm vir} < 0.52$, BX426b $D_{\rm Tran}/R_{\rm vir} < 0.93$, and CS13 $D_{\rm Tran}/R_{\rm vir} < 1.24$

Rudie et al. (2019, R19z2 hereafter) analyzed the inner CGM ($D_{\rm Tran} < 90$ kpc) of eight $z \sim 2$, M_* star-forming galaxies. The relevant points of their study to this work were that (1) the $z \sim 2$, M_* inner CGM is very complex and composed of at least 10 kinematically aligned components, (2) the CGM always exhibits low- and intermediate-ionization gas, and often exhibits high-ionization gas ($\sim 50\%$ of the sample), though this number is low due to Lyβ contamination from higher-z high-H I absorbers, (3) typical temperatures in the halo vary between $\log T = 4.3 - 5.0$ with more than half of absorbers showing $\log T = 4.5 - 5.5$ such that $b_{\rm turb}$ is sub-dominant compared to thermal broadening with typical values $b_{\rm turb} = 6$ km s^{-1}, and (4) halos commonly exhibit at least one absorber with a radial velocity that exceeds the escape velocity of the galaxy.

Mishra et al. (2024, M24z0 hereafter) recently analyzed the largest sample (N = 91) of nearby ($z \sim 0.3$) low-mass/dwarf galaxies ($\log{(M_*/M_\odot)_{\rm med}} \simeq 8.3$) within a few $R_{\rm vir}$ of a QSO sightline ($D_{\rm Tran}$ < 300 kpc). This is a larger impact parameter range than the galaxies analyzed in this study so we restrict their sample to galaxies within projected distances of $D_{\rm Tran} \lesssim 90$ kpc $\sim 1.25\ R_{\rm vir}$ of a QSO. They showed that (1) H I is almost always detected in the halo of galaxies within $R_{\rm vir}$, (2) low-ionization (C II, C III, Si II, Si III) and intermediate-ionization (C IV, Si IV) metal absorption is seldom detected unless within $0.5R_{\rm vir}$, (3) high-ionization metal absorption as probed by O VI is almost always detected within $0.5R_{\rm vir}$ and around 50% within $1R_{\rm vir}$, and (4) about 15% of galaxies in the sample have at least one O VI bearing absorber that is unbound.

The halos in this work exhibit a wide range of H I column densities $\log{(N_{\rm HI}/{\rm cm}^{-2})}$ = 15.1 – 18.01. This range is larger than but has overlap with the H I column densities measured in M24z0 (when restricted to $1.25R_{\rm vir}$), which are $\log{(N_{\rm HI}/{\rm cm}^{-2})}$ = 13.7 – 17.6, $\log{(N_{\rm HI}/{\rm cm}^{-2})_{\rm M24z0,avg}}$ = 14.2, $\log{(N_{\rm HI}/{\rm cm}^{-2})_{\rm M24z0,med}}$ = 14.1. Compared to R19z2 the range in this work is smaller than but has overlap with their H I column density measurements which are $\log{(N_{\rm HI}/{\rm cm}^{-2})_{\rm R19z2}}$ = 15.7 – 20, $\log{(N_{\rm HI}/{\rm cm}^{-2})_{\rm R19z2,avg}}$ = 17.0, $\log{(N_{\rm HI}/{\rm cm}^{-2})_{\rm R19z2,med}}$ = 16.4.

We measure a high detection rate (fraction of galaxies that show a detection of an ion or phase) of unity for intermediate- and high-ionization gas as seen in C IV and O VI, but a low detection rate (1/3) of low-ionization gas as seen in C II, Si II. These detection rates differ from both samples in that R19z2 measured high detection rates of low-, intermediate-, and high-ionization gas in their halos, whereas M24z0 measured low detection rates of low-ionization and intermediate-ionization gas but often detected high-ionization gas. In other words, for this subsample low-ionization gas is uncommon in the halos (contrary to $z \sim 2$ typical mass galaxies, similar to $z \sim 0.3$ dwarf galaxies), intermediate-ionization and high-ionization gas is common in the halos (similar to massive $z \sim 2$ halos, contrary to $z \sim 0.3$ halos).

The kinematic component structure and velocity range of metals in the halos in this work exhibit at least 6 unique components (up to 19) spread over at least $|\Delta v| \sim 150$ km s^{-1} (up to $|\Delta v| \sim 550$ km s^{-1}). This component and velocity range is smaller than but overlaps with R19z2 results that the $z \sim 2$ halos exhibit at least 10 components (up to 25) spread over a velocity range of at least $|\Delta v| \sim 200$ km s^{-1} (up to $|\Delta v| \sim 900$ km s^{-1}). Compared to M24z0, the range in this work is larger than but has overlap with their results which exhibit at most 4 components spread over $|\Delta v| \sim 200$ km s^{-1}. In this case, the velocity spread of the absorption is the ideal quantity to compare against because resolving component structure is tied to both the resolving power and S/N of the QSO spectra which for M24z0 is from *HST*/COS with $R \approx 15,000$ and $S/N \approx 12-31$ per resolution element (Chen et al., 2020a)), compared to this work (and R19z2) from HIRES with $R \approx 45,000$ and $S/N \approx 29-48$ per resolution element. This suggests that the halos in this subsample are more kinematically complex than $z \sim 0.3$ dwarf halos in terms of velocity range of ion absorption, but simpler than $z \sim 2$ massive galaxies in terms of both number of components and velocity range.

The thermal properties of the halos as inferred from the Doppler width decomposition show that they exhibit typical temperatures that are consistent with heating from photoionization or $T_{\rm med} = 10^4$ K, but that there is a wide range of temperatures that the absorber components exhibit $\log{(T/{\rm K})_{\rm med}} = 4-5.8$ ($\log{(T/{\rm K})_{\rm avg}} = 4.9$. The turbulent velocities are fairly small $b_{\rm turb,med} = 5.2$ km s^{-1} ($b_{\rm turb,avg} = 8.3$ km s^{-1}) but also exhibit a wide range of velocities $b_{\rm turb} = 2.5-71$ km s^{-1}. Interestingly, all of these values are slightly lower than but overall consistent with R19z2's results that temperatures in the $z \sim 2$ massive halos were $\log{(T/{\rm K})_{\rm R19z2,med}} = 4.4$ and showed a wide temperature range $\log{(T/{\rm K})_{R19z2}} = 2.5-6.5$. Though not measured explicitly, M24z0 reasoned based on their Voigt-Profilr fits that the majority of the gas in the halos of the $z \sim 0.3$ galaxy halos was around $T \sim 10^4$ K, and at $z \sim 1$, Qu et al. (2022) found a narrow temperature range for the 26 M_* halos examined in their work of $\log{(T/{\rm K})} = 4-4.6$. This all suggests that the absorbers in the halos of this subsample have typical temperatures that are ~ 0.4 dex less than more massive $z \sim 2$ galaxies, but exhibit temperature ranges that are much larger than low-mass and lower-z galaxies.

Adopting an escape velocity of $|\Delta v| < 200$ km s^{-1} results in two of the three (66%) galaxies exhibiting unbound gas (HU1 and CS13). Though there are only three galaxies in this sample it is interesting to note that the unbound gas fraction (number of galaxies that have at least one absorber with unbound gas compared to the total sample) measured by R19z2 was 75%, whereas M24z0 measured 15%.

Altogether, we have preliminary evidence from this small subsample that the low-mass $z \sim 2$ CGM may be distinct from the more massive $z \sim 2$ CGM and $z \sim 0.3$ dwarf galaxy sample in terms of its low-, intermediate-, and high-ionization metal absorption detection rate, kinematic complexity in terms of number of kinematic components and velocity range with which ion absorption is detected, thermal properties in terms of typical temperature and temperature range, and unbound gas fraction.

4.7 Summary & Conclusions

We have presented the first analysis of low-mass ($M_* < 10^{8.5}$ $M_\odot$) galaxies in the KBSS-InCLOSE survey. The three galaxies examined in this paper, HU1, BX426b, and CS13, are in the same KBSS QSO field towards Q1623, each within a projected distance of $D_{\rm Tran} < 75$ kpc of a luminous QSO (Figure 4.1).

Two of the galaxies, HU1 and CS13, were discovered in KCWI datacubes (Figures 4.2 and 4.3) while the other was discovered serendipitously on the same slit as a more massive galaxy with MOSFIRE (Figure 4.4). Analysis of their nebular spectra confirm that the galaxies are star-forming (Lyα, [O III], and Hα emitters) and that they are at the same redshift $z_{\rm sys,HU1} = 2.2450$, $z_{\rm sys,BX426b} = 2.2448$, $z_{\rm sys,CS13} = 2.2433$ which is a velocity spread of only $|\Delta v| \sim 160$ km s^{-1} (Sections 4.3 and 4.4).

Analysis of the galaxies' morphologies (via measurements from rest-optical *HST* images; Figures 4.1 and 4.5) and SEDs (via SED-fitting with BPASS models; Table 4.2) corroborates that they are low-mass based on their small projected sizes of $r_{1/2} \leq 0.89$ kpc, and small inferred stellar masses of $M_* \leq 10^{8.4}$ $M_\odot$ (Section 4.4).

The CGM of each galaxy, as seen in HIRES QSO spectra, shows neutral-phase absorption as seen in H I, intermediate-ionization absorption as seen in C IV, and high-ionization metal absorption as seen in O VI (Section 4.5). Only one galaxy exhibits weak low-ionization metal absorption in its halo as seen in C II and Si II (Figure 4.8) while the other two exhibit no low-ionization absorption (Figure 4.6, 4.7). Estimating an appropriate virial radius and therefore escape velocity, two of the galaxies have absorber components with radial velocities that exceed the gravitational potential of the galaxy.

By performing Voigt-profile decomposition of the CGM absorption we show that the three galaxies have kinematic component structures that require at least 6 components spread over a total velocity range of $|\Delta v| \sim 550$ km s^{-1}.

For the first time in KBSS-InCLOSE, we use the galaxies' Doppler width to infer a subset of individual absorber's temperature (T) and turbulent velocity $b_{\rm turb}$ by tieing together ions of different masses (typically C and Si) assuming that the ions arise from the same gas and that the gas is isothermal. We show that the typical temperature of the subset of absorbers is consistent with photoionization

$\log{(T/\mathrm{K})}_{\mathrm{med}} = 4.03$ and that the typical turbulent velocity is small ($b_{\mathrm{turb,med}} = 5.19$ km s^{-1}).

When compared to a subset of the largest CGM analysis of low-z dwarf galaxies by Mishra et al. (2024), the CGM of the three low-mass galaxies examined in this work (1) exhibit stronger H I, intermediate-ionization metal absorption (intermediate-ions), and high-ions (typically $\gtrsim$ 0.5 dex per ion), (2) possess more kinematically complex gas in terms of the velocity range over which metal absorption is detected ($|\Delta v_{z\sim 2}| \sim 550$ km s^{-1} compared to $|\Delta v_{z\sim 0}| \sim 200$ km s^{-1}), (3) exhibit a much higher detection rate of intermediate-ions ($f_{\mathrm{Int,z\sim2}} = 100\%$ compared to $f_{\mathrm{Int,z\sim0}} = 20\%$)), show a larger temperature range (when compared to a $z \sim 1$ sample; $|\Delta \log{(T/\mathrm{K})}_{z\sim2}| = 4 - 5.8$ compared to $|\Delta \log{(T/\mathrm{K})}_{z\sim1}| = 4 - 4.6$, and (4) exhibit a higher detection rate of unbound gas ($f_{\mathrm{vesc,\ z\sim2}} = 66\%$ compared to $f_{\mathrm{vesc,\ z\sim0}} = 15\%$).

When compared to the CGM of more massive $z \sim 2$ galaxies analyzed by Rudie et al. (2019), the low-mass halos examined in this work (1) show simpler kinematic structure in terms of total number of kinematic components detected per halo ($N_{\mathrm{Low\ Mass}} = 6 - 19$ compared to $N_{\mathrm{High\ Mass}} = 10 - 25$) and velocity range of metal absorption ($|\Delta v_{\mathrm{Low\ Mass}}| \sim 550$ km s^{-1} compared to $|\Delta v_{\mathrm{High\ Mass}}| \sim 900$ km s^{-1}), (2) exhibit a low detection rate of low-ions ($f_{\mathrm{Low\ Mass}} = 33\%$ vs $f_{\mathrm{High\ Mass}} \gtrsim 50\%$), (3) show smaller typical temperatures ($\log{(T/\mathrm{K})}_{\mathrm{med,Low\ Mass}} = 4.0$ compared to $\log{(T/\mathrm{K})}_{\mathrm{med,High\ Mass}} = 4.4$) and smaller temperature range ($|\Delta \log{(T/\mathrm{K})}_{\mathrm{Low\ Mass}}| = 4 - 5.8$ compared to $|\Delta \log{(T/\mathrm{K})}_{\mathrm{Low\ Mass}}| = 2.5 - 6.5$), and (5) possessed a slightly smaller fraction of unbound gas ($f_{\mathrm{vesc,\ Low\ Mass}} = 66\%$ compared to $f_{\mathrm{vesc,\ High\ Mass}} = 75\%$).

Altogether the results suggest that the low-mass $z \sim 2$ CGM may be be distinct from the CGM of low-z dwarf galaxies and $z \sim 2$ massive galaxies. In other words, there may be an evolution of the CGM both in terms of z and stellar mass that will require a larger sample to further investigate. KBSS-InCLOSE will shed light on this preliminary evolution.

Acknowledgements

We thank Zhiyuan Song for an insightful conversation that expanded and increased the quality of this work.

The authors wish to recognize and acknowledge the very significant cultural role and reverence that the summit of Maunakea has always had within the Native Hawaiian

community. We are most fortunate to have the opportunity to conduct observations from this mountain.

Chapter 5

KBSS-INCLOSE III: THE $z \sim 2.3$ CGM AS SEEN IN THE HALOS OF 55 STAR-FORMING GALAXIES

Thus far, this thesis has focused on individual galaxies from KBSS-InCLOSE that developed the necessary methods and tools for, and showcased the utility of, the survey. In this final chapter I will discuss preliminary work that focuses on the full KBSS-InCLOSE sample. Specifically, I discuss the ways that the survey can be leveraged to significantly expand our understanding of the $z \sim 2$ CGM of star-forming galaxies, and the sample's current limitations that must be addressed in order to more fully observe the $z \sim 2$ galaxy-scale baryon cycle.

Currently, KBSS-InCLOSE includes 55 galaxies, each with a wide range of luminosities, morphologies, nebular properties, stellar masses, and CGM absorption properties. All sources in the sample have at minimum (1) a confident rest-FUV detection from KCWI typically seen as Lyα emission ($SNR_{\mathrm{Ly}\alpha} \gtrsim 3$), and (2) CGM Ly$\alpha$ absorption detected in the KBSS HIRES QSO spectra within $v \pm 1000$ km s^{-1} of z_{sys}. The majority (41/55) of sources are detected in deep KBSS ground-based UGRJHK and/or *HST*/WFC3-IR F140W,F160W images. One quarter of the galaxies in the sample are detected in all ground-based and *HST* images (14/55), about half of the sample is detected only with *HST* (mostly *HST*/F160W; 27/55), and a quarter of the sample has no detection in any images (14/55). It is likely that the sources with detections only with *HST*, and the sources with no detection in any images, are low-mass ($\log(\mathrm{M}_*/\mathrm{M}_\odot) = 8.5 - 9.5$) and dwarf galaxies ($\log(\mathrm{M}_*/\mathrm{M}_\odot) < 8.5$), respectively. We will use these criteria later to divide the sample into mass bins.

Figure 5.1 shows the redshift distribution of the sample. Galaxies that have only a KCWI redshift are shown in blue. To convert $z_{\mathrm{Ly}\alpha}$ to z_{sys} we applied a velocity correction of -235 km s^{-1} (Steidel et al., 2018). For galaxies with a redshift from rest-optical nebular emission z_{neb} we adopted $z_{sys} = z_{neb}$. As mentioned in Section 3.3 we restricted the redshift range of KBSS-InCLOSE to $z = 1.9 - 2.6$ to ensure that strong rest-optical diagnostic emission lines (e.g., [OIII]$\lambda\lambda$4960, 5008,Hα) could be observed with ground-based NIR spectroscopy. Therefore, the redshift averages and medians for all three sub-populations are $z_{sys} \sim 2.3$ by construction.

Figure 5.2 shows the impact parameter distribution (b; transverse distance D_{Tran};

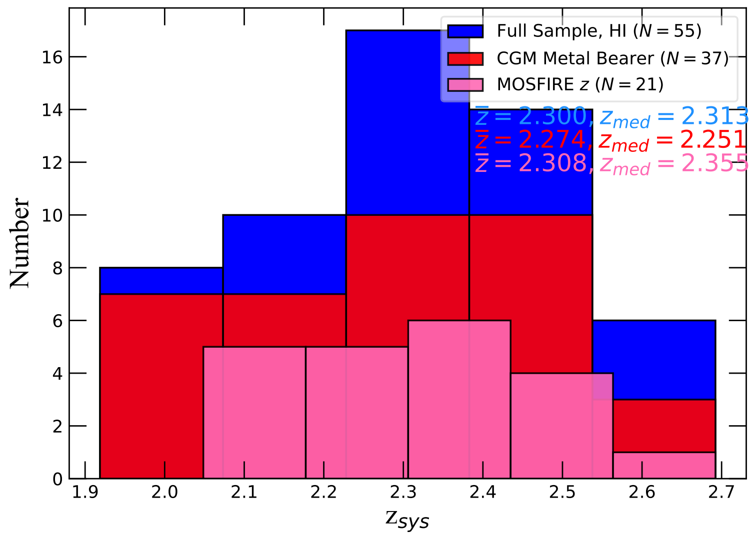

Figure 5.1: Systemic redshift histogram for the full KBSS-InCLOSE sample (blue), sources that show strong metal absorption in their CGM (red), and sources that have a nebular redshift from MOSFIRE (pink). Averages and medians for each distribution are shown in the top right. The sample peaks at $z_{\rm sys} \sim 2.3$ since that is the center of the redshift range that we are probing.

projected distance) of the full sample. The bar colors are the same as Figure 5.1. Before this thesis, there were 9 absorber-host galaxies (galaxies associated with QSO absorbers) at $z \sim 2$ with $D_{\rm Tran} \leq 100$ kpc in the literature. Therefore, the current sample represents more than a six-fold increase in close-in $z \sim 2$ galaxy-QSO pairs.

By analyzing the radial distribution ($D_{\rm Tran}$ vs $\log N_{\rm HI}$) of $\sim 6{,}000$ $z \sim 2$ H I absorbers, Rudie et al. (2012) showed that within $D_{\rm tran} \sim 300$ kpc and $|\Delta v_{\rm sys}| = 700$ km s^{-1} of $z \sim 2$ star-forming galaxies, there is significant H I excess; these values were adopted as the bounds of the $z \sim 2$ CGM. The virial radius for typical stellar mass ($\log(\mathrm{M}_*/\mathrm{M}_\odot) \approx 10$) KBSS star-forming galaxies was estimated by first measuring the galaxy-galaxy autocorrelation function to infer a typical halo mass of $\log(\mathrm{M}_*/\mathrm{M}_\odot) = 11.9$ which corresponds to a virial radius of $R_{\rm vir} \sim 80-90$ kpc (Trainor, Steidel, 2012). For lower stellar mass galaxies ($\mathrm{M}_* \lesssim 10^9\ \mathrm{M}_\odot$) their lower halo masses ($\mathrm{M_h} \sim 3 \times 10^{11}\ \mathrm{M}_\odot$) would result in a smaller virial radius of $R_{\rm vir,Low\ Mass} \sim 60$ kpc (Erb et al., 2023). For dwarf galaxies ($\mathrm{M}_* < 10^8\ \mathrm{M}_\odot$, $M_h \sim 10^{10.8}\ \mathrm{M}_\odot$) their virial radii would be smaller at $R_{\rm vir,Dwarf} \sim 45$ kpc (Mishra et al., 2024). When comparing these virial radii to the median and average impact parameter of the distribution, $b_{\rm med} \sim b_{\rm avg} \sim 49$ kpc, it is clear that each mass bin is decently sampled (more than 10 galaxies) within

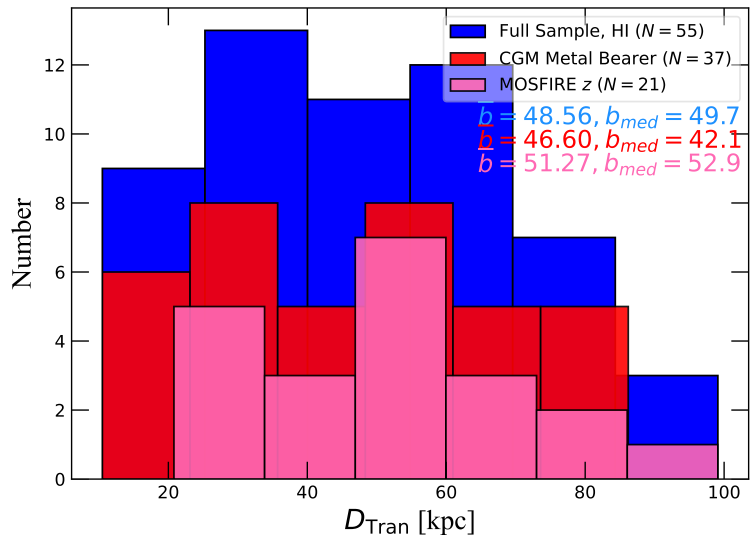

Figure 5.2: Impact parameter distribution (transverse projected physical distance of the galaxy from a QSO) for the full KBSS-InCLOSE sample (blue), sources that show strong metal absorption in their CGM (red), and sources that have a nebular redshift from MOSFIRE (pink). Averages and medians for each distribution are shown in the top right.

$b \leq 2.5R_{\rm vir}$ for all galaxy mass bins.

Getting closer to 25 galaxies per mass bin would be a reasonable goal for more statistically significant trends. This implies that finding more close-in galaxies is a priority that is attainable when considering that more than half of the KBSS QSOs lack deep pointings $t_{exp} \geq 2$ hr and/or lack 360° azimuthal coverage within $\sim$ 100 kpc of the QSOs. Ideally, with KCWI follow-up, or follow-up with a similar IFU, e.g., LLAMAS IFU on Magellan telescope, more galaxies will be discovered.

Figure 5.3 shows the $\log N_{\rm HI}$ distribution for the full sample. The majority of the sample had H I fits extracted from the H I absorber catalog presented in Rudie et al. (2012), who performed Voigt-profile decomposition of $\sim 6,000$ H I absorbers towards the 15 hyperluminous KBSS QSOs. The H I column density was calculated by summing individual components from the catalog over the range $v \sim \pm 1000$ km s^{-1} from z_{sys}. The total H I column densities span from Lyα forest strength absorbers through DLAs (see Table 1.1). The distribution follows the incidence rates shown in Table 1.1 which is surprising given the close proximity of the galaxies to the QSOs. But as mentioned previously, more than half of the galaxies are likely low-mass ($M_* < 10^9$ $M_\odot$), which implies that their virial radii are smaller than $\sim$ 100 kpc. Also, the CGM is known to be clumpy and multiphase which would naturally explain

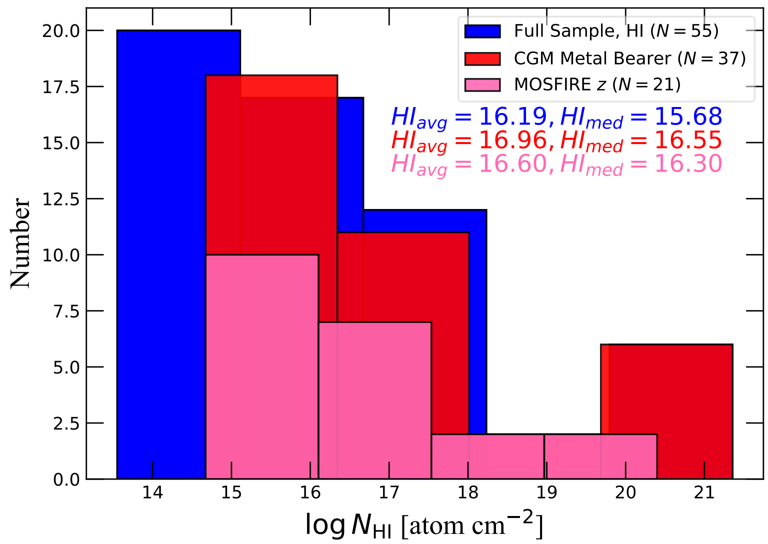

Figure 5.3: $\log N_{\rm HI}$ distribution for the full KBSS-InCLOSE sample (blue), sources that show strong metal absorption in their CGM (red), and sources that have a nebular redshift from MOSFIRE (pink). Averages and medians for each distribution are shown in the top right. The H I columns were calculated by summing over $\pm 1,000$ km s^{-1} from z_{sys}

the H I distribution. Indeed, it has been shown that low- and intermediate-ionization is clumpy on a scale $D_{\rm Tran} < 400$ pc in the $z \sim 2$ CGM (Rudie et al., 2019). Even in the MW disk there are sightlines that show very little extinction (Fitzpatrick, 1999) so it is plausible, if not expected, that the much more diffuse CGM could behave similarly. Regardless, there are still high-H I absorbers in KBSS that do not have associated galaxies which further motivates the need for IFU follow-up to find more galaxies.

Sources that show metal absorption in their CGM have higher $N_{\rm HI}$ on average (and median) compared to the full sample. This classification was made by visually analyzing ion velocity stackplots of the CGM absorption (e.g., see Figure 3.19) for strong metal absorption in *any* ion. C IV was the most commonly observed metal ion.

In Figure 5.4 we combine the impact parameter and $\log N_{\rm HI}$ distributions to examine the H I radial distribution of the sample. There is no obvious trend between $N_{\rm HI}$ and $D_{\rm Tran}$ (top panel). The galaxies span a large range of $N_{\rm HI}$ per fixed b even at the smallest impact parameters $D_{\rm Tran} < 30$ kpc.

There appears to be a $N_{\rm HI}$ threshold, $\log{(N_{\rm HI}/{\rm cm}^{-2})} \sim 15$, that divides metal-

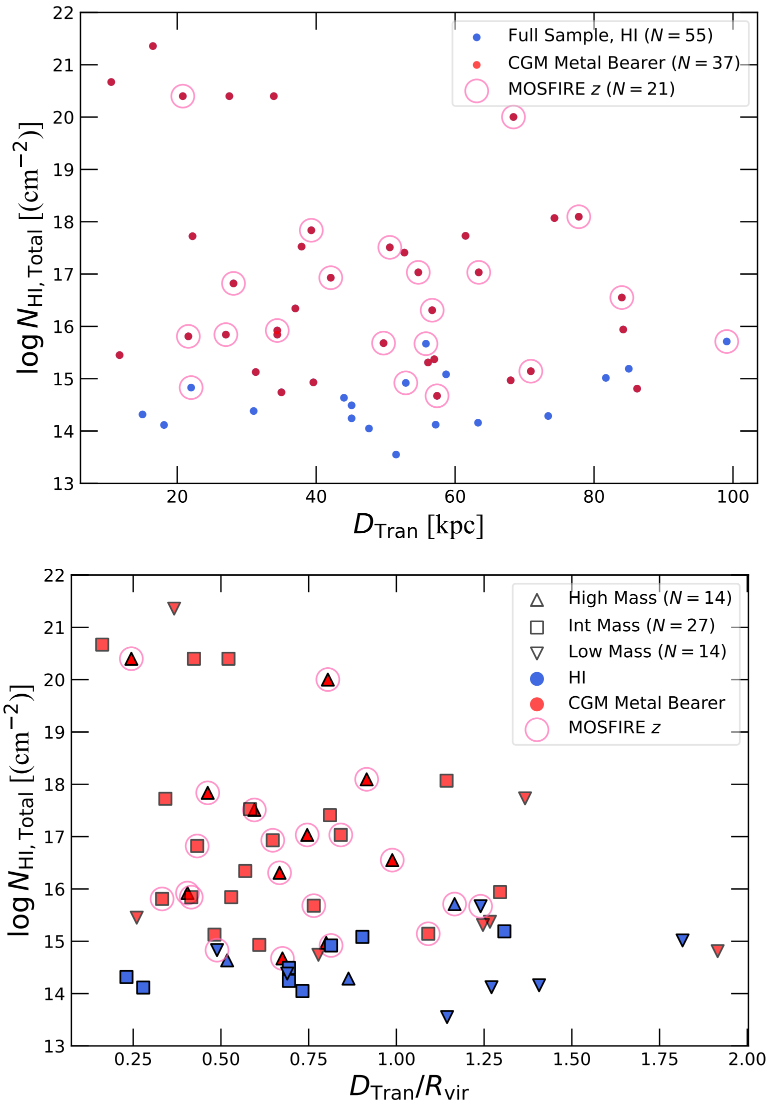

Figure 5.4: *Top panel:* $\log N_{\mathrm{HI}}$ as a function of projected distance for the full KBSS-InCLOSE sample (blue). Sources that show strong metal absorption in their CGM are shown in red, and sources that have a nebular redshift from MOSFIRE are denoted with pink circles. *Bottom panel:* Transverse distance normalized by R_{vir} with the sampled binned into three mass ranges based on their detection (or lack thereof) in KBSS ground-based and *HST* space-based images. Triangles pointing upwards show high-mass sources with $\log(\mathrm{M}_*/\mathrm{M}_\odot) \sim 9.5 - 10.5$ and $R_{\mathrm{vir}} \sim 85$ kpc (Trainor, Steidel, 2012), squares show intermediate-mass objects with ($\log(\mathrm{M}_*/\mathrm{M}_\odot) \sim 8.5 - 9.5$ and $R_{\mathrm{vir}} \sim 65$ kpc (Erb et al., 2023), and triangles pointing downwards show low-mass sources with $\log(\mathrm{M}_*/\mathrm{M}_\odot) \lesssim 8.5$ and $R_{\mathrm{vir}} \sim 45$ kpc (Mishra et al., 2024).

detected absorbers from the rest of the sample. This is interesting because low or high-$N_{\rm HI}$ alone is not a metallicity indicator since ionization levels within the gas can vary significantly. For example. Turner et al. (2015) found that some absorbers with $\log N_{\rm HI}$ at this strength are best explained by collisionally ionized, high-metallicity gas (see also, Simcoe et al., 2004). Similarly, if one were to take a random sample of QSO absorbers of all types there would be metal-poor objects that exist all the way up to DLA column densities (Cooke et al., 2011b; Lehner et al., 2022). This suggests that the galaxies' proximity affects the likelihood of detecting metals in the absorbers.

In the bottom panel of Figure 5.4 we show $\log N_{\rm HI}$ as a function of projected distance normalized by $R_{\rm vir}$ using the approximate radii discussed earlier. Though the binning is coarse and the virial radii are approximate, the sample is finely sampling the CGM of each mass bin within $b < 2R_{\rm vir}$. There is also a general trend that galaxies in the low-mass bin typically have weaker absorption compared to galaxies in the intermediate- and high-mass bins. This motivates the need to measure stellar masses to infer virial radii for each of the galaxies individually.

The left panel of Figure 5.5 shows the velocity difference between the highest $N_{\rm HI}$ component of CGM absorption and $z_{\rm sys}$ as determined from ISM nebular emission. We can see that the majority of galaxies with nebular redshifts from MOSFIRE show $\Delta v_{sys} \sim 0$ whereas the velocity offsets for sources with only $z_{\rm Ly\alpha}$ can vary significantly at fixed impact parameter. The majority of the sources with $|\Delta v| \gtrsim 500$ km s^{-1} do not exhibit strong CGM metal absorption. There appears to be an excess of sources with redshifted CGM absorbers. One would expect no significant correlation with velocity excess (red nor blue) assuming that the galaxies are being selected at random. With a large enough statistical sample one would expect $< \Delta v >= 0$ even when considering the substantial outflows that $z \sim 2$ star-forming galaxies ubiquitously drive. This same excess was seen recently by Prusinski et al. (2025) using the largest sample of galaxy-galaxy pairs at $z \sim 2$. It is therefore important to continue building the sample to explore if this red excess disappears with a large enough sample, and to investigate the implications if it does not.

The right panel of Figure 5.5 shows the difference between the closest (in z) H I component and $z_{\rm sys}$ (regardless of $\log N_{\rm HI}$). As expected, the majority of the sources are close to $v \sim 0$ km s^{-1}. Similar to the left panel, none of the sources with excess velocities $|\Delta v| > 500$ km s^{-1} have nebular redshifts.

Analyzing both panels together provides insight into the galaxy selection criteria for the sample. As mentioned previously, galaxies were included in the sample if their $z_{\rm sys}$ is within $z = 1.9 - 2.6$. Then, we searched within $v \pm 1000$ km s^{-1} of their $z_{\rm sys}$ for an H I absorber in the catalog from Rudie et al. (2012). We can see that there are at least a couple of galaxies with large LOS velocities that exceed the escape velocity of a typical M$_* \sim 10^{10}$ M$_\odot$ KBSS star-forming galaxy $|v| \gtrsim 500$ km s^{-1}. The high velocity of the H I absorbers suggest that either the galaxies exhibits unbound H I gas in their CGM (which is not typical) or that there is a mismatch between galaxy and absorber. It is important to note that no sources with $z_{\rm sys}$ have velocities that exceed $v \sim 500$ km s^{-1}, only sources with $z_{\rm Ly\alpha}$. The latter seems more likely because ISM redshifts from KCWI have a much lower $S/N \sim 3$ compared to the HIRES spectra $S/N \sim 50 - 100$. A rest-optical spectrum is required to distinguish between these two possibilities.

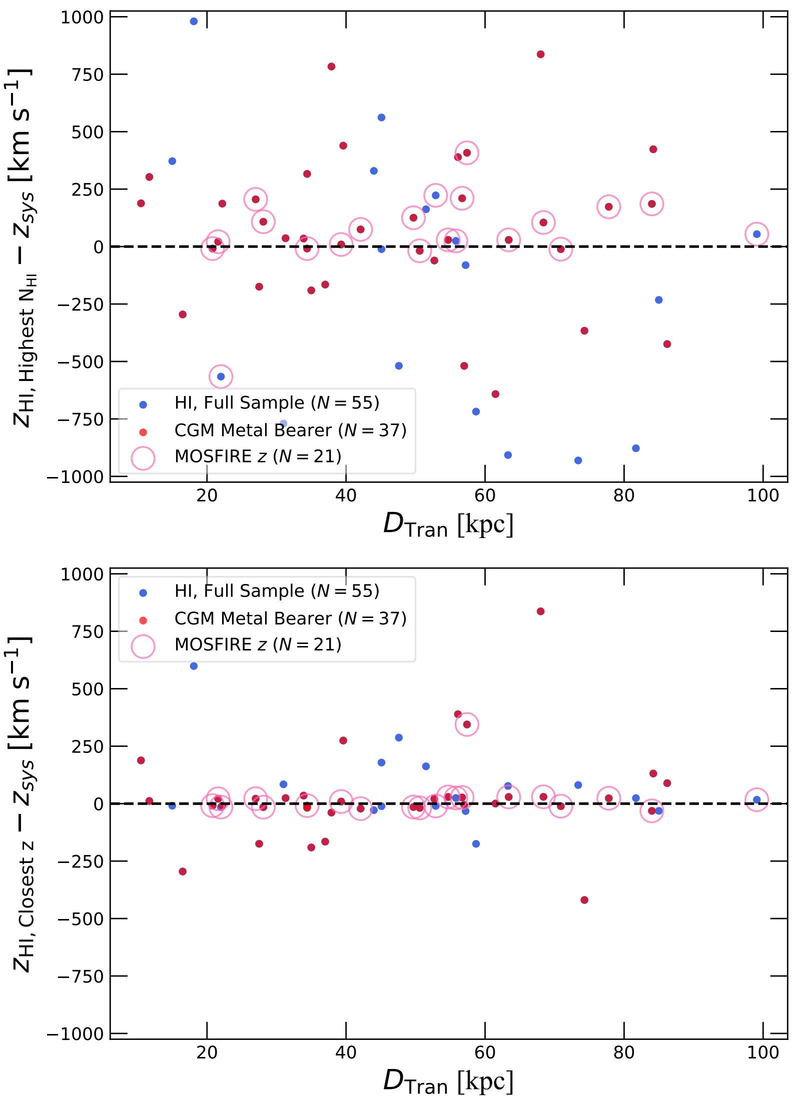

Figure 5.5: Velocity difference between CGM absorption and ISM emission as a function of transverse distance for the full sample. Sources with only H I CGM measurements are shown as blue points, sources that exhibit strong metal absorption in their CGM are shown as red points, and points circled in pink have secure systemic redshifts from MOSFIRE. The *left panel* shows the difference between the velocity of the largest N_{HI} component and z_{sys}. *Right panel* shows the velocity difference between the closest N_{HI} component to z_{sys}, and z_{sys}. Both panels show that there are at least a couple of objects that exceed $|\Delta v_{\mathrm{LOS}}| = 700$ km s^{-1}, the LOS bound for the CGM measured by Rudie et al. (2012).

Chapter 6

SUMMARY & CONCLUSIONS

I have shown in my dissertation that large observational samples of diffuse gas can shed light on our understanding on galactic chemical evolution and the circumgalactic medium (CGM) of $z \sim 2$ star-forming galaxies. I showed that very metal poor DLAs can be used to measure the yields from core-collapse supernovae, and that KBSS-InCLOSE will revolutionize our understanding of the $z \sim 2$ galaxy-scale baryon cycle by allowing us to directly connect CGM and ISM properties of $z \sim 2$ star-forming galaxies. These investigations both relied on QSO absorption line systems (QSO absorbers) to probe diffuse gas that otherwise would be unseen.

In Chapter 2 I show published work (Nuñez et al., 2021) where I compiled the largest sample (N=79) of very-metal poor (VMP; [Fe/H] < -2) Damped Lyman Alpha Absorbers (DLAs; QSO absorbers with high H I column density $\log(N_{\rm HI}/{\rm cm}^{-2}) > 20.3$) to place empirical constraints on the yields of low-metallicity CCSNe. I assumed that each VMP DLA was a protogalaxy early enough in its star-formation history that its enrichment was dominated by CCSNe. This is an alternative approach to using abundances in the atmospheres of metal-poor stars, which requires modeling of stellar atmospheres including accounting for stellar evolution and different equilibrium conditions per ion. I constrained the abundance ratios (with respect to Fe and O) of abundant metals including C, N, O, Si, S, Al, and Fe. I found that for [C,N,O,Al/Fe] VMP DLAs offer a superior approach for determining empirical yields compared to stars, and for [S,Si/Fe] the constraints are complementary. Most modern CCSN yield tables can reproduce the majority of the empirical yields but when imposing realistic constraints on the theoretical yields (i.e., SN energy landscape, Initial Rotation Velocity) only two of the five models could reproduce the empirical yields. The empirical yields I calculated are ready to be be used in galactic chemical evolution models during the earliest phases of galaxies' histories, which seldom have empirical constraints.

In Chapter 3 I show published work (Nuñez et al., 2024) that introduced the KBSS-InCLOSE survey that aims to increase the low number of close-in (within a projected distance of 100 kpc) galaxy-QSO pairs at $z \sim 2$ to analyze the physical properties of CGM gas seen in absorption in the QSO spectra. Before this thesis, there were only nine $z \sim 2$ galaxies with analyzed inner CGM (within 100 kpc) *and* with characterized nebular emission and stellar population properties. The survey builds on the Keck Baryonic Structure Survey (KBSS) and aims to find close-in galaxy-QSO pairs to directly connect the Inner CGM of QSO Line Of Sight Emitting (InCLOSE) galaxies with their ISM. KBSS-InCLOSE relies on new observations that I am conducting using the twin Keck telescopes on Mauna Kea in Hawaii. I use the new KCWI optical integral field unit (rest-FUV at $z \sim 2.3$) to discover new "InCLOSE" galaxies, Keck/MOSFIRE near infrared (NIR) spectroscopy to confirm their redshifts and infer nebular properties including star-formation rate, ground- and space-based optical and NIR images to infer stellar mass and age, and finally high-resolution optical spectra of the QSOs to perform detailed characterization of CGM gas. The novelty of KBSS-InCLOSE goes beyond its large size (55 galaxies currently); the NIR spectra and images allow for the direct determination of galaxy properties, including stellar mass, that are rarely included in similar high-z surveys.

The first results from KBSS-InCLOSE served as a proof of concept for the survey by focusing on the recovery and investigation of two known DLA-host galaxies, a massive $z \sim 2$ galaxy and a lower-mass $z \sim 3$ Lyman Break Galaxy (LBG; one of the first ever discovered). The galaxies were at small enough projected radii from bright QSOs ($b < 3''$) that bright flux extended far into the wings of the QSOs point spread function in the IFU and imaging data. This bright flux needed to be removed from the data to recover the faint close-in galaxies. I developed the tools and techniques required to remove the bright QSOs from the data, and successfully recovered the faint DLA-host galaxies. Additionally, KCWI revealed more than ten new galaxies between both fields, three of which were "underneath" the QSO PSF. I obtained rest-optical spectra of each galaxy, and performed SED fitting, which allowed for the characterization of their ionized ISM and stellar populations. By analyzing their CGM absorption and connecting with their galaxy properties, I showed that the massive $z \sim 2$ galaxy exhibited strong, multiphase, kinematically complex, and in some cases gravitationally unbound metals in its CGM. Jointly analyzing ISM and CGM metallicity, and dust content, supports the picture that outflows are driving metals and dust into the CGM but that the physics governing these processes may depend on the ion being discussed (e.g., O compared to N). Similar findings have been reported by previous studies, suggesting that a consensus picture of the $z \sim 2$ CGM of M_* may be emerging.

In Chapter 4 I show work that will be published soon which presented the second results from the sample, KBSS-InCLOSE II. KBSS-InCLOSE II focused on the first low-mass galaxies ($M < 10^9$) examined in the sample. The three galaxies are in the same field and within a projected distance of $b < 74$ kpc of one of the three QSOs in the field. Two of the galaxies were discovered via Lyα emission in KCWI pointings, while the other was discovered serendipitously on a MOSFIRE slit. Their nebular spectra showed that the galaxies were star-forming (Lyα [O III], and/or Hα emitters), and provided $z_{\rm sys}$which showed that the galaxies were at the same redshift $z_{HU1} = 2.2450$, $z_{BX426b} = 2.2448$, and $z_{CS13} = 2.2433$ which is only a velocity difference of $|\Delta v| \sim 160$ km s^{-1}. The galaxies' compact morphologies and low best-fit SED stellar masses showed that the galaxies were consistent with dwarf galaxies with upper limit on their masses of $M_* \leq 10^{8.4}$ $M_\odot$. Connecting their ISM properties with their CGM absorption showed preliminary evidence that the low-mass $z \sim 2$ CGM may be be distinct from the CGM of low-z dwarf galaxies and $z \sim 2$ massive galaxies. In other words, there may be an evolution of the CGM both in terms of z and stellar mass that will require a larger sample to further investigate.

Finally, in Chapter 5 I show preliminary work that remains to be completed. Specifically, I presented early results of KBSS-InCLOSE III, which examined the entire sample (currently 55 galaxies). At minimum each galaxy had a deep KCWI detection (image and spectrum), and H I absorption from HIRES coverage of the QSO spectra. 21/55 of the galaxies have a nebular redshifts, 37/55 show strong metal absorption in their CGM, and 46/55 have image counterparts in ground- and space-based UGRJHK and *HST*/F160W images. I showed that the $z \sim 2$ inner CGM always shows H I absorption within $v \pm 1,000$ km s^{-1} of $z_{\rm sys}$ for galaxies in the sample, is clumpy, and/or multiphase showing a large spread in log $N_{\rm HI}$ column density at fixed impact parameter, and that the presence of the galaxies appears to affect the properties of the QSO absorbers. The sample will benefit tremendously from IFU follow-up to find more close-in galaxies, and NIR spectroscopic follow-up to secure galaxy redshifts and reduce likelihood of galaxy-absorber mismatches, which I showed may affect at least two of the galaxies in the sample.

Altogether, this thesis has laid fundamental groundwork towards expanding our understanding of the galaxy-scale baryon cycle of $z \sim 2$ star-forming galaxies by building the largest $z \sim 2$ close-in galaxy-QSO pair observational dataset thus far. It provides the data required to perform the most detailed examination of the connection between galaxies and their CGM during the peak epoch for galaxy formation.

Bibliography

Abohalima Abdu, Frebel Anna. JINAbase—A Database for Chemical Abundances of Metal-poor Stars // . X 2018. 238, 2. 36.

Adams S. M., Kochanek C. S., Prieto J. L., Dai X., Shappee B. J., Stanek K. Z. Almost gone: SN 2008S and NGC 300 2008OT-1 are fainter than their progenitors // . VIII 2016. 460, 2. 1645–1657.

Adelberger Kurt L., Steidel Charles C., Shapley Alice E., Pettini Max. Galaxies and Intergalactic Matter at Redshift z~3: Overview // . II 2003. 584, 1. 45–75.

Aguado David S., Allende Prieto Carlos, González Hernández Jonay I., Rebolo Rafael. J0023+0307: A Mega Metal-poor Dwarf Star from SDSS/BOSS // . II 2018. 854, 2. L34.

Aihara Hiroaki, Allende Prieto Carlos, An Deokkeun, Anderson Scott F., Aubourg Éric, Balbinot Eduardo, Beers Timothy C., Berlind Andreas A., Bickerton Steven J., Bizyaev Dmitry, Blanton Michael R., Bochanski John J., Bolton Adam S., Bovy Jo, Brandt W. N., Brinkmann J., Brown Peter J., Brownstein Joel R., Busca Nicolas G., Campbell Heather, Carr Michael A., Chen Yanmei, Chiappini Cristina, Comparat Johan, Connolly Natalia, Cortes Marina, Croft Rupert A. C., Cuesta Antonio J., da Costa Luiz N., Davenport James R. A., Dawson Kyle, Dhital Saurav, Ealet Anne, Ebelke Garrett L., Edmondson Edward M., Eisenstein Daniel J., Escoffier Stephanie, Esposito Massimiliano, Evans Michael L., Fan Xiaohui, Femenía Castellá Bruno, Font-Ribera Andreu, Frinchaboy Peter M., Ge Jian, Gillespie Bruce A., Gilmore G., González Hernández Jonay I., Gott J. Richard, Gould Andrew, Grebel Eva K., Gunn James E., Hamilton Jean-Christophe, Harding Paul, Harris David W., Hawley Suzanne L., Hearty Frederick R., Ho Shirley, Hogg David W., Holtzman Jon A., Honscheid Klaus, Inada Naohisa, Ivans Inese I., Jiang Linhua, Johnson Jennifer A., Jordan Cathy, Jordan Wendell P., Kazin Eyal A., Kirkby David, Klaene Mark A., Knapp G. R., Kneib Jean-Paul, Kochanek C. S., Koesterke Lars, Kollmeier Juna A., Kron Richard G., Lampeitl Hubert, Lang Dustin, Le Goff Jean-Marc, Lee Young Sun, Lin Yen-Ting, Long Daniel C., Loomis Craig P., Lucatello Sara, Lundgren Britt, Lupton Robert H., Ma Zhibo, MacDonald Nicholas, Mahadevan Suvrath, Maia Marcio A. G., Makler Martin, Malanushenko Elena, Malanushenko Viktor, Mandelbaum Rachel, Maraston Claudia, Margala Daniel, Masters Karen L., McBride Cameron K., McGehee Peregrine M., McGreer Ian D., Ménard Brice, Miralda-Escudé Jordi, Morrison Heather L., Mullally F., Muna Demitri, Munn Jeffrey A., Murayama Hitoshi, Myers Adam D., Naugle Tracy, Neto Angelo Fausti, Nguyen Duy Cuong, Nichol Robert C., O'Connell Robert W., Ogando Ricardo L. C., Olmstead Matthew D., Oravetz Daniel J., Padmanabhan Nikhil, Palanque-Delabrouille Nathalie, Pan Kaike, Pandey Parul, Pâris Isabelle, Percival Will J., Petitjean Patrick, Pfaffenberger Robert, Pforr Janine, Phleps Stefanie, Pichon Christophe, Pieri Matthew M., Prada Francisco, Price-Whelan

Adrian M., Raddick M. Jordan, Ramos Beatriz H. F., Reylé Céline, Rich James, Richards Gordon T., Rix Hans-Walter, Robin Annie C., Rocha-Pinto Helio J., Rockosi Constance M., Roe Natalie A., Rollinde Emmanuel, Ross Ashley J., Ross Nicholas P., Rossetto Bruno M., Sánchez Ariel G., Sayres Conor, Schlegel David J., Schlesinger Katharine J., Schmidt Sarah J., Schneider Donald P., Sheldon Erin, Shu Yiping, Simmerer Jennifer, Simmons Audrey E., Sivarani Thirupathi, Snedden Stephanie A., Sobeck Jennifer S., Steinmetz Matthias, Strauss Michael A., Szalay Alexander S., Tanaka Masayuki, Thakar Aniruddha R., Thomas Daniel, Tinker Jeremy L., Tofflemire Benjamin M., Tojeiro Rita, Tremonti Christy A., Vandenberg Jan, Vargas Magaña M., Verde Licia, Vogt Nicole P., Wake David A., Wang Ji, Weaver Benjamin A., Weinberg David H., White Martin, White Simon D. M., Yanny Brian, Yasuda Naoki, Yeche Christophe, Zehavi Idit. The Eighth Data Release of the Sloan Digital Sky Survey: First Data from SDSS-III // . IV 2011. 193, 2. 29.

Akerman C. J., Carigi L., Nissen P. E., Pettini M., Asplund M. The evolution of the C/O ratio in metal-poor halo stars // . II 2004. 414. 931–942.

Akerman C. J., Ellison S. L., Pettini M., Steidel C. C. Zn and Cr abundances in damped Lyman alpha systems from the CORALS survey // . IX 2005. 440, 2. 499–509.

Amarsi A. M., Nissen P. E., Asplund M., Lind K., Barklem P. S. Carbon and oxygen in metal-poor halo stars // . II 2019a. 622. L4.

Amarsi A. M., Nissen P. E., Skúladóttir Á. Carbon, oxygen, and iron abundances in disk and halo stars. Implications of 3D non-LTE spectral line formation // . X 2019b. 630. A104.

Anderson Jay. Empirical Models for the WFC3/IR PSF. III 2016. 12.

Anderson Jay, King Ivan R. Toward High-Precision Astrometry with WFPC2. I. Deriving an Accurate Point-Spread Function // . X 2000. 112, 776. 1360–1382.

Anglés-Alcázar Daniel, Faucher-Giguère Claude-André, Kereš Dušan, Hopkins Philip F., Quataert Eliot, Murray Norman. The cosmic baryon cycle and galaxy mass assembly in the FIRE simulations // . X 2017. 470, 4. 4698–4719.

Asplund Martin. New Light on Stellar Abundance Analyses: Departures from LTE and Homogeneity // . IX 2005. 43, 1. 481–530.

Asplund Martin, Grevesse Nicolas, Sauval A. Jacques, Scott Pat. The Chemical Composition of the Sun // . IX 2009. 47, 1. 481–522.

Astropy Collaboration , Price-Whelan A. M., Sipőcz B. M., Günther H. M., Lim P. L., Crawford S. M., Conseil S., Shupe D. L., Craig M. W., Dencheva N., Ginsburg A., VanderPlas J. T., Bradley L. D., Pérez-Suárez D., de Val-Borro M., Aldcroft T. L., Cruz K. L., Robitaille T. P., Tollerud E. J., Ardelean C., Babej T., Bach Y. P., *Bachetti M., Bakanov A. V., Bamford S. P., Barentsen G., Barmby P., Baumbach A., Berry K. L., Biscani F., Boquien M., Bostroem K. A., Bouma L. G., Brammer G. B., Bray E. M., Breytenbach H., Buddelmeijer H., Burke D. J., Calderone G., Cano Rodríguez J. L., Cara M., Cardoso J. V. M., Cheedella S., Copin Y., Corrales L., Crichton D., D'Avella D., Deil C., Depagne É., Dietrich J. P., Donath A., Droettboom M., Earl N., Erben T., Fabbro S., Ferreira L. A., Finethy T., Fox R. T., Garrison L. H., Gibbons S. L. J., Goldstein D. A., Gommers R., Greco J. P., Greenfield P., Groener A. M., Grollier F., Hagen A., Hirst P., Homeier D., Horton A. J., Hosseinzadeh G., Hu L., Hunkeler J. S., Ivezić Ž., Jain A., Jenness T., Kanarek G., Kendrew S., Kern N. S., Kerzendorf W. E., Khvalko A., King J., Kirkby D., Kulkarni A. M., Kumar A., Lee A., Lenz D., Littlefair S. P., Ma Z., Macleod D. M., Mastropietro M., McCully C., Montagnac S., Morris B. M., Mueller M., Mumford S. J., Muna D., Murphy N. A., Nelson S., Nguyen G. H., Ninan J. P., Nöthe M., Ogaz S., Oh S., Parejko J. K., Parley N., Pascual S., Patil R., Patil A. A., Plunkett A. L., Prochaska J. X., Rastogi T., Reddy Janga V., Sabater J., Sakurikar P., Seifert M., Sherbert L. E., Sherwood-Taylor H., Shih A. Y., Sick J., Silbiger M. T., Singanamalla S., Singer L. P., Sladen P. H., Sooley K. A., Sornarajah S., Streicher O., Teuben P., Thomas S. W., Tremblay G. R., Turner J. E. H., Terrón V., van Kerkwijk M. H., de la Vega A., Watkins L. L., Weaver B. A., Whitmore J. B., Woillez J., Zabalza V., Astropy Contributors* . The Astropy Project: Building an Open-science Project and Status of the v2.0 Core Package // . IX 2018. 156, 3. 123.

Astropy Collaboration , Robitaille Thomas P., Tollerud Erik J., Greenfield Perry, Droettboom Michael, Bray Erik, Aldcroft Tom, Davis Matt, Ginsburg Adam, Price-Whelan Adrian M., Kerzendorf Wolfgang E., Conley Alexander, Crighton Neil, Barbary Kyle, Muna Demitri, Ferguson Henry, Grollier Frédéric, Parikh Madhura M., Nair Prasanth H., Unther Hans M., Deil Christoph, Woillez Julien, Conseil Simon, Kramer Roban, Turner James E. H., Singer Leo, Fox Ryan, Weaver Benjamin A., Zabalza Victor, Edwards Zachary I., Azalee Bostroem K., Burke D. J., Casey Andrew R., Crawford Steven M., Dencheva Nadia, Ely Justin, Jenness Tim, Labrie Kathleen, Lim Pey Lian, Pierfederici Francesco, Pontzen Andrew, Ptak Andy, Refsdal Brian, Servillat Mathieu, Streicher Ole. Astropy: A community Python package for astronomy // . X 2013. 558. A33.

Balashev S. A., Petitjean P., Ivanchik A. V., Ledoux C., Srianand R., Noterdaeme P., Varshalovich D. A. Partial coverage of the broad-line region of Q1232+082 by an intervening H_2-bearing cloud // . XI 2011. 418, 1. 357–369.

Baldwin J. A., Phillips M. M., Terlevich R. Classification parameters for the emission-line spectra of extragalactic objects. // . II 1981. 93. 5–19.

Bastian Nate, Kamann Sebastian, Amard Louis, Charbonnel Corinne, Haemmerlé Lionel, Matt Sean P. On the origin of the bimodal rotational velocity distribution in stellar clusters: rotation on the pre-main sequence // . VI 2020. 495, 2. 1978–1983.

Battisti A. J., Meiring J. D., Tripp T. M., Prochaska J. X., Werk J. K., Jenkins E. B., Lehner N., Tumlinson J., Thom C. The First Observations of Low-redshift Damped Lyα Systems with the Cosmic Origins Spectrograph: Chemical Abundances and Affiliated Galaxies // . I 2012. 744, 2. 93.

Berg Danielle A., Erb Dawn K., Henry Richard B. C., Skillman Evan D., McQuinn Kristen B. W. The Chemical Evolution of Carbon, Nitrogen, and Oxygen in Metal-poor Dwarf Galaxies // The Astrophysical Journal. mar 2019. 874, 1. 93.

Berg Michelle A., Lehner Nicolas, Howk J. Christopher, O'Meara John M., Schaye Joop, Straka Lorrie A., Cooksey Kathy L., Tripp Todd M., Prochaska J. Xavier, Oppenheimer Benjamin D., Johnson Sean D., Muzahid Sowgat, Bordoloi Rongmon, Werk Jessica K., Fox Andrew J., Katz Neal, Wendt Martin, Peeples Molly S., Ribaudo Joseph, Tumlinson Jason. The Bimodal Absorption System Imaging Campaign (BASIC). I. A Dual Population of Low-metallicity Absorbers at z < 1 // . II 2023. 944, 1. 101.

Berg T. A. M., Ellison S. L., Sánchez-Ramírez R., Prochaska J. X., Lopez S., D'Odorico V., Becker G., Christensen L., Cupani G., Denney K., Worseck G. Chemical abundances of the damped Lyman α systems in the XQ-100 survey // . XII 2016. 463, 3. 3021–3037.

Berg Trystyn A. M., Ellison Sara L., Prochaska J. Xavier, Venn Kim A., Dessauges-Zavadsky Miroslava. The chemistry of the most metal-rich damped Lyman α systems at z $\sim$ 2 - II. Context with the Local Group // . X 2015a. 452, 4. 4326–4346.

Berg Trystyn A. M., Ellison Sara L., Venn Kim A., Prochaska J. Xavier. A search for boron in damped Lyα systems // . X 2013. 434, 4. 2892–2906.

Berg Trystyn A. M., Fumagalli Michele, D'Odorico Valentina, Ellison Sara L., López Sebastián, Becker George D., Christensen Lise, Cupani Guido, Denney Kelly D., Sánchez-Ramírez Rubén, Worseck Gábor. Sub-damped Lyman α systems in the XQ-100 survey - II. Chemical evolution at 2.4 $\leq$ z $\leq$ 4.3 // . IV 2021. 502, 3. 4009–4025.

Berg Trystyn A. M., Neeleman Marcel, Prochaska J. Xavier, Ellison Sara L., Wolfe Arthur M. The Most Metal-rich Damped Lyα Systems at z $\gtrsim$ 1.5 I: The Data // . II 2015b. 127, 948. 167.

Bergeron J. The MG II absorption system in the QSO PKS 2128-12 : a galaxy disc/halo with a radius of 65 kpc. // . I 1986. 155. L8–L11.

Bernstein Rebecca, Shectman Stephen A., Gunnels Steven M., Mochnacki Stefan, Athey Alex E. MIKE: A Double Echelle Spectrograph for the Magellan Telescopes at Las Campanas Observatory // Instrument Design and Performance for Optical/Infrared Ground-based Telescopes. 4841. III 2003. 1694–1704. (Society of Photo-Optical Instrumentation Engineers (SPIE) Conference Series).

Blitz Leo, Spergel David N., Teuben Peter J., Hartmann Dap, Burton W. Butler. High-Velocity Clouds: Building Blocks of the Local Group // . IV 1999. 514, 2. 818–843.

Boettcher Erin, Chen Hsiao-Wen, Zahedy Fakhri S., Cooper Thomas J., Johnson Sean D., Rudie Gwen C., Chen Mandy C., Petitjean Patrick, Cantalupo Sebastiano, Cooksey Kathy L., Faucher-Giguère Claude-André, Greene Jenny E., Lopez Sebastian, Mulchaey John S., Penton Steven V., Putman Mary E., Rafelski Marc, Rauch Michael, Schaye Joop, Simcoe Robert A., Walth Gregory L. The Cosmic Ultraviolet Baryon Survey (CUBS). II. Discovery of an H_2-bearing DLA in the Vicinity of an Early-type Galaxy at z = 0.576 // . V 2021. 913, 1. 18.

Bordoloi Rongmon, Tumlinson Jason, Werk Jessica K., Oppenheimer Benjamin D., Peeples Molly S., Prochaska J. Xavier, Tripp Todd M., Katz Neal, Davé Romeel, Fox Andrew J., Thom Christopher, Ford Amanda Brady, Weinberg David H., Burchett Joseph N., Kollmeier Juna A. The COS-Dwarfs Survey: The Carbon Reservoir around Sub-L* Galaxies // . XII 2014. 796, 2. 136.

Borthakur Sanchayeeta, Heckman Timothy, Tumlinson Jason, Bordoloi Rongmon, Thom Christopher, Catinella Barbara, Schiminovich David, Davé Romeel, Kauffmann Guinevere, Moran Sean M., Saintonge Amelie. Connection between the Circumgalactic Medium and the Interstellar Medium of Galaxies: Results from the COS-GASS Survey // . XI 2015. 813, 1. 46.

Borthakur Sanchayeeta, Padave Mansi, Heckman Timothy, Gim Hansung B., Olvera Alejandro J., Koplitz Brad, Momjian Emmanuel, Jansen Rolf A., Thilker David, Kauffman Guinevere, Fox Andrew J., Tumlinson Jason, Kennicutt Robert C., Nelson Dylan, Monckiewicz Jacqueline, Naab Thorsten. DIISC Survey: Deciphering the Interplay Between the Interstellar Medium, Stars, and the Circumgalactic Medium Survey // arXiv e-prints. IX 2024. arXiv:2409.12554.

Bouvier J. Observational studies of stellar rotation // EAS Publications Series. 62. IX 2013. 143–168. (EAS Publications Series).

Bradley Larry, Sipőcz Brigitta, Robitaille Thomas, Tollerud Erik, Vinícius Zé, Deil Christoph, Barbary Kyle, Wilson Tom J, Busko Ivo, Donath Axel, Günther Hans Moritz, Cara Mihai, Lim P. L., Meßlinger Sebastian, Conseil Simon, Bostroem Azalee, Droettboom Michael, Bray E. M., Bratholm Lars Andersen, Barentsen Geert, Craig Matt, Rathi Shivangee, Pascual Sergio, Perren Gabriel, Georgiev Iskren Y., Val-Borro Miguel de, Kerzendorf Wolfgang, Bach Yoonsoo P., Quint Bruno, Souchereau Harrison. astropy/photutils: 1.5.0. VII 2022.

Brocklehurst M. Calculations of level populations for the low levels of hydrogenic ions in gaseous nebulae. // . I 1971. 153. 471.

Burrows Adam, Radice David, Vartanyan David. Three-dimensional supernova explosion simulations of 9-, 10-, 11-, 12-, and 13-M stars // . V 2019. 485, 3. 3153–3168.

Calura F., Matteucci F., Vladilo G. Chemical evolution and nature of damped Lyman α systems // . III 2003. 340, 1. 59–72.

Cameron Alex J., Fisher Deanne B., McPherson Daniel, Kacprzak Glenn G., Berg Danielle A., Bolatto Alberto, Chisholm John, Herrera-Camus Rodrigo, Nielsen Nikole M., Reichardt Chu Bronwyn, Rickards Vaught Ryan J., Sandstrom Karin, Trenti Michele. The DUVET Survey: Direct T_e-based Metallicity Mapping of Metal-enriched Outflows and Metal-poor Inflows in Markarian 1486 // . IX 2021. 918, 1. L16.

Cantalupo Sebastiano, Pezzulli Gabriele, Lilly Simon J., Marino Raffaella Anna, Gallego Sofia G., Schaye Joop, Bacon Roland, Feltre Anna, Kollatschny Wolfram, Nanayakkara Themiya, Richard Johan, Wendt Martin, Wisotzki Lutz, Prochaska J. Xavier. The large- and small-scale properties of the intergalactic gas in the Slug Ly α nebula revealed by MUSE He II emission observations // . III 2019. 483, 4. 5188–5204.

Cardelli Jason A., Clayton Geoffrey C., Mathis John S. The Relationship between Infrared, Optical, and Ultraviolet Extinction // . X 1989. 345. 245.

Cayrel R., Depagne E., Spite M., Hill V., Spite F., François P., Plez B., Beers T., Primas F., Andersen J., Barbuy B., Bonifacio P., Molaro P., Nordström B. First stars V - Abundance patterns from C to Zn and supernova yields in the early Galaxy // . III 2004. 416. 1117–1138.

Centurión M., Molaro P., Vladilo G., Péroux C., Levshakov S. A., D'Odorico V. Early stages of nitrogen enrichment in galaxies: Clues from measurements in damped Lyman alpha systems // . V 2003. 403. 55–72.

Chabanier Solène, Etourneau Thomas, Le Goff Jean-Marc, Rich James, Stermer Julianna, Abolfathi Bela, Font-Ribera Andreu, Gonzalez-Morales Alma X., de la Macorra Axel, Pérez-Ràfols Ignasi, Petitjean Patrick, Pieri Matthew M., Ravoux Corentin, Rossi Graziano, Schneider Donald P. The Completed Sloan Digital Sky Survey IV Extended Baryon Oscillation Spectroscopic Survey: The Damped Lyα Systems Catalog // . I 2022. 258, 1. 18.

Chapman S. C., Blain A. W., Smail Ian, Ivison R. J. A Redshift Survey of the Submillimeter Galaxy Population // . IV 2005. 622, 2. 772–796.

Chen Hsiao-Wen, Kennicutt Jr. Robert C., Rauch Michael. Abundance Profiles and Kinematics of Damped Lyα Absorbing Galaxies at z < 0.651, // . II 2005. 620, 2. 703–722.

Chen Hsiao-Wen, Lanzetta Kenneth M., Webb John K., Barcons Xavier. The Gaseous Extent of Galaxies and the Origin of Lyα Absorption Systems. III. Hubble Space Telescope Imaging of Lyα-absorbing Galaxies at z < 1 // . V 1998. 498, 1. 77–94.

Chen Hsiao-Wen, Qu Zhijie, Rauch Michael, Chen Mandy C., Zahedy Fakhri S., Johnson Sean D., Schaye Joop, Rudie Gwen C., Boettcher Erin, Cantalupo Sebastiano, Faucher-Giguère Claude-André, Greene Jenny E., Lopez Sebastian, Simcoe Robert A. The Cosmic Ultraviolet Baryon Survey: Empirical Characterization of Turbulence in the Cool Circumgalactic Medium // . IX 2023. 955, 1. L25.

Chen Hsiao-Wen, Zahedy Fakhri S., Boettcher Erin, Cooper Thomas M., Johnson Sean D., Rudie Gwen C., Chen Mandy C., Walth Gregory L., Cantalupo Sebastiano, Cooksey Kathy L., Faucher-Giguère Claude-André, Greene Jenny E., Lopez Sebastian, Mulchaey John S., Penton Steven V., Petitjean Patrick, Putman Mary E., Rafelski Marc, Rauch Michael, Schaye Joop, Simcoe Robert A., Weiner Benjamin J. The Cosmic Ultraviolet Baryon Survey (CUBS) - I. Overview and the diverse environments of Lyman limit systems at z < 1 // . IX 2020a. 497, 1. 498–520.

Chen Yuguang, Steidel Charles C., Erb Dawn K., Law David R., Trainor Ryan F., Reddy Naveen A., Shapley Alice E., Pahl Anthony J., Strom Allison L., Lamb Noah R., Li Zhihui, Rudie Gwen C. The KBSS-KCWI survey: the connection between extended Ly α haloes and galaxy azimuthal angle at z 2-3 // . XI 2021. 508, 1. 19–43.

Chen Yuguang, Steidel Charles C., Hummels Cameron B., Rudie Gwen C., Dong Bili, Trainor Ryan F., Bogosavljević Milan, Erb Dawn K., Pettini Max, Reddy Naveen A., Shapley Alice E., Strom Allison L., Theios Rachel L., Faucher-Giguère Claude-André, Hopkins Philip F., Kereš Dušan. The Keck Baryonic Structure Survey: using foreground/background galaxy pairs to trace the structure and kinematics of circumgalactic neutral hydrogen at z 2 // . XII 2020b. 499, 2. 1721–1746.

Chisholm J., Tremonti C., Leitherer C. Metal-enriched galactic outflows shape the mass-metallicity relationship // . XII 2018. 481, 2. 1690–1706.

Chiti Anirudh, Frebel Anna, Ji Alexander P., Jerjen Helmut, Kim Dongwon, Norris John E. Chemical Abundances of New Member Stars in the Tucana II Dwarf Galaxy // . IV 2018. 857, 1. 74.

Choi Bo-Eun, Werk Jessica K., Tchernyshyov Kirill, Prochaska J. Xavier, Zheng Yong, Putman Mary E., Fielding Drummond B., Strader Jay. Metallicity Mapping of the Ionized Diffuse Gas at the Milky Way Disk–Halo Interface // . XII 2024. 976, 2. 222.

Christensen L., Sánchez S. F., Jahnke K., Becker T., Wisotzki L., Kelz A., Popović L. Č., Roth M. M. Integral field spectroscopy of extended Lyα emission from the DLA galaxy in Q2233+131 // . IV 2004. 417. 487–498.

Christensen L., Wisotzki L., Roth M. M., Sánchez S. F., Kelz A., Jahnke K. An integral field spectroscopic survey for high redshift damped Lyman-α galaxies // . VI 2007. 468, 2. 587–601.

Christenson Holly M., Jorgenson Regina A. Keck/OSIRIS IFU Detection of a z ~ 3 Damped Lyα Host Galaxy // . IX 2019. 883, 1. 17.

Cooke Ryan, Pettini Max. The primordial abundance of deuterium: ionization correction // . I 2016. 455, 2. 1512–1521.

Cooke Ryan, Pettini Max, Jorgenson Regina A., Murphy Michael T., Rudie Gwen C., Steidel Charles C. The explosion energy of early stellar populations: the Fe-peak element ratios in low-metallicity damped Lyα systems // . V 2013. 431, 2. 1625–1637.

Cooke Ryan, Pettini Max, Murphy Michael T. A new candidate for probing Population III nucleosynthesis with carbon-enhanced damped Lyα systems // . IX 2012. 425, 1. 347–354.

Cooke Ryan, Pettini Max, Steidel Charles C., King Lindsay J., Rudie Gwen C., Rakic Olivera. A newly discovered DLA and associated Lyα emission in the spectra of the gravitationally lensed quasar UM673A,B // . XII 2010. 409, 2. 679–693.

Cooke Ryan, Pettini Max, Steidel Charles C., Rudie Gwen C., Jorgenson Regina A. A carbon-enhanced metal-poor damped Lyα system: probing gas from Population III nucleosynthesis? // . IV 2011a. 412, 2. 1047–1058.

Cooke Ryan, Pettini Max, Steidel Charles C., Rudie Gwen C., Nissen Poul E. The most metal-poor damped Lyα systems: insights into chemical evolution in the very metal-poor regime // . X 2011b. 417, 2. 1534–1558.

Cooke Ryan J., Madau Piero. Carbon-enhanced Metal-poor Stars: Relics from the Dark Ages // . VIII 2014. 791, 2. 116.

Cooke Ryan J., Pettini Max, Jorgenson Regina A. The Most Metal-poor Damped Lyα Systems: An Insight into Dwarf Galaxies at High-redshift // . II 2015. 800, 1. 12.

Cooke Ryan J., Pettini Max, Jorgenson Regina A., Murphy Michael T., Steidel Charles C. Precision Measures of the Primordial Abundance of Deuterium // . I 2014. 781, 1. 31.

Cooke Ryan J., Pettini Max, Nollett Kenneth M., Jorgenson Regina. The Primordial Deuterium Abundance of the Most Metal-poor Damped Lyman-α System // . X 2016. 830, 2. 148.

Cooke Ryan J., Pettini Max, Steidel Charles C. Discovery of the most metal-poor damped Lyman-α system // . V 2017. 467, 1. 802–811.

Cooper Thomas J., Rudie Gwen C., Chen Hsiao-Wen, Johnson Sean D., Zahedy Fakhri S., Chen Mandy C., Boettcher Erin, Walth Gregory L., Cantalupo Sebastiano, Cooksey Kathy L., Faucher-Giguère Claude-André, Greene Jenny E., Lopez Sebastian, Mulchaey John S., Penton Steven V., Petitjean Patrick, Putman Mary E., Rafelski Marc, Rauch Michael, Schaye Joop, Simcoe Robert A. The Cosmic Ultraviolet Baryon Survey (CUBS) - IV. The complex multiphase circumgalactic medium as revealed by partial Lyman limit systems // . XII 2021. 508, 3. 4359–4384.

D'Odorico V., Feruglio C., Ferrara A., Gallerani S., Pallottini A., Carniani S., Maiolino R., Cristiani S., Marconi A., Piconcelli E., Fiore F. Witnessing Galaxy Assembly at the Edge of the Reionization Epoch // . VIII 2018. 863, 2. L29.

D'Odorico V., Petitjean P., Cristiani S. High matter density peaks from UVES observations of QSO pairs: Correlation properties and chemical abundances // . VII 2002. 390. 13–25.

Danielson A. L. R., Swinbank A. M., Smail Ian, Simpson J. M., Casey C. M., Chapman S. C., da Cunha E., Hodge J. A., Walter F., Wardlow J. L., Alexander D. M., Brandt W. N., de Breuck C., Coppin K. E. K., Dannerbauer H., Dickinson M., Edge A. C., Gawiser E., Ivison R. J., Karim A., Kovacs A., Lutz D., Menten K., Schinnerer E., Weiß A., van der Werf P. An ALMA Survey of Submillimeter Galaxies in the Extended Chandra Deep Field South: Spectroscopic Redshifts // . V 2017. 840, 2. 78.

De Cia A., Ledoux C., Mattsson L., Petitjean P., Srianand R., Gavignaud I., Jenkins E. B. Dust-depletion sequences in damped Lyman-α absorbers. A unified picture from low-metallicity systems to the Galaxy // . XII 2016. 596. A97.

De Cia A., Ledoux C., Savaglio S., Schady P., Vreeswijk P. M. Dust-to-metal ratios in damped Lyman-α absorbers. Fresh clues to the origins of dust and optical extinction towards γ-ray bursts // . XII 2013. 560. A88.

De Cia Annalisa, Ledoux Cédric, Petitjean Patrick, Savaglio Sandra. The cosmic evolution of dust-corrected metallicity in the neutral gas // . IV 2018. 611. A76.

Dekker Hans, D'Odorico Sandro, Kaufer Andreas, Delabre Bernard, Kotzlowski Heinz. Design, construction, and performance of UVES, the echelle spectrograph for the UT2 Kueyen Telescope at the ESO Paranal Observatory // Optical and IR Telescope Instrumentation and Detectors. 4008. VIII 2000. 534–545. (Society of Photo-Optical Instrumentation Engineers (SPIE) Conference Series).

Dessauges-Zavadsky M., Calura F., Prochaska J. X., D'Odorico S., Matteucci F. A comprehensive set of elemental abundances in damped Lyα systems: Revealing the nature of these high-redshift galaxies // . III 2004. 416. 79–110.

Dessauges-Zavadsky M., Calura F., Prochaska J. X., D'Odorico S., Matteucci F. A new comprehensive set of elemental abundances in DLAs. III. Star formation histories // . VIII 2007. 470, 2. 431–448.

Dessauges-Zavadsky M., D'Odorico S., McMahon R. G., Molaro P., Ledoux C., Péroux C., Storrie-Lombardi L. J. UVES observations of a damped Lyalpha system at z_{abs} = 4.466 towards the quasar APM BR J0307-4945 // . V 2001. 370. 426–435.

Dessauges-Zavadsky M., Péroux C., Kim T. S., D'Odorico S., McMahon R. G. A homogeneous sample of sub-damped Lyman α systems - I. Construction of the sample and chemical abundance measurements // . X 2003. 345, 2. 447–479.

Dessauges-Zavadsky M., Prochaska J. X., D'Odorico S., Calura F., Matteucci F. A new comprehensive set of elemental abundances in DLAs. II. Data analysis and chemical variation studies // . I 2006. 445, 1. 93–113.

Draine Bruce T. Physics of the Interstellar and Intergalactic Medium. 2011.

Dutta R., Srianand R., Rahmani H., Petitjean P., Noterdaeme P., Ledoux C. A study of low-metallicity DLAs at high redshift and C II* as a probe of their physical conditions // . V 2014. 440, 1. 307–326.

Dutta Rajeshwari, Fumagalli Michele, Fossati Matteo, Lofthouse Emma K., Prochaska J. Xavier, Arrigoni Battaia Fabrizio, Bielby Richard M., Cantalupo Sebastiano, Cooke Ryan J., Murphy Michael T., O'Meara John M. MUSE Analysis of Gas around Galaxies (MAGG) - II: metal-enriched halo gas around z $\sim$ 1 galaxies // . XII 2020. 499, 4. 5022–5046.

Dutta Sayak, Muzahid Sowgat, Schaye Joop, Cantalupo Sebastiano, Chen Hsiao-Wen, Johnson Sean. MUSEQuBES: The Kinematics of O VI-bearing Gas in and around Low-redshift Galaxies // . II 2025. 980, 2. 264.

Ebinger Kevin, Curtis Sanjana, Ghosh Somdutta, Fröhlich Carla, Hempel Matthias, Perego Albino, Liebendörfer Matthias, Thielemann Friedrich-Karl. PUSHing Core-collapse Supernovae to Explosions in Spherical Symmetry. IV. Explodability, Remnant Properties, and Nucleosynthesis Yields of Low-metallicity Stars // . I 2020. 888, 2. 91.

Ellison S. L., Lopez S. Unusual metal abundances in a pair of damped Lyman alpha systems at z ~2 // . XII 2001. 380. 117–122.

Ellison Sara L., Prochaska J. Xavier, Hennawi Joseph, Lopez Sebastian, Usher Christopher, Wolfe Arthur M., Russell David M., Benn Chris R. The nature of proximate damped Lyman α systems // . VIII 2010. 406, 3. 1435–1459.

Erb Dawn K., Li Zhihui, Steidel Charles C., Chen Yuguang, Gronke Max, Strom Allison L., Trainor Ryan F., Rudie Gwen C. The Circumgalactic Medium of Extreme Emission Line Galaxies at z 2: Resolved Spectroscopy and Radiative Transfer Modeling of Spatially Extended Lyα Emission in the KBSS-KCWI Survey // . VIII 2023. 953, 1. 118.

Erb Dawn K., Pettini Max, Steidel Charles C., Strom Allison L., Rudie Gwen C., Trainor Ryan F., Shapley Alice E., Reddy Naveen A. A High Fraction of Lyα Emitters among Galaxies with Extreme Emission Line Ratios at z ∼2 // . X 2016. 830, 1. 52.

Erb Dawn K., Shapley Alice E., Pettini Max, Steidel Charles C., Reddy Naveen A., Adelberger Kurt L. The Mass-Metallicity Relation at z>∼2 // . VI 2006a. 644, 2. 813–828.

Erb Dawn K., Steidel Charles C., Shapley Alice E., Pettini Max, Reddy Naveen A., Adelberger Kurt L. The Stellar, Gas, and Dynamical Masses of Star-forming Galaxies at z ∼2 // . VII 2006b. 646, 1. 107–132.

Erni P., Richter P., Ledoux C., Petitjean P. The most metal-poor damped Lyman α system at z <3: constraints on early nucleosynthesis // . V 2006. 451, 1. 19–26.

Ertl T., Janka H. Th., Woosley S. E., Sukhbold T., Ugliano M. A Two-parameter Criterion for Classifying the Explodability of Massive Stars by the Neutrino-driven Mechanism // . II 2016. 818, 2. 124.

Ertl T., Woosley S. E., Sukhbold Tuguldur, Janka H. T. The Explosion of Helium Stars Evolved with Mass Loss // . II 2020. 890, 1. 51.

Fabbian D., Nissen P. E., Asplund M., Pettini M., Akerman C. The C/O ratio at low metallicity: constraints on early chemical evolution from observations of Galactic halo stars // . VI 2009. 500, 3. 1143–1155.

Faucher-Giguère Claude-André, Oh S. Peng. Key Physical Processes in the Circumgalactic Medium // . VIII 2023. 61. 131–195.

Feltzing S., Eriksson K., Kleyna J., Wilkinson M. I. Evidence of enrichment by individual SN from elemental abundance ratios in the very metal-poor dSph galaxy Boötes I // . XII 2009. 508, 1. L1–L4.

Field George B., Steigman Gary. Charge Transfer and Ionization Equilibrium in the Interstellar Medium // . V 1971. 166. 59.

Finkelstein Steven L., Bagley Micaela B., Arrabal Haro Pablo, Dickinson Mark, Ferguson Henry C., Kartaltepe Jeyhan S., Papovich Casey, Burgarella Denis, Kocevski Dale D., Huertas-Company Marc, Iyer Kartheik G., Koekemoer Anton M., Larson Rebecca L., Pérez-González Pablo G., Rose Caitlin, Tacchella Sandro, Wilkins Stephen M., Chworowsky Katherine, Medrano Aubrey, Morales Alexa M., Somerville Rachel S., Yung L. Y. Aaron, Fontana Adriano, Giavalisco Mauro, Grazian Andrea, Grogin Norman A., Kewley Lisa J., Kirkpatrick Allison, Kurczynski Peter, Lotz Jennifer M., Pentericci Laura, Pirzkal Nor, Ravindranath Swara, Ryan Russell E., Trump Jonathan R., Yang Guang, Almaini Omar, Amorín Ricardo O., Annunziatella Marianna, Backhaus Bren E., Barro Guillermo, Behroozi Peter, Bell Eric F., Bhatawdekar Rachana, Bisigello Laura, Bromm Volker, Buat

Véronique, Buitrago Fernando, Calabrò Antonello, Casey Caitlin M., Castellano Marco, Chávez Ortiz Óscar A., Ciesla Laure, Cleri Nikko J., Cohen Seth H., Cole Justin W., Cooke Kevin C., Cooper M. C., Cooray Asantha R., Costantin Luca, Cox Isabella G., Croton Darren, Daddi Emanuele, Davé Romeel, de La Vega Alexander, Dekel Avishai, Elbaz David, Estrada-Carpenter Vicente, Faber Sandra M., Fernández Vital, Finkelstein Keely D., Freundlich Jonathan, Fujimoto Seiji, García-Argumánez Ángela, Gardner Jonathan P., Gawiser Eric, Gómez-Guijarro Carlos, Guo Yuchen, Hamblin Kurt, Hamilton Timothy S., Hathi Nimish P., Holwerda Benne W., Hirschmann Michaela, Hutchison Taylor A., Jaskot Anne E., Jha Saurabh W., Jogee Shardha, Juneau Stéphanie, Jung Intae, Kassin Susan A., Le Bail Aurélien, Leung Gene C. K., Lucas Ray A., Magnelli Benjamin, Mantha Kameswara Bharadwaj, Matharu Jasleen, McGrath Elizabeth J., McIntosh Daniel H., Merlin Emiliano, Mobasher Bahram, Newman Jeffrey A., Nicholls David C., Pandya Viraj, Rafelski Marc, Ronayne Kaila, Santini Paola, Seillé Lise-Marie, Shah Ekta A., Shen Lu, Simons Raymond C., Snyder Gregory F., Stanway Elizabeth R., Straughn Amber N., Teplitz Harry I., Vanderhoof Brittany N., Vega-Ferrero Jesús, Wang Weichen, Weiner Benjamin J., Willmer Christopher N. A., Wuyts Stijn, Zavala Jorge A., Ceers Team . A Long Time Ago in a Galaxy Far, Far Away: A Candidate z ∼ 12 Galaxy in Early JWST CEERS Imaging // . XII 2022. 940, 2. L55.

Fitzpatrick Edward L. Correcting for the Effects of Interstellar Extinction // . I 1999. 111, 755. 63–75.

Fox Andrew J., Richter Philipp, Ashley Trisha, Heckman Timothy M., Lehner Nicolas, Werk Jessica K., Bordoloi Rongmon, Peeples Molly S. The Mass Inflow and Outflow Rates of the Milky Way // . X 2019. 884, 1. 53.

François P., Monaco L., Bonifacio P., Moni Bidin C., Geisler D., Sbordone L. Abundance ratios of red giants in low-mass ultra-faint dwarf spheroidal galaxies // . IV 2016. 588. A7.

Frebel Anna, Norris John E. Near-Field Cosmology with Extremely Metal-Poor Stars // . VIII 2015. 53. 631–688.

Frebel Anna, Simon Joshua D., Geha Marla, Willman Beth. High-Resolution Spectroscopy of Extremely Metal-Poor Stars in the Least Evolved Galaxies: Ursa Major II and Coma Berenices // . I 2010. 708, 1. 560–583.

Frebel Anna, Simon Joshua D., Kirby Evan N. Segue 1: An Unevolved Fossil Galaxy from the Early Universe // . V 2014. 786, 1. 74.

Fumagalli Michele, Mackenzie Ruari, Trayford James, Theuns Tom, Cantalupo Sebastiano, Christensen Lise, Fynbo Johan P. U., Møller Palle, O'Meara John, Prochaska J. Xavier, Rafelski Marc, Shanks Tom. Witnessing galaxy assembly in an extended z≈3 structure // . XI 2017. 471, 3. 3686–3698.

Fumagalli Michele, O'Meara John M., Prochaska J. Xavier. The physical properties of z > 2 Lyman limit systems: new constraints for feedback and accretion models // . II 2016. 455, 4. 4100–4121.

Fumagalli Michele, O'Meara John M., Prochaska J. Xavier, Rafelski Marc, Kanekar Nissim. Directly imaging damped Ly α galaxies at z > 2 - III. The star formation rates of neutral gas reservoirs at z ~ 2.7 // . I 2015. 446, 3. 3178–3198.

Fynbo J. P. U., Ledoux C., Noterdaeme P., Christensen L., Møller P., Durgapal A. K., Goldoni P., Kaper L., Krogager J. K., Laursen P., Maund J. R., Milvang-Jensen B., Okoshi K., Rasmussen P. K., Thorsen T. J., Toft S., Zafar T. Galaxy counterparts of metal-rich damped Lyα absorbers - II. A solar-metallicity and dusty DLA at z_{abs}= 2.58 // . VI 2011. 413, 4. 2481–2488.

Fynbo Johan P. U., Prochaska J. Xavier, Sommer-Larsen Jesper, Dessauges-Zavadsky Miroslava, Møller Palle. Reconciling the Metallicity Distributions of Gamma-Ray Burst, Damped Lyα, and Lyman Break Galaxies at z $\approx$ 3 // . VIII 2008. 683, 1. 321–328.

Galbiati Marta, Fumagalli Michele, Fossati Matteo, Lofthouse Emma K., Dutta Rajeshwari, Prochaska J. Xavier, Murphy Michael T., Cantalupo Sebastiano. MUSE Analysis of Gas around Galaxies (MAGG) – V: Linking ionized gas traced by CIV and SiIV absorbers to Lyα emitting galaxies at $z \approx 3.0 - 4.5$ // arXiv e-prints. I 2023. arXiv:2302.00021.

Gilmore Gerard, Norris John E., Monaco Lorenzo, Yong David, Wyse Rosemary F. G., Geisler D. Elemental Abundances and their Implications for the Chemical Enrichment of the Boötes I Ultrafaint Galaxy // . I 2013. 763, 1. 61.

Gim Hansung B., Borthakur Sanchayeeta, Momjian Emmanuel, Padave Mansi, Jansen Rolf A., Nelson Dylan, Heckman Timothy M., Kennicutt Robert C. Jr., Fox Andrew J., Pineda Jorge L., Thilker David, Kauffmann Guinevere, Tumlinson Jason. DIISC-I: The Discovery of Kinematically Anomalous H I Clouds in M 100 // . XI 2021. 922, 1. 69.

Gonçalves Thiago S., Steidel Charles C., Pettini Max. Detection of the Transverse Proximity Effect: Radiative Feedback from Bright QSOs // . IV 2008. 676, 2. 816–835.

Greif Thomas H., Springel Volker, White Simon D. M., Glover Simon C. O., Clark Paul C., Smith Rowan J., Klessen Ralf S., Bromm Volker. Simulations on a Moving Mesh: The Clustered Formation of Population III Protostars // . VIII 2011. 737, 2. 75.

Grevesse N., Asplund M., Sauval A. J., Scott P. The chemical composition of the Sun // . VII 2010. 328, 1-2. 179–183.

Griffith Emily, Weinberg David H., Johnson Jennifer A., Beaton Rachael, García-Hernández D. A., Hasselquist Sten, Holtzman Jon, Johnson James W., Jönsson Henrik, Lane Richard R., Nataf David M., Roman-Lopes Alexandre. The Similarity of Abundance Ratio Trends and Nucleosynthetic Patterns in the Milky Way Disk and Bulge // . III 2021a. 909, 1. 77.

Griffith Emily J., Sukhbold Tuguldur, Weinberg David H., Johnson Jennifer A., Johnson James W., Vincenzo Fiorenzo. The Impact of Black Hole Formation on Population Averaged Supernova Yields // arXiv e-prints. III 2021b. arXiv:2103.09837.

Grimmett J. J., Heger Alexander, Karakas Amanda I., Müller Bernhard. Nucleosynthesis in primordial hypernovae // . IX 2018. 479, 1. 495–516.

Hansen T. T., Simon J. D., Marshall J. L., Li T. S., Carollo D., DePoy D. L., Nagasawa D. Q., Bernstein R. A., Drlica-Wagner A., Abdalla F. B., Allam S., Annis J., Bechtol K., Benoit-Lévy A., Brooks D., Buckley-Geer E., Carnero Rosell A., Carrasco Kind M., Carretero J., Cunha C. E., da Costa L. N., Desai S., Eifler T. F., Fausti Neto A., Flaugher B., Frieman J., García-Bellido J., Gaztanaga E., Gerdes D. W., Gruen D., Gruendl R. A., Gschwend J., Gutierrez G., James D. J., Krause E., Kuehn K., Kuropatkin N., Lahav O., Miquel R., Plazas A. A., Romer A. K., Sanchez E., Santiago B., Scarpine V., Smith R. C., Soares-Santos M., Sobreira F., Suchyta E., Swanson M. E. C., Tarle G., Walker A. R., DES Collaboration . An r-process Enhanced Star in the Dwarf Galaxy Tucana III // . III 2017. 838, 1. 44.

Harris Charles R., Millman K. Jarrod, Walt Stéfan J. van der, Gommers Ralf, Virtanen Pauli, Cournapeau David, Wieser Eric, Taylor Julian, Berg Sebastian, Smith Nathaniel J., Kern Robert, Picus Matti, Hoyer Stephan, Kerkwijk Marten H. van, Brett Matthew, Haldane Allan, Río Jaime Fernández del, Wiebe Mark, Peterson Pearu, Weckesser Pierre Warren, Abbasi Hameer, Gohlke Christoph, Oliphant Travis E. Array programming with NumPy // Nature. IX 2020. 585, 7825. 357–362.

Heckman Timothy M., Alexandroff Rachel M., Borthakur Sanchayeeta, Overzier Roderik, Leitherer Claus. The Systematic Properties of the Warm Phase of Starburst-Driven Galactic Winds // . VIII 2015. 809, 2. 147.

Heckman Timothy M., Armus Lee, Miley George K. On the Nature and Implications of Starburst-driven Galactic Superwinds // . XII 1990. 74. 833.

Heger Alexander, Woosley S. E. Nucleosynthesis and Evolution of Massive Metal-free Stars // . XI 2010. 724, 1. 341–373.

Heintz K. E., Fynbo J. P. U., Ledoux C., Jakobsson P., Møller P., Christensen L., Geier S., Krogager J. K., Noterdaeme P. A quasar hiding behind two dusty absorbers. Quantifying the selection bias of metal-rich, damped Lyα absorption systems // . VII 2018. 615. A43.

Henry R. B. C., Prochaska Jason X. The Chemical Evolution of High-z Galaxies from the Relative Abundances of N, Si, S, and Fe in Damped Lyα Systems // . IX 2007. 119, 859. 962–979.

Hunter J. D. Matplotlib: A 2D graphics environment // Computing in Science & Engineering. 2007. 9, 3. 90–95.

Ishigaki M. N., Aoki W., Arimoto N., Okamoto S. Chemical compositions of six metal-poor stars in the ultra-faint dwarf spheroidal galaxy Boötes I // . II 2014. 562. A146.

Ishigaki Miho N., Hartwig Tilman, Tarumi Yuta, Leung Shing-Chi, Tominaga Nozomu, Kobayashi Chiaki, Magg Mattis, Simionescu Aurora, Nomoto Ken'ichi. Origin of metals in old Milky Way halo stars based on GALAH and Gaia // arXiv e-prints. VII 2021. arXiv:2107.04194.

Ishigaki Miho N., Tominaga Nozomu, Kobayashi Chiaki, Nomoto Ken'ichi. The Initial Mass Function of the First Stars Inferred from Extremely Metal-poor Stars // . IV 2018. 857, 1. 46.

Jenkins Edward B. A Unified Representation of Gas-Phase Element Depletions in the Interstellar Medium // . VIII 2009. 700, 2. 1299–1348.

Ji Alexander P., Frebel Anna, Chiti Anirudh, Simon Joshua D. R-process enrichment from a single event in an ancient dwarf galaxy // . III 2016a. 531, 7596. 610–613.

Ji Alexander P., Frebel Anna, Simon Joshua D., Geha Marla. High-resolution Spectroscopy of Extremely Metal-poor Stars in the Least-evolved Galaxies: Bootes II // . I 2016b. 817, 1. 41.

Ji Alexander P., Simon Joshua D., Frebel Anna, Venn Kim A., Hansen Terese T. Chemical Abundances in the Ultra-faint Dwarf Galaxies Grus I and Triangulum II: Neutron-capture Elements as a Defining Feature of the Faintest Dwarfs // . I 2019. 870, 2. 83.

Johnson Sean D., Chen Hsiao-Wen, Mulchaey John S., Schaye Joop, Straka Lorrie A. The Extent of Chemically Enriched Gas around Star-forming Dwarf Galaxies // . XI 2017. 850, 1. L10.

Juneau Stéphanie, Dickinson Mark, Alexander David M., Salim Samir. A New Diagnostic of Active Galactic Nuclei: Revealing Highly Absorbed Systems at Redshift >0.3 // . VIII 2011. 736, 2. 104.

Kamann S., Bastian N., Gossage S., Baade D., Cabrera-Ziri I., Da Costa G., de Mink S. E., Georgy C., Giesers B., Göttgens F., Hilker M., Husser T. O., Lardo C., Larsen S. S., Mackey D., Martocchia S., Mucciarelli A., Platais I., Roth M. M., Salaris M., Usher C., Yong D. How stellar rotation shapes the colour-magnitude diagram of the massive intermediate-age star cluster NGC 1846 // . II 2020. 492, 2. 2177–2192.

Kennicutt Robert C. Jr., Tamblyn Peter, Congdon Charles E. Past and Future Star Formation in Disk Galaxies // . XI 1994. 435. 22.

Khare P., Kulkarni V. P., Péroux C., York D. G., Lauroesch J. T., Meiring J. D. The nature of damped Lyman α and sub-damped Lyman α absorbers // . III 2007. 464, 2. 487–493.

Kirby Evan N., Cohen Judith G., Simon Joshua D., Guhathakurta Puragra, Thygesen Anders O., Duggan Gina E. Triangulum II. Not Especially Dense After All // . IV 2017. 838, 2. 83.

Kirby Evan N., Cohen Judith. G., Smith Graeme H., Majewski Steven R., Sohn Sangmo Tony, Guhathakurta Puragra. Multi-element Abundance Measurements from Medium-resolution Spectra. IV. Alpha Element Distributions in Milky Way Satellite Galaxies // . II 2011. 727, 2. 79.

Kirby Evan N., Guo Michelle, Zhang Andrew J., Deng Michelle, Cohen Judith G., Guhathakurta Puragra, Shetrone Matthew D., Lee Young Sun, Rizzi Luca. CARBON IN RED GIANTS IN GLOBULAR CLUSTERS AND DWARF SPHEROIDAL GALAXIES // The Astrophysical Journal. mar 2015. 801, 2. 125.

Kirby Evan N., Xie Justin L., Guo Rachel, de los Reyes Mithi A. C., Bergemann Maria, Kovalev Mikhail, Shen Ken J., Piro Anthony L., McWilliam Andrew. Evidence for Sub-Chandrasekhar Type Ia Supernovae from Stellar Abundances in Dwarf Galaxies // . VIII 2019. 881, 1. 45.

Kobayashi Chiaki, Umeda Hideyuki, Nomoto Ken'ichi, Tominaga Nozomu, Ohkubo Takuya. Galactic Chemical Evolution: Carbon through Zinc // . XII 2006. 653, 2. 1145–1171.

Koch A., Feltzing S., Adén D., Matteucci F. Neutron-capture element deficiency of the Hercules dwarf spheroidal galaxy // . VI 2013. 554. A5.

Koch Andreas, McWilliam Andrew, Grebel Eva K., Zucker Daniel B., Belokurov Vasily. The Highly Unusual Chemical Composition of the Hercules Dwarf Spheroidal Galaxy // . XI 2008. 688, 1. L13.

Konstantopoulou Christina, De Cia Annalisa, Krogager Jens-Kristian, Ledoux Cédric, Noterdaeme Pasquier, Fynbo Johan P. U., Heintz Kasper E., Watson Darach, Andersen Anja C., Ramburuth-Hurt Tanita, Jermann Iris. Dust depletion of metals from local to distant galaxies. I. Peculiar nucleosynthesis effects and grain growth in the ISM // . X 2022. 666. A12.

Konstantopoulou Christina, De Cia Annalisa, Krogager Jens-Kristian, Ledoux Cédric, Noterdaeme Pasquier, Fynbo Johan P. U., Heintz Kasper E., Watson Darach, Andersen Anja C., Ramburuth-Hurt Tanita, Jermann Iris. Dust depletion of metals from local to distant galaxies. I. Peculiar nucleosynthesis effects and grain growth in the ISM (Corrigendum) // . VI 2023. 674. C1.

Konstantopoulou Christina, De Cia Annalisa, Ledoux Cédric, Krogager Jens-Kristian, Mattsson Lars, Watson Darach, Heintz Kasper E., Péroux Céline, Noterdaeme Pasquier, Andersen Anja C., Fynbo Johan P. U., Jermann Iris, Ramburuth-Hurt Tanita. Dust depletion of metals from local to distant galaxies. II. Cosmic dust-to-metal ratio and dust composition // . I 2024. 681. A64.

Koplitz Brad, Borthakur Sanchayeeta, Heckman Timothy, Padave Mansi, McCabe Tyler, Tumlinson Jason, Fox Andrew J., Kauffmann Guinevere. DIISC-VI (COS-DIISC): Ultraviolet Metal Absorption Relative to the H I Disk of Galaxies // . IV 2025. 982, 2. 171.

Kriek Mariska, Shapley Alice E., Reddy Naveen A., Siana Brian, Coil Alison L., Mobasher Bahram, Freeman William R., de Groot Laura, Price Sedona H., Sanders Ryan, Shivaei Irene, Brammer Gabriel B., Momcheva Ivelina G., Skelton Rosalind E., van Dokkum Pieter G., Whitaker Katherine E., Aird James, Azadi Mojegan, Kassis Marc, Bullock James S., Conroy Charlie, Davé Romeel, Kereš Dušan, Krumholz Mark. The MOSFIRE Deep Evolution Field (MOSDEF) Survey: Rest-frame Optical Spectroscopy for ~1500 H-selected Galaxies at 1.37 < z < 3.8 // . VI 2015. 218, 2. 15.

Krogager J. K., Møller P., Fynbo J. P. U., Noterdaeme P. Consensus report on 25 yr of searches for damped Ly α galaxies in emission: confirming their metallicity-luminosity relation at z $\gtrsim$ 2 // . VIII 2017. 469, 3. 2959–2981.

Krogager Jens-Kristian. VoigtFit: A Python package for Voigt profile fitting // arXiv e-prints. III 2018. arXiv:1803.01187.

Kroupa Pavel. On the variation of the initial mass function // . IV 2001. 322, 2. 231–246.

Lai David K., Lee Young Sun, Bolte Michael, Lucatello Sara, Beers Timothy C., Johnson Jennifer A., Sivarani Thirupathi, Rockosi Constance M. The [Fe/H], [C/Fe], and [α/Fe] Distributions of the Boötes I Dwarf Spheroidal Galaxy // . IX 2011. 738, 1. 51.

Langen Vivienne, Cantalupo Sebastiano, Steidel Charles C., Chen Yuguang, Pezzulli Gabriele, Gallego Sofia G. Characterizing the circumgalactic medium of quasars at z 2.2 through H α and Ly α emission // . III 2023. 519, 4. 5099–5113.

Lanzetta Kenneth M., Bowen David V., Tytler David, Webb John K. The Gaseous Extent of Galaxies and the Origin of Lyman-Alpha Absorption Systems: A Survey of Galaxies in the Fields of Hubble Space Telescope Spectroscopic Target QSOs // . IV 1995a. 442. 538.

Lanzetta Kenneth M., Wolfe Arthur M., Turnshek David A. The IUE Survey for Damped Lyman- alpha and Lyman-Limit Absorption Systems: Evolution of the Gaseous Content of the Universe // . II 1995b. 440. 435.

Ledoux C., Noterdaeme P., Petitjean P., Srianand R. Neutral atomic-carbon quasar absorption-line systems at z> 1.5. Sample selection, H i content, reddening, and 2175 Å extinction feature // . VIII 2015. 580. A8.

Ledoux C., Petitjean P., Fynbo J. P. U., Møller P., Srianand R. Velocity-metallicity correlation for high-z DLA galaxies: evidence of a mass-metallicity relation? // . X 2006. 457, 1. 71–78.

Ledoux Cedric, Petitjean Patrick, Bergeron Jacqueline, Wampler E. Joseph, Srianand R. On the kinematics of damped Lyman-alpha systems // . IX 1998. 337. 51–63.

Ledoux Cédric, Petitjean Patrick, Srianand R. The Very Large Telescope Ultraviolet and Visible Echelle Spectrograph survey for molecular hydrogen in high-redshift damped Lyman α systems // . XI 2003. 346, 1. 209–228.

Lehner N., O'Meara J. M., Fox A. J., Howk J. C., Prochaska J. X., Burns V., Armstrong A. A. Galactic and Circumgalactic O VI and its Impact on the Cosmological Metal and Baryon Budgets at 2 < z <~3.5 // . VI 2014. 788, 2. 119.

Lehner Nicolas, Kopenhafer Claire, O'Meara John M., Howk J. Christopher, Fumagalli Michele, Prochaska J. Xavier, Acharyya Ayan, O'Shea Brian W., Peeples Molly S., Tumlinson Jason, Hummels Cameron B. KODIAQ-Z: Metals and Baryons in the Cool Intergalactic and Circumgalactic Gas at 2.2 $\lesssim$ z $\lesssim$ 3.6 // . IX 2022. 936, 2. 156.

Levshakov S. A., Agafonova I. I., Centurión M., Mazets I. E. Metal abundances and kinematics of quasar absorbers. I. Absorption systems toward J2233-606 // . III 2002. 383. 813–822.

Limongi Marco, Chieffi Alessandro. Presupernova Evolution and Explosive Nucleosynthesis of Rotating Massive Stars in the Metallicity Range -3 ≤ [Fe/H] ≤ 0 // . VII 2018. 237, 1. 13.

Lindsay Kevin, Casertano S., Stankiewicz M. The Hubble Legacy Archive (HLA): Over 100 Million Sources Served // American Astronomical Society Meeting Abstracts #215. 215. I 2010. 469.01. (American Astronomical Society Meeting Abstracts).

Lodders Katharina. Solar System Abundances and Condensation Temperatures of the Elements // . VII 2003. 591, 2. 1220–1247.

Lofthouse Emma K., Fumagalli Michele, Fossati Matteo, Dutta Rajeshwari, Galbiati Marta, Arrigoni Battaia Fabrizio, Cantalupo Sebastiano, Christensen Lise, Cooke Ryan J., Longobardi Alessia, Murphy Michael T., Prochaska J. Xavier. MUSE Analysis of Gas around Galaxies (MAGG) - IV. The gaseous environment of z 3-4 Ly α emitting galaxies // . I 2023. 518, 1. 305–331.

Lofthouse Emma K., Fumagalli Michele, Fossati Matteo, O'Meara John M., Murphy Michael T., Christensen Lise, Prochaska J. Xavier, Cantalupo Sebastiano, Bielby Richard M., Cooke Ryan J., Lusso Elisabeta, Morris Simon L. MUSE Analysis of Gas around Galaxies (MAGG) - I: Survey design and the environment of a near pristine gas cloud at z 3.5 // . I 2020. 491, 2. 2057–2074.

Lopez S., Ellison S. L. Distinct abundance patterns in multiple damped Ly alpha galaxies: Evidence for truncated star formation? // . V 2003. 403. 573–584.

Lopez S., Reimers D., D'Odorico S., Prochaska J. X. Metal abundances and ionization conditions in a possibly dust-free damped Lyalpha system at z=2.3 // . IV 2002. 385. 778–792.

Lopez Sebastian, Reimers Dieter, Rauch Michael, Sargent Wallace L. W., Smette Alain. First Comparison of Ionization and Metallicity in Two Lines of Sight toward HE 1104-1805 AB at z=1.66 // . III 1999. 513, 2. 598–618.

Lu Limin, Sargent Wallace L. W., Barlow Thomas A. Evidence for Rotation in the Galaxy at z = 3.15 Responsible for a Damped Lyman-Alpha Absorption System in the Spectrum of Q2233+1310 // . VII 1997. 484, 1. 131–134.

Lu Limin, Sargent Wallace L. W., Barlow Thomas A. The N/Si Abundance Ratio in 15 Damped Lyalpha Galaxies: Implications for the Origin of Nitrogen // . I 1998. 115, 1. 55–61.

Lu Limin, Sargent Wallace L. W., Barlow Thomas A., Churchill Christopher W., Vogt Steven S. Abundances at High Redshifts: The Chemical Enrichment History of Damped Ly alpha Galaxies // . XII 1996. 107. 475.

Marigo P. Chemical yields from low- and intermediate-mass stars: Model predictions and basic observational constraints // . IV 2001. 370. 194–217.

Marshall J. L., Hansen T., Simon J. D., Li T. S., Bernstein R. A., Kuehn K., Pace A. B., DePoy D. L., Palmese A., Pieres A., Strigari L., Drlica-Wagner A., Bechtol K., Lidman C., Nagasawa D. Q., Bertin E., Brooks D., Buckley-Geer E., Burke D. L., Carnero Rosell A., Carrasco Kind M., Carretero J., Cunha C. E., D'Andrea C. B., da Costa L. N., De Vicente J., Desai S., Doel P., Eifler T. F., Flaugher B., Fosalba P., Frieman J., García-Bellido J., Gaztanaga E., Gerdes D. W., Gruendl R. A., Gschwend J., Gutierrez G., Hartley W. G., Hollowood D. L., Honscheid K., Hoyle B., James D. J., Kuropatkin N., Maia M. A. G., Menanteau F., Miller C. J., Miquel R., Plazas A. A., Sanchez E., Santiago B., Scarpine V., Schubnell M., Serrano S., Sevilla-Noarbe I., Smith M., Soares-Santos M., Suchyta E., Swanson M. E. C., Tarle G., Wester W., DES Collaboration . Chemical Abundance Analysis of Tucana III, the Second r-process Enhanced Ultra-faint Dwarf Galaxy // . IX 2019. 882, 2. 177.

Martin Crystal L., Kobulnicky Henry A., Heckman Timothy M. The Metal Content of Dwarf Starburst Winds: Results from Chandra Observations of NGC 1569 // . VIII 2002. 574, 2. 663–692.

Matthews K., Soifer B. T. The Near Infrared Camera on the W. M. Keck Telescope // Astronomy with Arrays, The Next Generation. 190. I 1994. 239. (Astrophysics and Space Science Library).

McConnachie Alan W. The Observed Properties of Dwarf Galaxies in and around the Local Group // . VII 2012. 144, 1. 4.

McGaugh Stacy S. H II Region Abundances: Model Oxygen Line Ratios // . X 1991. 380. 140.

McGaugh Stacy S., Schombert James M., de Blok W. J. G., Zagursky Matthew J. The Baryon Content of Cosmic Structures // . I 2010. 708, 1. L14–L17.

McLean Ian S., Steidel Charles C., Epps Harland W., Konidaris Nicholas, Matthews Keith Y., Adkins Sean, Aliado Theodore, Brims George, Canfield John M., Cromer John L., Fucik Jason, Kulas Kristin, Mace Greg, Magnone Ken, Rodriguez Hector, Rudie Gwen, Trainor Ryan, Wang Eric, Weber Bob, Weiss Jason. MOSFIRE, the multi-object spectrometer for infra-red exploration at the Keck Observatory // Ground-based and Airborne Instrumentation for Astronomy IV. 8446. IX 2012. 84460J. (Society of Photo-Optical Instrumentation Engineers (SPIE) Conference Series).

Milone A. P., Marino A. F., Di Criscienzo M., D'Antona F., Bedin L. R., Da Costa G., Piotto G., Tailo M., Dotter A., Angeloni R., Anderson J., Jerjen H., Li C., Dupree A., Granata V., Lagioia E. P., Mackey A. D., Nardiello D., Vesperini E. Multiple stellar populations in Magellanic Cloud clusters - VI. A survey of multiple sequences and Be stars in young clusters // . VI 2018. 477, 2. 2640–2663.

Mintz Abby, Rafelski Marc, Jorgenson Regina A., Fumagalli Michele, Dutta Rajeshwari, Martin Crystal L., Lusso Elisabeta, Rubin Kate H. R., O'Meara John M. Constraining the Size of the Circumgalactic Medium Using the Transverse Autocorrelation Function of C IV Absorbers in Paired Quasar Spectra // . VIII 2022. 164, 2. 51.

Mishra Nishant, Johnson Sean D., Rudie Gwen C., Chen Hsiao-Wen, Schaye Joop, Qu Zhijie, Zahedy Fakhri S., Boettcher Erin T., Cantalupo Sebastiano, Chen Mandy C., Faucher-Giguére Claude-André, Greene Jenny E., Li Jennifer I. Hsiu, Liu Zhuoqi (Will), Lopez Sebastian, Petitjean Patrick. The Cosmic Ultraviolet Baryon Survey (CUBS). IX. The Enriched Circumgalactic and Intergalactic Medium Around Star-forming Field Dwarf Galaxies Traced by O VI Absorption // . XI 2024. 976, 1. 149.

Mitchell Peter D., Blaizot Jérémy, Devriendt Julien, Kimm Taysun, Michel-Dansac Léo, Rosdahl Joakim, Slyz Adrianne. Gas flows in the circumgalactic medium around simulated high-redshift galaxies // . III 2018. 474, 4. 4279–4301.

Moe Maxwell, Di Stefano Rosanne. Mind Your Ps and Qs: The Interrelation between Period (P) and Mass-ratio (Q) Distributions of Binary Stars // . VI 2017. 230, 2. 15.

Molaro Paolo, Bonifacio Piercarlo, Centurión Miriam, D'Odorico Sandro, Vladilo Giovanni, Santin Paolo, Di Marcantonio Paolo. UVES Observations of QSO 0000-2620: Oxygen and Zinc Abundances in the Damped Lyα Galaxy at Z_{abs}=3.3901 // . IX 2000. 541, 1. 54–60.

Molaro Paolo, Levshakov Sergei A., D'Odorico Sandro, Bonifacio Piercarlo, Centurión Miriam. UVES Observations of QSO 0000-2620: Argon and Phosphorus Abundances in the Dust-free Damped Lyα System at z_{abs}=3.3901 // . III 2001. 549, 1. 90–99.

Møller P., Warren S. J., Fall S. M., Fynbo J. U., Jakobsen P. Are High-Redshift Damped Lyα Galaxies Lyman Break Galaxies? // . VII 2002. 574, 1. 51–58.

Morrison Sean, Kulkarni Varsha P., Som Debopam, DeMarcy Bryan, Quiret Samuel, Péroux Celine. Element Abundances in a Gas-rich Galaxy at z = 5: Clues to the Early Chemical Enrichment of Galaxies // . X 2016. 830, 2. 158.

Morrissey Patrick, Matuszewski Matuesz, Martin D. Christopher, Neill James D., Epps Harland, Fucik Jason, Weber Bob, Darvish Behnam, Adkins Sean, Allen Steve, Bartos Randy, Belicki Justin, Cabak Jerry, Callahan Shawn, Cowley Dave, Crabill Marty, Deich Willian, Delecroix Alex, Doppman Greg, Hilyard David, James Ean, Kaye Steve, Kokorowski Michael, Kwok Shui, Lanclos Kyle, Milner Steve, Moore Anna, O'Sullivan Donal, Parihar Prachi, Park Sam, Phillips Andrew, Rizzi Luca, Rockosi Constance, Rodriguez Hector, Salaun Yves, Seaman Kirk, Sheikh David, Weiss Jason, Zarzaca Ray. The Keck Cosmic Web Imager Integral Field Spectrograph // . IX 2018. 864, 1. 93.

Mösta Philipp, Ott Christian D., Radice David, Roberts Luke F., Schnetter Erik, Haas Roland. A large-scale dynamo and magnetoturbulence in rapidly rotating core-collapse supernovae // . XII 2015. 528, 7582. 376–379.

Muller C. A., Oort J. H., Raimond E. Hydrogène neutre dans la couronne galactique? // Academie des Sciences Paris Comptes Rendus. I 1963. 257. 1661–1662.

Münch Guido, Zirin Harold. Interstellar Matter at Large Distances from the Galactic Plane. // . I 1961. 133. 11.

Murphy Michael T., Kacprzak Glenn G., Savorgnan Giulia A. D., Carswell Robert F. The UVES Spectral Quasar Absorption Database (SQUAD) data release 1: the first 10 million seconds // . I 2019. 482, 3. 3458–3479.

Muzahid Sowgat, Schaye Joop, Cantalupo Sebastiano, Marino Raffaella Anna, Bouché Nicolas F., Johnson Sean, Maseda Michael, Wendt Martin, Wisotzki Lutz, Zabl Johannes. MUSEQuBES: characterizing the circumgalactic medium of redshift ≈3.3 Ly α emitters // . XII 2021. 508, 4. 5612–5637.

Muzahid Sowgat, Schaye Joop, Marino Raffaella Anna, Cantalupo Sebastiano, Brinchmann Jarle, Contini Thierry, Wendt Martin, Wisotzki Lutz, Zabl Johannes, *Bouché Nicolas, Akhlaghi Mohammad, Chen Hsiao-Wen, Claeyssens Adélaîde, Johnson Sean, Leclercq Floriane, Maseda Michael, Matthee Jorryt, Richard Johan, Urrutia Tanya, Verhamme Anne*. MUSEQuBES: calibrating the redshifts of Ly α emitters using stacked circumgalactic medium absorption profiles // . VIII 2020. 496, 2. 1013–1022.

Nagasawa D. Q., Marshall J. L., Li T. S., Hansen T. T., Simon J. D., Bernstein R. A., Balbinot E., Drlica-Wagner A., Pace A. B., Strigari L. E., Pellegrino C. M., DePoy D. L., Suntzeff N. B., Bechtol K., Walker A. R., Abbott T. M. C., Abdalla F. B., Allam S., Annis J., Benoit-Lévy A., Bertin E., Brooks D., Carnero Rosell A., Carrasco Kind M., Carretero J., Cunha C. E., D'Andrea C. B., da Costa L. N., Davis C., Desai S., Doel P., Eifler T. F., Flaugher B., Fosalba P., Frieman J., García-Bellido J., Gaztanaga E., Gerdes D. W., Gruen D., Gruendl R. A., Gschwend J., Gutierrez G., Hartley W. G., Honscheid K., James D. J., Jeltema T., Krause E., Kuehn K., Kuhlmann S., Kuropatkin N., March M., Miquel R., Nord B., Roodman A., Sanchez E., Santiago B., Scarpine V., Schindler R., Schubnell M., Sevilla-Noarbe I., Smith M., Smith R. C., Soares-Santos M., Sobreira F., Suchyta E., Tarle G., Thomas D., Tucker D. L., Wechsler R. H., Wolf R. C., Yanny B. Chemical Abundance Analysis of Three α-poor, Metal-poor Stars in the Ultrafaint Dwarf Galaxy Horologium I // . I 2018. 852, 2. 99.

Neeleman Marcel, Kanekar Nissim, Prochaska J. Xavier, Christensen Lise, Dessauges-Zavadsky Miroslava, Fynbo Johan P. U., Møller Palle, Zwaan Martin A. Molecular Emission from a Galaxy Associated with a z ~ 2.2 Damped Lyα Absorber // . III 2018. 856, 1. L12.

Nielsen Nikole M., Kacprzak Glenn G., Sameer , Murphy Michael T., Nateghi Hasti, Charlton Jane C., Churchill Christopher W. A complex multiphase DLA associated with a compact group at z = 2.431 traces accretion, outflows, and tidal streams // . VIII 2022. 514, 4. 6074–6101.

Nomoto K., Iwamoto K., Nakasato N., Thielemann F. K., Brachwitz F., Tsujimoto T., Kubo Y., Kishimoto N. Nucleosynthesis in type Ia supernovae // . II 1997. 621. 467–476.

Nomoto Ken'ichi, Tominaga Nozomu, Umeda Hideyuki, Kobayashi Chiaki, Maeda Keiichi. Nucleosynthesis yields of core-collapse supernovae and hypernovae, and galactic chemical evolution // . X 2006. 777. 424–458.

Nordlander T., Lind K. Non-LTE aluminium abundances in late-type stars // . XI 2017. 607. A75.

Norris John E., Wyse Rosemary F. G., Gilmore Gerard, Yong David, Frebel Anna, Wilkinson Mark I., Belokurov V., Zucker Daniel B. Chemical Enrichment in the Faintest Galaxies: The Carbon and Iron Abundance Spreads in the Boötes I Dwarf Spheroidal Galaxy and the Segue 1 System // . XI 2010. 723, 2. 1632–1650.

Noterdaeme P., Ledoux C., Petitjean P., Srianand R. Molecular hydrogen in high-redshift damped Lyman-α systems: the VLT/UVES database // . IV 2008. 481, 2. 327–336.

Noterdaeme P., López S., Dumont V., Ledoux C., Molaro P., Petitjean P. Deuterium at high redshift. Primordial abundance in the z_{abs} = 2.621 damped Ly-α system towards CTQ 247 // . VI 2012. 542. L33.

Noterdaeme P., Petitjean P., Srianand R., Ledoux C., Le Petit F. Physical conditions in the neutral interstellar medium at z = 2.43 toward Q 2348-011 // . VII 2007. 469, 2. 425–436.

Nuñez Evan H., Kirby Evan N., Steidel Charles C. Empirical Constraints on Core Collapse Supernova Yields using Very Metal Poor Damped Lyman Alpha Absorbers // arXiv e-prints. VIII 2021. arXiv:2108.00659.

Nuñez Evan H., Kirby Evan N., Steidel Charles C. Empirical Constraints on Core-collapse Supernova Yields Using Very Metal-poor Damped Lyα Absorbers // . III 2022. 927, 1. 64.

Nuñez Evan Haze, Steidel Charles C., Kirby Evan N., Rudie Gwen C., Prusinski Nikolaus Z., Chen Yuguang, Zhuang Zhuyun, Strom Allison L., Erb Dawn K., Pettini Max, Welsh Louise, Rupke David S. N., Cooke Ryan J. KBSS-InCLOSE. I. Design and First Results from the Inner Circumgalactic Medium of QSO Line-of-sight Emitting Galaxies at z ~ 2–3 // . XI 2024. 976, 1. 41.

O'Meara J. M., Lehner N., Howk J. C., Prochaska J. X., Fox A. J., Peeples M. S., Tumlinson J., O'Shea B. W. The Second Data Release of the KODIAQ Survey // . IX 2017. 154, 3. 114.

O'Meara J. M., Lehner N., Howk J. C., Prochaska J. X., Fox A. J., Swain M. A., Gelino C. R., Berriman G. B., Tran H. The First Data Release of the KODIAQ Survey // . X 2015. 150, 4. 111.

O'Meara John M., Burles Scott, Prochaska Jason X., Prochter Gabe E., Bernstein Rebecca A., Burgess Kristin M. The Deuterium-to-Hydrogen Abundance Ratio toward the QSO SDSS J155810.16-003120.0 // . X 2006. 649, 2. L61–L65.

O'Meara John M., Lehner Nicolas, Howk J. Christopher, Prochaska J. Xavier. The Third Data Release of the KODIAQ Survey // . I 2021. 161, 1. 45.

O'Meara John M., Prochaska Jason X., Burles Scott, Prochter Gabriel, Bernstein Rebecca A., Burgess Kristin M. The Keck+Magellan Survey for Lyman Limit Absorption. I. The Frequency Distribution of Super Lyman Limit Systems // . II 2007. 656, 2. 666–679.

O'Meara John M., Tytler David, Kirkman David, Suzuki Nao, Prochaska Jason X., Lubin Dan, Wolfe Arthur M. The Deuterium to Hydrogen Abundance Ratio toward a Fourth QSO: HS 0105+1619 // . V 2001. 552, 2. 718–730.

Ogura Kazuyuki, Umehata Hideki, Taniguchi Yoshiaki, Matsuda Yuichi, Kashikawa Nobunari, Sheth Kartik, Murata Katsuhiro, Kajisawa Masaru, Kobayashi Masakazu A. R., Murayama Takashi, Nagao Tohru. ALMA band 8 observations of DLA 2233+131 at z = 3.150 // . IV 2020. 72, 2. 29.

Oke J. B., Cohen J. G., Carr M., Cromer J., Dingizian A., Harris F. H., Labrecque S., Lucinio R., Schaal W., Epps H., Miller J. The Keck Low-Resolution Imaging Spectrometer // . IV 1995. 107. 375.

Olano C. A. The high-velocity clouds and the Magellanic Clouds // . IX 2004. 423. 895–907.

Osterbrock Donald E. Astrophysics of gaseous nebulae and active galactic nuclei. 1989.

Otsuki Mau, Hirashita Hiroyuki. Dust enrichment in the circum-galactic medium // . III 2024. 528, 3. 5008–5018.

Oyarzún Grecco A., Blanc Guillermo A., González Valentino, Mateo Mario, Bailey III John I. A Comprehensive Study of Lyα Emission in the High-redshift Galaxy Population // . VII 2017. 843, 2. 133.

Oyarzún Grecco A., Rafelski Marc, Kanekar Nissim, Prochaska J. Xavier, Neeleman Marcel, Jorgenson Regina A. A Survey of Lyα Emission around Damped Lyα Absorbers at z $\approx$ 2 with the Keck Cosmic Web Imager // . II 2024. 962, 1. 72.

Pahl Anthony J., Shapley Alice, Steidel Charles C., Reddy Naveen A., Chen Yuguang, Rudie Gwen C., Strom Allison L. The connection between the escape of ionizing radiation and galaxy properties at z $\sim$ 3 in the Keck Lyman continuum spectroscopic survey // . V 2023. 521, 3. 3247–3259.

Peebles P. J. E. The large-scale structure of the universe. 1980.

Peeples Molly S., Werk Jessica K., Tumlinson Jason, Oppenheimer Benjamin D., Prochaska J. Xavier, Katz Neal, Weinberg David H. A Budget and Accounting of Metals at z $\sim$0: Results from the COS-Halos Survey // . V 2014. 786, 1. 54.

Penprase Bryan E., Prochaska J. Xavier, Sargent Wallace L. W., Toro-Martinez Irene, Beeler Daniel J. Keck Echellette Spectrograph and Imager Observations of Metal-poor Damped Lyα Systems // . IX 2010. 721, 1. 1–25.

Perego A., Hempel M., Fröhlich C., Ebinger K., Eichler M., Casanova J., Liebendörfer M., Thielemann F. K. PUSHing Core-collapse Supernovae to Explosions in Spherical Symmetry I: the Model and the Case of SN 1987A // . VI 2015. 806, 2. 275.

Péroux Céline, Bouché Nicolas, Kulkarni Varsha P., York Donald G., Vladilo Giovanni. A SINFONI integral field spectroscopy survey for galaxy counterparts to damped Lyman α systems - I. New detections and limits for intervening and associated absorbers // . II 2011. 410, 4. 2237–2250.

Péroux Céline, Howk J. Christopher. The Cosmic Baryon and Metal Cycles // . VIII 2020. 58. 363–406.

Persson S. E., Murphy D. C., Smee S., Birk C., Monson A. J., Uomoto A., Koch E., Shectman S., Barkhouser R., Orndorff J., Hammond R., Harding A., Scharfstein G., Kelson D., Marshall J., McCarthy P. J. FourStar: The Near-Infrared Imager for the 6.5 m Baade Telescope at Las Campanas Observatory // . VI 2013. 125, 928. 654.

Petitjean P., Ledoux C., Srianand R. The nitrogen and oxygen abundances in the neutral gas at high redshift // . III 2008. 480, 2. 349–357.

Pettini M. The First Stars: clues from quasar absorption systems // Proceedings of the Royal Society of London Series A. X 2011. 467, 2134. 2735–2751.

Pettini M., Ellison S. L., Bergeron J., Petitjean P. The abundances of nitrogen and oxygen in damped Lyman alpha systems // . VIII 2002. 391. 21–34.

Pettini Max, Ellison Sara L., Steidel Charles C., Shapley Alice E., Bowen David V. Si and Mn Abundances in Damped Lyα Systems with Low Dust Content // . III 2000. 532, 1. 65–76.

Pettini Max, King David L., Smith Linda J., Hunstead Richard W. Dust in High-Redshift Galaxies // . III 1997. 478, 2. 536–541.

Pettini Max, Lipman Keith, Hunstead Richard W. Element Abundances at High Redshifts: The N/O Ratio in a Primeval Galaxy // . IX 1995. 451. 100.

Pettini Max, Zych Berkeley J., Steidel Charles C., Chaffee Fred H. C, N, O abundances in the most metal-poor damped Lyman alpha systems // . IV 2008. 385, 4. 2011–2024.

Pilyugin L. S., Vílchez J. M., Mattsson L., Thuan T. X. Abundance determination from global emission-line SDSS spectra: exploring objects with high N/O ratios // . IV 2012. 421, 2. 1624–1634.

Placco Vinicius M., Frebel Anna, Beers Timothy C., Stancliffe Richard J. Carbon-enhanced Metal-poor Star Frequencies in the Galaxy: Corrections for the Effect of Evolutionary Status on Carbon Abundances // . XII 2014. 797, 1. 21.

Planck Collaboration , Aghanim N., Akrami Y., Ashdown M., Aumont J., Baccigalupi C., Ballardini M., Banday A. J., Barreiro R. B., Bartolo N., Basak S., Battye R., Benabed K., Bernard J. P., Bersanelli M., Bielewicz P., Bock J. J., Bond J. R., Borrill J., Bouchet F. R., Boulanger F., Bucher M., Burigana C., Butler R. C., Calabrese E., Cardoso J. F., Carron J., Challinor A., Chiang H. C., Chluba J., Colombo L. P. L., Combet C., Contreras D., Crill B. P., Cuttaia F., de Bernardis P., de Zotti G., Delabrouille J., Delouis J. M., Di Valentino E., Diego J. M., Doré O., Douspis M., Ducout A., Dupac X., Dusini S., Efstathiou G., Elsner F., Enßlin T. A., Eriksen H. K., Fantaye Y., Farhang M., Fergusson J., Fernandez-Cobos

R., Finelli F., Forastieri F., Frailis M., Fraisse A. A., Franceschi E., Frolov A., Galeotta S., Galli S., Ganga K., Génova-Santos R. T., Gerbino M., Ghosh T., González-Nuevo J., Górski K. M., Gratton S., Gruppuso A., Gudmundsson J. E., Hamann J., Handley W., Hansen F. K., Herranz D., Hildebrandt S. R., Hivon E., Huang Z., Jaffe A. H., Jones W. C., Karakci A., Keihänen E., Keskitalo R., Kiiveri K., Kim J., Kisner T. S., Knox L., Krachmalnicoff N., Kunz M., Kurki-Suonio H., Lagache G., Lamarre J. M., Lasenby A., Lattanzi M., Lawrence C. R., Le Jeune M., Lemos P., Lesgourgues J., Levrier F., Lewis A., Liguori M., Lilje P. B., Lilley M., Lindholm V., López-Caniego M., Lubin P. M., Ma Y. Z., Macías-Pérez J. F., Maggio G., Maino D., Mandolesi N., Mangilli A., Marcos-Caballero A., Maris M., Martin P. G., Martinelli M., Martínez-González E., Matarrese S., Mauri N., McEwen J. D., Meinhold P. R., Melchiorri A., Mennella A., Migliaccio M., Millea M., Mitra S., Miville-Deschênes M. A., Molinari D., Montier L., Morgante G., Moss A., Natoli P., Nørgaard-Nielsen H. U., Pagano L., Paoletti D., Partridge B., Patanchon G., Peiris H. V., Perrotta F., Pettorino V., Piacentini F., Polastri L., Polenta G., Puget J. L., Rachen J. P., Reinecke M., Remazeilles M., Renzi A., Rocha G., Rosset C., Roudier G., Rubiño-Martín J. A., Ruiz-Granados B., Salvati L., Sandri M., Savelainen M., Scott D., Shellard E. P. S., Sirignano C., Sirri G., Spencer L. D., Sunyaev R., Suur-Uski A. S., Tauber J. A., Tavagnacco D., Tenti M., Toffolatti L., Tomasi M., Trombetti T., Valenziano L., Valiviita J., Van Tent B., Vibert L., Vielva P., Villa F., Vittorio N., Wandelt B. D., Wehus I. K., White M., White S. D. M., Zacchei A., Zonca A. Planck 2018 results. VI. Cosmological parameters // . IX 2020. 641. A6.

Pontzen Andrew, Pettini Max. Dust biasing of damped Lyman alpha systems: a Bayesian analysis // . II 2009. 393, 2. 557–568.

Poudel Suraj, Kulkarni Varsha P., Cashman Frances H., Frye Brenda, Péroux Céline, Rahmani Hadi, Quiret Samuel. Metal-enriched galaxies in the first ~1 billion years: evidence of a smooth metallicity evolution at z ~ 5 // . I 2020. 491, 1. 1008–1025.

Prantzos N., Abia C., Limongi M., Chieffi A., Cristallo S. Chemical evolution with rotating massive star yields - I. The solar neighbourhood and the s-process elements // . V 2018. 476, 3. 3432–3459.

Pratt Cameron T., Stocke John T., Keeney Brian A., Danforth Charles W. The Spread of Metals into the Low-redshift Intergalactic Medium // . III 2018. 855, 1. 18.

Prochaska J. Xavier, O'Meara John M., Fumagalli Michele, Bernstein Rebecca A., Burles Scott M. The Keck + Magellan Survey for Lyman Limit Absorption. III. Sample Definition and Column Density Measurements // . XI 2015. 221, 1. 2.

Prochaska J. Xavier, Werk Jessica K., Worseck Gábor, Tripp Todd M., Tumlinson Jason, Burchett Joseph N., Fox Andrew J., Fumagalli Michele, Lehner Nicolas, Peeples Molly S., Tejos Nicolas. The COS-Halos Survey: Metallicities in the Low-redshift Circumgalactic Medium // . III 2017. 837, 2. 169.

Prochaska J. Xavier, Wolfe Arthur M. On the (Non)Evolution of H I Gas in Galaxies Over Cosmic Time // . V 2009. 696, 2. 1543–1547.

Prochaska Jason X., Gawiser Eric, Wolfe Arthur M. Galactic Chemical Abundances at z>3. I. First Results from the Echellette Spectrograph and Imager // . V 2001a. 552, 1. 99–105.

Prochaska Jason X., Gawiser Eric, Wolfe Arthur M., Castro Sandra, Djorgovski S. G. The Age-Metallicity Relation of the Universe in Neutral Gas: The First 100 Damped Lyα Systems // . IX 2003a. 595, 1. L9–L12.

Prochaska Jason X., Gawiser Eric, Wolfe Arthur M., Cooke Jeff, Gelino Dawn. The ESI/Keck II Damped Lyα Abundance Database // . VIII 2003b. 147, 2. 227–264.

Prochaska Jason X., Herbert-Fort Stéphane, Wolfe Arthur M. The SDSS Damped Lyα Survey: Data Release 3 // . XII 2005. 635, 1. 123–142.

Prochaska Jason X., Howk J. Christopher, O'Meara John M., Tytler David, Wolfe Arthur M., Kirkman David, Lubin Dan, Suzuki Nao. The UCSD HIRES/Keck I Damped Lyα Abundance Database. III. An Empirical Study of Photoionization in the Damped Lyα System toward GB 1759+7539 // . VI 2002a. 571, 2. 693–711.

Prochaska Jason X., Ryan-Weber Emma, Staveley-Smith Lister. Probing the H I Kinematics of the Large Magellenic Cloud: Toward Interpreting Quasar Absorption-Line Observations of Protogalactic Velocity Fields // . XI 2002b. 114, 801. 1197–1205.

Prochaska Jason X., Wolfe Arthur M. On the Kinematics of the Damped Lyman-α Protogalaxies // . IX 1997. 487, 1. 73–95.

Prochaska Jason X., Wolfe Arthur M. Chemical Abundances of the Damped Lyα Systems at z>1.5 // . IV 1999. 121, 2. 369–415.

Prochaska Jason X., Wolfe Arthur M. Metallicity Evolution in the Early Universe // . IV 2000. 533, 1. L5–L8.

Prochaska Jason X., Wolfe Arthur M. The UCSD HIRES/Keck I Damped Lyα Abundance Database. II. The Implications // . II 2002a. 566, 1. 68–92.

Prochaska Jason X., Wolfe Arthur M. The UCSD HIRES/Keck I Damped Lyα Abundance Database. II. The Implications // . II 2002b. 566, 1. 68–92.

Prochaska Jason X., Wolfe Arthur M., Howk J. Christopher, Gawiser Eric, Burles Scott M., Cooke Jeff. The UCSD/Keck Damped Lyα Abundance Database: A Decade of High-Resolution Spectroscopy // . VII 2007a. 171, 1. 29–60.

Prochaska Jason X., Wolfe Arthur M., Howk J. Christopher, Gawiser Eric, Burles Scott M., Cooke Jeff. The UCSD/Keck Damped Lyα Abundance Database: A Decade of High-Resolution Spectroscopy // . VII 2007b. 171, 1. 29–60.

Prochaska Jason X., Wolfe Arthur M., Tytler David, Burles Scott, Cooke Jeff, Gawiser Eric, Kirkman David, O'Meara John M., Storrie-Lombardi Lisa. The UCSD HIRES/Keck I Damped Lyα Abundance Database. I. The Data // . XI 2001b. 137, 1. 21–73.

Prusinski Nikolaus Z., Chen Yuguang. KCWIKit: KCWI Post-Processing and Improvements. IV 2024.

Prusinski Nikolaus Z., Erb Dawn K., Martin Crystal L. Connecting Galactic Outflows and Star Formation: Inferences from Hα Maps and Absorption-line Spectroscopy at $1 \lesssim z \lesssim 1.5$ // . V 2021. 161, 5. 212.

Prusinski Nikolaus Z., Steidel Charles C., Chen Yuguang. Tomography of the z ~2 Circumgalactic Medium using KBSS Galaxy Pairs // arXiv e-prints. III 2025. arXiv:2503.20037.

Qu Zhijie, Bregman Joel N. Absorption Line Search through Three Local Group Dwarf Galaxy Halos // . III 2022. 927, 2. 228.

Qu Zhijie, Chen Hsiao-Wen, Rudie Gwen C., Johnson Sean D., Zahedy Fakhri S., DePalma David, Boettcher Erin, Cantalupo Sebastiano, Chen Mandy C., Cooksey Kathy L., Faucher-Giguère Claude-André, Li Jennifer I. Hsiu, Lopez Sebastian, Schaye Joop, Simcoe Robert A. The Cosmic Ultraviolet Baryon Survey (CUBS) - VI. Connecting physical properties of the cool circumgalactic medium to galaxies at $z \approx 1$ // . IX 2023. 524, 1. 512–528.

Qu Zhijie, Chen Hsiao-Wen, Rudie Gwen C., Zahedy Fakhri S., Johnson Sean D., Boettcher Erin, Cantalupo Sebastiano, Chen Mandy C., Cooksey Kathy L., DePalma David, Faucher-Giguère Claude-André, Rauch Michael, Schaye Joop, Simcoe Robert A. The Cosmic Ultraviolet Baryon Survey (CUBS) V: on the thermodynamic properties of the cool circumgalactic medium at $z \lesssim 1$ // . XI 2022. 516, 4. 4882–4897.

Rafelski Marc, Wolfe Arthur M., Prochaska J. Xavier, Neeleman Marcel, Mendez Alexander J. Metallicity Evolution of Damped Lyα Systems Out to z ~5 // . VIII 2012. 755, 2. 89.

Rakic Olivera, Schaye Joop, Steidel Charles C., Rudie Gwen C. Neutral Hydrogen Optical Depth near Star-forming Galaxies at $z \approx 2.4$ in the Keck Baryonic Structure Survey // . VI 2012. 751, 2. 94.

Ramburuth-Hurt T., De Cia A., Krogager J. K., Ledoux C., Petitjean P., Péroux C., Dessauges-Zavadsky M., Fynbo J., Wendt M., Bouché N. F., Konstantopoulou C., Jermann I. Chemical diversity of gas in distant galaxies. Metal and dust enrichment and variations within absorbing galaxies // . IV 2023. 672. A68.

Ramírez-Agudelo O. H., Sana H., de Mink S. E., Hénault-Brunet V., de Koter A., Langer N., Tramper F., Gräfener G., Evans C. J., Vink J. S., Dufton P. L., Taylor

W. D. The VLT-FLAMES Tarantula Survey. XXI. Stellar spin rates of O-type spectroscopic binaries // . VIII 2015. 580. A92.

Reddy Naveen A., Kriek Mariska, Shapley Alice E., Freeman William R., Siana Brian, Coil Alison L., Mobasher Bahram, Price Sedona H., Sanders Ryan L., Shivaei Irene. The MOSDEF Survey: Measurements of Balmer Decrements and the Dust Attenuation Curve at Redshifts z ~1.4-2.6 // . VI 2015. 806, 2. 259.

Reddy Naveen A., Pettini Max, Steidel Charles C., Shapley Alice E., Erb Dawn K., Law David R. The Characteristic Star Formation Histories of Galaxies at Redshifts z ~2-7 // . VII 2012. 754, 1. 25.

Reddy Naveen A., Steidel Charles C. A Steep Faint-End Slope of the UV Luminosity Function at z ~2-3: Implications for the Global Stellar Mass Density and Star Formation in Low-Mass Halos // . II 2009. 692, 1. 778–803.

Richards Gordon T., Fan Xiaohui, Newberg Heidi Jo, Strauss Michael A., Vanden Berk Daniel E., Schneider Donald P., Yanny Brian, Boucher Adam, Burles Scott, Frieman Joshua A., Gunn James E., Hall Patrick B., Ivezić Željko, Kent Stephen, Loveday Jon, Lupton Robert H., Rockosi Constance M., Schlegel David J., Stoughton Chris, SubbaRao Mark, York Donald G. Spectroscopic Target Selection in the Sloan Digital Sky Survey: The Quasar Sample // . VI 2002. 123, 6. 2945–2975.

Roederer Ian U., Kirby Evan N. Detailed abundance analysis of the brightest star in Segue 2, the least massive galaxy // . V 2014. 440, 3. 2665–2675.

Roederer Ian U., Mateo Mario, Bailey III John I., Song Yingyi, Bell Eric F., Crane Jeffrey D., Loebman Sarah, Nidever David L., Olszewski Edward W., Shectman Stephen A., Thompson Ian B., Valluri Monica, Walker Matthew G. Detailed Chemical Abundances in the r-process-rich Ultra-faint Dwarf Galaxy Reticulum 2 // . III 2016. 151, 3. 82.

Rogers Noah S. J., Strom Allison L., Rudie Gwen C., Trainor Ryan F., Raptis Menelaos, von Raesfeld Caroline. CECILIA: Direct O, N, S, and Ar Abundances in Q2343-D40, a Galaxy at z ~ 3 // . III 2024. 964, 1. L12.

Romano D., Karakas A. I., Tosi M., Matteucci F. Quantifying the uncertainties of chemical evolution studies. II. Stellar yields // . XI 2010. 522. A32.

Romano M., Nanni A., Donevski D., Ginolfi M., Jones G. C., Shivaei I., Junais , Salak D., Sawant P. Star-formation-driven outflows in local dwarf galaxies as revealed from [CII] observations by Herschel // . IX 2023. 677. A44.

Rudie Gwen C., Newman Andrew B., Murphy Michael T. A Unique View of AGN-driven Molecular Outflows: The Discovery of a Massive Galaxy Counterpart to a Z = 2.4 High-metallicity Damped Lyα Absorber // . VII 2017. 843, 2. 98.

Rudie Gwen C., Steidel Charles C., Pettini Max, Trainor Ryan F., Strom Allison L., Hummels Cameron B., Reddy Naveen A., Shapley Alice E. Column Density, Kinematics, and Thermal State of Metal-bearing Gas within the Virial Radius of z ~ 2 Star-forming Galaxies in the Keck Baryonic Structure Survey // . XI 2019. 885, 1. 61.

Rudie Gwen C., Steidel Charles C., Trainor Ryan F., Rakic Olivera, Bogosavljević Milan, Pettini Max, Reddy Naveen, Shapley Alice E., Erb Dawn K., Law David R. The Gaseous Environment of High-z Galaxies: Precision Measurements of Neutral Hydrogen in the Circumgalactic Medium of z ~2-3 Galaxies in the Keck Baryonic Structure Survey // . V 2012. 750, 1. 67.

Rupke David S. N. IFSFIT: Spectral Fitting for Integral Field Spectrographs. IX 2014. ascl:1409.005.

Rupke David S. N., Gültekin Kayhan, Veilleux Sylvain. Quasar-mode Feedback in Nearby Type 1 Quasars: Ubiquitous Kiloparsec-scale Outflows and Correlations with Black Hole Properties // . XI 2017. 850, 1. 40.

Sameer , Charlton Jane C., Norris Jackson M., Gebhardt Matthew, Churchill Christopher W., Kacprzak Glenn G., Muzahid Sowgat, Narayanan Anand, Nielsen Nikole M., Richter Philipp, Wakker Bart P. Cloud-by-cloud, multiphase, Bayesian modelling: application to four weak, low-ionization absorbers // . II 2021. 501, 2. 2112–2139.

Sánchez-Ramírez R., Ellison S. L., Prochaska J. X., Berg T. A. M., López S., D'Odorico V., Becker G. D., Christensen L., Cupani G., Denney K. D., Pâris I., Worseck G., Gorosabel J. The evolution of neutral gas in damped Lyman α systems from the XQ-100 survey // . III 2016. 456, 4. 4488–4505.

Sanders Ryan L., Shapley Alice E., Topping Michael W., Reddy Naveen A., Brammer Gabriel B. Direct T $_e$-based Metallicities of z = 2–9 Galaxies with JWST/NIRSpec: Empirical Metallicity Calibrations Applicable from Reionization to Cosmic Noon // . II 2024. 962, 1. 24.

Sargent Wallace L. W., Boksenberg A., Steidel Charles C. C IV Absorption in a New Sample of 55 QSOs: Evolution and Clustering of the Heavy-Element Absorption Redshifts // . XII 1988. 68. 539.

Sargent Wallace L. W., Steidel Charles C., Boksenberg A. A Survey of Lyman-Limit Absorption in the Spectra of 59 High-Redshift QSOs // . IV 1989. 69. 703.

*Schady P., Yates R. M., Christensen L., De Cia A., Rossi A., D'Elia V., Heintz K. E., Jakobsson P., Laskar T., Levan A., Salvaterra R., Starling R. L. C., Tanvir N. R., Thöne C. C., Vergani S., Wiersema K., Arabsalmani M., Chen H. W., De Pasquale M., Fruchter A., Fynbo J. P. U., García-Benito R., Gompertz B., Hartmann D., Kouveliotou C., Milvang-Jensen B., Palazzi E., Perley D. A., Piranomonte S., Pugliese G., Savaglio S., Sbarufatti B., Schulze S., Tagliaferri G., Postigo

A. de Ugarte, Watson D., Wiseman P. Comparing emission- and absorption-based gas-phase metallicities in GRB host galaxies at z = 2-4 using JWST // . IV 2024. 529, 3. 2807–2831.

Schmidt M. 3C 273 : A Star-Like Object with Large Red-Shift // . III 1963. 197, 4872. 1040.

Shapley Alice E. Physical Properties of Galaxies from z = 2-4 // . IX 2011. 49, 1. 525–580.

Shapley Alice E., Steidel Charles C., Erb Dawn K., Reddy Naveen A., Adelberger Kurt L., Pettini Max, Barmby Pauline, Huang Jiasheng. Ultraviolet to Mid-Infrared Observations of Star-forming Galaxies at z$\sim$2: Stellar Masses and Stellar Populations // . VI 2005. 626, 2. 698–722.

Sheinis A. I., Bolte M., Epps H. W., Kibrick R. I., Miller J. S., Radovan M. V., Bigelow B. C., Sutin B. M. ESI, a New Keck Observatory Echellette Spectrograph and Imager // . VIII 2002. 114, 798. 851–865.

Simcoe Robert A., Sargent Wallace L. W., Rauch Michael. The Distribution of Metallicity in the Intergalactic Medium at z$\sim$2.5: O VI and C IV Absorption in the Spectra of Seven QSOs // . V 2004. 606, 1. 92–115.

Simcoe Robert A., Sargent Wallace L. W., Rauch Michael, Becker George. Observations of Chemically Enriched QSO Absorbers near z$\sim$2.3 Galaxies: Galaxy Formation Feedback Signatures in the Intergalactic Medium // . II 2006. 637, 2. 648–668.

Simon Joshua D., Frebel Anna, McWilliam Andrew, Kirby Evan N., Thompson Ian B. High-resolution Spectroscopy of Extremely Metal-poor Stars in the Least Evolved Galaxies: Leo IV // . VI 2010. 716, 1. 446–452.

Skúladóttir Á., Salvadori S., Pettini M., Tolstoy E., Hill V. The chemical connection between damped Lyman-α systems and Local Group dwarf galaxies // . VII 2018. 615. A137.

Smartt S. J. Observational Constraints on the Progenitors of Core-Collapse Supernovae: The Case for Missing High-Mass Stars // . IV 2015. 32. e016.

Smith Graeme H., Briley Michael M. CN Abundance Inhomogeneities in the Globular Cluster Messier 13 (NGC 6205): Results Based on Merged Data Sets from the Literature // . V 2006. 118, 843. 740–753.

Smithsonian Astrophysical Observatory . SAOImage DS9: A utility for displaying astronomical images in the X11 window environment. III 2000.

Sosey Megan, Bradley Larry, SipÅcz Brigitta, Yoachim Peter, Jeschke Eric, Lim P. L., Tollerud Erik, Craig Matt, Bray E. M., Kurtz Heather, Soref Josh, Robitaille Thomas, Hoyt Taylor, Deil Christoph, Eisenhamer Jonathan. imexam: IMage EXAMination and plotting. III 2022.

Spite M., Spite F., François P., Bonifacio P., Caffau E., Salvadori S. A CEMP-no star in the ultra-faint dwarf galaxy Pisces II // . IX 2018. 617. A56.

Spitzer Lyman Jr. On a Possible Interstellar Galactic Corona. // . VII 1956. 124. 20.

Srianand R., Gupta N., Petitjean P., Noterdaeme P., Ledoux C. Detection of 21-cm, H_2 and deuterium absorption at z > 3 along the line of sight to J1337+3152 // . VII 2010. 405, 3. 1888–1900.

Srianand R., Gupta N., Petitjean P., Noterdaeme P., Ledoux C., Salter C. J., Saikia D. J. Search for cold gas in z > 2 damped Lyα systems: 21-cm and H_2 absorption // . III 2012. 421, 1. 651–665.

Srianand Raghunathan, Petitjean Patrick, Ledoux Cédric, Ferland Gary, Shaw Gargi. The VLT-UVES survey for molecular hydrogen in high-redshift damped Lyman α systems: physical conditions in the neutral gas // . IX 2005. 362, 2. 549–568.

Stacy Athena, Bromm Volker, Lee Aaron T. Building up the Population III initial mass function from cosmological initial conditions // . X 2016. 462, 2. 1307–1328.

Stanway E. R., Eldridge J. J. Re-evaluating old stellar populations // . IX 2018. 479, 1. 75–93.

Steidel Charles C., Adelberger Kurt L., Shapley Alice E., Pettini Max, Dickinson Mark, Giavalisco Mauro. Lyman Break Galaxies at Redshift z $\sim$3: Survey Description and Full Data Set // . VIII 2003. 592, 2. 728–754.

Steidel Charles C., Bogosavljević Milan, Shapley Alice E., Kollmeier Juna A., Reddy Naveen A., Erb Dawn K., Pettini Max. Diffuse Lyα Emitting Halos: A Generic Property of High-redshift Star-forming Galaxies // . VIII 2011. 736, 2. 160.

Steidel Charles C., Bogosavljević Milan, Shapley Alice E., Reddy Naveen A., Rudie Gwen C., Pettini Max, Trainor Ryan F., Strom Allison L. The Keck Lyman Continuum Spectroscopic Survey (KLCS): The Emergent Ionizing Spectrum of Galaxies at z ~ 3 // . XII 2018. 869, 2. 123.

Steidel Charles C., Erb Dawn K., Shapley Alice E., Pettini Max, Reddy Naveen, Bogosavljević Milan, Rudie Gwen C., Rakic Olivera. The Structure and Kinematics of the Circumgalactic Medium from Far-ultraviolet Spectra of z $\sim$= 2-3 Galaxies // . VII 2010. 717, 1. 289–322.

Steidel Charles C., Giavalisco Mauro, Pettini Max, Dickinson Mark, Adelberger Kurt L. Spectroscopic Confirmation of a Population of Normal Star-forming Galaxies at Redshifts Z > 3 // . V 1996. 462. L17.

Steidel Charles C., Pettini Max, Hamilton Donald. Lyman Imaging of High-Redshift Galaxies.III.New Observations of Four QSO Fields // . XII 1995. 110. 2519.

Steidel Charles C., Rudie Gwen C., Strom Allison L., Pettini Max, Reddy Naveen A., Shapley Alice E., Trainor Ryan F., Erb Dawn K., Turner Monica L., Konidaris Nicholas P., Kulas Kristin R., Mace Gregory, Matthews Keith, McLean Ian S. Strong Nebular Line Ratios in the Spectra of z ∼2-3 Star Forming Galaxies: First Results from KBSS-MOSFIRE // . XI 2014. 795, 2. 165.

Steidel Charles C., Shapley Alice E., Pettini Max, Adelberger Kurt L., Erb Dawn K., Reddy Naveen A., Hunt Matthew P. A Survey of Star-forming Galaxies in the 1.4<<∼2.5 Redshift Desert: Overview // . IV 2004. 604, 2. 534–550.

Steidel Charles C., Strom Allison L., Pettini Max, Rudie Gwen C., Reddy Naveen A., Trainor Ryan F. Reconciling the Stellar and Nebular Spectra of High-redshift Galaxies // . VIII 2016. 826, 2. 159.

Steigman Gary, Werner Michael W., Geldon Fred M. Ionization Equilibrium of Interstellar Nitrogen: a Probe for the Intercloud Medium? // . IX 1971. 168. 373.

Strickland David K., Heckman Timothy M. Supernova Feedback Efficiency and Mass Loading in the Starburst and Galactic Superwind Exemplar M82 // . VI 2009. 697, 2. 2030–2056.

Strom Allison L., Rudie Gwen C., Steidel Charles C., Trainor Ryan F. Chemical Abundance Scaling Relations for Multiple Elements in z 2-3 Star-forming Galaxies // . II 2022. 925, 2. 116.

Strom Allison L., Steidel Charles C., Rudie Gwen C., Trainor Ryan F., Pettini Max. Measuring the Physical Conditions in High-redshift Star-forming Galaxies: Insights from KBSS-MOSFIRE // . XII 2018. 868, 2. 117.

Strom Allison L., Steidel Charles C., Rudie Gwen C., Trainor Ryan F., Pettini Max, Reddy Naveen A. Nebular Emission Line Ratios in z 2-3 Star-forming Galaxies with KBSS-MOSFIRE: Exploring the Impact of Ionization, Excitation, and Nitrogen-to-Oxygen Ratio // . II 2017. 836, 2. 164.

Sukhbold Tuguldur, Ertl T., Woosley S. E., Brown Justin M., Janka H. T. Core-collapse Supernovae from 9 to 120 Solar Masses Based on Neutrino-powered Explosions // . IV 2016. 821, 1. 38.

Theios Rachel L., Steidel Charles C., Strom Allison L., Rudie Gwen C., Trainor Ryan F., Reddy Naveen A. Dust Attenuation, Star Formation, and Metallicity in z $\sim$ 2-3 Galaxies from KBSS-MOSFIRE // . I 2019. 871, 1. 128.

Trainor Ryan F., Steidel Charles C. The Halo Masses and Galaxy Environments of Hyperluminous QSOs at z ∼= 2.7 in the Keck Baryonic Structure Survey // . VI 2012. 752, 1. 39.

Trainor Ryan F., Steidel Charles C., Strom Allison L., Rudie Gwen C. The Spectroscopic Properties of Lyα-Emitters at z ~2.7: Escaping Gas and Photons from Faint Galaxies // . VIII 2015. 809, 1. 89.

Tremonti Christy A., Heckman Timothy M., Kauffmann Guinevere, Brinchmann Jarle, Charlot Stéphane, White Simon D. M., Seibert Mark, Peng Eric W., Schlegel David J., Uomoto Alan, Fukugita Masataka, Brinkmann Jon. The Origin of the Mass-Metallicity Relation: Insights from 53,000 Star-forming Galaxies in the Sloan Digital Sky Survey // . X 2004. 613, 2. 898–913.

Tumlinson J., Thom C., Werk J. K., Prochaska J. X., Tripp T. M., Weinberg D. H., Peeples M. S., O'Meara J. M., Oppenheimer B. D., Meiring J. D., Katz N. S., Davé R., Ford A. B., Sembach K. R. The Large, Oxygen-Rich Halos of Star-Forming Galaxies Are a Major Reservoir of Galactic Metals // Science. XI 2011. 334, 6058. 948.

Tumlinson Jason, Peeples Molly S., Werk Jessica K. The Circumgalactic Medium // . VIII 2017. 55, 1. 389–432.

Tumlinson Jason, Thom Christopher, Werk Jessica K., Prochaska J. Xavier, Tripp Todd M., Katz Neal, Davé Romeel, Oppenheimer Benjamin D., Meiring Joseph D., Ford Amanda Brady, O'Meara John M., Peeples Molly S., Sembach Kenneth R., Weinberg David H. The COS-Halos Survey: Rationale, Design, and a Census of Circumgalactic Neutral Hydrogen // . XI 2013. 777, 1. 59.

Turner Monica L., Schaye Joop, Steidel Charles C., Rudie Gwen C., Strom Allison L. Metal-line absorption around z ≈ 2.4 star-forming galaxies in the Keck Baryonic Structure Survey // . XI 2014. 445, 1. 794–822.

Turner Monica L., Schaye Joop, Steidel Charles C., Rudie Gwen C., Strom Allison L. Detection of hot, metal-enriched outflowing gas around z ≈ 2.3 star-forming galaxies in the Keck Baryonic Structure Survey // . VI 2015. 450, 2. 2067–2082.

Vartanyan David, Burrows Adam. Gravitational Waves from Neutrino Emission Asymmetries in Core-collapse Supernovae // . X 2020. 901, 2. 108.

Veilleux Sylvain, Osterbrock Donald E. Spectral Classification of Emission-Line Galaxies // . II 1987. 63. 295.

Vernet J., Dekker H., D'Odorico S., Kaper L., Kjaergaard P., Hammer F., Randich S., Zerbi F., Groot P. J., Hjorth J., Guinouard I., Navarro R., Adolfse T., Albers P. W., Amans J. P., Andersen J. J., Andersen M. I., Binetruy P., Bristow P., Castillo R., Chemla F., Christensen L., Conconi P., Conzelmann R., Dam J., de Caprio V., de Ugarte Postigo A., Delabre B., di Marcantonio P., Downing M., Elswijk E., Finger G., Fischer G., Flores H., François P., Goldoni P., Guglielmi L., Haigron R., Hanenburg H., Hendriks I., Horrobin M., Horville D., Jessen N. C., Kerber F., Kern L., Kiekebusch M., Kleszcz P., Klougart J., Kragt J., Larsen H. H., Lizon J. L., Lucuix C., Mainieri V., Manuputy R., Martayan C., Mason E., Mazzoleni R., Michaelsen N., Modigliani A., Moehler S., Møller P., Norup Sørensen A., Nørregaard P., Péroux C., Patat F., Pena E., Pragt J., Reinero C., Rigal F., Riva M., Roelfsema R., Royer F., Sacco G., Santin P., Schoenmaker T., Spano P., Sweers E., Ter Horst R., Tintori M., Tromp N., van Dael P., van der Vliet H., Venema L., *Vidali M., Vinther J., Vola P., Winters R., Wistisen D., Wulterkens G., Zacchei A.* X-shooter, the new wide band intermediate resolution spectrograph at the ESO Very Large Telescope // . XII 2011. 536. A105.

Vladilo G. Chemical abundances of damped Ly alpha systems:. A new method for estimating dust depletion effects // . VIII 2002. 391. 407–415.

Vladilo G., Centurión M., Levshakov S. A., Péroux C., Khare P., Kulkarni V. P., York D. G. Extinction and metal column density of HI regions up to redshift z 2 // . VII 2006. 454, 1. 151–164.

Vladilo Giovanni. Dust and Elemental Abundances in Damped Lyα Absorbers // . I 1998. 493, 2. 583–594.

Vladilo Giovanni, Gioannini Lorenzo, Matteucci Francesca, Palla Marco. Evolution of the Dust Composition in Damped Lyα Systems // . XII 2018. 868, 2. 127.

Vogt S. S., Allen S. L., Bigelow B. C., Bresee L., Brown B., Cantrall T., Conrad A., Couture M., Delaney C., Epps H. W., Hilyard D., Hilyard D. F., Horn E., Jern N., Kanto D., Keane M. J., Kibrick R. I., Lewis J. W., Osborne J., Pardeilhan G. H., Pfister T., Ricketts T., Robinson L. B., Stover R. J., Tucker D., Ward J., Wei M. Z. HIRES: the high-resolution echelle spectrometer on the Keck 10-m Telescope // Instrumentation in Astronomy VIII. 2198. VI 1994. 362. (Society of Photo-Optical Instrumentation Engineers (SPIE) Conference Series).

Wakker B. P., van Woerden H. High-Velocity Clouds // . I 1997. 35. 217–266.

Wang Wei-Hao, Kanekar Nissim, Prochaska J. Xavier. A search for Hα emission in high-metallicity damped Lyman α systems at z ~ 2.4 // . IV 2015. 448, 3. 2832–2839.

Watson D. The Galactic dust-to-metals ratio and metallicity using gamma-ray bursts // . IX 2011. 533. A16.

Weatherley S. J., Warren S. J., Møller P., Fall S. M., Fynbo J. U., Croom S. M. The first detection of [OIII] emission from high-redshift damped Lyman-α galaxies // . IV 2005. 358, 3. 985–997.

Welsh Louise, Cooke Ryan, Fumagalli Michele. Modelling the chemical enrichment of Population III supernovae: the origin of the metals in near-pristine gas clouds // . VIII 2019. 487, 3. 3363–3376.

Welsh Louise, Cooke Ryan, Fumagalli Michele, Pettini Max. A bound on the $^{12}C/^{13}C$ ratio in near-pristine gas with ESPRESSO // . III 2020. 494, 1. 1411–1423.

Werk Jessica K., Prochaska J. Xavier, Thom Christopher, Tumlinson Jason, Tripp Todd M., O'Meara John M., Peeples Molly S. The COS-Halos Survey: An Empirical Description of Metal-line Absorption in the Low-redshift Circumgalactic Medium // . II 2013. 204, 2. 17.

Werk Jessica K., Prochaska J. Xavier, Tumlinson Jason, Peeples Molly S., Tripp Todd M., Fox Andrew J., Lehner Nicolas, Thom Christopher, O'Meara John M., Ford Amanda Brady, Bordoloi Rongmon, Katz Neal, Tejos Nicolas, Oppenheimer Benjamin D., Davé Romeel, Weinberg David H. The COS-Halos Survey: Physical Conditions and Baryonic Mass in the Low-redshift Circumgalactic Medium // . IX 2014. 792, 1. 8.

Wetzel Andrew R., Deason Alis J., Garrison-Kimmel Shea. Satellite Dwarf Galaxies in a Hierarchical Universe: Infall Histories, Group Preprocessing, and Reionization // . VII 2015. 807, 1. 49.

Wilson John C., Eikenberry Stephen S., Henderson Charles P., Hayward Thomas L., Carson Joseph C., Pirger Bruce, Barry Donald J., Brandl Bernhard R., Houck James R., Fitzgerald Gregory J., Stolberg T. M. A Wide-Field Infrared Camera for the Palomar 200-inch Telescope // Instrument Design and Performance for Optical/Infrared Ground-based Telescopes. 4841. III 2003. 451–458. (Society of Photo-Optical Instrumentation Engineers (SPIE) Conference Series).

Wolfe A. M., Turnshek D. A., Smith H. E., Cohen R. D. Damped Lyman-Alpha Absorption by Disk Galaxies with Large Redshifts. I. The Lick Survey // . VI 1986. 61. 249.

Wolfe Arthur M., Gawiser Eric, Prochaska Jason X. C II* Absorption in Damped Lyα Systems. II. A New Window on the Star Formation History of the Universe // . VIII 2003. 593, 1. 235–257.

Wolfe Arthur M., Gawiser Eric, Prochaska Jason X. Damped Ly α Systems // . IX 2005. 43, 1. 861–918.

Woosley S. E. Pulsational Pair-instability Supernovae // . II 2017. 836, 2. 244.

Woosley S. E., Heger A., Weaver T. A. The evolution and explosion of massive stars // Reviews of Modern Physics. XI 2002. 74, 4. 1015–1071.

Woosley S. E., Weaver Thomas A. The Evolution and Explosion of Massive Stars. II. Explosive Hydrodynamics and Nucleosynthesis // . XI 1995. 101. 181.

York Donald G., Adelman J., Anderson John E. Jr., Anderson Scott F., Annis James, Bahcall Neta A., Bakken J. A., Barkhouser Robert, Bastian Steven, Berman Eileen, Boroski William N., Bracker Steve, Briegel Charlie, Briggs John W., Brinkmann J., Brunner Robert, Burles Scott, Carey Larry, Carr Michael A., Castander Francisco J., Chen Bing, Colestock Patrick L., Connolly A. J., Crocker J. H., Csabai István, Czarapata Paul C., Davis John Eric, Doi Mamoru, Dombeck Tom, Eisenstein Daniel, Ellman Nancy, Elms Brian R., Evans Michael L., Fan Xiaohui, Federwitz Glenn R., Fiscelli Larry, Friedman Scott, Frieman Joshua A., Fukugita Masataka, Gillespie Bruce, Gunn James E., Gurbani Vijay K., de Haas Ernst, Haldeman Merle, Harris Frederick H., Hayes J., Heckman Timothy M., Hennessy G. S., Hindsley Robert B., Holm Scott, Holmgren Donald J., Huang Chi-hao, *Hull Charles, Husby Don, Ichikawa Shin-Ichi, Ichikawa Takashi, Ivezić Željko, Kent Stephen, Kim Rita S. J., Kinney E., Klaene Mark, Kleinman A. N., Kleinman S., Knapp G. R., Korienek John, Kron Richard G., Kunszt Peter Z., Lamb D. Q., Lee B., Leger R. French, Limmongkol Siriluk, Lindenmeyer Carl, Long Daniel C., Loomis Craig, Loveday Jon, Lucinio Rich, Lupton Robert H., MacKinnon Bryan, Mannery Edward J., Mantsch P. M., Margon Bruce, McGehee Peregrine, McKay Timothy A., Meiksin Avery, Merelli Aronne, Monet David G., Munn Jeffrey A., Narayanan Vijay K., Nash Thomas, Neilsen Eric, Neswold Rich, Newberg Heidi Jo, Nichol R. C., Nicinski Tom, Nonino Mario, Okada Norio, Okamura Sadanori, Ostriker Jeremiah P., Owen Russell, Pauls A. George, Peoples John, Peterson R. L., Petravick Donald, Pier Jeffrey R., Pope Adrian, Pordes Ruth, Prosapio Angela, Rechenmacher Ron, Quinn Thomas R., Richards Gordon T., Richmond Michael W., Rivetta Claudio H., Rockosi Constance M., Ruthmansdorfer Kurt, Sandford Dale, Schlegel David J., Schneider Donald P., Sekiguchi Maki, Sergey Gary, Shimasaku Kazuhiro, Siegmund Walter A., Smee Stephen, Smith J. Allyn, Snedden S., Stone R., Stoughton Chris, Strauss Michael A., Stubbs Christopher, SubbaRao Mark, Szalay Alexander S., Szapudi Istvan, Szokoly Gyula P., Thakar Anirudda R., Tremonti Christy, Tucker Douglas L., Uomoto Alan, Vanden Berk Dan, Vogeley Michael S., Waddell Patrick, Wang Shu-i., Watanabe Masaru, Weinberg David H., Yanny Brian, Yasuda Naoki, SDSS Collaboration* . The Sloan Digital Sky Survey: Technical Summary // . IX 2000. 120, 3. 1579–1587.

Zafar T., Centurión M., Molaro P., Péroux C., D'Odorico V., Vladilo G. Nitrogen abundances in damped Lyalpha absorbers // . I 2014a. 85. 363.

Zafar T., Péroux C., Popping A., Milliard B., Deharveng J. M., Frank S. The ESO UVES advanced data products quasar sample. II. Cosmological evolution of the neutral gas mass density // . VIII 2013. 556. A141.

Zafar Tayyaba, Centurión Miriam, Péroux Céline, Molaro Paolo, D'Odorico Valentina, Vladilo Giovanni, Popping Attila. The ESO UVES advanced data products quasar sample - III. Evidence of bimodality in the [N/α] distribution // . X 2014b. 444, 1. 744–756.

Zafar Tayyaba, Vladilo Giovanni, Péroux Céline, Molaro Paolo, Centurión Miriam, D'Odorico Valentina, Abbas Kumail, Popping Attila. The ESO UVES Advanced Data Products Quasar Sample - IV. On the deficiency of argon in DLA systems // . XII 2014c. 445, 2. 2093–2105.

Zahedy Fakhri S., Chen Hsiao-Wen, Cooper Thomas M., Boettcher Erin, Johnson Sean D., Rudie Gwen C., Chen Mandy C., Cantalupo Sebastiano, Cooksey Kathy L., Faucher-Giguère Claude-André, Greene Jenny E., Lopez Sebastian, Mulchaey John S., Penton Steven V., Petitjean Patrick, Putman Mary E., Rafelski Marc, Rauch Michael, Schaye Joop, Simcoe Robert A., Walth Gregory L. The Cosmic Ultraviolet Baryon Survey (CUBS) - III. Physical properties and elemental abundances of Lyman-limit systems at z < 1 // . IX 2021. 506, 1. 877–902.

Zheng Yong, Faerman Yakov, Oppenheimer Benjamin D., Putman Mary E., McQuinn Kristen B. W., Kirby Evan N., Burchett Joseph N., Telford O. Grace, Werk Jessica K., Kim Doyeon A. A Comprehensive Investigation of Metals in the Circumgalactic Medium of Nearby Dwarf Galaxies // . I 2024. 960, 1. 55.

Zheng Zheng, Miralda-Escudé Jordi. Self-shielding Effects on the Column Density Distribution of Damped Lyα Systems // . IV 2002. 568, 2. L71–L74.

de los Reyes Mithi A. C., Kirby Evan N., Seitenzahl Ivo R., Shen Ken J. Manganese Indicates a Transition from Sub- to Near-Chandrasekhar Type Ia Supernovae in Dwarf Galaxies // . III 2020. 891, 1. 85.